A-Site Compensated Donor-Doped $SrTiO_3$

Chloe Jane Fisher

Supervisor: Professor Andrew Bell
Sponsors: Thales UK and EPSRC

The University of Leeds
School of Chemical and Process Engineering

January 2022

Acknowledgements

To Professor Andrew Bell, my project supervisor at the University of Leeds. Thank you for initially accepting me into your research group as a Master's student back in 2015, and then encouraging me to take up a PhD with you in 2017. Thank you for trusting me with an exciting and novel subject and for helping me to stay motivated throughout the project; our meetings always left me with a renewed sense of enthusiasm and determination to achieve our goals.

Thank you to EPSRC and Thales UK for funding the PhD project, as well as to Dr. Laura Stoica for being a supportive industrial supervisor.

A huge thank you to Rob Simpson for all of his technical assistance and support throughout my project.

To Danielle Woodruff, thank you for taking my SEM images throughout my project, and for your friendship since our Masters' degrees.

To Dr. Tim Comyn thank you for my time working at Ionix, I learnt a lot of valuable information about piezoelectric ceramics and will always be grateful for the support you have given me.

Thank you to Dr. Faye Esat and Dr. Sam Parry for their assistance with X-ray diffraction and Rietveld refinement throughout the project.

A big thank you to my proof-readers Andy, Tim, Laura, and Sam for your prompt and helpful responses.

To my family and Sam. Thank you for encouraging me through an unpredictable pandemic-ridden PhD. Thank you for your unwavering support, patience, and for helping me to believe I can do anything I set my mind to. All my love always.

For my Mum, Jane…

Abstract

The initial motivations of this thesis were to dope paraelectric $SrTiO_3$ with niobium alongside an A-site vacancy compensation scheme so as to study the resulting chemical defects and potentially manipulate them in order to create a macroscopic dipole to induce a piezoelectric effect. However, it is made clear that this thesis is not an attempt at creating a new, nor modifying an existing, *ferroelectric* system.

This thesis will cover an introduction to piezoelectric and ferroelectric materials, due to the author's inclusion within a piezoelectric research group, from which stemmed the idea for this research. A literature review into the defect chemistry of $SrTiO_3$ was carried out, including the effects of non-stoichiometric $SrTiO_3$, acceptor and donor doping, followed by a review of existing defect dipole research. Samples of $Sr_{1-x/2}Ti_{1-x}Nb_xO_3$, $Sr_{0.9}Ti_{1-x}Nb_xO_3$, $SrTi_{1-x}Nb_xO_3$, $SrTi_{1-x}Mn_xO_3$ and $SrTi_{1-x}Co_xO_3$ were produced via the mixed oxide solid state reaction technique. Samples were characterised using X-ray diffraction and scanning electron microscopy. Following this electrical characterisation was carried out and impedance, electric modulus and permittivity data were examined in order to better understand the defect mechanisms taking place. Complex impedance analysis was used as an initial comparison of conductivity before deeper analysis of the frequency dependence of impedance and modulus data was conducted.

Detailed analysis of the impedance and modulus data showed that electronic conduction dominated the electrical behaviour of all Nb-doped $SrTiO_3$ samples. The conductivity was much more electron-dominated in the B-site Nb-doped samples compared to the A-site vacancy samples. This resulted in a blue colouration of sample pellets, indicating the reduction of Ti^{4+} to Ti^{3+} and higher conductivities. The influence of Sr vacancies is also apparent from the lack of increase in conductivity in the $Sr_{1-x/2}$ samples despite ten times the increase in Nb content. It was shown that the addition of large concentrations of A-site vacancies to the perovskite system enabled it structurally to accommodate large amounts of Nb, but it also significantly reduced the increase in conductivity seen by Nb doping. Equally, the large amount of Nb doping enabled the $SrTiO_3$ system to accept large amounts of Sr deficiencies (up to 15%) by charge compensation. The vacancy/donor compensation scheme is shown to be key to maintaining the $SrTiO_3$ perovskite structure by charge compensation, proven by the $Sr_{0.9}$ sample set which began to eject TiO_2 as a secondary phase as Nb dopant decreased.

Table of Contents

Table of Figures

Table of Tables

Nomenclature

A – electrode/pellet area

a – unit cell parameter

BCTZ – barium calcium-titanate zirconate

C – capacitance

CPE – constant phase element

Ϭ – conductivity

d – piezoelectric strain constant

DFT – density functional theory

d^{33} – piezoelectric charge coefficient

ε^{X} – relative permittivity

E – electric field

E_A – activation energy

E_c – coercive field

EPR – electron paramagnetic resonance spectroscopy

f – frequency

FIB – focused ion beam

g – piezoelectric voltage constant

G - conductance

i – current

j – current density

ICDD – international centre for diffraction data

k – electromechanical coupling coefficient

K_B – Boltzmann constant

KNN – potassium sodium niobate

L – pellet thickness

M – electric modulus

MPB – morphotropic phase boundary

NBT-BT – sodium bismuth titanate – barium titanate

ω – angular frequency

P – polarisation

PNR – polar nano region

P_{O2} – partial pressure of oxygen

P_r – remnant polarisation

PTCR – positive temperature coefficient of resistivity

PZT – $PbZr_{1-x}Ti_xO_3$

Q_m – mechanical quality factor

R – resistance

ρ – density/resistivity

RoHS – restriction of the use of hazardous substances

SEM – scanning electron microscopy

SOFC – solid oxide fuel cell

t – Goldschmidt tolerance factor

T_C – Curie temperature

TEM – transmission electron microscopy

U – voltage signal

V – voltage

WEEE – waste electronic and electrical equipment

X – stress

XPS – X-ray photoelectron spectroscopy

XRD – X-Ray Diffraction

x – strain

YSZ – yttria stabilised zirconia

Z – impedance

1 Introduction

1.1 History of Piezoelectrics

In 1880 α-SiO_2 (quartz) was discovered as the first material displaying the direct piezoelectric effect by the Curie brothers[1], [2]. The term for "pressure" in Greek, "piezo" was used to convey the observed "pressure-electricity"[2]. The converse piezoelectric effect of strain occurring from an applied electric field was discovered by Gabriel Lippmann in 1881[2]. With the outbreak of World War One in 1914, the development of underwater acoustic technology was accelerated leading to the first ultrasonic signal transmission in 1917 off the coast of France by Dr. Paul Langevin with the support of the French Navy[2]. By 1921 Rochelle salt ($KNaC_4H_4O_6$•$4H_2O$) was the first piezoelectric crystal to be artificially synthesised and, despite having a stronger piezoelectric response than quartz, had a poor temperature stability, motivating the search for new materials. In the 1940s Barium Titanate, $BaTiO_3$, was the first polycrystalline ceramic piezoelectric material to be discovered and research into the material accelerated due to pressures from the Second World War. It was quickly implemented in acoustic transducers. $BaTiO_3$ was found to have a much higher dielectric constant than any other ceramics at the time (eg. TiO_2) and the cause of this was discovered to be ferroelectricity, not brought on by hydrogen bonding for the first time[3]. Another important milestone surrounding $BaTiO_3$ was the development of the poling process, whereby rods of $BaTiO_3$ were bent and voltages were observed[3], and a voltage was used to reverse the polarised regions (domains) within the ceramic. Following the research into $BaTiO_3$, Lead Niobite ($Pb(NbO_3)_2$) was discovered in 1952 which was structurally quite different to $BaTiO_3$, and a series of niobate-based materials were investigated. Arguably the greatest milestone in the progress of piezoelectric materials was the development of Lead Zirconate Titanate, PZT, with its strong and stable piezoelectric properties; the leaps in technology subsequently were significant. The current dominant material used in piezoelectric applications is still PZT[4]. PZT is so widely used because it displays the most competitive piezoelectric properties, and is also made from relatively cheap raw materials, which enables it to be used in a wide array of technological applications. Figure 1.1 displays a timeline of the development of piezoelectric materials and the improvement in properties over time. In the book Piezoelectric Ceramics 1971, written by Jaffe et al.[3]. Jaffe comments that "exciting future developments may be expected". Let us hope this is still as true today as it was only 30 years after the initial discovery of piezoelectric materials.

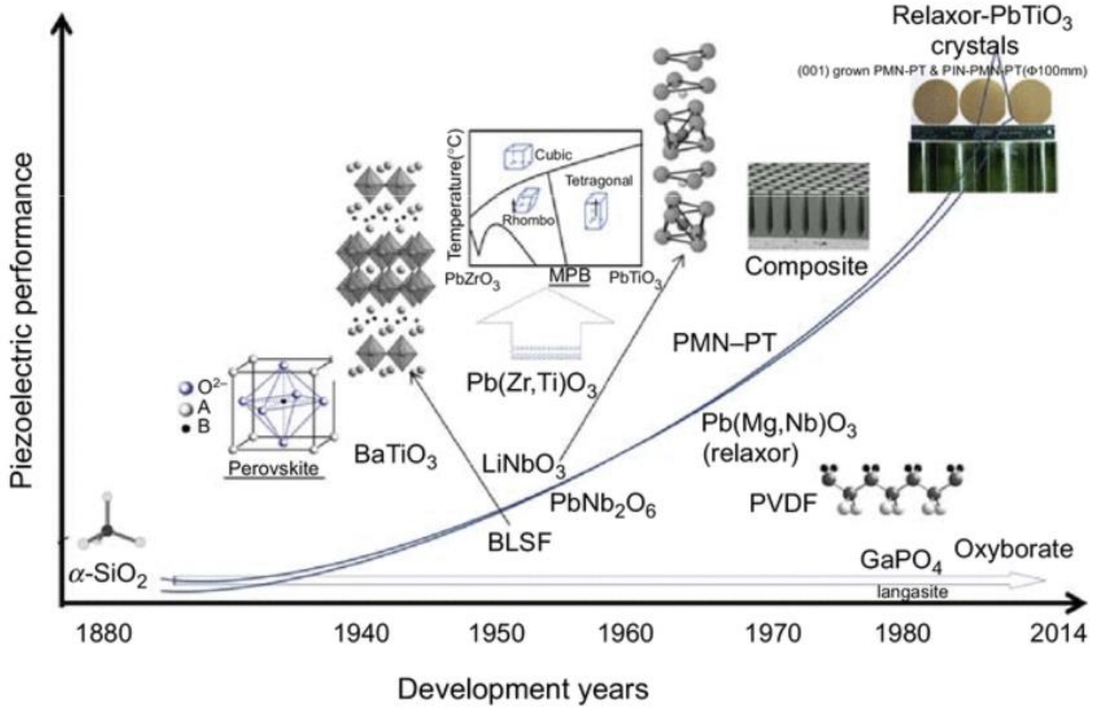

Figure 1.1: Taken from Structural Health Monitoring in Aerospace Structures Book pp. 61[1]. Timeline of piezoelectric discovery and developments.

1.2 Fundamentals of Piezoelectrics

Ferroelectricity is defined by Jaffe et al.[3] as a spontaneous dipole reversible by 180° due to the application of an electric field. In equal conditions it is seen that ferroelectricity is harder to observe in a ceramic in comparison to a single crystal because of the random orientation of grains within a ceramic. There are a number of criteria that are observed in ferroelectrics such as a hysteresis loop of polarisation under an applied alternating electric field and a Curie point, but it is the reversible dipole that is the differentiating criterion for ferroelectricity. Piezoelectric materials are functional materials that can convert mechanical energy into electrical energy, and also convert electrical energy into mechanical energy. This is known as the direct and converse effect, respectively. Piezoelectric materials should be poled to produce a controlled direction of domain orientation in order for them to be used in technological applications, this “freezes in” the domain orientation to create a permanent dipole.

The difficulty or confusion arises when differentiating between piezoelectric and ferroelectric materials, as all ferroelectrics are piezoelectric, but not all piezoelectrics are ferroelectric. Quartz and Rochelle salt are good examples of this. The main property-based difference between ferroelectrics and non-ferroelectric piezoelectrics is their temperature-dependent behaviour[1]. The temperature-dependent properties of non-ferroelectric piezoelectrics, before their melting and/or phase transition temperature is reached, are associated with their electronic/ionic polarisation contributions and thermal expansion as a function of temperature[1]. If the crystal has low resistivity, ionic conduction or space charges dominate their temperature-dependent conduction, for example at high temperatures[1].

An original classical model of ferroelectricity is the “rattling ion model” by Slater[5]. This model suggests that the off-centre position of a B-site cation is due to its size being too small for the surrounding octahedral cage, allowing it to move off-centre when acted upon by electrostatic forces of the surrounding atoms thus creating an asymmetry, and these forces cancel out the long range repulsive forces. This model does not however explain why the majority of ferroelectric materials seem to have B-site cations with a d^0 lowest unoccupied band (conduction band), eg. Ti^{4+}, Zr^{4+}, Nb^{5+}, Ta^{5+}. Energetically speaking long range Coulombic forces prefer an off-center equilibrium position, i.e. it is energetically unfavourable for the structure to form the ‘ideal cubic perovskite’, which is why it is often the high temperature phase of most ferroelectric materials[6].

1.2.1 Crystal Structures and Symmetry

The term ferroelectric refers to a material that has a spontaneous net dipole moment, which can be reversed when subjected to an applied electric field[7]. In order for a net dipole moment to be possible, the crystal structure of the material must be non-centrosymmetric[8]. There are 7 crystal systems: cubic, tetragonal, orthorhombic, trigonal, hexagonal, monoclinic, triclinic, (Figure 1.2) within which there are 32 point groups. 11 of these point groups are centro-symmetric and 21 are non-centrosymmetric[4]. Of these 21 non-centrosymmetric point groups, 10 are polar (pyroelectric)[9]. Non-centrosymmetric point groups (those without inversion centres) can be polar, chiral, both or neither. A polar point group is one whose symmetry operation leaves more than one point in the shape unmoved, and the line between these points is defined as a unique direction within the point group[10]. A chiral point group contains only rotational symmetry operations[10]. A diagram is shown below to show the separation and overlap between materials which fall into the above categories, as their differentiation will be important later in this study. In summary, all ferroelectric materials are pyroelectric, but not all piezoelectrics are ferro- or pyro-electric (Figure 1.3).

Lattice planes can be used to interpret x-ray diffraction data and explain the orientation of a crystal lattice[11]. In a unit cell, the edges of the cell are the lattice parameters, and the axes stemming from a single point of origin are labelled x, y, and z. If a plane within the cell intercepts the x axis at a/2, the y axis at b/1 and z at c/2 then the reciprocal of these are the miller indices 212. If all three axes are not intercepted for example the x axis a/1, y axis b/2 and no interception of the z axis, this would be the 120 plane[11]. Miller indices are represented in round brackets (uvw), directions or vectors in square brackets [uvw] and symmetrically equivalent directions or planes written in triangular brackets <uvw>[11].

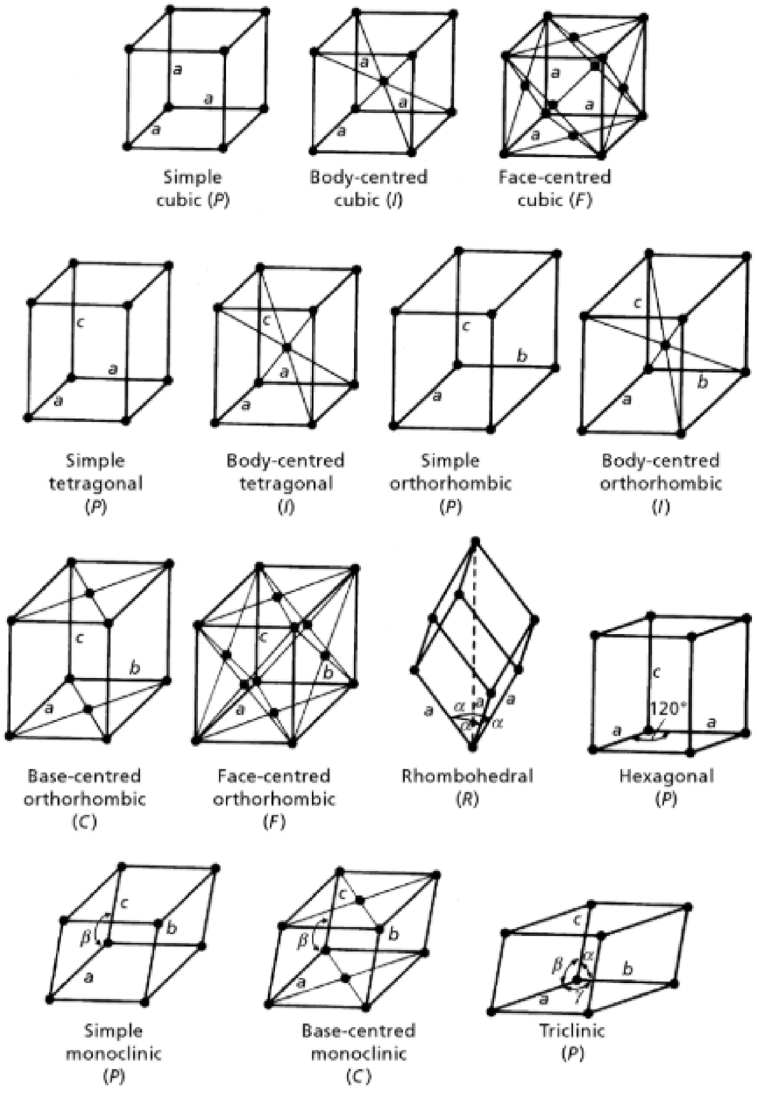

Figure 1.2: Illustration of Bravais lattices or crystal systems[10].

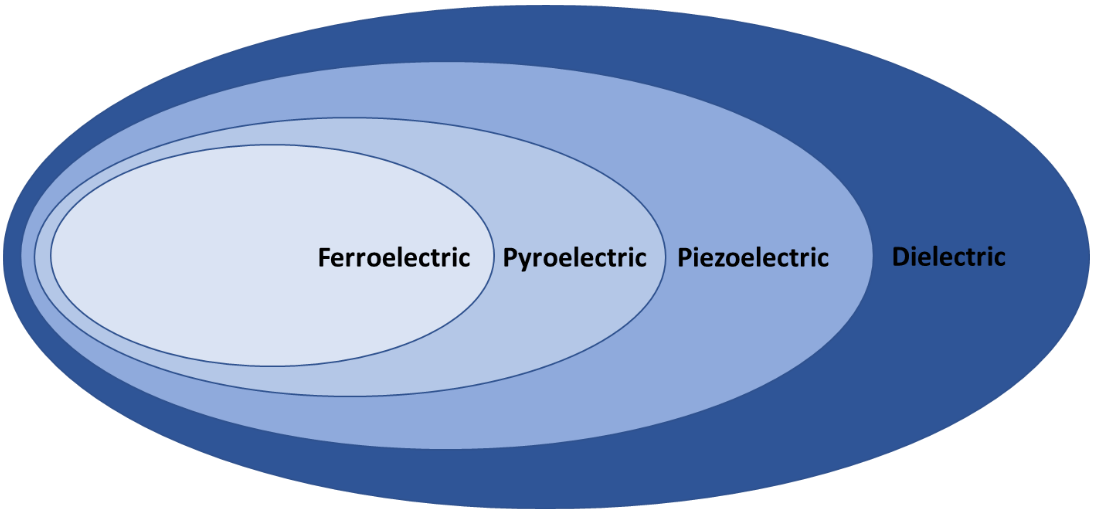

Figure 1.3: Illustration of material types and their relationships, adapted from Shahrokhi et al.[12].

1.2.2 The Perovskite Structure

The most common crystal structure found in piezoelectric materials is the perovskite[13]. The perovskite unit cell structure is a simple cubic unit cell modelled after calcium titanate with the basic chemical formula ABX_3, with the metal cations at the corners (A-site), a traditionally smaller cation in the body-centre location (B-site), and oxygen or fluoride in the face centre locations[13]. This work will consider oxide-based materials. The oxygen ions form an octahedron around the central smaller cation. The larger cations and the oxygen anions form a cubic close packing sublattice across the structure[14]. Ironically $CaTiO_3$ isn't actually the ideal cubic perovskite structure as it is an orthorhombic structure, $SrTiO_3$ is a more accurate representation (Figure 1.4). The 'ideal' perovskite structure is cubic with the space group *Pm-3m* which is often the highest symmetry structure for most materials, and from this parent structure others can form[15].

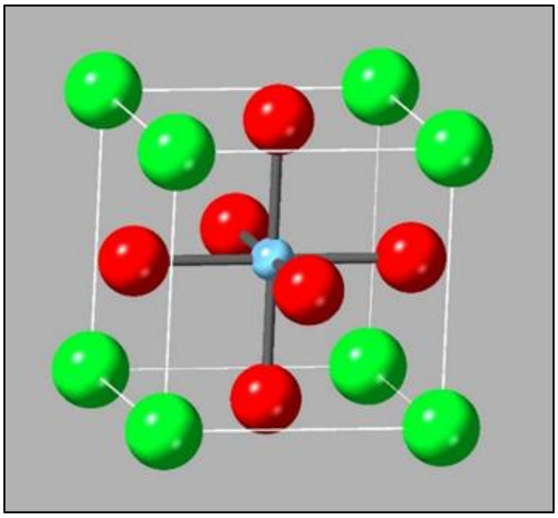

Figure 1.4: Cubic $SrTiO_3$ *Pm-3m* perovskite structure. Made on CrystalMaker software, O is red, Ti is blue and Sr is green.

The perovskite structure can tolerate A, B and O site vacancies along with differences in sizes of the A and B site ions, which can affect the piezoelectric properties of a material[13]. The perovskite unit cell has the flexibility to be able to distort or elongate in certain directions that enables a material to shift between crystal structures under varying conditions, which leads to the resulting piezoelectric properties. There are three ways that have been identified that a perovskite structure can distort[15]. These are: B-site cation displacement, for example that seen in $BaTiO_3$ with the tetragonal structure stemming from the movement of the Ti atom along the c-axis, distortion of the BO_6 octahedra relative to one another, and finally octahedral tilting. Octahedral tilting is defined as movement around a symmetry axes with strict connectivity of the A-site cations. Howard and Stokes[15] observe that this allows flexibility in the A-site coordination whilst the B-site octahedra remain relatively unchanged. In an ‘ideal’ cubic perovskite structure with all elements having perfect spherical radii of R_A, R_B and R_O the following relationship exists:

$$t = \frac{R_A + R_O}{\sqrt{2}(R_B + R_O)} = 1 \qquad [13]$$

Where t = the Goldschmidt tolerance factor. This relationship should be interpreted with caution as it is based on the ionic radii of the atoms, which can change according to coordination number and that in turn can affect the structure itself. There are also many versions of “ionic radii”, the one most people use and the one used in this thesis is that by Shannon[16].

In order for the perovskite structure to be stable *t* must be between 0.9 and 1.1, and significant deviations from this will prevent the material forming the perovskite structure[13]. For example, $LiNbO_3$ despite appearing to be a good candidate for the perovskite structure based on its chemical formula, has a tolerance factor which is too low due to the small size of the Li ion[13]. Instead it forms a structure with the Nb ion still in an octahedral cage, but the Li ions are interstitial ions among the octahedra which are linked at the corners[13]. In occasions where the perovskite unit is formed however, materials with $t<1$ tend to be lower symmetry orthorhombic or rhombohedral structures, and materials with $t>1$ tend to be higher symmetry tetragonal or cubic structures, the cubic of course being paraelectric[13].

1.2.3 Non-Perovskite Piezoelectrics

Besides the most common perovskite structure, there are also three other important structures in piezoelectric materials. Bismuth layered structures behave similarly to perovskites in that they are layers of perovskite with intermediate layers of $(Bi_2O_2)^{2+}$[13]. These structures are frequently tetragonal structure at high temperatures, as there are limitations to distortions and orientation changes, but they do sometimes transition into orthorhombic or monoclinic structures at lower temperatures[13]. Tungsten bronze structured materials have the chemical formula $A_xB_2O_6$, and are particularly complex structures with three types of interstitial cell and five formula units per unit cell[13] and the B-site is often occupied by W, Ti, Ta, or Nb, hence the name tungsten bronze.

There is an emerging group of new ferroelectric materials, which are in the form of simple binary oxides such as HfO_2-ZrO_2 based materials. There is currently a large body of work demonstrating the ferroelectric properties of doped HfO_2 in thin film form for memory devices. Hafnia is a simple binary oxide (non-perovskite) with a good compatibility with silicon and low permittivity and is relatively easy to deposit, which makes it appealing for use in memory device applications[17]. As there has been an increasing area of work into thin film HfO_2, it has been considered that if the same ferroelectric properties could be reproduced in bulk HfO_2 or similar compounds, this could be a promising new area of research for bulk ferroelectrics. HfO_2 in the bulk forms a thermodynamically stable monoclinic crystal structure of the space group $P2_1/c$[18]. This is a centro-symmetric structure and therefore is non-ferroelectric. Phases of higher symmetry HfO_2, such as tetragonal and cubic, were found and stabilised by optimising a combination of processing conditions such as thermal treatment and mechanical strain, among others[19], some of which were ferroelectric. ZrO_2 is chemically very similar to HfO_2 and as such can be used in conjunction with hafnium to form binary structures or used in doping other HfO_2 based systems in order to induce ferroelectricity. This sub-chapter serves to illustrate that there is an expanding body of research into the less traditional ferroelectric perovskite route to piezoelectricity.

1.2.4 Polycrystalline Ceramics

Piezoelectric materials are produced in many forms to suit the requirements of the application, such as polycrystalline ceramics, single crystals and thin films. Polycrystalline ceramics are the focus of this research and consist of crystallites of random orientation, joined by grain boundaries[20] . The advantages to producing polycrystalline ceramics are that production is much quicker and cheaper than single crystal or thin film production as well as much more scalable and repeatable in an industrial setting; some single crystal techniques take up to a month to grow a crystal (Bridgeman method) and a high yield single crystal is not guaranteed at the end of it. Very often the process is unsuccessful and a polycrystal results of a composition that was unintended. The piezoelectric coefficients of polycrystals can sometimes be competitive to those displayed in single crystals and thin films through doping and processing techniques[20]. The piezoelectric properties of a material can vary with direction across the sample[9], however, polycrystalline materials largely possess less anisotropy in comparison to single crystals (poled $PbTiO_3$ being one exception) due to the greater degree of random orientation across all directions of the material[9]. Single crystals are anisotropic and therefore display different properties according to the directional cut of the sample[2].

The main distinguishing factor in polycrystalline ceramics is the presence of grain boundaries. Grain boundaries separate the crystallite grains and can be either secondary phases or the same phase as the grain but in a disordered form[21]. Grain boundaries are often less dense than the grain material and can provide diffusion pathways for species such as vacancies and gas molecules to pass through the sample[21]. One of the main negative aspects of polycrystalline ceramics to be cautious of is that due to the presence of both grains and grain boundaries, significant compositional variation and inhomogeneity can be seen across a sample which can have a negative impact on electrical and electromechanical properties. Grain size and sample density are also points to consider in the production of polycrystalline ceramics as these can also affect the properties of the sample. These conditions must be consistent in ceramics production which can be difficult.

1.2.5 Phases and Phase Transitions

As discussed in Section 1.1, the first commercial ferroelectric material to be developed was polycrystalline $BaTiO_3$. $BaTiO_3$ has a perovskite crystal structure and is tetragonal below its Curie temperature of 130 °C[2][4]. The structure of $BaTiO_3$ has a spontaneous dipole moment along the [001] direction in the tetragonal phase, [011] in the orthorhombic phase below 5 °C and the [111] direction in the rhombohedral phase which occurs below -90 °C [2]. The dipole moment and crystal structure give rise to ferroelectric properties (Figure 1.5). $BaTiO_3$ has been adapted through years of experimentation to modify its ferroelectric properties by microstructural modification, stoichiometric modification, and by doping on the A- and B-sites. These dopants such as Pb or Ca can stabilise the tetragonal phase of the material at different temperatures[2]. $BaTiO_3$ was found to have a relatively low Curie temperature[22], which meant that the material could not be used in high temperature applications. The Curie temperature (T_C) of a piezoelectric material is important as it is the temperature above which the material ceases to be ferroelectric; that is, there is a spontaneous de-poling and phase transition into a paraelectric state with a centrosymmetric structure[20]. Following the discovery of ferroelectric $BaTiO_3$ came the development of lead zirconate titanate (PZT) which has a much greater ferroelectric temperature stability.

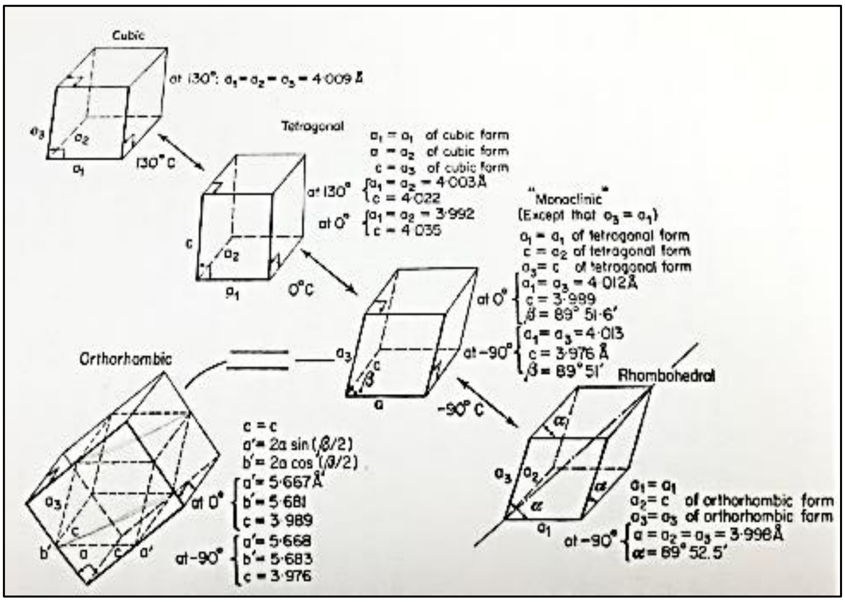

Figure 1.5: Illustration of crystallographic structure shifts of $BaTiO_3$[3].

PZT was produced combining the tetragonal $PbTiO_3$ and the orthorhombic $PbZrO_3$ with the effect of achieving the morphotropic phase boundary found in $Pb(Zr_{1-x}Ti_x)O_3$ [4] at Zr/Ti = 52/48 %. The variation of the Zr/Ti content influences the shifting crystal phases of this material between rhombohedral and tetragonal. A maximisation of piezoelectric properties (often the piezoelectric strain constant *d*) frequently occurs on a morphotropic phase boundary (MPB); a sometimes temperature-dependent (polymorphic phase transition, PPB), compositionally driven region where the crystal is shifting between two or more crystal structures[4]. The superior piezoelectric properties arise from the ease at which the composition can shift between two ferroelectric phases, giving rise to large strain values. In the case of PZT this would be between a tetragonal, rhombohedral, and a recently discovered monoclinic phase along the MPB[13] (Figure 1.6).

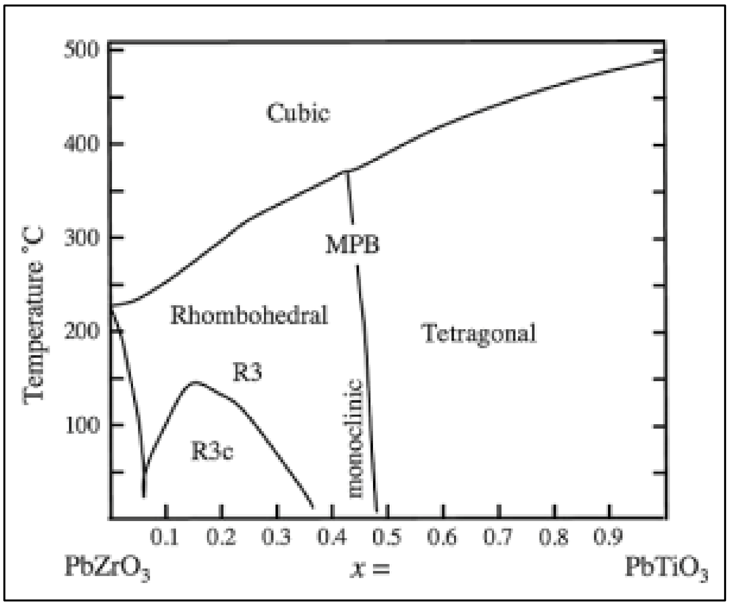

Figure 1.6: Phase diagram of PZT illustrating morphotropic phase boundary[23].

1.2.6 Poling, Domains and Hysteresis

A ferroelectric polycrystalline ceramic, despite having a spontaneous polarisation, has crystallites within the ceramic that are randomly oriented. In order to induce a net polarisation direction and to align the majority of the dipoles within the ceramic, the sample must be "poled" under an applied electric field. This results in a permanent alignment of dipoles or crystallites within the material in line with the electric field direction[24] (Figure 1.7).

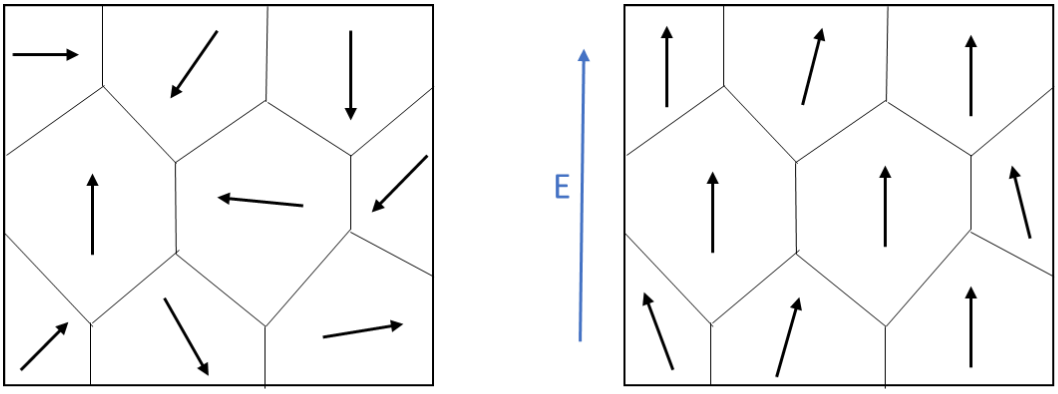

Figure 1.7: Illustration of poling and alignment of dipoles under an applied electric field.

The Curie Temperature (T_C) is the temperature above which the polarisation is lost and the sample then becomes paraelectric – i.e. has no polarisation direction. Ferroelectric domains are clusters of small dipoles within grains of a ceramic, and the interface between them are referred to as domain walls. The formation of domains on cooling from the T_C creates strain within the ceramic due to unit cell distortion, and so domain walls are limited in their direction according to the newly assumed crystal structure of the ceramic, for example in a tetragonal structure the domain walls will be at 90° and 180°, whereas in a rhombohedral structure the walls will be at 71°, 109° and 180°[6].

Under the effect of an alternating electric field the domains orientate with the direction of the applied electric field [20] and the delay or "lag" that comes from the domain switching process produces the classic characteristic hysteresis loop of ferroelectrics (Figure 1.8). The hysteresis loop seen in the P-E measurements of a sample is the clear characteristic of a ferroelectric material. The hysteresis loop provides a number of details about the behaviour such as the remnant polarisation (P_r), and the coercive field (E_c)[6].

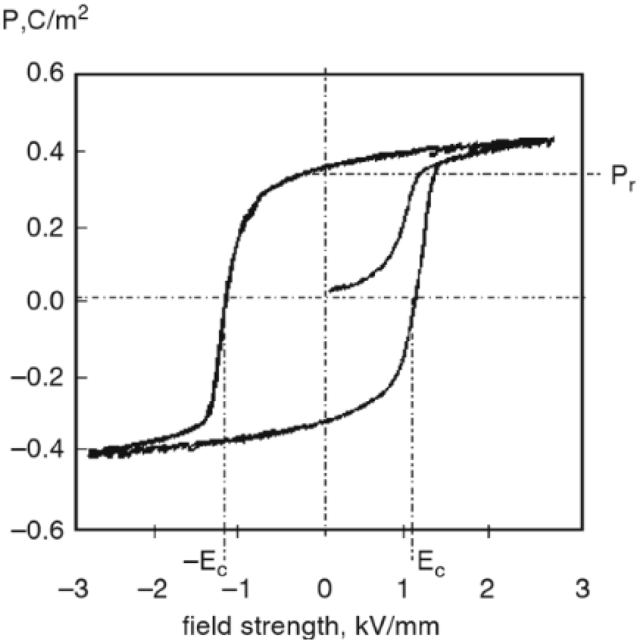

Figure 1.8: An illustration of the classic P-E loop seen in ferroelectric materials[6].

As previously stated, a ferroelectric material requires an electric field to switch its state of polarisation by 180°. The energy required to remove the spontaneous polarisation can be overcome without a field at high enough temperatures resulting in the material transitioning into the paraelectric state and it is de-poled. Above these temperatures, most ferroelectric materials obey the Curie-Weiss law shown below[3]:

$$\varepsilon_r - 1 = \frac{C}{T - T_0}$$

Where ε_r is the relative permittivity, C is the Curie constant and T_0 is the Curie temperature[3]. With regards to $SrTiO_3$, it no longer obeys the Curie-Weiss law below approximately 105 K, which coincides with structural phase transition from paraelectric cubic to low temperature incipient ferroelectric tetragonal phase[25].

1.3 Defect Chemistry and Doping

This thesis will place a large focus on doping of perovskite materials, and the changing effect of their defect chemistry on electrical transport properties such as diffusion and conductivity[14], and as such a brief explanation of defect chemistry of metal oxide materials is important. The equations below describing the different types of chemical defect are all written using the conventional Kröger-Vink notation. They also show the balance between defect species and new defect species such as electrons or oxygen vacancies that are created or absorbed in the material in order to preserve charge neutrality across the lattice. Kröger-Vink notation will be used throughout the rest of this work. The system is as follows[14]:

$$X_y^z$$

(X) Main symbol – This is the defect species and is represented by the atomic symbol for the species, an electron (e), a hole (h), or a vacancy (V).

(Y) Subscript symbol – This is the original site that is being occupied by the new defect species, including an *i* for an interstitial site.

(Z) Superscript symbol – This shows the charge difference on the defect species compared to the original perfect lattice site, for example X= neutral, • = plus one positive charge, ′ = plus one negative charge.

Chemical defects in materials can take several forms. The first most basic is non-stoichiometry, the intentional or unintentional variation of ions from their intended formula and lattice composition. Changes in stoichiometry can affect the valence states of remaining ions, unit cell expansion and charge balances across the lattice[4]. Line defects are long range disorder to the lattice periodicity and although these can have an effect on the macroscopic properties of a material, will not be discussed in great detail in this work. Point defects are atoms that are vacant, newly added (such as dopants or impurities), or displaced[14]. There are both intrinsic and extrinsic types of point defect.

Intrinsic point defects are either Schottky defects, or Frenkel defects. Schottky defects are an electrically neutral pair of anion and cations removed from and then relocated to different lattice sites, leaving behind a complementary pair of neutral vacancies[4], [14]. For example, in NaCl, (where nil represents a perfect neutral crystal lattice):

$$nul \rightleftarrows V_{Na}' + V_{Cl}^{\bullet} \text{ [14]}$$

or in Cr_2O_3:

$$nul \rightleftarrows 2V_{Cr}''' + 3V_O^{\bullet\bullet} \text{ [14]}$$

Schottky disorders occur at surfaces, which is an important factor of electroceramics due to the presence of grains and grain boundaries that provide surfaces for formation and transport routes for vacancies, this is much less the case for single crystals which do not possess these grain boundaries. Frenkel defects are simply one relocated ion from its original position in the crystal lattice to an unoccupied site[4]. This is often an interstitial site (a site between existing atoms), so factors such as ion size vs site size and the accommodating electrostatic environment are key to determining if the relocation can take place. For example, AgBr, where subscript I represents an interstitial site:

$$Ag_{Ag} \rightleftarrows Ag_I^{\bullet} + V_{Ag}' \text{ [14]}$$

In this case Ag is well suited to moving through the lattice and locating on an interstitial site due to its unique electronic structure[14]. This case is an example of a cation Frenkel defect. An example of an anion Frenkel defect is that seen in CaF_2:

$$F_F \rightleftarrows F_I' + V_F^{\bullet} \text{ [14]}$$

Anion Frenkel defects are less common because of the site size and electrostatic environment required by the relocating anion.

Extrinsic defects are those created by an external addition to the ideal lattice, either by intentional doping, or accidental impurity. Dopant atoms replace original site ions up to the solubility limit of the new system, and dopant atoms occupying interstitial sites are rare[14]. Dopant atoms can be isovalent or aliovalent. Isovalent dopants are the simplest case as a substitution occurs such that there is no charge discrepancy at the lattice site. As such no new defect species need to be created in order to maintain charge neutrality. An example of this would be the binary system NiO-CoO. The Co substitutes on a Ni site easily and with minimal disruption, resulting in complete miscibility until a temperature is reached at which phase separation occurs.

Aliovalent dopants, however, are much more complicated and are the basis of much research. Doping with aliovalent ions can be used to affect the diffusion and transport properties of a material because of the new defect species that must be created in order to maintain charge neutrality across the lattice[14]. It is these defects that are often involved in the fluctuation of electrical properties such as conductivity in a material, for example oxygen vacancies or free electrons. Donor dopants can be compensated by either cation vacancies, electrons or more complex interactions such as the reduction in anion vacancies. The new compensating defect species that is created often matches the size and charge of the original defect species to match the electrostatic environment[14]. The type of defect species present in a material are key to understanding and influencing the electrical properties of it, and as such doping will play a key role in the experiments carried out in this work to use defect-dipole techniques to influence the piezoelectricity of a material.

Defect dipoles are a species that were first identified by Lambeck and Jonker in 1978[26], and were found to be responsible for the aging phenomenon seen in ferroelectric materials – where the polarisation strength of a poled sample decreases with time. Defect dipoles are commonly an acceptor defect (such as Cu''_{Ti} in PZT) paired with a nearby oxygen vacancy. Experiments have shown that the binding energy between an acceptor defect and the closest oxygen vacancy is thermodynamically favourable[27], and so after a period of time the oxygen vacancies in a poled sample diffuse through the lattice until they arrive next to an acceptor defect and a defect dipole is formed. Examples of defect dipoles in different ferroelectric materials are shown below[27]:

$(Mn''_{Ti} - V^{\bullet\bullet}_{O})^{x}$ in $BaTiO_3$

$(Cu''_{Ti} - V^{\bullet\bullet}_{O})^{x}$ in PZT

$(Fe'_{Ti} - V^{\bullet\bullet}_{O})^{\bullet}$ in PZT

$(Cu'''_{Nb} - V^{\bullet\bullet}_{O})'$ in KNN

These defect dipoles are able to orientate with the polarisation direction of a ferroelectric lattice. In a cubic paraelectric structure all orientation directions are energetically favourable, but when a sample is poled the defect dipoles orient along the polarisation direction in line with the electric field. As cation defects are considered to be relatively immobile at equilibrium conditions, it is the oxygen vacancies that are responsible for the observed re-orientation of defect dipoles[27]. As yet defect dipoles have only been identified in the oriented formation in ferroelectric materials that are poled. This work will aim to determine if any of the defect dipoles that form in doped-$SrTiO_3$, a paraelectric material at room temperature, and attempt to orient them under an electric field in order to produce a macroscopic dipole, and in turn a piezoelectric effect.

1.3.1 Aging and Fatigue

A decrease in the polarisation strength of a piezoelectric material can occur naturally over time, this is known as aging. If the material degrades from an externally applied electric field this is fatigue. Aging and fatigue have similar effects and occur via similar mechanisms; those of point defects from dopants or impurities forming defect dipoles with present oxygen vacancies[27]. The defect dipoles that are formed are charged defects creating an internal bias field and these have the effect of pinning the domains in place when under an applied electric field such that when the field is reversed, domain switching is more difficult.

The three primary mechanisms for degradation are a volume effect, domain effect and interface effect. The volume effect is seen in acceptor-doped materials where the acceptor dopant ion forms a defect dipole with an oxygen vacancy present. The defect dipole has both an electrical and elastic dipole moment and movement occurs due to the deformation of the unit cell to accommodate the defect dipole[27]. The domain effect is the movement of charged defects to domain walls, stabilising them in place. The driving force for this effect is the minimisation of electric and elastic forces local to the defect dipole[27]. The interface effect is similar to that of the domain effect except that the charged defects diffuse into grain boundaries or towards secondary phase walls and form space charge layers[27] that are insulating regions from which the charged species have vacated. There is a final degradation mechanism which is specific to fatigue and that is microcracking occurring towards the surface of a sample near to the electrode. The effects of aging are observed as a "pinching" to the P-E hysteresis loop in acceptor-doped materials, and in fatigue a reduction in the remnant polarisation is seen during the electric field cycling in donor-doped materials[27].

An example of the effect of oxygen vacancies on aging and fatigue is observed in $BaTiO_3$. Acceptor-doped $BaTiO_3$ creates a large concentration of oxygen vacancies, which facilitate the aging process by forming defect-dipoles with acceptor cation impurities, pinning domains in place and sustaining piezoelectric properties under applied mechanical stress at room temperature[4]. However at increasing temperatures these oxygen vacancies contribute towards conductivity under an applied electric field resulting in fatigue[4]. Donor-doped $BaTiO_3$ generates less oxygen vacancies, so levels of aging and fatigue are decreased[4].

1.3.2 Band Theory and Electronic Structure

The materials covered in this study are classed as semiconductors. It is important to understand the chemistry of semiconductor materials and also metallic materials and their conductivities, in order to be able to understand and manipulate the effect of defect chemistry and doping.

The first step in understanding the conductivity of inorganic materials is band theory[28]. A metal atom can have an electron in the 2s orbital. If there are two metal atoms bonded together the two overlapping 2s orbitals form a molecular orbital. Multiple metal atoms together create multiple molecular orbitals of the same energy to each other, and this is known as a band. Not all of the molecular orbitals have to be filled and can be partially occupied with electrons. The movement of these electrons by an applied electric field across the partially filled molecular orbitals results in electrical conductivity. The electrons in the lower level occupy the valance band, and the higher energy band above is the conduction band. It is often only the electrons found in the valence band that contribute to the conductivity of a material, not the electrons deeper in the molecular structure[4]. Materials such as metals, semi-conductors and insulators all have different conductivity properties (Figure 1.9) If there is a large energy gap between the valence band and the conduction band, the material is an insulator. If the valence band is partially occupied such that there is room for the electrons to move within that band, or if there are overlapping molecular orbitals of similar energy, the material is metallic. Metallic materials see an increase in resistivity (or decrease in conductivity) as temperature increases due to increasing electron-phonon interactions from thermal lattice vibrations[4]. If the conduction band and the valence band only have a small energy gap between them then the material is a semiconductor. The resistivity of semiconductors generally decreases with increasing temperature (there are exceptions – PTCR positive temperature coefficient of resistivity), which is due to the thermal occupation of the conduction band with electrons from the valence band.

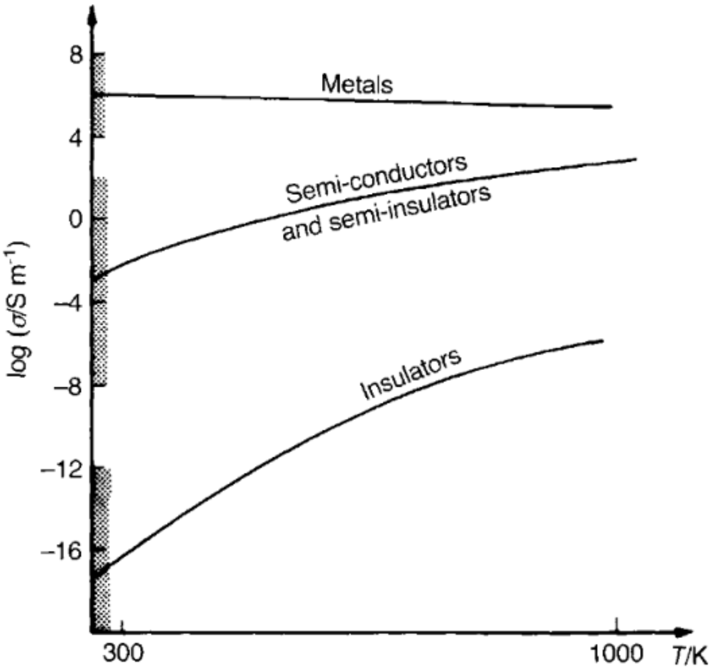

Figure 1.9: Conductivity vs Temperature graph showing properties of metals, semi-conductors and insulators (Moulson pp. 26) [4].

Intrinsic semiconductors are materials which have electrons that are thermally promoted into the conduction band due to the small band gap (for example Si and Ge) and exist without the presence of dopants and their conductivity arises from naturally occurring chemical defects or thermal electron promotion[28]. Extrinsic semiconductors are created by either acceptor or donor dopants. Doping a group 14 material with a group 13 material (for example) creates an acceptor level close in energy to the valence band for electrons to be promoted into, leaving behind positively charged holes. This is a “p-type” semiconductor. An “n-type” semiconductor arises from doping a group 14 material with a small amount of a group 15 material (for example) creating an electron rich donor level just below the conduction band for the negatively charged electrons to move into[28] (Figure 1.10).

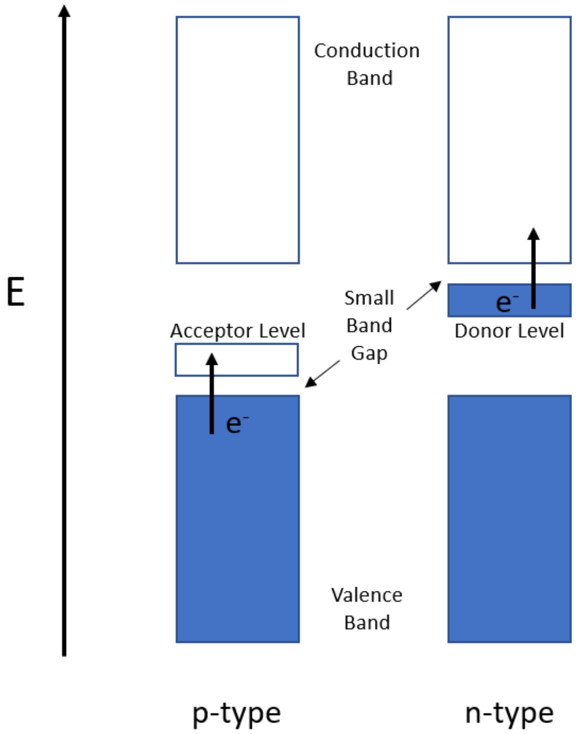

Figure 1.10: Illustration of p-type and n-type semiconductors, adapted from[28] pp161.

Electrons move around freely with thermal energy, but at absolute zero the electrons are located in bands in the material either filling them or leaving them partially empty[4]. The Fermi level is the highest energy level of the electron band at absolute zero (T=0 K) that is occupied by electrons. The electrons do not have any thermal energy to move to occupy a higher level. From this it can be used to calculate the density of electrons or holes in a material. The Fermi-Dirac function is an equation which represents the "fraction of states occupied by an electron"[4], or more simply, the probability that an energy level is occupied by an electron.

$$F(\varepsilon) = \left\{exp\left(\frac{\varepsilon-\varepsilon_F}{kT}\right) + 1\right\}^{-1} \quad [4]$$

This provides the Fermi energy (ε_F) which is a characteristic of each individual material[4]. The Fermi level can also be expressed as the probability of occupancy of an energy state being

½ at temperatures other than absolute zero when $\varepsilon=\varepsilon_F$[29]. For a metallic material or conductor, the Fermi level is found within the conduction band, and for intrinsic insulators and semiconductors the Fermi level is found in the middle of the band gap[29].

$BaTiO_3$ is a good example which demonstrates the effects of donor/acceptor doping and the change in electrical properties from band theory. $BaTiO_3$, like most mixed oxides, has acceptor impurity cations present such as Al^{3+}, Fe^{3+} Mg^{2+} and these will likely substitute on the Ti^{4+} in the perovskite. The acceptor nature of these impurities leaves a charge deficit in the lattice which is then compensated by the creation of oxygen vacancies, normally of a concentration of 1 in 10^4[4], which is not insignificant and is higher than any intrinsic defects present. At high temperatures, $BaTiO_3$ shows both n- and p-type conduction behaviour. Conductivity measurements on semiconductors are routinely taken at high temperatures due to the high resistivities seen at low temperatures. Temperature and equilibration time are key to affecting the diffusivity of defects in a lattice, i.e. generally high temperatures increase conductivity in semiconductors (with the exception of PTCR semi-conductors). At room temperature however, p-type $BaTiO_3$ created from doping is observed to be a good insulator but n-type $BaTiO_3$ is semi-conductive at room temperature[4]. The difference in behaviour is caused by the orbital structure of Ti^{4+} and O^{2-}. The electronic structure of Ti is $[Ar]3d^24s^2$, so that of Ti^{4+} is just [Ar], leaving an empty 3d orbital. This 3d orbital can become a conduction band if the electrons from defects are transferred to it, and this requires little energy, so at room temperature n-type conductivity exists in $BaTiO_3$.

Another example of the effects of electronic structure, but this time on ferroelectric properties, is observed in PZT. PZT can be doped with donor and acceptor ions in order to manufacture ‘soft’ and ‘hard’ versions of PZT respectively to manipulate the resulting properties to suit the application[13]. The significant effectiveness of doping in PZT is considered to be due to a number of coinciding effects. Firstly, the perovskite structure of lead-containing unit cells is distorted to a much greater degree than that of other piezoelectric perovskites[13]. Rödel notes that the distortion of a unit cell is related to the polarizability of the ions in the crystal, whereby those with a higher polarizability are more likely to cause significant distortion of the unit cell. An increased piezoelectric performance is also thought to be induced by a highly anisotropic polarizability across the unit cell[13]. This shows it is not enough to consider just the ionic radii differences when considering the distortion of the unit cell; the polarizability of the ions and the potential for orbital hybridization is also key[13].The electronic structure is also a factor to be considered, for example that of lead in PZT. Pb^{2+} has an electronic structure of [Xe] $4f^{14}$ $5d^{10}$ $6s^2$, combined with a large ionic radius. The $6s^2$ lone pair is not involved in bonding and creates an uneven electron density around the atom which leads to a significant polarizability and distortion of the unit cell[13]. The 6*s* electrons can also be involved in hybridisation of the oxygen 2*p* orbitals in a structure like PZT, which can affect the distortion of the unit cell[13]. Bi has a large ionic radius and a lone pair of electrons similar to Pb and has therefore been used as an alternative for Pb in piezoelectric materials. It will be important to consider the potential electronic contributions to piezoelectricity and how to manufacture these effects in an attempt to create a new piezoelectric material in this work.

1.4 Properties

1.4.1 Electric Properties

If a voltage is applied, a current flows through a solid material. In the most basic form, before considering the identity of the charge carriers, they have density n and charge Q when the material is subjected to applied electric field E. The velocity of the charges is limited by the ‘friction’ produced by the lattice from atomic thermal motion which limits their speed, or “drift velocity”, ʋ[4]. These factors can all be related by the current density, *j*.

$$j = nQv \text{ [4]}$$

The drift velocity per unit of field applied is described as the mobility of the charge carriers, *u*.

$$j = nQuE \text{ [4]}$$

and *nQu* is an expression that is uniform at constant temperatures for a material that obeys Ohm’s law so:

$$j = \sigma E \text{ [4]}$$

where σ is the conductivity of the material. Conductivity can therefore be expressed as:

$$\sigma = nQu \text{ [4]}$$

Resistivity, ρ, is another important electrical property, and is the inverse of conductivity:

$$\rho = \frac{1}{\sigma}\ [4]$$

Conductivity and resistivity are often found in conjunction with sample geometric information (area A and length L) in relation to *conductance G*:

$$G = \frac{\sigma A}{L}\ [4]$$

At initial inspection, it is not obvious as to the identity of the charge carriers contributing to the conductivity and to what degree each species is contributing. The total conductivity through a system is a sum of the conductivity from ions, electrons and holes[4], and there will be a considerable portion of this work dedicated to conductivity measurements and charge carrier studies.

1.4.2 Dielectric Properties

Ferroelectric and piezoelectric materials are insulating materials, which have a wide range of associated dielectric properties that can be measured. A dipole moment is defined as two opposing charges (+Q and -Q) separated by distance δ_x[4]:

$$p = Q\delta_x$$

If that dielectric material is placed in between two parallel plates and an electric field *E* applied across the dielectric material between the two plates, the plates will carry surface charge density σ in a vacuum[4]:

$$E = \sigma/\varepsilon_0$$

The polarisation of a dielectric material is the dipole moment per unit volume of the material and can vary across it, for example the surface charge density (σ_p) can be a contribution to total charge density (σ_T), which is equivalent to the electric displacement density[4]:

$$D = \varepsilon_0 E + P$$

If the polarisation is proportional to the applied electric field E, the dielectric is “linear” and[4]:

$$P = \chi_e \varepsilon_0 E$$

Where χ_e is the electrical susceptibility, which is a quantification of how the material is polarised under the applied electric field[4] and is related to the permittivity by the following expression:

$$\varepsilon = \varepsilon_0 + \varepsilon_0 \chi_e$$

The relative permittivity ε_r is derived from the following equation:

$$\varepsilon_r = \frac{\varepsilon}{\varepsilon_0} = 1 + \chi_e$$

Permittivity is a complex quantity, ε^* composed of real (ε') and imaginary (ε'') parts:

$$\varepsilon^* = \varepsilon' - i\varepsilon''$$

The loss component of permittivity is tan δ (also called the dissipation factor) and is the result of resonant processes or dipolar losses[30]:

$$tan\delta = \frac{\varepsilon''}{\varepsilon'}$$

2 Literature Review

2.1 Lead-Free Piezoelectric Materials

In 2003 legislation was passed by the EU Council Directives and the Restriction of the use of Hazardous Substances (RoHS) with respect to reusing and recycling waste electronic and electrical equipment (WEEE) restricting the use of lead in quantities greater than 0.1 wt%[13]. The material PZT in electronic applications is currently exempt from this ban due to its extensive invaluable use, and exemptions are reviewed every 5 years to assess any developments in competitive lead-free materials which could replace PZT[13]. This exemption will be reviewed and potentially revoked as soon as a suitable alternative to PZT is found. A paper by Saito et al. published in Nature in 2004, alongside the new legal directives surrounding the use of lead in technological applications led to an explosion of research into lead-free piezoelectric materials[31]. The main problem has been to find a material that is able to compete with or surpass lead in PZT technology. The overwhelming success of PZT in electronic applications has led to increasing amounts of lead being released into the environment during both production, and disposal in PZT processing[13], mainly from dissolution, acid rain etching and ground water for lead leaching[32]. Lead as a metal can lead to hypertension, kidney disease, fertility impairment and lead to growth and development problems in children. However, in the production of piezoelectric ceramics PbO is used, which has a LD50 toxicity of 4300 mg/kg compared to 450 mg/kg of pure lead but caution must still be taken[32]. There are similar toxicities seen in other heavy metals such as bismuth and antimony which are often used in successful “lead-free” piezoelectrics[32], so there should be questions raised as to the motivations for the search for a lead-free material, is it just to satisfy the trend of “lead-free” or is it to reduce the negative health and environmental impacts of such metals in technology?

There are two main categories of lead-free materials; those which compete with PZT, and those which are incomparable as they possess properties PZT does not. The former being materials such as KNN (potassium-sodium niobate), NBT-BT (sodium-bismuth titanate and barium titanate) and BCTZ (barium-calcium-titanate-zirconate) systems, and the latter category being materials such as AlN, SiO_2 and $LiNbO_3$ single crystals, Bi-layered structures etc, which are high temperature piezoelectrics[32]. Figure 2.1 shows the evolution of the development and filing of patents for lead-free electroceramic-based technology up to 2016, and shows the shift in popularity in each of the material groups[33].

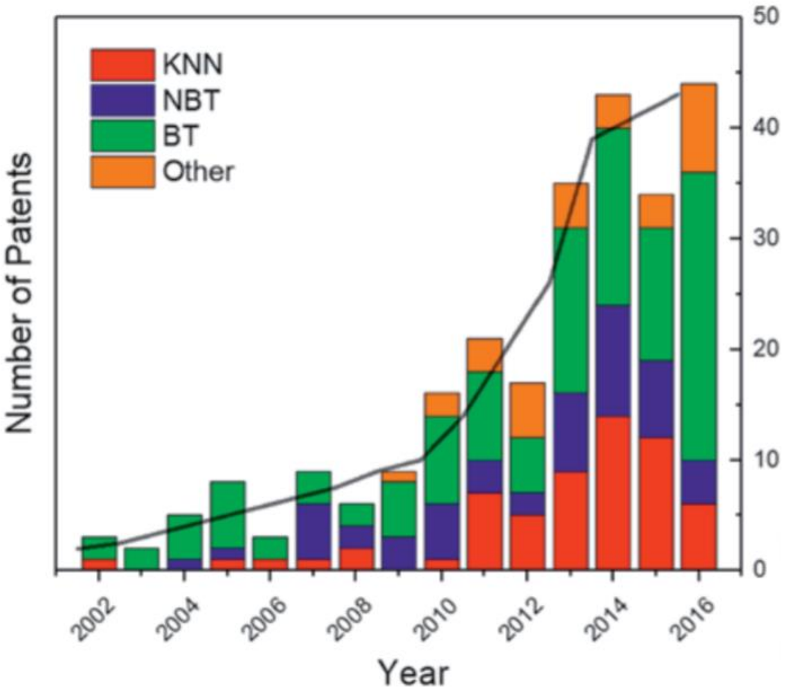

Figure 2.1: Review of lead-free piezoelectric ceramic patents filed up to 2016 [33].

KNN systems exhibit the highest piezoelectric properties due to an MPB between an orthorhombic and tetragonal phase, whereas in the NBT-BT systems, it is due to a tetragonal-rhombohedral MPB as with PZT[22]. The drawbacks to the KNN systems are that they have a narrow sintering range and suffer from stoichiometric variance from volatility, but their d_{33} values can be between 200-400 pC/N with a T_C greater than 400 °C, but these properties are strongly temperature dependent due to the polymorphic phase transition observed in this material[22]. BNT and BKT (bismuth sodium/potassium titanates) are another branch of lead-free piezoceramics. Developments in these materials with doping and sintering techniques (namely hot-pressing to avoid volatility losses) enabled a d_{33} of approximately 200 pC/N and a T_C of 280 °C but these materials have their issues. They are highly alkaline which makes them corrosive and their volatility and narrow sintering range doesn't make them an obvious replacement for PZT[34]. Figure 2.2 is a graph comparing the achieved d_{33} values against their T_C for some groups of lead-free piezoelectric materials from 2018[2]. As shown, the KNN and BF (Bismuth-ferrite) groups have much more impressive T_C properties in comparison to BT and NBT-based materials, however the BT-based materials do have d_{33} values to rival those of KNN, just not at a suitably high T_C.

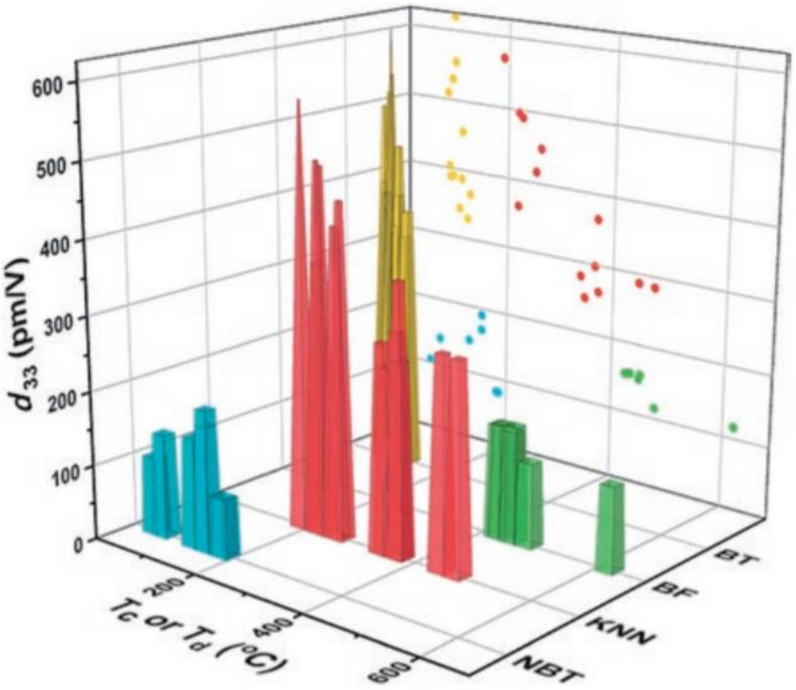

Figure 2.2: Comparison of d_{33} and T_C of common lead-free piezoelectric ceramic groups up to 2018[33].

There are a number of secondary considerations besides piezoelectric properties when discussing replacing PZT with a lead-free piezoelectric. The first of these is temperature dependence due to the changing temperature conditions of the device. The most obvious of the consequences of this are the phase changes that are inherent with ferroelectric materials[32]. These phase changes, which are often temperature dependent, can greatly vary the magnitude of the piezoelectric properties displayed. More subtly, in piezoelectric materials that fall into pyroelectric space groups, a pyroelectric charge can build up due to the thermal sensitivity of polarisation[32]. In the same vein, ferroelectric materials can develop a charge due to the thermally activated movement of domain walls within the material[32]. Another consideration when replacing PZT is cost. The infrastructure is already in place for PZT in the devices and technologies in use, be it the size, shape or frequencies used in said devices, if a suitable material is found there will still be significant changes to be made by the industry to incorporate it, presumably at large costs. Not only infrastructure costs have to be accounted for, but also raw material costs, and accompanying device elements such as electrode material. Nb and Ta are much more expensive raw materials than those used in the manufacturing of PZT and are used in a lot of current lead-free piezoelectric materials such as KNN[32]. Conversely however, nickel electrodes when using KNN are cheaper than the silver equivalent with PZT[32].

Density is another consideration when replacing PZT. Due to the high lead content of PZT, it is a very dense electroceramic. Materials with a lower density are preferred because the overall weight of a device can have an impact on practical costs such as fuel to move the carrier of the device, for example a submarine.

As shown in this section there is a considerable body of ongoing research into lead-free piezoelectric materials, of which this research will hopefully contribute.

2.2 Strontium Titanate

Strontium titanate ($SrTiO_3$) is the ‘prototype’ perovskite, being cubic in structure at room temperature with a very slight distortion to tetragonal structure at around 110 K[35]. The electrical properties of $SrTiO_3$ are highly modifiable under a variety of doping conditions, producing desirable properties such as tuneable electronic conductivity, high permittivity, low dielectric loss and high temperature stability for a wide variety of applications in semiconductor, oxygen conductor, capacitor and solid oxide fuel cell technologies [36]–[39],[40][41]. The cubic structure of $SrTiO_3$ results in it being paraelectric, meaning it does not possess a spontaneous polarisation direction and cannot currently be used for ferroelectric applications. A large body of research into $SrTiO_3$ and its dopants is related to the research for a new solid oxide fuel cell (SOFC) material. Whilst this is not the motivation for this thesis, some of the literature provides useful information into the electrical properties of $SrTiO_3$-based materials. The Ni-YSZ anodes of solid oxide fuel cells are prone to failings such as sulphur poisoning, coking and sintering, as such there is a focus on current research to attempt to find a replacement material that is more reliable and cost efficient[39][42]. $SrTiO_3$ materials are currently being considered for this application because of their resistance to these failings, as well as possessing other attractive electrical properties. Dopants are employed in a range of studies in an attempt to reach a high conductivity in $SrTiO_3$. For example work by Lemanov 1997[43] shows that doping $SrTiO_3$ with small impurity amounts of Ca, Ba and Pb removes the stability of the paraelectric phase, and introduces a ferroelectric phase at low temperatures. Substitution of Sr or Nb on the titanium (Ti) sites has been shown to be responsible for improved metallic conductivity in $SrTiO_3$ materials, and ongoing research aims to optimise these dopant concentrations, currently found to be between 20-40 %, however, there are limitations based on the solubility limit of these dopants[39].

The following literature review studies the variety of chemical defects existing in $SrTiO_3$, including those from doping, non-stoichiometry, and impurities. The literature review concludes with defect dipole research in the hope of further understanding the effect of defect dipoles on the piezoelectric effect. Due to the combination of its simple cubic perovskite structure and tuneable electrical properties, $SrTiO_3$ was considered to be a good prototype material to build upon the complex nature of research into defect dipoles. The lack of ferroelectric behaviour in $SrTiO_3$ should allow any subsequent engineered piezoelectricity to be more easily identified.

2.2.1 Non-Stoichiometric $SrTiO_3$

Non-stoichiometric samples of $SrTiO_3$ were made by Baurer and Kungl in 2009 with Sr/Ti ratios of 0.996-1.005 with the intention of investigating the effect on density[44]. The sintering range seemed to be between 1350-1400 °C, and the heating rates and times differed according to the composition of each sample with theoretical densities being above 97 %. Changes were observed in the sintering behaviour according to the ratio of Sr/Ti rich phases of each composition[44]. The main initial findings were that samples with Sr-excess shrink and densify faster between 1100-1200 °C and the Ti-rich samples between 1300-1330 °C[44]. At stoichiometric Sr/Ti the shrinkage matched that of Ti-rich samples, namely fastest densification at 1300 °C. Grains grew faster in Sr-rich samples at lower temperatures compared to Ti-rich samples. Liquid sintering was found not to be happening in the Sr-rich samples because this eutectic liquid only exists in the Ti-rich side of the phase diagram[44]. Grain growth experiments showed that the grain boundaries at high temperatures were similar for both the Sr and Ti-rich samples, meaning diffusion during sintering was not affected by Sr/Ti excess. Possible reasons for this included excess Ti, hindering grain boundary diffusion, but which was then absorbed, and also a defect chemistry phenomenon regarding the ratio of Sr/Ti.

Computer simulations in this paper showed that at high temperatures, both types of cation vacancies are possible, but with a small energetic inclination towards Sr and O vacancies[44]. Baurer and Kungl observed that in Ti-rich samples there was increased formation of Sr and O vacancies, whereas Sr-rich samples were compensated by the formation of SrO Ruddleston-Popper layers, without the need to form vacancies[44]. However, a paper by Meyer et al.[45] stated that the equation below takes place in a Sr-rich material, with the production of Sr vacancies occurring in a reducing environment (RHS):

$$\frac{1}{2}O_2(g) + 2e' + Sr_{Sr}^{x} \rightleftarrows V_{Sr}'' + SrO$$

Ruddlesden-Popper layers are a secondary phase of $SrTiO_3$ that form when there is an excess of Sr in the perovskite structure, and has the formula $Sr_{x+1}Ti_xO_{3x+1}$[41]. It is a double layer of SrO, and often occurs as a result of high temperatures or oxidising conditions or with non-stoichiometric compositions[41]. Gomann and colleagues were referenced in the paper by Meyer et al. as saying that both Sr and Ti cation diffusion was possible through the presence of Sr vacancies, and therefore overall diffusion was enhanced by Sr vacancies[44]. Bulk diffusion in Ti-rich samples was therefore likely to be higher due to the increased number of Sr vacancies in Ti-rich samples. This increased diffusion resulted in faster shrinkage at higher temperatures, hence why the Ti-rich samples were denser[44].

Chan, Sharma and Smyth in 1981 conducted research on single crystal $SrTiO_3$ suggesting that the main defects at low P_{O2} were doubly ionised oxygen vacancies with compensating electrons[46]. This work was supported by the paper by Trabelsi et al. 2017[47] who successfully varied the oxygen vacancy levels in samples of $SrTiO_3$ resulting in compensation by extra electrons. Trabelsi et al. showed that the electrons created to compensate the increase in oxygen vacancies could become thermally activated and contribute to conduction, with doubly ionised oxygen vacancies being the primary contributor to conductivity in mixed oxide perovskites[47]. Chan et al. suggested that oxygen vacancies were the rate determining defect to the conductivity properties observed in the samples in this study and formed via three pathways[46]:

1. Reduction of, or loss of, oxygen

$$O_O^x \rightleftarrows \frac{1}{2}O_2 + V_O^{\bullet\bullet} + 2e'$$

2. Cation non-stoichiometry, ie. excess TiO_2

$$TiO_2 \rightleftarrows Ti_{Ti} + 2O_O^x + V_{Sr}'' + V_O^{\bullet\bullet}$$

3. Acceptor impurities, either by intent or impurity (eg. Al)

$$Al_2O_3(-2TiO_2) \rightleftarrows 2Al_{Ti}' + 3O_O^x + V_O^{\bullet\bullet}$$

Some excess TiO_2 was thought to be accommodated into the $SrTiO_3$ structure by compensating Sr vacancies and O vacancies, as discussed by Baurer and Kungl[44]. However, significant absorption of excesses of SrO into the perovskite were less likely due to the higher energy required to absorb the larger Sr ion interstitially, and the formation of interstitial Sr and O, or Ti/O vacancies[44]. Also, there was the relatively high charge on a Ti vacancy site which made it unlikely[44]. The work by Chan et al. investigated the conductivity changes with varying P_{O2}, as well as acceptor (Al) and donor doping (Nb)[46]. These dopants were expected to only substitute onto the Ti-site based on size similarity. Their main finding from this study was that conductivity increased with decreasing P_{O2} in the n-type region[46]. This suggested that the conduction properties were determined by the Ti-O sublattice[46]. Chan et al. describe how the solubility limit for TiO_2 depended on the number of oxygen vacancies present from acceptor impurities and the oxygen reduction reaction equation shown above. The charge neutrality condition for undoped and acceptor doped $SrTiO_3$ therefore was [46]:

$$2[V_O^{\bullet\bullet}] + p = 2[V_{Sr}^{\prime\prime}] + [A^{\prime}] + n$$

Plots of the $SrTiO_3$ conductivity vs P_{O2} were used to better understand the changing defect chemistry as a result of changing sintering and measurement atmospheres. At the lowest P_{O2}, the material was oxygen deficient and process 1 above (reduction of oxygen) was the most prevalent source of oxygen vacancies[46]. The intermediate region of P_{O2} was highly atmosphere dependent; if the atmosphere was deficient in oxygen, n-type conductivity behaviour resulted[46]. In an atmosphere with a high P_{O2}, p-type conductivity behaviour dominated. It was proposed by the authors that the stoichiometric excess of oxygen was compensated by the extrinsic additions of oxygen vacancies from species such as excess acceptor impurities or TiO_2[46]. The P_{O2} data from this paper gave an activation energy of undoped $SrTiO_3$ of 0.98 eV at P_{O2}=1 atm[46].

As previously stated $SrTiO_3$-based materials can have a high relative permittivity. Wang et al. 2018[48] stated the relative permittivity of undoped $SrTiO_3$ to be approximately 300 at room temperature, rising to 24000 at low temperatures (4 K) where the material reached its paraelectric state. In this work, Wang et al. produced samples of non-stoichiometric $SrTi_{1-x}O_3$ where x=-0.06 to +0.06 and measured the relative permittivity and dielectric loss of the samples. The first observation in the measurements was noted to be two peaks at 183 °C and 168 °C in the -0.06 and -0.03 (Sr excess) samples respectively[48]. These peaks moved to higher temperatures as the frequency increased, indicating typical dielectric relaxation behaviour. The same behaviour was observed in the Ti-excess samples. The authors then examined the activation energies of each system to try to better understand the defect chemistry of the system. The activation energies for the -0.06 and -0.03 samples were 0.97 eV and 0.91 eV respectively, closely related to typical 1.0 eV for oxygen vacancy diffusion in related oxide structures/perovskites[48][49]. The samples were all re-oxidised and the permittivity measurements repeated. The intention was to reduce the concentration of oxygen vacancies and therefore reduce the magnitude in the loss tangent of the permittivity measurement. However, this did not occur. This indicated that it was not in fact oxygen vacancies contributing to the dielectric relaxation behaviour, but something else. The authors believed that polar nano regions (PNRs) were responsible for the relaxation processes that happened[48]. PNRs are a “partitioning” of the structure into small regions of local spontaneous polarisation [48]. The authors discussed the pinning of domains and that if the number of point defects in the sample were increased, then the concentration of PNRs increased. It was not specifically mentioned but from a review of defect dipoles in Section 2.3, it seems that defect dipoles could be the reason behind the domain pinning and dielectric relaxation in these materials. No specific defect dipole species were mentioned in this work, however.

2.2.2 Acceptor-doped $SrTiO_3$

De Souza in his informative 2015 review paper on oxygen diffusion in $SrTiO_3$[50] found that as temperatures increase more defect reactions began to occur in acceptor doped, or undoped, $SrTiO_3$. The concept of acceptor dopants in un-doped $SrTiO_3$ comes from acceptor impurities from reagent materials such as Al, Fe and Mg[50]. Temperature regimes in chemical defect studies are often separated into low, medium and high temperature ranges, with more defect reactions appearing as the temperature is increased. De Souza classed the temperature regimes as low temp at <277 °C, the intermediate regime >477 °C and the high temperature regime as >1027 °C[50]. It is worth noting that it was not specified what the region between 277 and 477 °C is. In the low temperature regime, the main defect generation reaction was the creation of holes and electrons by “thermal excitation across the band gap”:

$$null \rightleftarrows h^{\bullet} + e'$$

There was also the creation of both singly and doubly ionised oxygen vacancies alongside free electrons in this low temperature regime[51]:

$$V_O^x \rightleftarrows V_O^\bullet + e'$$

$$V_O^\bullet \rightleftarrows V_O^{\bullet\bullet} + e'$$

According to experimental work by De Souza the doubly ionised oxygen vacancy has a much lower formation energy of 0.3 eV compared to the singly ionised which is valued at 3 eV[50]. These defects only became significant under experimentally reducing conditions because their energy value existed just below the conduction band of the material and in reducing conditions this resulted in the Fermi level being close to the conduction band in the low temperature range[50]. In the low temperature range, there was also the ionisation of Sr vacancies occurring which resulted in the formation of holes:

$$V_{Sr}^x \rightleftarrows V_{Sr}' + h^\bullet$$

$$V_{Sr}' \rightleftarrows V_{Sr}'' + h^\bullet$$

These had energies of 0.1 and 1.4 eV respectively. Acceptor dopants in $SrTiO_3$ were also ionised in this temperature regime (for example the reduction of Ti^{4+} to Ti^{3+}):

$$Acc_{Ti}^x \rightleftarrows Acc_{Ti}' + h^\bullet$$

Acceptor dopants could mop up electron holes and reduce the level of p-type conductivity[50]. These acceptor dopants could be positively or negatively charged, neutral, or also be compensated by and paired with the creation of oxygen vacancies.

In the intermediate temperature range above 477 °C an equilibrium developed between solid and gaseous oxygen:

$$\frac{1}{2}O_2(g) + V_O^{\bullet\bullet} \rightleftarrows O_O^x + 2h^\bullet$$

De Souza explained that the incorporation of water into $SrTiO_3$ was a possibility and did not have the coverage to the same extent as oxygen incorporation in the literature, but that it may even occur quicker and easier than oxygen incorporation[50]:

$$H_2O(g) + O_O^x + V_O^{\bullet\bullet} \rightleftarrows 2OH_O^{\bullet}$$

The high temperature regime covered experimental temperatures above approximately 1027 °C, and finally the movement of cations was discussed, primarily the low mobility of cation vacancies at low temperatures[50]:

$$Sr_{Sr}^x + O_O^x \rightleftarrows V_{Sr}'' + V_O^{\bullet\bullet} + SrO(s)$$

Taking all of these possible defect pathways into account a charge neutrality equation could be drawn up to account for all of them present in acceptor-doped $SrTiO_3$[50]:

$$[e'] + [Acc_{Ti}'] + [V_{Sr}'] + 2[V_{Sr}''] = [h^{\bullet}] + [V_O^{\bullet}] + 2[V_O^{\bullet\bullet}] + [OH_O^{\bullet}] + [\{Acc_{Ti}' - V_O^{\bullet\bullet}\}^{\bullet}]$$

It was noted that not all of these defect reactions were happening all at once, depending on the temperature regime and other experimental conditions, for example water was not a consideration in a dry reaction environment, similarly oxygen vacancies and Sr vacancies were fully ionised at high temperatures. It was also noted that although a species concentration was constant, in that there was no great increase in their production, it could still move around the sample and be involved in diffusion/conductivity.

The paper by De Souza went into detail about the diffusivity and conductivity of perovskite oxides. In particular to this study the observations of oxygen ion conductivity in $SrTiO_3$ were especially relevant. It was discussed that at high and intermediate temperatures it was mainly electrons and holes that influenced the conductivity as they were the most mobile species. Oxygen vacancies and then strontium (Sr) vacancies were much less mobile after that. Due to the high temperature conductivity measurements being dominated by free electron movement it was difficult to measure the effect of ionic conductivity as the contribution from free electrons was so great as to overwhelm the result, and as such it was easier to determine the level of ionic conductivity at lower temperatures[50]. De Souza carried out a review of vacancy diffusion experiments and found an average activation enthalpy of oxygen vacancy migration to be between 0.62-0.67 eV[50]. This matched typical experimental values of 0.4-0.6 eV[41]. With regards to oxygen diffusion specifically it was found that migration across extended defects and grain boundaries was found to be much slower than that in the bulk material[50].

The study on bulk conductivity by Waser[52] investigated the conductivity and defect chemistry of Ni-doped $SrTiO_3$. In the titanate perovskite lattices, oxygen vacancies are the most mobile species across the structure, all other ionic species have much lower mobility. Interstitials, in agreement with De Souza et al. [50] do not need to be considered as a significant type of defect in these structures with regard to conductivity. $SrTiO_3$ was doped with Ni, which substitutes as Ni^{2+} for Ti^{4+} on the B-site. The Ni^{2+} ions were created by annealing under reducing atmospheres and acted as doubly valent acceptor sites[52]. If the samples were annealed in an oxidizing atmosphere, the Ni sites became Ni^{3+}, and acted as singly valent acceptor sites[52]. This study investigated the differences in conductivity measurements according to oxygen vacancies in a high temperature regime (above 477 °C) vs. a low temperature regime (below 277 °C) similar if not identical to the work by De Souza [50]. The author discussed the understood phenomena that at high temperatures oxygen vacancies are very mobile and are the dominant conduction mechanism in titanate perovskites. The low temperature regime conduction mechanisms are less well known, as such the study by Waser[52] investigated the impact of quenching into the low temperature regime to lock-in oxygen vacancies and observed the effect on conduction using impedance spectroscopy. One point to note from the impedance spectroscopy analysis was in the high temperature regime, grain boundary contribution could be ignored because the grains were large enough and conductive enough such that the contribution to impedance from grain boundaries was not significant enough to have an impact on the result as a whole, due to the ratio of grain to grain boundary[52]. In both the high and low temperature regimes, electrons and holes were being generated, as well as acceptors being ionised or trapped. In the high temperature regime, if a sample was quenched into the low temperature regime under reducing conditions then the high electron concentration remained unchanged because of the low energy level of the oxygen vacancy donors[52]. If the sample was quenched under oxidising conditions then a drop in hole concentration was observed[52]. This was because the acceptor energy levels were located in the middle of the band gap. The conclusions from the Waser study[52] were that at a wide range of oxygen partial pressures it was the mobility of oxygen vacancies that resulted in a temperature dependent ionic conduction, and the activation energy for the diffusion of these oxygen vacancies was 1.0 to 1.1 eV[52]. As well as this, annealing under high oxygen partial pressure created p-type conductivity, and there it was suggested to be a defect-pair type association between the Ni acceptor centres and the oxygen vacancies[52].

A paper produced in 2014 by Schie et al.[53] provided a detailed simulation study with calculations of the energies of interactions between oxygen vacancies and acceptor dopants including Ni^{2+}, Al^{3+}, Fe^{2+} and Co^{2+}. They noted the formation of a Ni-oxygen vacancy complex, which could be that mentioned by Waser[52], of the form:

$$(Ni''_{Ti} - V_O^{\bullet\bullet})^x$$

The authors' main conclusion from this complex computational study was that below temperatures of 700 K (427 °C) most of the oxygen vacancies were trapped by the acceptor dopant, in this case Ni, resulting in an increased activation energy for diffusion and conductivity of approximately 1 eV. Above temperatures of approximately 800 K (507 °C) the oxygen vacancies dissociated and moved freely through the lattice resulting in an activation energy of 0.62 eV[53]. The authors discussed the observation in literature that there are often two activation energies associated with acceptor-doped $SrTiO_3$, and they are often approximately 0.6 eV and 1 eV, but that there is a discrepancy between those who believe the higher value represents the movement of free oxygen vacancies and those who believe it represents the energy of oxygen vacancy defect complexes, and vice versa[53]. The other finding from this study to contribute to the literature was the observed trapping of oxygen vacancies by dopant cations at first nearest neighbour (1NN) lattice locations, but that at the second nearest neighbour (2NN) location the interaction between the oxygen vacancy and dopant cation became slightly repulsive, with the interaction energy reducing to zero the further apart they became[53] .

In this thesis the two main extrinsic acceptor-doped $SrTiO_3$ are those of cobalt and manganese, the literature for which is reviewed in the following two sections.

2.2.2.1 Cobalt-doping of $SrTiO_3$

Work by Echeverri and Arnache in 2016 covered Co-doped $SrTiO_3$ from 3-20 %[54]. All samples were found to be single phase cubic *Pm-3m* via XRD. They found that the lattice cell parameter decreased according to increasing cobalt concentration up to 5%, after which the cell parameter began to increase[54]. This observation was thought to be due to a distribution of Co^{2+} and Co^{3+} throughout the lattice on the B-site, and the potential for oxygen vacancies in the material[54]. Impedance spectroscopy was carried out on the Co-doped $SrTiO_3$ samples and two semi-circles were seen in the impedance plots for the Co-doped $SrTiO_3$ samples at a range of temperatures, which indicated both grain boundary and bulk contributions. The authors discussed that the significant grain boundary contribution came from Ti-rich grain boundaries[54]. The bulk conductivity contribution was particularly pronounced in the Co-10 % and Co-20 % samples. Similar to the work carried out in this thesis, the Echeverri work calculated the conductivity of the bulk or grain conductivity based on the impedance plot semi-circles intercepting the x-axis and calculated using the Arrhenius equation for 3, 5 and 20 % Co[54]. The activation energies of these samples with respect to bulk conductivity were 1.90, 1.89 and 1.08 eV respectively[54]. The lowest value was for the 20 % Co sample, which was explained to be due to Cobalt's ability to reduce the height of "moving barrier of charges" in the bulk or grain setting, resulting in a larger leakage current. The authors also imply that polarisation relaxation is related to the conductivity of the grain material[54].

Though the work by Mitra et al. 2014[55] refers to ferromagnetism, and despite this project being tailored towards piezoelectricity and other electrical properties, it is still a useful study of acceptor-doped $SrTiO_3$ and the chemical defects and corresponding electronic structures within it[55]. Mitra et al. found that Co was in the 2+ state when substituted onto the Ti-site in $SrTiO_3$ rather than the 4+ state as imagined[55], which is a positive result for this project as the Co was added as a dopant for $SrTiO_3$ with the intention of it forming a 2+ ion on the B-site. It was thought that the creation of oxygen vacancies, which are commonplace in oxide materials like $SrTiO_3$, could provide the extra electrons to convert the Co^{4+} to Co^{2+} due to the donor nature of oxygen vacancies. Mitra et al. used DFT calculations to determine if an oxygen vacancy was more likely to form close to a Co ion, or further removed from it. They found that the energy of formation of an oxygen vacancy nearest to a Co ion was lower and therefore more favourable than that of an oxygen vacancy formed 7Å away from the nearest Co ion. This indicated that oxygen vacancies in this material at least prefer to form closer to Co ions, potentially as a defect complex.

DFT calculations were also used to predict the changing lattice parameters with Co-doping of $SrTiO_3$ in a 2x2x2 supercell. A decrease in lattice parameter of 0.5 % was seen with Co concentration of x=0.125[55]. There was also a significant movement seen in the ions surrounding the oxygen vacancy, with the nearest Ti to the vacancy moving away from it by 0.07 Å[55]. The Co ion didn't seem to move, but the surrounding oxygens all appeared to move towards the vacancy[55]. Mitra et al. also found that the Co stabilised in the high spin state in the presence of an oxygen vacancy[55]. It was determined that the formation of the oxygen vacancy near to a Co ion within the perovskite broke the octahedral symmetry and "causes local hybridization of the Co *3d* with its *4s* and *4p* states"[55]. Work by Cuong et al. using LDA+U DFT calculations concluded that linear oxygen vacancy clustering in $SrTiO_3$ occurred, and occurred more predominantly at interfaces and grain boundaries[56]. This was developed upon by Mitra et al. with respect to Co-OV linear clustering in $SrTiO_3$ 2x2x2 supercells[55]. Mitra et al. repeated what Cuong et al. found in that these linear vacancy clusters appeared to decrease the mobility of vacancies throughout the material and reduced free carrier density[55], [56].

2.2.2.2 Manganese-doping of $SrTiO_3$

Similar to the work by Mitra et al. in 2014, the paper by Valant et al. 2012 covers the origin of magnetism in Mn-doped $SrTiO_3$, but still has interesting points to be taken about acceptor doping of $SrTiO_3$[57]. The first piece of interesting information from this article was the presence of both Mn^{2+} *and* Mn^{4+} in the doped materials. When doping $SrTiO_3$ with Mn, Valant's research showed that Mn^{2+} substituted on the Sr^{2+} site, whereas Mn^{4+} substituted on the Ti^{4+} site. It is noted that the valence of the Mn ion can be affected by oxygen partial pressure, heat treatment regime and stoichiometric manipulation, i.e. creating a deficiency in either the A or B site which can drive the Mn substitution[57]. It is noted that selectivity was not possible for the A-site no matter the experiment methodology and that the B-site was always at least partially substituted for Mn even when not intended[57]. This makes it very difficult to experimentally determine the solubility limit for A-site doping with Mn in $SrTiO_3$. The experimental work by Valant et al. showed that heat treatment at 1500 °C of Ti-deficient $SrTiO_3$ in an oxygen atmosphere resulted in Mn substitution at the B-site, whereas heat treatment under a nitrogen atmosphere of Sr-deficient $SrTiO_3$ resulted in A-site substitution of Mn[57]. It seemed that the atmosphere on heat treatment was responsible for the distribution of A-site or B-site substitution but could not affect the fact that Mn^{2+} incorporated onto the A-site and Mn^{4+} incorporated onto the B-site. This work in this thesis incorporates Mn^{2+} onto the B-site.

As the Valant paper[57] was based on a ferromagnetic study of these materials they provided some magnetic property information about these compositions, which although not the focus of this report, is useful to observe as any magnetic properties could have an unknown impact on the potential piezoelectric properties of a material due to the use of electric fields in testing.

Valant stated that no long-range magnetic order was seen in samples with an Mn-dopant concentration less than 3 %. There was some apparent disagreement with regards to the magnetic properties of A-site doped $SrTiO_3$ amongst other authors described in Valant's paper, but this thesis is primarily concerned with B-site Mn doping of $SrTiO_3$, so this should not be an issue.

In recent conference proceedings from ISAF2020 work by Ryu and Dickey[58] was presented on the co-doping of $BaTiO_3$ with Mn and also co-doping with Mn *and* Y (a donor dopant) in a co-doping system. The conclusions of this work were that the $BaTiO_3$ co-doped system was more resistive than the purely acceptor-doped $BaTiO_3$ and had a better resistance to degradation. The co-doped system also showed more P_{O2} independent conductivity. Charge neutrality equations of these two systems showed that the increase in resistivity from the co-doped system came from a decrease in oxygen vacancies and also a P_{O2} independence[58]. Evidence for ionic conduction was observed at 500 °C in the Mn-doped $BaTiO_3$ sample which was attributed to a high concentration of oxygen vacancies at 500 °C.

2.2.3 B-Site Donor-doped $SrTiO_3$

Donor-doping is the addition of cations to the crystal lattice with a higher valence number, such as La^{3+} in place of the Sr^{2+}, or Nb^{5+} in place of the Ti^{4+}[59]. This difference in cation valence creates an excess of electrons across the material. The band gap in undoped $SrTiO_3$, which is an insulator, is approximately 3.2 eV at 0 K and the valence band is constructed mainly of the oxygen 2p orbital[59]-[60]. The bottom of the conduction band is contributed to by Ti 3d orbitals, which also contribute to the lower half of the valence band[61]. The mixture in the valence band of the oxygen 2p orbitals and the Ti 3d orbitals results in covalent behaviour between the ions creating the well-known oxygen octahedron cage in the perovskite structure[61]. In donor(Nb)-doped $SrTiO_3$, the 4d orbitals of the Nb contribute further to this covalency in the valence band[61]. The excess electrons donated from Nb-doping, however, creates a situation where the Fermi level moves up into the conduction band of the material, reducing the Ti^{4+} ions to Ti^{3+} increasing the size of the band gap[62]. The extra donated electrons collect around the new Ti^{3+} ion increasing its ionic radius and therefore increasing the unit cell size of the material to accommodate it and the newly substituted larger Nb ions[61]. Work by Nishiyama et al. 2019 on charge density distribution indicated that Nb donor-doping decreased the covalency of the Ti-O bonding due to the change in charge distribution that occurred between newly substituted B-site cations and the O-octahedra[61]. The authors suggested the donated electrons reduced Ti^{4+} to Ti^{3+} which lead to smaller local dipole moments, decreasing the overall longer-range Coulombic forces[61].

A 1997 paper by Moos and Hardtl, which covers a sample series of $Sr_{1-x}La_xTiO_3$ where x=0-0.1[63] discussed the primary defects in donor-doped $SrTiO_3$ under varying oxygen partial pressures and at different temperatures with regards to conductivity in comparison to undoped $SrTiO_3$ or acceptor-doped $SrTiO_3$. At low oxygen pressures the main defect was oxygen vacancies compensated by free electrons[63][45]. At medium oxygen pressures the concentration of these defects fell whilst the contribution to conductivity arose mainly from donor-dopants and a conductivity plateau occurred (Figure 2.3). This situation became independent of oxygen pressure but a temperature dependence on conductivity developed. At the highest oxygen partial pressures, Sr vacancies began to appear which compensated for the donor defects[63][45]. In acceptor-doped and undoped $SrTiO_3$ at low oxygen pressures oxygen vacancies and compensating electrons were still the main defect contributing to conductivity as with the donor-doped $SrTiO_3$, and as the oxygen pressure increased the gradient of the conductivity line decreased as oxygen vacancies were met by the intrinsic or extrinsic acceptor content. At maximum oxygen partial pressures, the conductivity changed to p-type as the density of holes increased[63]. This description is summed up in the diagram from this paper below:

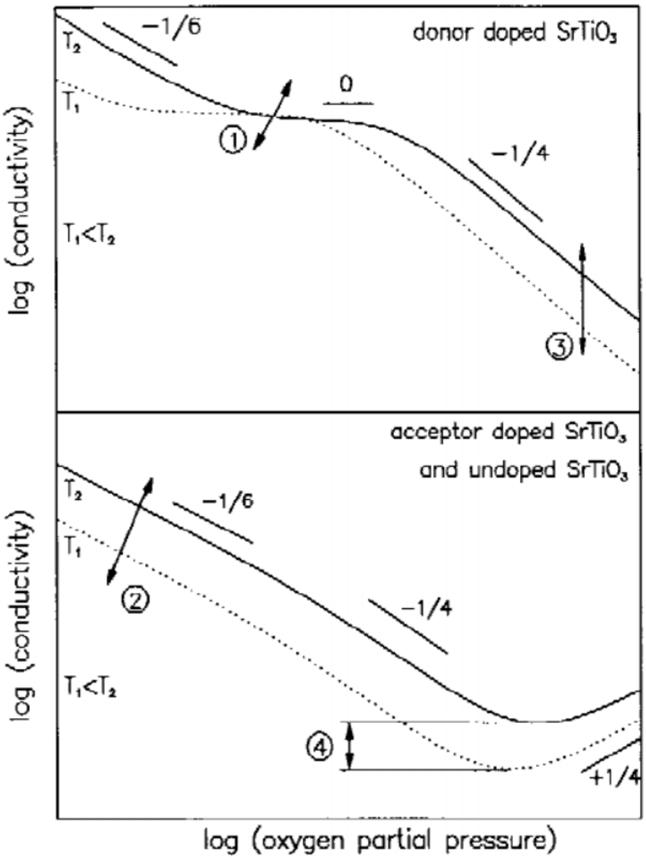

Figure 2.3: An arbitrary log conductivity vs. oxygen partial pressure graph illustrating the conductivity behaviour of donor-doped and acceptor-/undoped $SrTiO_3$ [63].

A paper released in 1994 by Cho and Johnson explored the evolution of the microstructure of Nb-doped $SrTiO_3$[36]. Firstly, the microstructure of un-doped $SrTiO_3$ was examined as a reference. Samples with excess TiO_2 were sintered in air above and below the eutectic temperature, and larger grains were observed in the microstructure of the sample sintered above the eutectic temperature whereas smaller grains were observed in the microstructure of the sample sintered below the eutectic temperature[36]. These fine grains were thought to be the result of a secondary TiO_2 phase in the grain boundaries of the sample sintered at lower temperatures. Next, samples of 0.4 at% Nb-doped $SrTiO_3$ were air fired at the higher temperature and the grain size was surprisingly large (surprising due to the body of literature that describes Nb as having the effect of creating smaller grains), but samples of 1.2 at% Nb-doped $SrTiO_3$ were observed to have a fine-grained microstructure that was also porous[36]. The majority of the Nb-doped samples sintered at the temperature below the eutectic had a fine grained porous structure[36]. This was thought to be due to a compensation of Nb donor centres by Sr vacancies, which in turn increased the solubility of the TiO_2. The samples with Nb dopant concentrations between 0.4-1.2 at% and sintered at 1480°C (above the eutectic) had large grains, not because of the Nb, but because of the amount of TiO_2 excess in these samples that promotes liquid-phase sintering. Samples in this study that had an excess of Sr, or inversely a lack of excess TiO_2 to form $SrTiO_3$ with the SrO, led to the formation of Ruddleson Popper phases and a poor sintering density[36]. Samples of Nb-doped $SrTiO_3$ sintered in both air and H_2 (reducing environment) by Chung et al. however, showed that H_2 greatly inhibited the growth of grains both above and below the eutectic sample[64]. This was attributed to “grain boundary dragging” of Nb which has segregated to the grain boundaries alongside the reduction of Ti vacancy concentration[64].

Research by Karczewski et al. in 2010 stated that the predominant defect of donor-doped $SrTiO_3$ was Sr defects that were formed to fulfil electroneutrality conditions[65]. It was then developed that if this was the case a SrO phase would be developed to accommodate the diffusing Sr from the perovskite structure. This was in agreement with a paper by Xiao et al. 2011 on Nb and Ga doped $SrTiO_3$ [66] who discussed the observation that additions of Nb to $SrTiO_3$ created secondary phases of SrO through the following reaction series:

$$SrO + (1-x)TiO_2 + \left(\frac{x}{2}\right)Nb_2O_5$$

$$= \left(1-\frac{x}{2}\right)Sr_{Sr}^{x} + \frac{x}{2}V_{Sr}'' + (1-x)Ti_{Ti}^{x} + xNb_{Ti}^{\bullet} + 3O_O^{x} + \left(\frac{x}{2}\right)SrO \text{ [66]}$$

In simpler terms, adding one Nb in place of one Ti atom, created $x/2$ Sr vacancies and therefore $x/2$ SrO molecules[65]. This had the effect of reducing the Nb and Ti atoms to Nb^{4+} and Ti^{3+} via the following two reactions:

$$SrO + V_{Sr}'' + 2Ti_{Ti}^{x} \rightleftarrows 2Ti_{Ti}' + Sr_{Sr}^{x} + \frac{1}{2}O_2$$

$$SrO + V_{Sr}'' + 2Nb_{Ti}^{\bullet} \rightleftarrows 2Nb_{Ti}^{x} + Sr_{Sr}^{x} + \frac{1}{2}O_2$$

This was agreed by Slater et al.[38] who discussed two possible mechanisms for the creation of free electrons in the system, either by reducing niobium (Nb) from Nb^{5+} to Nb^{4+}, or by reducing Ti from Ti^{4+} to Ti^{3+}. Slater also suggested that due to the inherently larger concentration of Ti ions in comparison to the Nb ions, the creation of electrons from Nb was not significant enough to affect conduction[38].

The study by Karczewski et al. covered samples that were doped with up to x=0.08 Nb dopant concentration. From XRD studies they found that at x=0.03 Nb separate phases other than cubic perovskite began to appear. From Rietveld refinement they found that samples that were sintered in a reducing atmosphere had larger lattice parameters than those that were not reduced, this was thought to be due to the larger Ti^{3+} and Nb^{4+} ions[65]. The addition of Nb to the $SrTiO_3$ structure increased the size of the unit cell in order to accommodate the larger Nb^{5+} in comparison to the Ti^{4+} ion [38][40]. Slater et al. estimated this to be approximately 4.5 x 10^{-4} Å per percentage of Nb added for the $Sr_{1-x/2}Ti_{1-x}Nb_xO_3$ samples. Irvine et al.[67] also noted the potential for unit cell expansion by up to 0.3 % if the samples were sintered in a reducing atmosphere, (eg. H_2/Ar) due to the presence of the larger Ti^{3+} and Nb^{4+} cations. There was not found to be a linear correlation between Nb content and lattice parameter by Karczewski et al. but a peak unit cell size was observed at x=0.02Nb, and this was thought to be due to the presence of the secondary SrO phase (Sr_2NbO_4) which removed some of the atoms from the perovskite unit cell[65]. Wang at al. 2016 stated that the inclusion of Nb into $SrTiO_3$ greatly affected the microstructure by reducing the grain size, and sometimes encouraged abnormal grain growth depending on the Nb dopant content[40]. The samples maintained the perovskite structure up to x=0.015 in this paper[40]. XPS analysis indicated that the addition of donor Nb^{5+} created free electrons which are then absorbed by local Ti^{4+} creating Ti^{3+} [40].

Conductivity measurements were carried out which showed that samples that were sintered in a reducing atmosphere and increasing temperatures showed an increase in conductivity. Samples sintered at 1200 °C showed thermally activated conductivity behaviour, but as the sintering temperatures rose to 1300 °C and 1400 °C, metallic behaviour began to occur. They also found that conductivity, when compared to Nb-dopant content, was largest for the sample with the largest unit cell parameter, which related to the Ti^{3+} and Nb^{4+} content maximum suggesting they were acting as charge carriers in the material[65]. Conductivity vs. porosity measurements in Nb-doped samples were also recorded and it was found that an increase in porosity of up to 30 % saw a decrease in conductivity by more than a factor of ten. There was also observed to be a weaker temperature dependence of conductivity in the more porous samples which was suggested to be related to the decrease in grain boundaries and their effect on conductivity[65].

A 2002 paper on grain boundary segregation and grain growth in Nb-doped $SrTiO_3$ by Chung and Kang highlighted previous work that showed acceptor dopants segregating to grain boundaries whereas donor dopants do not[64], and they suggested that more studies need to take place regarding grain boundaries in titanate materials and their effect on conductivity. EDX analysis was carried out on samples of Nb-doped $SrTiO_3$ sintered in air and no apparent segregation of Nb at the grain boundary was observed, corresponding with their previous statement. Ti was found in excess at the grain boundaries, however, which supported the pre-existing theory that Ti ions migrated into the grain boundaries. Samples of Nb-doped $SrTiO_3$ sintered in a reducing environment (H_2), however, were found to have up to 20 % of grain boundaries with an intergranular phase with a higher concentration of Nb content than the air-sintered sample[64]. The reason for this was thought to be down to space-charge segregation occurring in response to excess charge within the grain boundary itself, that being a negatively charged grain boundary core potentially caused by acceptor impurities, and a positively charged space charge region. It was suggested that an excess of free electrons produced to compensate for oxygen vacancies or donor dopants could also have been the cause for this negative charge, although this was more likely in acceptor-doped $SrTiO_3$ in an oxidising atmosphere[64]. Cation vacancies were not thought to be a likely contributor as they rarely form under a reducing atmosphere where mainly oxygen vacancies are produced[64].

The paper by Wang et al. 2016 investigated the effect of Nb-doping and reaction conditions on $SrTiO_3$ to see if the relative permittivity values could be improved. It was found that $SrTiO_3$ samples doped with Nb and treated under a nitrogen atmosphere had higher permittivity and lower loss values than regular $SrTiO_3$ or $SrTiO_3$ sintered under an oxygen rich environment. This was because an oxygen rich sintering environment suppressed the formation of oxygen vacancies. It was suggested that under the nitrogen atmosphere, oxygen vacancies were created in the Nb-doped $SrTiO_3$ samples and attached to local Ti^{3+} defects that were caused by the donated electrons from Nb and formed a defect dipole which 'tied up' the free electrons and reduced the dielectric loss[40]:

$$[Ti^{3+} - V_O^{\bullet\bullet} - Ti^{3+}]$$

See more on defect dipoles in Section 2.3.

An interesting paper by Drozdz and Kolezynski 2017[62] was based on the concept of creating intentionally porous ceramics, whereas the majority of literature is based on the production of dense ceramics. The authors suggested that the diffusion time for porous ceramics was up to 6 times faster than that of dense ceramics, presumably due to the increased surface areas for diffusion in the pores. The concern however with these porous materials and their faster diffusivities was the potential for extraneous reactions to occur according to the environment such as CO_2 or H_2O[62]. It was found that the samples in this paper were observed to decrease in crystallite size and increase in unit cell size with increasing Nb content, and that the samples had up to 22 vol.% porosity[62]. Porous ceramics are of interest in this thesis because initial experiments carried out in the earlier segments of the project resulted in Nb-doped $SrTiO_3$ ceramics which were very porous, and dense ceramics were difficult to achieve particularly at high dopant concentrations. However, if the diffusivity was higher in porous ceramics this could be a positive outcome for this thesis as the long-term goal is to relocate and reorient defect dipoles with a field. It is an initial criticism that this work only covers 3 compositions besides undoped $SrTiO_3$ which is not sufficient to draw significant conclusions from. This study places Nb as a substitute for Ti on the B-site in the perovskite lattice. Conductivity measurements were taken under both a reducing and oxidising (synthetic air) atmosphere and the differences were recorded. Firstly, the vacancy situation was outlined for undoped $SrTiO_3$. The main defects were noted to be Sr vacancies, Ti vacancies and oxygen vacancies, and the reminder was given that undoped $SrTiO_3$ behaves as mildly acceptor-doped. There were two different temperatures zones discussed. Below 300 °C Sr vacancies were ionised resulting in the production of hole carriers[62]:

$$V_{Sr}^{x} = V_{Sr}' + h^{\bullet}$$

$$V_{Sr}' = V_{Sr}'' + h^{\bullet}$$

Then at higher temperatures oxygen was incorporated into the $SrTiO_3$, and as temperatures increase there is a shift in the mechanism of conduction to ionic conductivity:

$$\frac{1}{2}O_2(g) + V_O^{\bullet\bullet} = O_O^{x} + 2h^{\bullet}$$

However, this paper was a study of the Nb donor doping of $SrTiO_3$, and extra electrons were created via the following reaction:

$$Nb_2O_5 \rightleftarrows 2Nb_{Ti}^{\bullet} + 2e' + 5O_O^{x}$$

These electrons could occupy empty states in the conduction band and recombine with holes, get trapped at Ti sites reducing Ti^{4+} to Ti^{3+}, or could trap oxygen vacancies. This could cause small polarons around the Ti sites[62], which are tiny regions of charge dipoles that results from the extra negative electron cloud surrounding an ion. The authors noted that Sr and Ti vacancies were created in this system to compensate for the extra oxygen incorporated than usual with Nb doping, however the formation energy of a Sr vacancy was much lower than that for a Ti vacancy and so Sr vacancies were much more likely to form and in greater numbers[62].

With regards to the conductivity of these samples, the observed effects of an oxidising atmosphere were as follows. Undoped $SrTiO_3$ was found to be much more conductive than any of the Nb-doped samples and the difference between them increased with increasing temperature. The 2 and 3 % Nb-doped samples were found to be more resistive than the 1 % sample. In all traces there was clearly a mechanism change from electronic at lower temperatures to ionic at the higher temperatures[62]. Under a reducing environment, undoped $SrTiO_3$ created extra oxygen vacancies via the following equation:

$$O_O^x = \frac{1}{2} O_2 + V_O^{\bullet\bullet} + 2e'$$

Following doping with Nb, due to the donor nature of the dopant, extra electrons were introduced as well as the extra oxygen vacancies from the reducing environment, and both could be incorporated into the conduction band or around the Ti ion, increasing the conductivity[46][62]. The conductivity results achieved in the reducing atmosphere were that the doped samples were much more conductive than the undoped $SrTiO_3$ sample[62]. Interestingly the 1% sample was more conductive than the 2/3 %. This was suggested to be because there was expected to be more localisation and trapping of the electrons in the 2/3% samples due to the greater amount of Nb added, leading to an oxidation of Nb^{3+} to Nb^{5+}. The samples were observed to change according to increasing Nb from light cream to blue grey, and this matches the observations seen in initial experimental work in this thesis. Finally, it was found that these samples had increasing chemical instability in line with increasing Nb content in a H_2O/CO_2 environment and it was thought that this was in part due to weakening Sr-O bonds due to a distorted TiO_6 octahedra from the substituted larger Nb at the corner sites and the longer Nb-O bond length.

A paper mentioned earlier by Chan et al.[46] on the effects of non-stoichiometric $SrTiO_3$ has a section whereby samples of non-stoichiometric $SrTiO_3$ were doped with a constant concentration of Nb. It was found that sample with compositions of Sr/Ti=0.999 the conductivity was significantly reduced by the presence of Nb, but that by compositions Sr/Ti=0.995 the effect of Nb was non-existent. This was suggested to be due to the amount of oxygen vacancies produced by the excess TiO_2, such that the increasing amount of oxygen brought to the lattice by the Nb dopant fully saturated the lattice and donor-behaviour was lost, alongside an increase in the solubility of TiO_2[46].

2.2.3.1 A-Site Vacancy Compensation of Donors

The inspiration for this PhD work stems from a paper by Fujii et al. [41] whereby PZT thin films were created for miniaturised actuator structures and compared undoped PZT films against those with additions of Nb. It was discussed in this paper that the addition of Nb improved the piezoelectric performance of the material, and in this case with respect to the dielectric constant. This particular research noted the achievement of a relatively large content of Nb was added and absorbed by the PZT film (13 %) compared to that of bulk PZT (3 %) before loss of the perovskite structure occurred [41]. This was a significantly large dopant concentration to be absorbed into a system with no significant disruption to the perovskite structure, but it was thought that it was the low sputtering temperature that was able to achieve this in comparison to traditional bulk ceramic processing high temperatures. It was also stated in conference proceedings of the same work that the films were piezoelectric well above the conventional T_C of PZT[68] with no degradation observed and that the displacement results were more linear than typical PZT with less hysteresis even without poling. This is significant as it suggests that a defect mechanism is either increasing the T_C or resulting in a defect dipole piezoelectric effect.

In work carried out by Kolodiazhnyi and Petric, samples were made of Nb-doped bulk $SrTiO_3$ sintered in air on the assumption of Sr-vacancy compensation of donors [40], and it was confirmed that their samples remained single phase up to a Nb concentration of x=0.30. However, it was also discussed that work by Slater et al. was able to achieve single phase material at up to x=0.4[43]. The work by Slater observed an impurity phase at Nb concentrations higher than x=0.4. This was impressive as some literature had considered the solubility limit of Nb to be around approximately 2-3 % in air fired samples without intentional

A-site vacancies [37]. For comparison $SrTiO_3$ doped with yttrium only achieved a solubility limit of 4% [40], above which pyrochlore phases began to appear repeatedly. Co-doping with Y and Nb jointly only served to lower the solubility limit of the Nb[40]. It was the inclusion of A-site vacancies in the Kolodiazhnyi and Petric work that provided the space to accommodate so much Nb-dopant. Another important conclusion from this study was that the presence of Nb appeared to "stabilise the small levels of Ti^{3+} generated by reduction" [38]. Samples with more Nb content appeared to be more resistant to reoxidation.

Brant et al. produced a study in 2010 on the $Sr_{1-x}Ti_{1-2x}Nb_{2x}O_3$ (STN) series of materials and conducted neutron diffraction, electron diffraction and high resolution synchrotron analysis on the samples[69]. This work was of most interest to this thesis due to the matching formula, which although initially seems different to that of this thesis ($Sr_{1-/2x}Ti_{1-x}Nb_xO_3$), it equates to the same stoichiometry. Three separate compositional blocks were observed. The first of the formula $Sr_{1-x}Ti_{1-2x}Nb_{2x}O_3$ with intergrowth of $SrTiO_3$ where x=0-0.125, a middle region where single phase $Sr_{1-x}Ti_{1-2x}Nb_{2x}O_3$ existed at x=0.15-0.20, and a final phase where mixed phases existed between x=0.2-0.4, only one of which matched the intended formula. The second phase present was identified as $Sr_3TiNb_4O_{15}$. Synchrotron data that was taken for samples between x=0-0.2 indicated that the structure of all samples matched that of undoped $SrTiO_3$ (*Pm-3m*) which agreed with the refinement data produced in this study. These samples are of interest because there has been much work carried out on the B-site doping of $SrTiO_3$ with Nb, but there is not much discussion on the structural effects of intentionally creating a large amount of A-site vacancies. Brant discussed that the creation of an A-site vacancy in the perovskite structure, resulted in the surrounding oxygen anions moving closer to the remaining Sr atoms, which resulted in an octahedral tilting of the structure, however this was not observed in their X-ray diffraction data. As such they conducted subsequent electron diffraction experiments. The conclusions from this experiment were that the large defect content of this perovskite gave rise to a flexible structure which was stable down to approximately 75 K before a tilt to tetragonal symmetry occurred, which is seen in $SrTiO_3$ at 105 K. This indicated that this particular STN series was more stable than the $SrTiO_3$ parent structure.

Work by Whittle et al. in 2017 was "tailoring phase transition temperatures in perovskites via A-site vacancy generation". They worked on a series of samples with the formula $Sr_{1-x}Zr_{1-2x}Nb_{2x}O_3$ with x=0-0.15 where the B-site ratio of Ti to Zr is varied[70]. The samples studied had the same formulas as those used in this thesis, with the exception of the Zr content. The authors noted that the structure changed from the cubic *Pm-3m* to tetragonal *I4/mcm* at x=0.2

which was why the compositional range in the paper was chosen (x=0-0.15)[70]. They mentioned that *Pm-3m* cubic perovskite is not ferroelectric but susceptible to relaxor ferroelectric behaviour, which could be increased by creating regions of inhomogeneity within the material by changing the ratio of Ti to Zr on the B-site. Zr also induced a tetragonal phase, and so there was the possibility of changing phase stability with temperature by manipulating the B-site[70]. Following Rietveld refinement of XRD data and neutron diffraction analysis it was found that there was a linear correlation between increasing Zr content and cell parameter increase, due to the larger cation size of Zr compared to Ti, which was causing the octahedral tilting and a lowering of the symmetry of the system to tetragonal. This supported the observation of octahedral tilting observed by Brant et al.[69].

Bond valence calculations were made to assess the effect of increasing unit cell size on chemical bonding within the perovskite structure by Whittle et al[70]. It was observed that as the zirconium content was increased and the unit cell expanded, the Sr bonding became weaker[70]. The B-site bonding was slightly more complex due to the variety of cations on this site in these samples (Zr, Ti, Nb). In the end member sample of the series where Ti and Nb were both present in the sample ($Sr_{0.8}Ti_{0.6}Nb_{0.4}O_3$), the bond distances to oxygen were similar and within the ideal bond length for an oxygen octahedron. As the larger Zr is substituted onto the B-site in place of the Ti, the bonding to oxygen became weaker as the distance between the B-site and oxygen became greater[70]. A-site vacancies were assessed in this work, and it was initially observed that it is not possible to assign a radius to a vacancy as with other effective ionic radii[16]. This meant it was difficult to assign Goldschmidt tolerance factors to perovskites with a significant concentration of defects, such as those in this thesis, so it is commonplace to assign radii of Sr^{2+} to the vacancy sites[70]. A decrease in tolerance factor indicated an increase in likelihood of a phase transition, as seen when the Zr is increased in the series $Sr_{0.8}Ti_{0.6-x}Zr_xNb_{0.4}O_3$. The paper by Whittle et al., as with the work in this thesis, compared a system with defects to an equivalent defect-free system ($SrTi_{1-x}Zr_xO_3$). It was found that the distortion to the lower symmetry tetragonal structure happened at a much smaller Zr content (x=0.05) than for the system with A-site vacancies, and there was even a second phase transition to orthorhombic[70]. In conclusion the inclusion of A-site vacancies appears to allow a higher symmetry phase to exist for wider composition ranges and to lower temperatures. Another structural conclusion from this work was that there is likely to be widespread local disorder across the material with different sized octahedra with either the larger or smaller B-site cations at the centre. This may match the work carried out in this thesis with a larger Nb^{5+}

ion in place of the Ti^{4+} cation in different areas throughout the lattice. A brief explanation of the effect of A-site vacancies was given by Whittle et al[70]. They state that tolerance factors appear to be smaller in the samples containing A-site vacancies, which they interpreted to mean that the vacancies occupy more space than the relevant cation would, and that the surrounding atoms counterintuitively moved away from the space due to the decrease in bonding contribution from the missing cation[70].

Oxygen position and bonding in the perovskite structure is key to understanding electrical properties and phase transitions. Neutron diffraction is a technique used to assess this as the scattering power of oxygen atoms is more significant in this technique compared to others. For example, in the study by Whittle et al. 2017[70] it was found that oxygen has one independent site in the cubic *Pm-3m* structure of $Sr_{1-x}Zr_{1-2x}Nb_{2x}O_3$ and two in the tetragonal, so this technique is clearly a useful one to more clearly observe transitions occurring between structural symmetries.

A theoretical paper produced by Baker et al. in 2018 was a study of the mechanisms governing metal vacancy formation (including A-site) in $SrTiO_3$ and $BaTiO_3$ and the effect of doping with donor dopants Nb and Fe to create n-type materials[71]. Cubic phases of each material were studied for comparison. The main differences between the metal vacancies that formed in these two similar materials were that in $BaTiO_3$ the metal vacancy forms on the B-site (V_{Ti}) whereas in $SrTiO_3$ it was on the A-site (V_{Sr}). In oxidising conditions and in doped samples B-site vacancies can occur[71]. This tells us that it is more energetically favourable for $SrTiO_3$ to lose a Sr atom than for $BaTiO_3$ to lose a Ba atom. In energetic terms it takes less energy to produce an A-site vacancy in $SrTiO_3$ than $BaTiO_3$ because of differences in chemical potential. The A-site vacancy in $SrTiO_3$ is 0.6-0.8 eV lower in formation energy than in $BaTiO_3$, whereas the B-site vacancy in $SrTiO_3$ is 1.1-1.3 eV *higher* in formation energy compared to $BaTiO_3$[71].

$SrTiO_3$ has a predicted bandgap of 3.25 eV, and a lattice parameter of 3.901 Å and $BaTiO_3$ has a predicted bandgap of 3.20 eV with a lattice parameter of 3.990 Å[71]. Oxygen vacancies are the primary vacancy in $SrTiO_3$/$BaTiO_3$ as with most metal oxides. The have a 2+ charge and can be located in the band gap in both materials. If the oxygen vacancy transitions to the Fermi level, and the Fermi level is near to the conduction band then the oxygen vacancy can trap an electron and change to a 1+ charge, and if the Fermi level is close to the valence band then the oxygen vacancy can capture a hole and become 3+ charge[71]. A-site vacancies were also found in the band gap of these materials but had a 2- charge and degenerate states also existed near to the valence band and multiple different charged states could exist in these materials such as 2-/4-/5- etc[71]. The V_{Ti} (B-site vacancy) has a 4- charge and can have many different valences up to a neutral 0. As the reaction conditions changed to a more oxidising atmosphere the formation energy of a V_{Ti} compared to that of V_{Sr} drops significantly due to changes occurring in phase stoichiometry[71]. The authors described that in $SrTiO_3$, the energy of formation of a V_{Sr} was lower than both a V_{Ti} and a V_{Ti}-V_O defect dipole, and this energy difference increased with increasing TiO_2 excess[71], which made the V_{Sr} the major metal vacancy in $SrTiO_3$[71]. The authors discussed that the reasoning for this stemmed from how A-site vacancies predominantly interacted with the crystal lattice ionically[71]. The lattice parameter as stated previously was smaller for $SrTiO_3$ than $BaTiO_3$, so the ionic interaction between the lattice and Sr atom should have been stronger than that of Ba in $BaTiO_3$[71]. However, the Sr had higher electronegativity than Ba, meaning it had more ionic characteristic than Ba and as such behaved in a weaker less covalent way than Ba and was easier to remove from the lattice, hence why it was easier to form a V_{Sr} than a V_{Ba}[71]. When explaining the V_{Ti} however, one must consider the Ti-O octahedron. It is covalent in nature, and the p-states of the oxygens present create a valence band, whilst the Ti d-states form a conduction band[71]. Titanium and oxygen have similar charges in both the $SrTiO_3$ and $BaTiO_3$ environment, however $BaTiO_3$ has the larger lattice parameter which makes the Ti-O interactions weaker, making a B-site V_{Ti} easier to create in $BaTiO_3$ than $SrTiO_3$[71]. The DFT calculations from this paper match this description[71]. This DFT-based paper also carried out calculations based on donor-doping with Nb. It was found that when $SrTiO_3$ and $BaTiO_3$ were doped with Nb, it was unlikely that Nb will dope on the A-site of both materials due to high formation energies. They also found that Nb_{Ti}-V_O defect complexes were also not energetically favourable in either material. The most common and energetically favourable location for the Nb dopant ion was on the B-site as Nb'_{Ti}, at which point the 4d electrons of Nb moved into the p-orbital of the oxygen valence band[71]. The existence of metal vacancies compensated the increased level of electrons in a donor-doped material.

A 2011 paper produced by G. Xiao et al. created a series of $SrTiO_3$ samples deficient in A-site cations, with Ga and Nb used as B-site donor-dopants where $x=0.05$-0.2[66]. The study was conducted in order to investigate the conductivity properties observed in donor-doped $SrTiO_3$ and the effect of A-site vacancies on the maximum donor dopants able to be added to the perovskite system. A Sr-deficiency was created in their samples in order to minimise any secondary SrO-rich phase: $Sr_{0.9}Ti_{0.8-x}Ga_xNb_{0.2}O_3$, resulting in a single phase cubic perovskite structure[66]. The inclusion of Ga in the Nb-doped $SrTiO_3$ samples created an increased level of oxygen vacancies via the following reaction:

$$\left(\frac{y}{2}\right) Ga_2O_3 = yGa'_{Ti} + \left(\frac{y}{2}\right) V_O^{\bullet\bullet} + (3\frac{y}{2})O_O^x \text{ [66]}$$

This has the effect of reducing the sample and influencing conductivity. The Ga co-doped sample was found to be twice as conductive as the solely Nb-doped sample[66]. The addition of Ga to the Nb-doped $SrTiO_3$ sample increased the lattice parameter of the material, but this could be due to the reducing effect of Ga, and in particular the reduced Nb^{5+} and Ti^{4+} species[66]. The addition of Ga was also found to decrease the sinterability of the samples. As such from these findings it was decided that Ga-doping would not be suitable for this thesis.

Slater et al. in 1996 and 1997 produced two papers with La and Nb co-doped and singly-doped $SrTiO_3$ with compensating Sr vacancies[67][38] and examined their conductivity relationship to oxygen partial pressure. The Nb-doped samples were of particular interest as they matched the formula of some samples produced in this thesis; $Sr_{1-x/2}Ti_{1-x}Nb_xO_3$, however in the 1996 paper the samples after sintering were then reduced in a H_2/Ar atmosphere which will make the samples behave differently to those in this thesis. The authors found that for the La-doped samples the unit cell decreased with increasing La content, due to the smaller cation size of La compared to Sr[38]. Samples of Nb and La co-doped samples were found to have expanding unit cell sizes of 0.10 % compared to more than 0.15 % for purely Nb-doped samples[38]. With regards to conductivity, the purely La-doped samples were found to have good conductivity at low oxygen partial pressures and increasing conductivity with La-content up to x=0.6. When comparing Nb-doped samples to La-doped samples, it was found that the samples containing Nb, including both the purely Nb-doped samples *and* the Nb and La co-doped samples, appeared to have a resistance to re-oxidation despite being held for a week in an oxidising environment[38][67]. This was suggested to be an oxygen transport issue in relation to high Nb-contents. This was not as much the case with intentionally porous samples. Resistivity vs. temperature measurements on samples that were reduced in a H_2-Ar mixture showed metallic behaviour with resistivity decreasing with decreasing temperature. A "deviation from linearity" was seen approaching room temperature which was attributed to grain boundary effects[38]. The authors also noted in this work that there was the potential for uncertainty surrounding the exact composition of the samples, as TiO_2 could be an impurity and there could also be Sr-losses in excess of those intended via compositional A-site vacancy from sintering[38]. This will be taken into consideration in this thesis. Conclusions from the conductivity experiments stated that a change in oxygen concentration within the samples of $\delta=0.04$ was enough to induce metallic behaviour through the introduction of Ti^{3+} ions in the reduced samples[38].

This thesis will initially attempt to recreate the work of Kolodiazhnyi and Petric by creating samples of $SrTiO_3$ with up to $Nb_x=0.30$ with intentional Sr vacancies before carrying out electrical measurements to attempt to determine the electrical behaviour of the samples, along with ascertaining the existence of any defect dipoles that could be engineered.

2.3 Defect Dipoles

PZT ceramics doped with manganese are commonly used to provide the high mechanical Q and low dielectric loss commonly used in high power applications. This avoids heat loss whilst still delivering high power[72]. The manganese acts as an acceptor dopant to create the “hard” piezoelectric effect and has a lower valence than the ion which it is intended to be substituted for. The use of acceptor ions as dopants creates oxygen vacancies (positively charged) due to charge compensation mechanisms that act to balance the charge neutrality of the lattice. These oxygen vacancies then form defect dipoles with the negatively charged acceptor dopant ion[72]. Although the concentration of defect dipoles is often low in a material, they can play a significant role in the piezoelectric behaviour as they act as pinning centres for ferroelectric domains and stop them switching under applied alternating electric fields[72].

During the ageing process of piezoelectric ceramics, the oxygen vacancies that are present migrate to occupy the lattice site closest to the acceptor dopant ion (site *i*)[72]. If we use cubic $BaTiO_3$ as an example, the probability of the oxygen vacancy being located at site “*i*” is Pi where i=1-6 of the oxygen sites in the ABO_3 unit cell. In the cubic $BaTiO_3$ unit cell above the T_C the P_i of the six oxygen sites is equivalent as the oxygen sites are equivalent within the cell[72]. However, below the T_C for $BaTiO_3$ following the transition to the tetragonal structure, the dopant cation shifts along the 001 axis. This creates non-equivalent oxygen sites within the unit cell[72]. It is of note at this point that the tetragonal phase of $BaTiO_3$ is a ferroelectric phase. It is in this phase that the defect dipole orients along the same axis as the direction of spontaneous polarisation. This minimises the electrostatic energy of the lattice[72]. The defect dipole that has formed at this point is $(X_{Ti}'- V_o^{\cdot\cdot})^{\cdot}$. The orientation of the dipole may be different in different materials but will likely always be in the direction closest to the direction of spontaneous polarisation.

Cation vacancies will be discussed in more detail later, but they are often generated through sintering processes where volatile metals are lost such as Bi^{3+}, Na^{+} or K^{+} in BNT-based or KNN-based ceramics. Oxygen vacancies are formed again in this case in order to charge compensate but they pair instead with the V_{Na}' or V_{Bi}''' for example.

A seminal paper by Lambeck and Jonker in 1978 was the first to discuss in detail the existence of defect dipole pairs and their effect on the electrical properties of a ferroelectric ceramic. Their work involved doping $BaTiO_3$ single crystals with 1 % Mn-doping. In this case it was found that the Mn^{2+} ion was substituted onto the Ti^{4+} site, and paired with a doubly ionised oxygen vacancy to form a defect dipole[26]. This negatively charged acceptor dopant ion when paired with the positively charged oxygen vacancy created what Lambeck and Jonker termed an “internal bias field”[26]. Their paper also discussed the ageing effect which caused a shrinking of the hysteresis loop, a reduction in tan delta and increased the piezoelectric quality factor Q[26], but also that the existence of these defect dipoles could suppress the ageing phenomenon. Ageing is a result of a combination of 4 effects; a bulk effect from the relaxation of aligned anisotropic lattice defects by the polarisation direction, a wall effect from the diffusion of defects into the walls of grains, a boundary layer effect which fixes domain structures because electric fields are cancelled out by the diffusion of defects into walls, and finally the stress effect from which macroscopic effects can rearrange the domain structure[26]. It is believed that the existence of defect dipoles stabilises ageing as a result of the bulk effect of a systematic repeating defect dipole aligning with the polarisation direction[26].

The 1988 paper by Arlt and Neumann covered the internal bias in ferroelectric ceramics caused by defect dipoles, and suggested that they cause a hysteresis curve (P-E loop) that is shifted on the x-axis, stabilise the ferroelectric nature of the material and stop the depolarisation that can occur at moderate electric fields[73]. In similar agreement to Lambeck and Jonker, Arlt and Neumann believed that the addition of acceptor dopants increased the presence of defect dipoles in a ferroelectric material, which created an “internal bias”[73], and that the sintering step of ceramic processing created oxygen vacancies to neutralise the acceptor dopants. In this work they doped $BaTiO_3$ with 1 % Ni, with the Ni^{2+} ions substituting on the Ti^{4+} sites[73]. They also found that the degree of internal bias formed was proportional to the concentration of dopant added[73]. The defect dipole in this case formed from the Ni^{2+} on the

Ti^{4+} site and the positively charged oxygen vacancy. Arlt and Neumann found that the unit cell with this defect dipole present differed from that of the normal $BaTiO_3$ unit cell by having a different permittivity, and a distortion of the unit cell caused by an elastic dipole moment from the defect dipole[73]. With regards to the movement of the defect dipole, Arlt and Neumann found that at high temperatures the oxygen vacancy could swap to the other oxygen sites within the octahedron, and that on cooling through the T_C a spontaneous polarisation occurred with the characteristic $BaTiO_3$ tetragonal distortion[73]. A closer look at the structure of the defect dipole showed that as with a typical $BaTiO_3$ tetragonal distortion, the Ti ion was shifted upwards off-centre, but the substituted Ni ion was not. This meant that between the Ni-doped cell and the next regular $BaTiO_3$ cell above, there was a larger gap than there would be usually and as such the oxygen vacancy would preferentially choose this spot in which to exist spatially and electrostatically[73].

De Souza mentioned in his 2015 paper on oxygen diffusion in $SrTiO_3$ that the oxygen vacancies found in $SrTiO_3$ materials began to interact with acceptor defects at lower temperatures such as Mn, Ni and Fe on the Ti B-site and that this occurred in the nearest neighbour location. This paper discussed that some acceptor-dopants such as Ni have the effect of changing the activation energies for diffusion across more than nearest neighbour sites from the dopant ion, up to approximately 1 eV from a 0.65 eV average in un-doped $SrTiO_3$[50]. Interesting work by Shi et al.[74] showed Fe-doped BNT-BT regarding the defect dipole $(Fe_{Ti}'-V_o^{\cdot\cdot})^{\cdot}$ and its effect on reducing the conductivity and enhancing the fatigue resistance of electroceramics. This was due to the restrained migration of oxygen vacancies, i.e. by “mopping up” oxygen vacancies in the lattice and preventing the movement of charge carriers, as described by De Souza[50]. This could be useful in this thesis with the attempt to reduce conductivity across samples and manipulate defect dipoles.

Up until a paper produced by Warren et al. in 1995, there had been no intentional alignment of defect dipoles in ferroelectric ceramics, only the detection of them. In this work a concentration of Fe^{3+} centres were found in a sample of undoped $BaTiO_3$ single crystal which were presumed to be due to impurity acceptor doping[75]. The defect dipole identified in this work was Fe^{3+} and an oxygen vacancy. Again, the Fe^{3+} was substituted onto the Ti^{4+} site[75]. There were also signals present in the analysis that were thought to be either from a (Fe^{1+} - oxygen vacancy) defect dipole or a (Fe^{5+} - V_{Ba}'') defect dipole. This work then attempted to align these defect dipoles and used electron paramagnetic resonance spectroscopy (EPR) to analyse the results. The regime used by Warren et al. was to apply a DC bias of -450 V for one hour at a temperature of 110 °C to the material[75]. Single crystal $BaTiO_3$ had three principal directions for alignment; parallel, perpendicular, and antiparallel, and EPR spectroscopy was used to determine the alignment of these defect dipoles with the magnetic field from the fluctuations in the local environment. For example, a perpendicular alignment to the magnetic field yielded a dipole signal which was twice as strong in comparison to a parallel one[75]. It was suggested in this particular paper (yet disproved in the subsequent paper by the same author) that cation motion and defect dipole alignment could be possible in $SrTiO_3$, because the reorientation of oxygen vacancies to align the dipole in the $BaTiO_3$ single crystal occurred over atomic distances. A test was performed to see if the defects were re-orientable after an initial alignment, by flipping the DC bias at temperature for three minutes when the defects were seen to be partially randomised, and then the bias continued for another hour and the defect dipoles were mostly aligned in the new direction[75].

The 1996 paper by Warren on defect dipole alignment and tetragonal strain was a development on the earlier paper by the same author and previous works on defect dipole alignment[26], [73] and looks at the alignment of defect dipoles in $BaTiO_3$, $SrTiO_3$, PZT and PLZT[76]. There was a suggestion by Warren which could be problematic for this project if found to be correct, which was that it is only possible to align dipoles in the ferroelectric non-cubic phase of these materials and in the ferroelectric direction[76]. Similar to the work in the 1995 paper[75], a small concentration of Fe^{3+} impurity acceptor centres were also found in $SrTiO_3$. Another development on the 1995 Warren paper was the confirmation of the existence of an Fe^{1+}- oxygen vacancy pair in $BaTiO_3$, which was also able to be aligned like the Fe^{3+} defect[76]. Another development in this paper was the alignment of defect dipoles in a polycrystalline material. This was much more difficult to do because each grain in a polycrystalline material had a different principal axis of direction relative to the field, and as such the alignment of dipoles tended to form a Gaussian distribution curve around the field direction[76]. High temperatures in the presence of an electric field were used to align the dipoles, and it was thought that it was the oxygen vacancies that were moving around the oxygen octahedra, and that the cation vacancies were much less mobile even at high temperatures[76]. This movement of dipoles only occurred below the Curie temperature when ferroelectric distortion (for tetragonal $BaTiO_3$) and spontaneous polarisation occur[76].

After the discovery of the same Fe^{3+} and Fe^{1+} oxygen vacancy defect dipoles existing in $SrTiO_3$, there was an attempt to orientate them similar to the work done on $BaTiO_3$. A field at 1000 V at 100 °C was applied to the samples for three days and the sample cooled to room temperature with the voltage left on[76]. Some degradation resistance was observed but no defect orientation occurred based on rotational studies carried out before and after treatment showing no difference. This suggested that defect alignment under this treatment regime did not align defect dipoles in $SrTiO_3$.

Warren also reported the presence of defect dipoles in PZT. That is an Fe^{3+}-oxygen vacancy pair, and Ti^{3+}, Pb^{3+} and Cu^{2+} lone centres; the lone centres locating on the Ti^{4+} B-site[76]. The Ti^{3+} lone centre has a larger radius than Ti^{4+} and a greater negative charge, as such it was more difficult to move around the lattice and therefore harder to align[76]. A study of PLZT was also carried out in this paper and the Pb^{3+} lone centre was identified. This constituted a hole in the place of the Pb^{2+} ion. The Pb ion as previously discussed has the $6s^2$ lone pair of electrons which makes the defect highly polarisable, as such poling at room temperature was sufficient to induce alignment[76]. A Cu^{2+} ion observed in the sample was not stable in a state of alignment following poling for 12 hours at 140 °C and 1000 V due to its large radius and doubly negative charge with respect to the original lattice, repelling oxygen ions[76]. The Fe^{3+} lone centre in the PLZT sample could not be aligned under any poling regime and this was suggested to be because of a half-filled $3d^5$ orbital and its placement in a distorted unit cell[76].

A paper by Liu and Cohen 2017[77] used DFT and a first principles study to further understand defect dipoles and their effect in $BaTiO_3$. The first principles study produced by Liu and Cohen proposed that dipolar defects coupled with ferroelectric domains through long-range electrostatic and elastic interactions[77]. The DFT study consisted of placing a pair of "dummy atoms" of opposite charge and equal distance from the nearest Ti atom. From there the number, position and charge of atoms was varied in order to replicate changing defect dipole concentration and orientation, which provided a simulation for defect dipoles that had not previously been carried out[77]. These DFT calculations were modelled on a tetragonal $BaTiO_3$ structure and found that the defect dipoles do increase the overall polarisation but that the type of dipole species does not affect the magnitude of the polarisation increase[77]. Liu and Cohen described the defect dipoles that commonly form from the inclusion of acceptor impurity elements in samples. For example:

$$(Cu_{Ti}'' - V_o^{\cdot\cdot})^x$$

$$(Mn_{Ti}'' - V_o^{\cdot\cdot})^x$$

$$(Fe_{Ti}' - V_o^{\cdot\cdot})^{\cdot}$$

The addition of 0.1 at% Mn^{2+} on the B-site of $BaTiO_3$, was found to enhance the mechanical quality factor Q_m[77]. The authors then went on to discuss donor doping in lead-based perovskites which are often then charge compensated by lead vacancies to form a cation dipole pair which can form from sintering losses:

$$(Nb_{Ti}^{\bullet} - VPb'')'$$

However, this cation pair appeared to have no orientation preference. This could be due to the lack of cation mobility observed in these studies making it difficult to orient the dipole. The authors noted that lead-vacancy dipoles were more likely to orient randomly having the effect of reducing the coercive field whilst maintaining a symmetric hysteresis loop profile, which would be consistent with a “softened” ferroelectric[77].

KNN systems in lead-free piezoelectric ceramics are known for their high T_C, large d_{33} and low hysteresis SE-loops[72]. There was an example of a CuO-doped KNN system where a defect dipole formed between the Cu^{2+} on the Nb^{5+} site and an oxygen vacancy $(Cu_{Nb}'''-V_o^{\bullet\bullet})'$[78]. The presence of this defect dipole created the expected effects of domain pinning and an increase in Q_m, however, when extra amounts of CuO were added this caused the formation of extra oxygen vacancies. These excess oxygen vacancies then combined with the pre-existing defect dipole creating an electrically neutral defect with no polarity $(V_o^{\bullet\bullet}- Cu_{Nb}'''-V_o^{\bullet\bullet})^{\bullet}$, hence lessening the hardening effect as the concentration of dopant was increased[78]. This study showed that each defect dipole reaction case is individual and based on the chemical profile of the material and that there can be an optimum dopant level to maximise the effect of defect dipoles. A $KNbO_3$-based system doped with CuO was also studied by Yin et al. 2021[79], with materials of the formula KN-$_x$CuO. In this system two possible defect complexes form:

$$(V_O^{\bullet\bullet} - Cu_{Nb} - V_O^{\bullet\bullet})^{\bullet} \text{ or } (Cu_{Nb} - V_O^{\bullet\bullet})'$$

These complexes both contributed to the overall polarisation when aligned either parallel or anti-parallel with the polarisation direction, and depending on the composition, the external field and the temperatures used, superior piezoelectric properties were observed.

A recent paper by Maier et al. 2020[80], used a variety of analytical techniques to attempt to characterise the defects and defect dipoles present in Mn-doped $SrTiO_3$. The techniques used were EPR, DFT and XAFS (X-ray absorption fine structure; gives local structure and unoccupied electronic states). This paper showed that a combination of techniques must be used in order to arrive at a complete picture for the defect states of a material. For example, EPR does not detect the presence of Mn^{3+} ions, whereas XAFS and DFT does. However each of these techniques also has a detection limit, be it low or high, for example 0.05 mol% Mn as a lower limit of detection for XAFS, and 2 mol% as an upper limit for EPR[80]. Another interesting conclusion was the discovery of a linear defect by DFT, which was detected as a possible defect energetically, and yet the likelihood of its formation under experimental conditions was questionable. The Mn^{3+} ion substitution on the Ti^{4+} site resulted in charge compensation in the form of oxygen vacancies to produce the linear defect complex:

$$(Mn_{Ti}' - V_O^{\bullet\bullet} - Mn_{Ti}')^x$$

However, the likelihood of two Mn defects existing in neighbouring cells with random doping was dependent on the concentration of Mn-dopant in the system; the more dopant, the increased chance of this defect complex occurring. It was unlikely, especially due to the slow mobility of cations in perovskite structures. There was also the probability that the complex could form and then dissociate at high temperatures when the mobility of oxygen vacancies greatly increased[80]. This proved that it was necessary to consider the defect species present in varying dopant concentration samples as opposed to assuming that the same would occur in each sample. In this case the more likely defect was the below defect dipole due to nearest neighbour defects[80]:

$$(Mn_{Ti}' - V_O^{\bullet\bullet})^{\bullet}$$

2.3.1 Defect Dipole Effect on Properties

Zhao, Dai and Huang in 2019[72] conducted a review of studies of lead free electroceramics that contain defect dipoles. This review paper, as did the paper by Liu and Cohen[77], discussed the effects of defect dipoles on the following electrical properties.

2.3.1.1 Large Permittivity

A paper by Pan, Cao and Qi in 2019[81] conducted research into a $SrTiO_3$-based system investigating the effects of defect structure on dielectric properties. The system in question was $SrTi_{1-x}(Zn_{1/3}Nb_{2/3})_xO_3$, whereby two Nb^{5+} ions were acting as donor dopants and compensating for one Zn^{2+} which was acting as an acceptor. Dopant concentrations were such that charge neutrality was maintained without the addition of oxygen vacancies. It was thought that through a series of defect equations that two possible defect dipoles were forming in this system:

$Nb_{Ti}^{\bullet} - Ti'$ - formed by the electron from a Nb^{5+} ion and weakly localised by a Ti^{4+} ion and Nb^{5+} ion. In this case the electron acted as a polaron and hopped amongst said Ti^{4+} and Nb^{5+} ions.

$Ti' - V_O^{\bullet\bullet} - Ti'$ - this defect dipole was thought to be the cause of enhanced dielectric properties in the system. It was thought to tangle and form clusters which localised an active region of electrons, which decreased the loss tangent caused by conduction[81].

These defects were thought to interact electrostatically and cause the Zn^{2+}/Ti^{3+} - O octahedron to shift off-centre which created polarisation in the lattice, resulting in the improvement of dielectric properties. In this research, a peak in permittivity was seen at x=0.015 (≈9100) accompanied by the lowest tan δ value (≈0.03). The permittivity increased up to this dopant concentration due to the larger number of defects that began ordering, lowering the local symmetry resulting in improved dielectric properties. Above this dopant concentration (x=0.02) the effects of ionic conductivity took over due to the higher content of impurity ions and local polarisation was suppressed due to the Zn^{2+} and Nb^{5+} ions being closer to one another with increasing dopant concentration[81]. This work was developed on by Pan et al. in 2020[82], where the group varied the valence states in order to attempt to defect engineer similar materials. They showed that the increasing valence states of the dopants could increase lattice parameter, relative permittivity but also tan δ.

A second $SrTiO_3$-based system, this time co-doped with Al and Nb, was studied by He at al. 2017[83]. Material compositions of the formula $Sr(Nb_{0.5}Al_{0.5})_xTi_{1-x}O_3$ (SNAT) were thermally treated in environments of air, O_2 and N_2 and their dielectric properties compared. The air-SNAT6 sample was found to have the highest permittivity (10500) and the lowest tan δ (0.03). This giant permittivity was thought to be due to an off-centering of Ti^{3+} in the TiO_6 octahedron identified by Raman spectroscopy, and the movement of electrons between Ti^{3+} and Ti^{4+} ions. The air sintered samples had a higher permittivity over the O_2 sintered samples due to the increased number of Ti^{3+} which caused polarisation of the lattice. Samples sintered in N_2 had too many oxygen vacancies which resulted in ionic conductivity. The low tan δ was again caused by the defect dipole formed from the oxygen vacancies introduced by the acceptor dopant Al_2O_3 on air- and O_2-sintering:

$$Ti' - V_O^{\bullet\bullet} - Ti'$$

Another paper similar to the previous two is that by Zhong et al. 2020[84], consisting of research into $SrTiO_3$ co-doped on the B-site with Mg^{2+} and Nb^{5+}. Permittivities of 1.5×10^4 and tan δ values of 0.1 were seen despite sintering in air due to the distortion of the cubic unit cell to pseudo-cubic. As seen with the Al co-doping system above, the acceptor dopant (Mg^{2+}) supplied oxygen vacancies to suppress the delocalised electrons resulting from the donor dopant (Nb^{5+}).

2.3.1.2 Asymmetric P-E Loops

In some acceptor doped piezoelectrics after ageing the usual ferroelectric PE loops appear to be "pinched" which can indicate a ferroelectric-antiferroelectric phase transition[72] (Figure 2.4). The applied alternating electric field switches the polarisation of the ferroelectric by displacing the ion, in the case of $BaTiO_3$ along the 001 direction, off centre with the field[72]. This process is quick, easy and doesn't require much energy. However, the defect dipole under an applied alternating field could switch orientation, but this takes more time and energy as it involves the diffusion of vacancies which is a more difficult process than moving an ion off-centre. When measuring a ferroelectric with PE loops, the defect dipole will often remain in the starting orientation as the alternating field is switching too fast for the dipole to match[72]. The dipole remaining in its original orientation also pins the host ferroelectric domain and prevents it from switching as well. This results in a higher switching field across the sample. The higher the concentration of defect dipoles the greater the internal bias field and the larger the switching field required to flip the polarisation direction of the sample[77]. A lower applied electric field results in a fall in polarisation so PE-hysteresis loops for acceptor-doped aged piezoelectrics show pinched loops. Generally the rate for oxygen migration around an acceptor centre should be much slower than that of the domain switching rate, this results in the "pinched" hysteresis loop[79]. When the alternating electric field is removed after testing, the defect dipole and host domain in the original orientation act as an "anchor" or restoring force for the rest of the material to return to the spontaneous polarisation direction[72].

The ideal PE-hysteresis loops for a defect-free ferroelectric material would be symmetrical over the y axis showing equal coercive fields, E_C ($E_+ = E_-$)[72], this indicates an isotropic response to the applied electric field[77]. PE loops for samples that have been acceptor doped and aged are often asymmetric. This is due to the internal bias field (E_i) that is caused by the presence of defect dipoles. This is an internal field that is formed by the macroscopic collection of the defect dipoles which all normally follow the direction of spontaneous polarisation. If the sample with an internal bias field is subjected to an alternating electric field the field needs to be higher in order to overcome the internal bias field and switch the orientation of the domains. When the applied field is in the same direction as the internal bias field, the remaining domains switch into alignment easily and quickly, resulting in a low field strength. When the applied electric field is in the opposite direction to the internal bias field the domains are much harder to switch orientation, needing a much higher field strength. This is what causes the asymmetric PE loop along the field axis. This value is by the equation:

$$E_i = \frac{(E_+ + E_-)}{2}$$

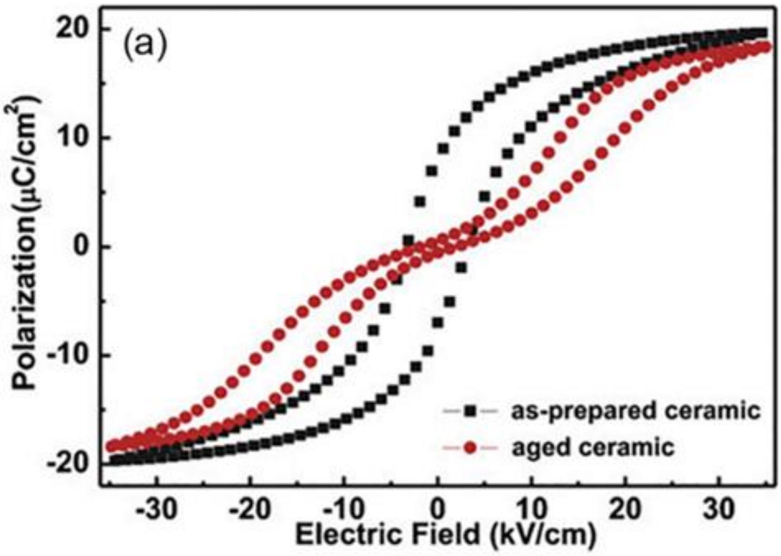

Figure 2.4: Illustration of "pinched" hysteresis loop effect caused by defect dipoles[72].

2.3.1.3 Electro-strain performance

The electro-strain performance of piezoelectrics is an important factor for application in actuators. The interaction between defect dipoles and ferroelectric domains has a marked effect on the electro-strain property of ferroelectrics. The previously discussed “restorative force” that the defect dipoles provide to the material after the electric field is removed reduces the electro-strain to 0 %. For tetragonal ferroelectrics such as $BaTiO_3$, the maximum the electro-strain can reach is c/a=1. If there are no defect dipoles in a ferroelectric material, there is no hindering of the domain switching under an applied electric field, and the strain vs. field curve slowly rises and follows linearly with the field with a sudden increase in strain at a critical electric field. With defect dipoles, an aged sample and an applied field that is opposite to the internal bias field, the defect dipoles pin ferroelectric domains hindering the switching of polarisation direction. As such only a partial or incomplete switch occurs, limiting the electro-strain of the sample. A concentration of 0.1 at% of defect dipoles in a sample however is enough to create the restorative force in strain recovery[77].

Li et al.[85] described a “giant strain and low hysteresis” in BNT-based ceramics in which defect dipoles existed between A-site vacancies and oxygen vacancies. This facilitated the nucleation and growth of the ferroelectric phase in the material and resulted in the reduction of the electric field during relaxor-to-ferroelectric transition. This in turn lead to the increase of the electro-strain of the material.

Mn-doped KNN systems were discussed by Zhao et al. due to their potential for creating very large electrostrain with PE/SE loops varying in shape according to different treatment conditions such as sintering regimes[86]. Oxygen vacancies were often formed from the volatile losses of K/Na in KNN-based ceramics which was thought to cause the observed asymmetric SE curves and high electrostrain at low electric fields[86]. Zhen et al. [87]showed that the valence state of Mn when substituted had an effect on properties, for example single-doped low valence Mn^{2+} showed high electro-strain whilst doping KNN with Mn^{3+} and Mn^{4+} resulted in a higher d_{33} temperature stability[87].

Another example of electric field induced strain is shown by Zeng et al. 2021[88] who substituted Fe^{2+} for Fe^{3+} in $BiFeO_3$, inducing the formation of oxygen vacancies that go on to form the defect complex: $Fe_{Fe3+}^{2+} - V_{O}^{\bullet}$. This defect dipole disrupted local structure symmetry and resulted in an electric field induced strain of 0.34 %. The Fe^{2+} ion created a tilting of the

Ti-O/Fe-O octahedron thus changing the structure of the material from cubic to pseudo-cubic and creating a polar non-ferroelectric phase, enhancing the piezoelectric properties.

2.3.1.4 Switching Defect Dipoles

The orientation direction switching of defect dipoles is slow and difficult. This is because it involves the migration/hopping process of vacancies and cations which can be a slow process depending on the species[72], [77]. This slow reorientation of dipoles must be balanced with the fast diffusion of oxygen throughout ceramic oxide materials[77]. Despite this it is possible under certain environmental conditions, such as low frequencies of measurement, a large applied electric field, electric field cycling and high temperatures. Fast measuring frequencies during PE-hysteresis loop testing do not allow for the required time it takes for the dipoles to switch orientation, however if the frequency is much lower the asymmetry previously described is seen to decrease suggesting the dipoles are able to switch orientation with the polarisation direction, leading to an increase in remnant polarisation. Increasing the electric field strength has a similar effect, but essentially overpowering the strength of the internal bias field and forcibly switching the direction of the defect dipole orientation, as is the effect with electric field cycling. High temperatures are effective at switching defect dipole orientation because they provide the thermal energy to overcome the potential energy barriers and activation energy for switching. High temperatures are a balancing act however, as if the temperatures are too high, they can break the bonds that hold defect dipoles together. This being said the high temperatures and fields used to reorient defect dipoles suggest that the binding energy of the oxygen vacancies to the cation is high enough to maintain the dipole bond whilst other species are diffusing quickly through the material around it[77].

3 Research Methodology

3.1 Motivations

A basic schematic of cubic perovskite $SrTiO_3$ is shown below in Figure 3.1. It is not this simple however, as discussed in Section 1.3: all ceramics naturally have chemical defects throughout the material. They can be from sintering losses, impurities, dopants etc. These defects carry charges, either positive or negative, and have been shown to naturally form defect dipole pairs, often between a cation defect and oxygen vacancy[26], but others exist as described in Section 2.3. What if it was possible to create a macroscopic dipole across a cubic, paraelectric material by orienting defect dipole pairs with an electric field? Figure 3.2 below shows two possibilities. Option *a* (left) is that the defects pair up, either a cation vacancy-dopant defect pair, or dopant defect-oxygen vacancy pair, and orient themselves with an applied electric field resulting in an overall net polarisation. Option *b* (right) is a situation where the individual chemical defects migrate through the material when an electric field is applied to create a negative and positive end of the sample. Both of these scenarios would be considered to be a macroscopic dipole.

It has been proven to be possible in ferroelectric materials in the ferroelectric phase, but has not yet been achieved in a material without a spontaneous polarisation direction[27]. Cation vacancies in perovskite structures have very low diffusion rates[50], and as such it would be necessary to pole the samples at high temperature and for a long time, in order to orient the vacancies with the field. If samples are too conductive, the applied electric field will be screened by free charges and oxygen vacancies which move around the lattice much more freely. As such, it is important to find samples which are suitably resistive. This is why the materials proposed below are an attempt at investigating chemical defects whilst observing electrical conductivity. If it is possible to align defect dipoles with an electric field in a paraelectric material, the next challenge would be locking their position in place once the field and temperature are removed in order for the material to be useful in a device application setting. If successful, this could result in a new branch of piezoelectric material which is non-ferroelectric. There is the potential for optimising the engineering of chemical defects to create a material with high electromechanical coupling efficiency in relatively inexpensive ceramics.

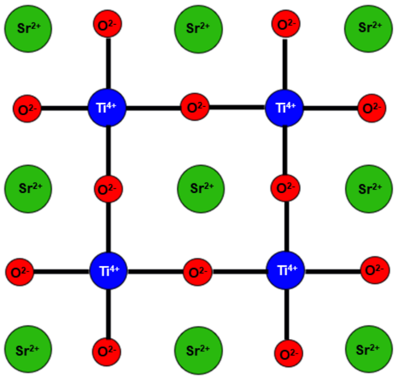

Figure 3.1: $SrTiO_3$ cubic perovskite. Green centres Sr, blue centres Ti, red centres O.

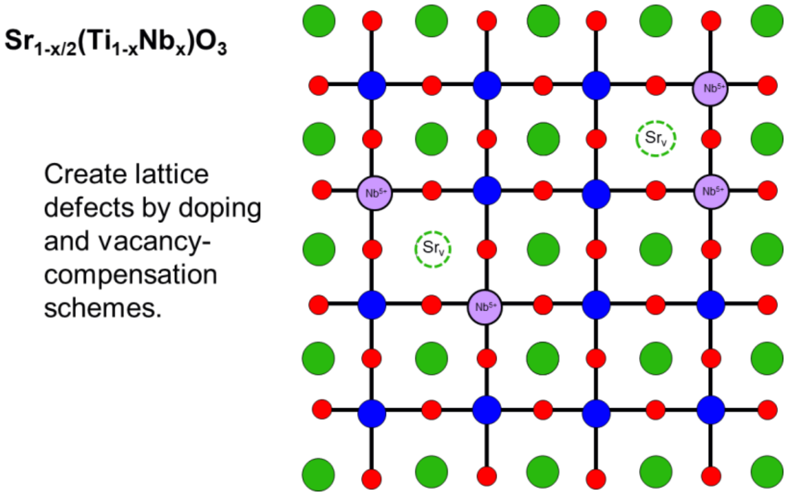

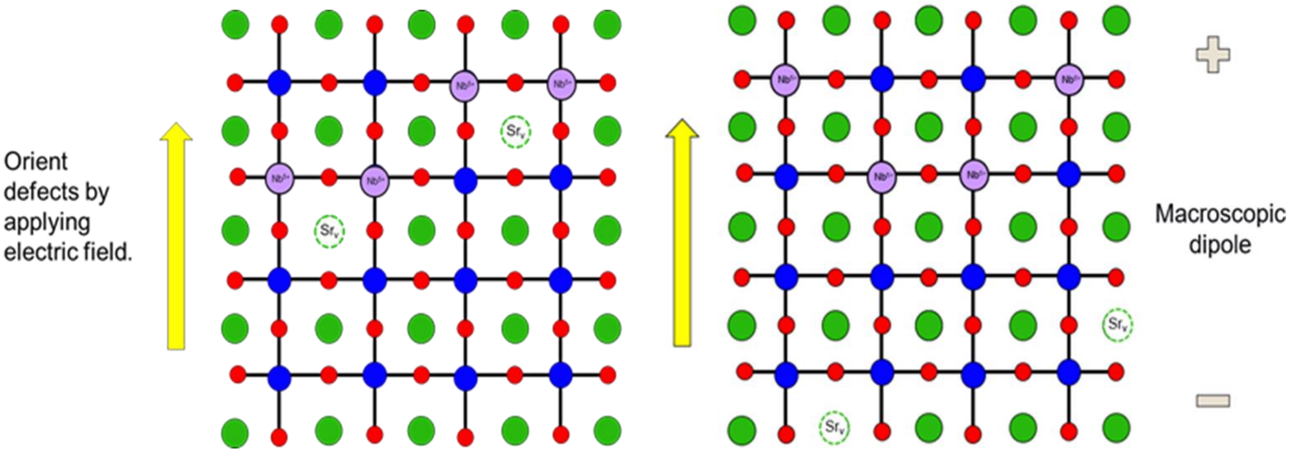

Figure 3.2: Illustration of macroscopic dipole concepts *a* (left) and *b* (right). Green centres Sr, blue centres Ti, purple centres Nb, red centres O.

3.1.1 Materials Selection

- $SrTiO_3$ samples with both excesses and deficiencies of Sr, at the amounts of 1.020, 1.010, 1.005, 1.002, 0.998, 0.995, 0.990 and 0.980 to investigate the role of Sr/Ti excesses and deficiencies on the conductivity and defect behaviour of un-doped $SrTiO_3$.
- Compositions of $SrTiO_3$ donor-doped with Nb and compensated by Sr vacancies were made according to the following formula: $Sr_{1-(x/2)}(Ti_{1-x}Nb_x)O_3$, where x=0.10, 0.15, 0.20, 0.25, 0.30, 0.35. Additions of Nb were made to initially investigate the solid solubility limit of Nb in the perovskite structure alongside Sr vacancies up to 30% Nb before electrical characterisation was carried out to investigate defect species behaviour. The inclusion of large amounts of Sr vacancies were to balance the Nb^{5+}/Ti^{4+} substitution.
- Samples of $SrTiO_3$ were made with donor dopant Nb on the B-site without Sr vacancies included following the formula $Sr(Ti_{1-x}Nb_x)O_3$ where x=0.002, 0.005, 0.010 and 0.020, to investigate donor doping on the B-site without the inclusion of Sr vacancies.
- Samples of $SrTiO_3$ were made with acceptor dopants Mn and Co, following the formula $Sr(Ti_{1-x}Co_x)O_3$ and $Sr(Ti_{1-x}Mn_x)O_3$, with x=0.01, 0.02, 0.05, 0.10, 0.20 to investigate the effect of acceptor doping on the B-site without the presence of Sr vacancies.
- The presence of high concentrations of either free (or hopping) electrons or oxygen vacancies is found to be detrimental to the conductivity of the samples. Hence, it was considered whether it was possible to reduce their concentrations by fixing the number of Sr vacancies and changing the donor dopant concentration.

$$Nb_2O_5 \rightarrow 2Nb_{Ti}^{\cdot} + V_{Sr}'' + 5O_O^{\times}$$

Assuming that the mechanism above does not fully compensate for Sr vacancies by Nb-doping, then reducing the Nb concentration whilst leaving the Sr deficiency constant, may result in a reduction of the free electron concentration. As such the sample set $Sr_{0.9}Ti_{1-x}Nb_xO_3$ was created. Samples of $SrTiO_3$ donor-doped with Nb and compensated by Sr vacancies but with a fixed level of Sr vacancies according to the following formula: $Sr_{0.9}(Ti_{1-x}Nb_x)O_3$, where x=0.19, 0.15, 0.10, 0.05, 0.01, 0.005. This will be to determine the effect of Sr vacancies electrically compensating for Nb substitution on the Ti-site.

Table 3-1: Sample list

$SrTiO_3$	**Sr-excess $SrTiO_3$**	**Sr-deficient $SrTiO_3$**	**$Sr_{1-x/2}Ti_{1-x}Nb_xO_3$**	**$Sr_{0.9}Ti_{1-x}Nb_xO_3$**	**$SrTi_{1-x}Nb_xO_3$**	**$SrTi_{1-x}Co_xO_3$**	**$SrTi_{1-x}Mn_xO_3$**
$SrTiO_3$	$Sr_{1.002}Ti_1O_3$	$Sr_{0.998}Ti_1O_3$	$Sr_{0.95}Ti_{0.90}Nb_{0.10}O_3$	$Sr_{0.9}Ti_{0.81}Nb_{0.19}O_3$	$SrTi_{0.998}Nb_{0.002}O_3$	$SrTi_{0.99}Co_{0.01}O_3$	$SrTi_{0.99}Mn_{0.01}O_3$
	$Sr_{1.005}Ti_1O_3$	$Sr_{0.995}Ti_1O_3$	$Sr_{0.925}Ti_{0.85}Nb_{0.15}O_3$	$Sr_{0.9}Ti_{0.85}Nb_{0.15}O_3$	$SrTi_{0.995}Nb_{0.005}O_3$	$SrTi_{0.99}Co_{0.02}O_3$	$SrTi_{0.99}Mn_{0.02}O_3$
	$Sr_{1.010}Ti_1O_3$	$Sr_{0.990}Ti_1O_3$	$Sr_{0.90}Ti_{0.80}Nb_{0.20}O_3$	$Sr_{0.9}Ti_{0.90}Nb_{0.10}O_3$	$SrTi_{0.99}Nb_{0.01}O_3$	$SrTi_{0.95}Co_{0.05}O_3$	$SrTi_{0.95}Mn_{0.05}O_3$
	$Sr_{1.020}Ti_1O_3$	$Sr_{0.980}Ti_1O_3$	$Sr_{0.875}Ti_{0.75}Nb_{0.25}O_3$	$Sr_{0.9}Ti_{0.95}Nb_{0.05}O_3$	$SrTi_{0.98}Nb_{0.02}O_3$	$SrTi_{0.90}Co_{0.10}O_3$	$SrTi_{0.90}Mn_{0.10}O_3$
			$Sr_{0.85}Ti_{0.70}Nb_{0.30}O_3$	$Sr_{0.9}Ti_{0.99}Nb_{0.01}O_3$		$SrTi_{0.80}Co_{0.20}O_3$	$SrTi_{0.80}Mn_{0.20}O_3$
				$Sr_{0.9}Ti_{0.995}Nb_{0.005}O_3$			

3.2 Ceramic Processing

Polycrystalline samples of the previously mentioned proposed materials were synthesised by the mixed oxide solid state reaction technique. Stoichiometric fractions of oven dried, raw materials $SrCO_3$ (99.9+ %), TiO_2 (98%), Nb_2O_5 (99.9 %), CoO (99%) and MnO_2 (99%) were mixed and ball milled for 24 hours in isopropyl alcohol (IPA). The mixed wet powders were then dried for approximately 90 minutes using a Kenwood induction-heated mixer to remove the IPA; samples were then placed in an oven overnight to be thoroughly dried. The dry sample powders were then sieved through a 300 µm mesh to remove any large solid agglomerations before being separated and calcined at 1100 °C for 4 hours in a furnace. The resulting powders were then examined under X-ray diffraction to confirm the perovskite structures and note any phase separations with the addition of increasing dopant content. After the crystallography was determined, the calcined powder samples were then mixed with 2 wt.% polyvinyl alcohol (PVA) binder, ball milled in distilled water for 24 hours, dried and sieved again before being pressed into pellets with a diameter of approximately 10 mm and thickness of approximately 3 mm using a uniaxial press and 1 tonne pressure. The pellets were then subjected to a sintering regime which consisted of an initial ramp up to and dwell at 550 °C in order to burn off the PVA binder, followed by an 8 hour sinter between 1200-1500 °C depending on the material.

The volumetric densities of the pellets were measured before and after sintering in order to monitor the change in density and the success of sintering. A fully sintered pellet of each sample composition was then examined using X-ray diffraction in order to note any changes from the calcined samples. The remaining pellets were then ground down to approximately 1mm thickness and then had their surfaces painted with a silver/glass mixture and placed in a furnace to fire at 550 °C for 30 minutes in order to form electrode surfaces. Electrical characterisation of each sample could then begin.

3.2.1 Calcination

Calcination of the sample powders was carried out in order to react the starting materials together to form the beginning of the intended material products. Calcination serves as a method of homogenising the material by diffusion of ions (including dopants) prior to sintering[4] and is a form of pre-reaction that promotes phase nucleation that encourages strain-free grain growth during the following sintering process[89], ensuring maximum densification. Ball-milling is an important step to carry out before calcination as it ensures that all reactants are equally distributed, and agglomerates broken up to reveal optimum surface areas for reaction. Calcination also involves reacting and burning off any excess carbon and oxygen atoms in the form of CO_2 or O_2, along with any solvents that were used in the processing up to this point such as IPA. As such the weight of the powders decreases after calcination, and this can be an indication of a successful calcination. Calcination is often carried out at temperatures lower than sintering of the same material by a few hundred degrees. The resulting calcined powder will be coarser as a reaction has begun between starting materials, and as such ball milling is repeated after calcination to break apart agglomerates before sintering to ensure a homogenous reaction.

3.2.2 Sintering

There are different types of sintering, but this work uses solid state sintering to densify the ceramic samples. Before sintering the calcined and ball-milled powder with added binder is shaped and compressed under pressure into a pellet. The first stage of the sintering regime is carried out at approximately 550 °C and serves to burn out the binder and any remaining solvents for approximately 2-4 hours. The second stage of sintering occurs at temperatures anywhere between 1200-1500 °C, depending on the material, and is the grain growth and densification process of ceramic production. The driving force for sintering is the decrease in surface energy of the reactant particles[4], as the atoms in the grain boundary have a higher energy than atoms in the grains, which means that grain growth and decrease in grain boundary volume in the ceramic decreases the free energy of the system[90]. Mass transport occurs through the diffusion of atoms and charged species across the ceramic, with the reduction of pores and the growth of grains as the result[21]. The type of defect present in the lattice is influential on the success of sintering. For example Jaffe et al. state that A-site vacancies, as intended in this $SrTiO_3$-Nb work, aid diffusion within a lattice, whereas oxygen vacancies can actually inhibit lattice diffusion, which can hinder successful sintering[3]. A-site vacancies can decrease the overall size of the lattice but provide sites for ions to diffuse into. Grain growth occurs when atoms diffuse from one side of a grain boundary to another, resulting in the growth of one grain and the decrease in size of the previous grain[90]. Some ceramics, depending on the melting point of their reactant components, can have their sintering accelerated by the presence of a liquid phase that facilitates mass transport of ions into pores quicker than the solid state would[21]. A bulk liquid phase is stable at higher temperatures and also acts to wet grain boundaries at lower temperatures[44]. This increases diffusion in sintering as the liquid phase is easier for species to move through. $BaTiO_3$ is a good example of liquid sintering whereby a Ti-rich phase forms a liquid phase and promotes densification of the ceramic.

Sintering times and temperatures can be used to modify the grain size of a ceramic, for example at increased temperatures and sintering times, larger grains grow absorbing smaller grains which maintains the conservation of matter[90]. This can control the electrical and mechanical properties of the ceramic. In order for high density ceramics to be achieved mass transport diffusion occurs from the grains to the pores which act as a sink for the incoming matter[90]. Sometimes pores can get trapped in the ceramic, normally from abnormal grain growth and long diffusion pathways in abnormally large grains, resulting in a less-dense ceramic[90]. The theories surrounding sintering and sintering studies that have been carried out on the production of electroceramics are plentiful and complex and is its own field of research.

3.3 Structural Characterisation

3.3.1 X-Ray Diffraction

X-ray diffraction is a technique used in this work to characterise the samples across the range of compositions and can determine the phase/structure of the sample, the purity, the crystallite size, the cell parameters, and the orientation among other things. X-ray radiation is used because the wavelength of X-rays is similar to that of the interatomic distances of atoms within a crystal structure[91].

X-rays are produced in an X-ray diffractometer by heating a tungsten filament which then emits electrons. These electrons are accelerated and collide with a cooled metal plate, in this case copper, and interact with the copper atoms, exciting inner electrons to a higher energy level causing higher electrons to fall into these empty energy levels resulting in the emittance of X-rays[91]. These X-rays are directed at the sample stage through divergent slits as the sample is tilted through a range of specified angles. When the X-rays pass through the sample, they either interact with the electrons of the atoms within the sample and are scattered in all directions or transmit through it. If the scattered X-rays constructively interfere by scattering from two planes separated by an integer number of wavelengths and satisfy Bragg’s law, then a peak will be seen on the XRD spectrum (Figure 3.3).

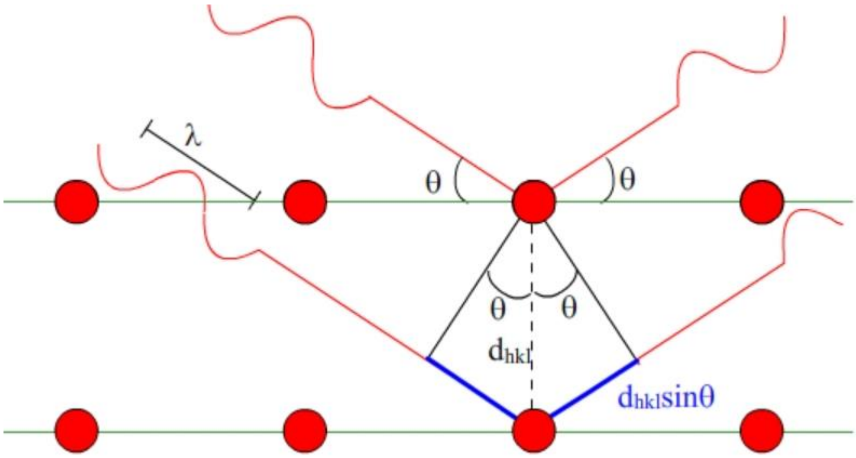

Figure 3.3: Diagram of constructive interference satisfying Bragg's law, sourced from University of Cambridge DoITPoMs website[91].

Each peak is representative of a plane within the crystal sample and gives information about the structure and chemistry of the sample. For example, the 100 peak in cubic $SrTiO_3$ (Figure 3.4) represents the 100 plane of the crystal. In non-cubic structures, some peaks split into two or even three peaks according to the crystal structure. For example, a tetragonal crystal such as $BaTiO_3$ will cause splitting to the 100 into a doublet, because the lattice parameter *c* is unequal to *a* and *b*, i.e. *a*=*b*≠*c* resulting in a multiplicity stemming from the reflection of the c-axis.

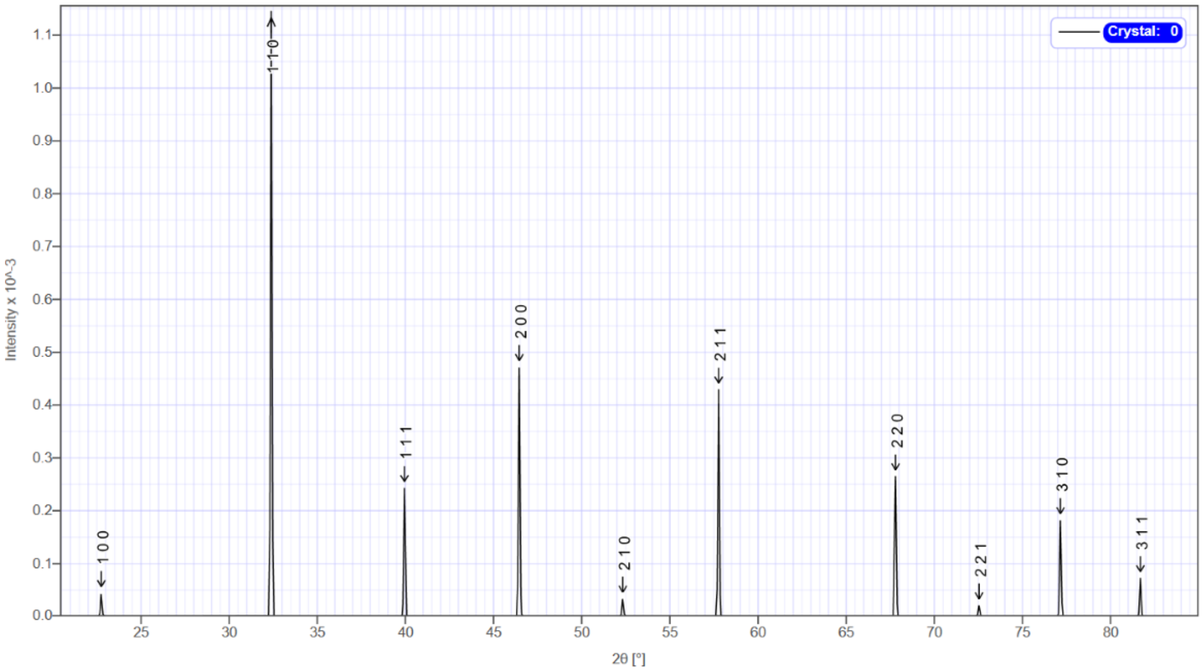

Figure 3.4: Example XRD spectrum produced on CrystalMaker of cubic $SrTiO_3$.

Bragg's law is shown below and is the equation that shows the conditions that must be fulfilled for constructive interference of reflected X-rays to occur[10]:

$$n\lambda = 2d_{hkl}sin\theta$$

Where n is the order of reflection, λ is the wavelength of the incident radiation, d_{hkl} is the lattice spacing size, and θ is the angle of the incident radiation and also the reflection of the planes[10]. The Bragg equation can be rearranged to find the lattice spacing d, which in turn can be used to find the unit cell parameter a, which in the case of a cubic unit cell such as $SrTiO_3$ is:

$$d = \frac{a}{\sqrt{N}}$$

Where: $N = h^2 + k^2 + l^2$

The data in this work were collected on a D8, Bruker Diffractometer, using Cu K_α radiation to characterise the crystallographic structure. A Bragg – Brentano configuration was used to produce scans with a 2θ range from 20 - 80°, a step size of 0.033° and a scan time of 0.35 sec/step. These parameters were put in place as a compromise between scan speed and resolution.

3.3.2 Rietveld Refinement

Rietveld refinement is a technique used to analyse X-ray diffraction data and compares the observed data to a crystallographic model of the material, often from an ICDD file, and minimises the differences between the two. When this is achieved it can be viewed as a representation of the structure and reveal information about the material[92]. The tool exists to deal with errors in powder diffraction such as from the inherent nature of the random orientation of grains in a polycrystalline sample, and also information loss from peak overlap. The loss of information from peak overlap is overcome by using profile intensities instead of integrated intensities of the overlapping peaks in the scan in the refinement.

In order to carry out refinement of these structures longer XRD scans were carried out to provide better signal to noise (2θ range from 20 - 80°, a step size of 0.033°). Refinement of the structures in this work (initially $SrTiO_3$ doped with Nb, both the B-site doped, and Sr vacancy compensated) were carried out in the cubic Pm-3m space group. The software used to carry out the refinement was High Score by Panalytical. The refinement was carried out in a specific order unless stated. All compositions were refined against both an undoped $SrTiO_3$ file, and also against a $SrTiO_3$ doped with Nb file, and the best fitting data taken. Nb was added as a dopant atom when refining to undoped $SrTiO_3$ and all occupancies were adjusted to match each intended composition. Equipment based physical parameters such as the background, zero shift and scale factors were refined, followed by the U, W, (positively constrained) and V (negatively constrained) halfwidth parameters. These consider peak variations caused by particle size variation and scattering angle. Peak shape was then refined as the final base step before each composition was then refined individually. Peak shape refinement considers the ratio between Lorentzian and Gaussian peak profile shapes. Elemental occupancies were then freed.

3.3.3 Electron Microscopy

Electron microscopy (both scanning and transmission) use accelerated electrons to analyse the surface and subsurface of a sample specimen. The wavelength of the accelerated electrons is much smaller than that of visible or UV light (used in light microscopy) and therefore much greater resolutions can be achieved.

Scanning electron microscopy (SEM) generates electrons by heating a tungsten cathode filament, which are then collimated to a beam size of approximately 50 μm with an accelerating voltage of approximately 1-30 kV[93]. There are a range of analysis techniques used within SEM including secondary electron, backscattered electron, and Auger electrons/X-rays analysis. Secondary electrons are those escaping from the sample from ionised material close to the surface. They have a high signal level combined with a high lateral and depth resolution[93]. Backscattered electrons are primary electrons which undergo large deflections and leave the surface with very little change in kinetic energy[93]. This technique can be used to differentiate phases and atomic composition, and in well-polished samples can distinguish between orientations. Auger electrons are produced when higher level electrons drop into lower shells emptied by ionisation from the electron beam, resulting in characteristic x-rays being produced which can be used for elemental analysis[93].

Samples for SEM analysis were mounted in resin and polished in order to remove scratches and surface dirt. The polishing regime consisted of grinding both clockwise and anticlockwise with p800 SiC paper from Beuhler at a pressure of 4 lbs per sample and speed of 150 rpm. This was then followed by a using diamond polishing agents of 9 μm, 3 μm (TexMetP) and 1μm (Trident), finally followed by MasterMet Colloidal Silica. Samples were then mounted to an SEM stub and carbon coated to prevent charge build up. Images were produced on a Hitachi SU8230. The sample grain size was calculated using imaging software ImageJ to calibrate to scale bars and then using the average grain boundary intercept method using the correction factor 1.56 from Mendelson[94].

Transmission electron microscopy (TEM) was carried out on ultra-thin slices of material produced by a focus ion beam and was analysed by electrons produced by a LaB_6/tungsten/field emission gun with an accelerating voltage of 100-400 kV, such that the electron beam passes straight through the sample interacting with the material on the way[93]. The increased penetration and decreased electron wavelength results in much improved image resolution. The transmission of electrons through the material results in the thicker or denser areas appearing darker in contrast due to the greater scattering of electrons and this is the case with all sample types, both amorphous and crystalline[93]. TEM of crystalline materials, as well as images, can also produce a diffraction pattern of spots and rings that appear after the diffracted beams satisfy Bragg's law and constructively interfere similar to X-ray diffraction. It is possible to measure these diffraction patterns and match them with the XRD spectra produced. The TEM analysis in this work was carried out on a FEI Titan Themis Cubed 300 TEM.

3.4 Electrical Characterisation

3.4.1 Impedance Spectroscopy

Impedance spectroscopy in its simplest terms, is the application of a voltage to a sample and a measured current response [95]. These measurements are carried out at a range of frequencies between $10^{-4} – 10^{7}$ Hz. They should also be carried out across a range of temperatures as most electrical processes are thermally activated, leaving specific windows of observable effects[96]. Impedance spectroscopy can be carried out in two ways. The first; a time dependent approach with a step function of voltage applied and a time dependent current response is measured. These results can then be converted into the frequency domain[97]. The second (and most common) way to measure impedance is in the frequency domain so that conversions don't have to be made. A time dependent voltage is applied and the amplitude and phase shift of the current response is measured[97]. The voltage signal, U, that is applied has an angular frequency of ω and an amplitude of:

$$U(\omega,t) = U_0\cos(\omega t) \text{ [97]}$$

and the current response is measured by the equation:

$$I(\omega,t) = I_0\cos(\omega t + \delta) \text{ [97]}$$

The current responses are either in or out of phase by the following amount for each type of material[97]:

- Resistor: in phase with the applied voltage
- Capacitor: out of phase by $\delta = -\pi/2$
- Inductor: out of phase by $\delta = +\pi/2$

The angle by which the current response is out of phase, are time independent, and as such impedance is a time independent complex number[97]. Impedance is represented by the equation $Z=Z' - iZ''$, whereby $i = \sqrt{-1}$ [95].

In this work, impedance measurements were taken at a range of frequency decades (1 MHz to 100 mHz at 1 V) through a range of temperatures in order to assess the relaxation periods of the materials tested. The electrical properties of titanate ceramics (such as $SrTiO_3$) can be modified by changing the relationship between grain boundary vs bulk properties and also by changing the defect chemistry of the material. In the case of $SrTiO_3$, which is used for several high temperature applications, bulk vs grain boundary conductivities may be affected by high temperatures[98]. Impedance spectroscopy is a good method to investigate the separate contributions from bulk, grain boundary and electrodes.

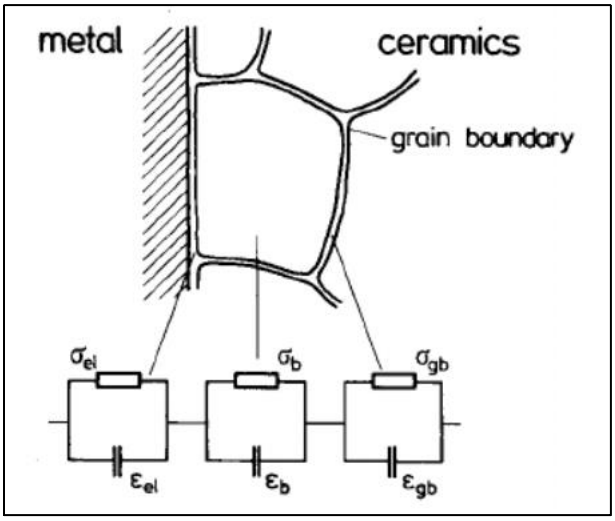

Figure 3.5: Illustration of the contributions to impedance from grain (bulk), grain boundary and electrode interface by Waser 1991[52].

There are assumptions that are made when using the simplistic “brick layer” model which describes bulk, boundary, and interface components of impedance contribution (Figure 3.5). These are that all grain boundary areas display similar properties to one another and that their impedance can be averaged out, and secondly that the grain boundaries have very distinct properties in comparison to the interface or bulk [97]. However, these generalised assumptions must be taken with care, because compositional variation across a sample and between grains can lead to false interpretations based on averaging. For example, current will pass through more compositionally conductive grains and bypass more resistive areas, in which case the data is only a representation of the more conductive zones.

Equivalent circuit modelling is a technique used to analyse impedance data, by simulating electrical circuits to fit the measured data in order to determine the most likely scenario that best represents the dielectric relaxations that are taking place in the material. There are a variety of contributors to the impedance behaviour of a material, such as the bulk grain behaviour, the grain boundary behaviour and the sample/electrode interface behaviour and each of them must be analysed individually in a heterogeneous sample[97]. In an ideal, well made, homogeneous sample, each dielectric relaxation process can be described by an RC circuit (an ideal resistor and capacitor in parallel – see Figure 3.6) [97]. The impedance of the sample as a whole is then calculated by summing each individual contributing impedance in the circuit. In an RC circuit when describing an electroceramic, the capacitor represents the insulating dielectric properties, and the resistor describes the leakage current as there is no such thing as a “perfect insulator”[97]. Examples of contributions to impedance analysis capacitance are shown in Table 3-2 below.

Table 3-2: Table of capacitances of relaxation contributions taken from Schmidt[97] who took it from Irvine Sinclair and West[30].

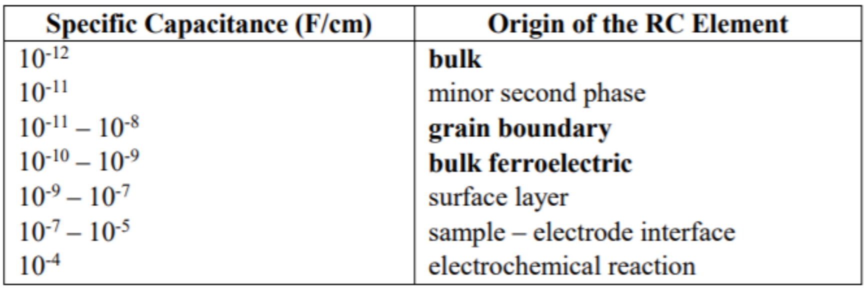

Specific Capacitance (F/cm)	Origin of the RC Element
10^{-12}	**bulk**
10^{-11}	minor second phase
$10^{-11} – 10^{-8}$	**grain boundary**
$10^{-10} – 10^{-9}$	**bulk ferroelectric**
$10^{-9} – 10^{-7}$	surface layer
$10^{-7} – 10^{-5}$	sample – electrode interface
10^{-4}	electrochemical reaction

A non-ideal impedance response results in the use of more complicated circuits such as the Debye circuit for modelling (Figure 3.6), which consists of a resistor and two capacitors both in series and in parallel.

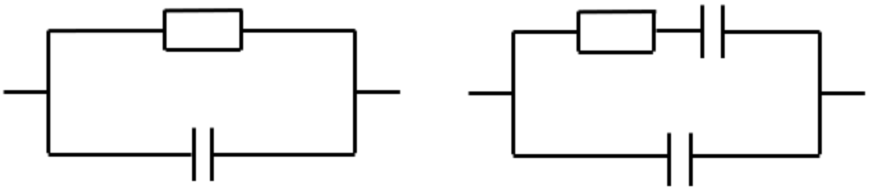

Figure 3.6: Illustration of RC circuit (left) and Debye circuit (right).

The Debye circuit acts to fit data at both the high and low frequency regions of the data set, eg. a frequency dependent dielectric constant[97]. A non-ideal impedance response can also be fit with a CPE (constant phase element) in place of the ideal RC capacitor.

Impedance data can be plotted in two formats. The first, a Z' vs Z'' plot, from which the semi-circle diameter provides the resistance (Figure 3.7 below), or a ε' vs. ε'' plot from which the semicircle diameter gives the high and low frequency limit of the real part of the relative permittivity[97]. The shape and number of semi-circles produced helps to determine physical effects and processes happening within the electroceramic under certain conditions such as in the bulk or at the grain boundaries, or in multiple phases that could be present which can help to identify homogeneity within the sample at various temperatures[30]. Multiple semicircles can exist, and each semicircle is descriptive of the contributor to impedance and there are often cases where the semicircles overlap one another, making it difficult to analyse, in which case electrical circuit fitting software must be employed.

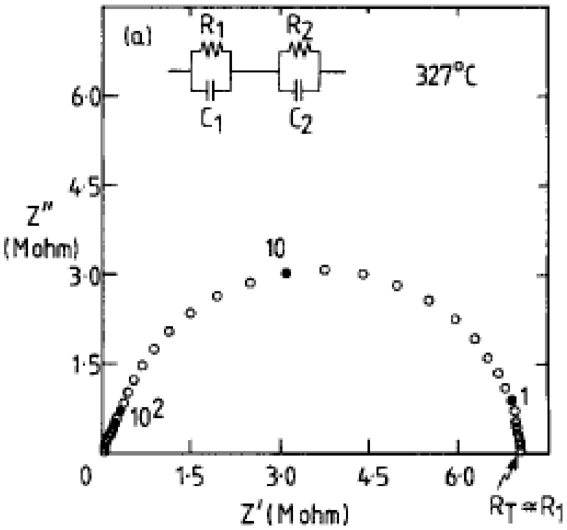

Figure 3.7: Z′ vs. Z″ plot of $BaTiO_3$[30].

One of the recurring problems with circuit modelling is that it is possible to choose the wrong circuit to fit the data leading to an incorrect interpretation of the data, and as such it is necessary to compare multiple circuits against each other in order to make sure that the entire frequency range of data is fitted[96]. The presentation of impedance data is often in the form of logarithmic plots due to the wide range of frequencies across which data is collected; linear plots can cause crucial smaller magnitude data to be missed[96]. The correct presentation of data is important in order to identify any experimental errors and to be able to accurately identify the physical processes that are occurring[95].

In single crystal materials, impedance graphs often appear as a single well-formed semicircle, because there are no grain boundary contributions to the overall impedance[97]. Often with single crystal impedance analysis, one RC circuit is enough to analyse the bulk grain contribution with a narrow distribution of relaxation times due to the absence of extended defects in the sample[97]. In polycrystalline ceramics however there are multiple semicircles to consider because of the variety of contributors to impedance previously discussed. In most electroceramics the grain boundaries have a greater resistance than the bulk grain, leading to a larger second semicircle. Ideally the semicircles would be clear and distinct from each other, but this is not always the case and fitting software and CPEs must be used.

Impedance spectroscopy produces a large amount of data, and there are a series of formalisms that can be converted between using equations in order to present the best data to investigate the electrical process of one's choice. Table 3-3 below presented by Rainer Schmidt illustrates this:

Table 3-3: Table of complex impedance formalisms presented in Impedance Spectroscopy of Electroceramics by Rainer Schmidt pp324 [97].

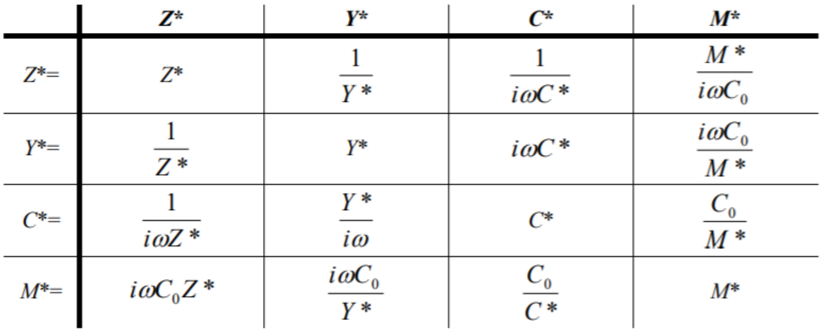

	Z^*	Y^*	C^*	M^*
$Z^*=$	Z^*	$\frac{1}{Y^*}$	$\frac{1}{i\omega C^*}$	$\frac{M^*}{i\omega C_0}$
$Y^*=$	$\frac{1}{Z^*}$	Y^*	$i\omega C^*$	$\frac{i\omega C_0}{M^*}$
$C^*=$	$\frac{1}{i\omega Z^*}$	$\frac{Y^*}{i\omega}$	C^*	$\frac{C_0}{M^*}$
$M^*=$	$i\omega C_0 Z^*$	$\frac{i\omega C_0}{Y^*}$	$\frac{C_0}{C^*}$	M^*

An ideal impedance data set as previously discussed can be fitted and analysed by a simple RC circuit. From the immediate electrical data output, it is possible to determine by analysis the capacitance, and the resistance:

$$\omega_{max} RC = 1 \text{ [96]}$$

$$\text{where } \omega_{max} = 2\pi f_{max} \text{ [96]}$$

and f_{max} is the frequency at the top of the arc of the semicircle. The resistivity, and therefore a plot of conductivity, can also be calculated from the plot semicircle by taking the resistance from the point at which the semicircle crosses the x-axis for the second time and inputting into the following equations:

$$Conductivity\ (\sigma) = Resistivity^{-1}$$

$$Resistivity = \frac{RA}{L} \quad \text{[99]}$$

$$ln\sigma = ln\sigma_0 - \frac{E_A}{K_BT} \quad [99]$$

A graph of the natural log of conductivity vs 1/T provides vital information regarding the activation energies of the conduction mechanisms taking place in the material under analysis. The data lines from this analysis should be linear, with the exception of phase transitions, order-disorder transitions and curvature associated with defect dissociation [96]. It is worth noting that unexpected deviations from a linear plot, or surprisingly high E_A values are both indicators of the wrong equivalent circuit being picked in the fitting phase of data analysis.

Another way to present impedance data is a graph of frequency vs. the imaginary part of impedance (Z″), and also frequency vs. electric modulus (M″). In each case these graphs show a Debye peak, but the Z″ graph is scaled by the resistance, and the M″ the inverse of the capacitance for a parallel RC element[100]. These graphs can be compared to one another or presented next to each other, and highlight different points in the data[96]; Z* graphs tend to give more information about the grain boundary effects, whereas M* graphs give more information about the bulk properties. Electric modulus is the reciprocal of permittivity and corresponds to dielectric relaxations within the material[101]. Complex electric modulus can be represented as follows[101]:

$$M^* = \frac{1}{\varepsilon^*} = \frac{1}{(\varepsilon' - j\varepsilon'')} = M' + jM''$$

The peak in graphs of frequency against M″ that is often displayed can move to higher frequencies with increasing temperatures which illustrates a decrease in the dielectric relaxation time due to a decrease in resistance with increasing temperature[97]. The modulus value at the peak maximum can indicate the temperature independent capacitance[97]. The capacitance is also temperature independent in non-ferroelectrics in general. As this work relates primarily to the doping of paraelectric $SrTiO_3$, frequency vs. modulus/impedance graphs will be constructed for analysis, along with Z′ vs Z″ and conductivity plots.

3.4.2 Permittivity vs. Temperature

The relative permittivity, or dielectric constant of a ferroelectric material, is the time delay seen for the dipoles to switch by 180° when an electric field is applied[102]. As the frequency of the AC supply is increased, the dipoles may reach a point at which they cannot switch quickly enough to match the field, and this results in the dissipation of energy from the system. This critical frequency is dependent on the material and the type of dipole present. Tan δ, or dielectric loss, which is also extracted from this experimental technique comes from losses from resonant processes or dipolar losses[102]. These are either elastic displacement of ions and/or electrons caused by the fluctuating field (resonant), or from the reorientation of the dipole or movement away from equilibrium of ions (dipolar loss)[102]. Similar to dielectric losses, ferroelectric materials can suffer from polarisation decay, or ageing. This can be caused by a variety of factors which include; thermal excitations at temperature causing dipolar reorientation or the drifting of charges, and also the freeing of space charges resulting in an overall increase in conductivity[102]. In typical ferroelectric materials there is always competition between the conduction of charge carriers and the dielectric relaxation. That is why the study of permittivity is useful, and can also tell us about the presence of oxygen vacancies which are one of the most mobile charge carrier in perovskite oxides[102].

Measuring the permittivity of a sample is a good way to get a representation of the physical and chemical processes taking place during the reorientation of the dipoles with the applied field, and it can be expressed by the below equation[102]:

$$\varepsilon(\omega) = \varepsilon'(\omega) - i\varepsilon''(\omega)$$

where ε' is the real component and ε'' is the imaginary component, and ω is angular frequency.

The relative permittivity or dielectric constant can vary in ceramics according to processing factors such as grain size[103].

4 Results

4.1 Structural Characterisation

4.1.1 X-Ray Diffraction

4.1.1.1 Non-Stoichiometric $SrTiO_3$

The samples of the formula $SrTiO_3$ where Sr/Ti=0.980, 0.990, 0.995, 0.998, 0, 1.002, 1.005, 1.010, 1.020 were subjected to X-ray diffraction analysis as sintered pellets. It is noted that $k_{\alpha 2}$ stripping was carried out on the data before plotting. The peaks were labelled on the black pattern representing undoped $SrTiO_3$. Theoretical densities were calculated from the d-spacing of the (200) peak of the XRD data and compared to geometric values, and densities of 94-96% for this sample set were achieved on sintering.

The XRD patterns (Figure 4.1) show a single phase cubic perovskite structure for all samples. There are no apparent impurity phases present, as evidenced by Figure 4.2 which is a pattern of Log_{10} of the y-axis for $SrTiO_3$ for the most deficient and excess samples (0.980 and 1.020). This would more clearly illustrate any impurity peaks so if there are SrO-based RP phases present in the samples it was not at a significant enough concentration to be represented in the XRD pattern which was expected due to the minimal excess and deficient Sr levels.

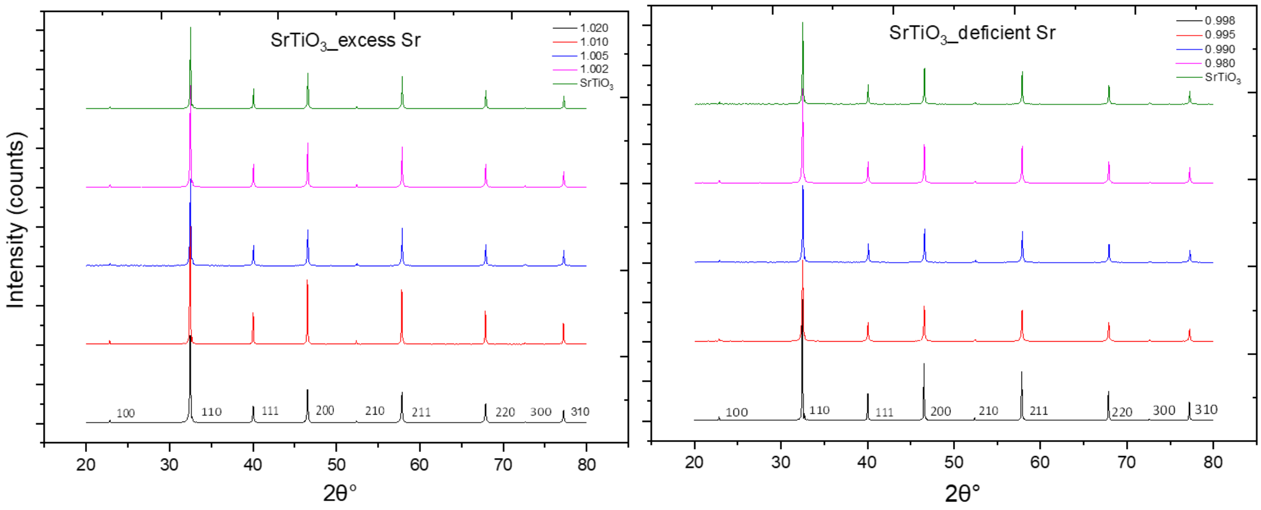

Figure 4.1: XRD pattern of $SrTiO_3$ excess and deficient samples where Sr/Ti=0.980, 0.990, 0.995, 0.998, 0, 1.002, 1.005, 1.010, 1.020.

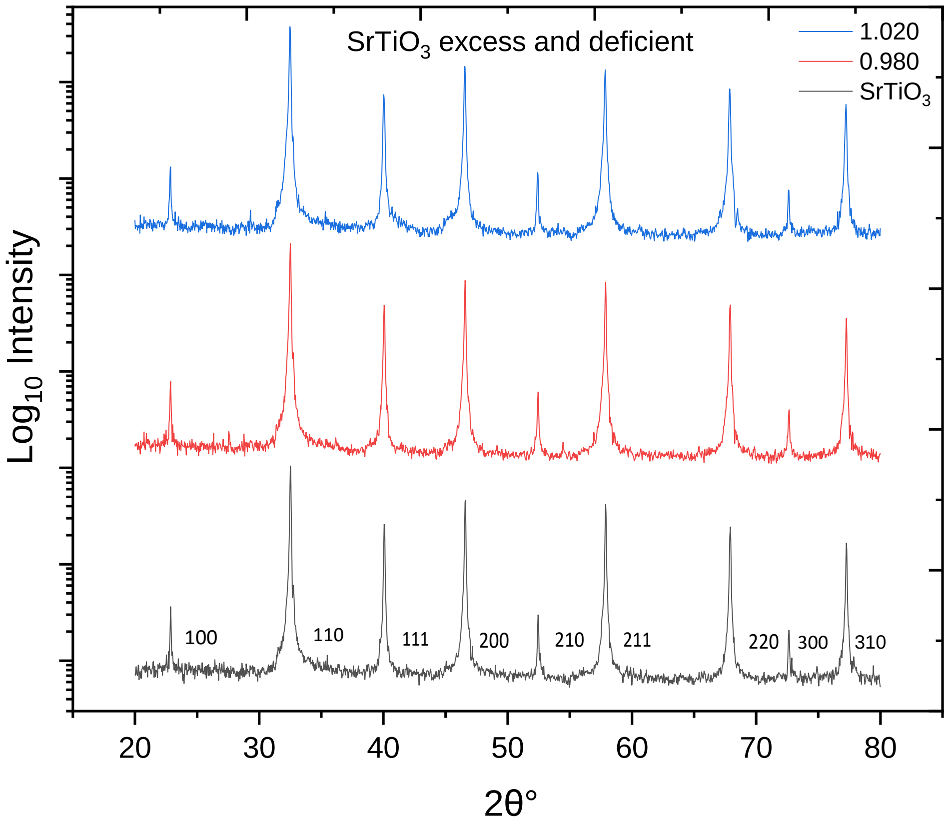

Figure 4.2: Log_{10} XRD pattern of $SrTiO_3$ excess and deficient samples where Sr/Ti=0.980, 0 and 1.020.

4.1.1.2 A-Site Vacancy Compensation of Donors

$Sr_{(1-x/2)}Ti_{(1-x)}Nb_xO_3$ Samples:

The samples of the formula $Sr_{(1-x/2)}Ti_{(1-x)}Nb_xO_3$ where x=0, 0.10, 0.15, 0.20, 0.25, 0.30, 0.35 were subjected to X-ray diffraction analysis as sintered pellets. It is noted that $k_{\alpha2}$ stripping was carried out on the data before plotting (Figure 4.3). Peaks are labelled on the black pattern representing undoped $SrTiO_3$. Theoretical densities were calculated from the d-spacing of the (200) peak of the XRD data and compared to geometric values, and densities of 95-98% for this sample set were achieved on sintering. It was originally intended to make an Nb_x=0.35 sample but this was difficult to produce consistently as it repeatedly cracked on sintering (Figure 4.20). The work by Kolodiazhnyi and Petric[39] shows an XRD pattern for $SrTiO_3$ with Nb additions of x=0.4 and x=0.6 which shows phase separation of $Sr_3TiNb_4O_{15}$ (Figure 4.4). According to Kolodiazhnyi and Petric[39] the defect chemistry model for Sr-deficient n-doped $SrTiO_3$ sintered at low oxygen partial pressures can create a multiphase material, such as the presence of Ti-rich secondary phases. Sintering in air, such as the samples in this work, should result in single phase cubic materials and this was generally seen in the XRD data up to Nb_x=0.30.

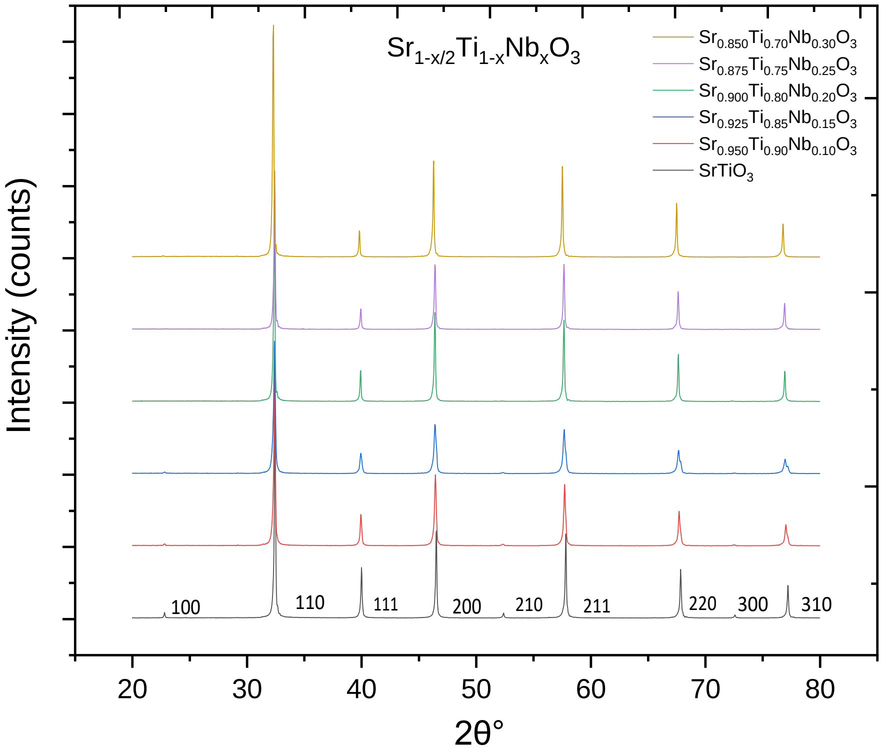

Figure 4.3: XRD pattern of $Sr_{(1-x/2)}Ti_{(1-x)}Nb_xO_3$ where x=0, 0.10, 0.15, 0.20, 0.25, 0.30, 0.35.

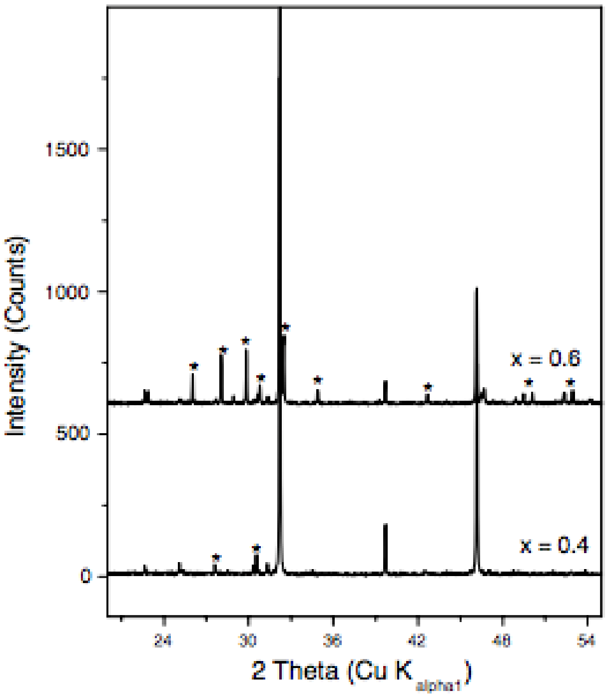

Figure 4.4: Illustration of phase separation with increasing Nb content in XRD pattern of $Sr_{1-x/2}Nb_xTi_{1-x}O_3$ where x=0.4 and x=0.6 by Kolodiazhnyi and Petric[39].

The study by Slater et al.[67] showed a tungsten bronze impurity phase of $Sr_{0.6}Ti_{0.2}Nb_{0.8}O_3$ with a tetragonal unit cell appearing at concentrations above Nb_x=0.4. The spectrum of the samples analysed in Figure 4.3 showed a clear single phase cubic perovskite structure. This is promising, because it supports the work done by Kolodiazhnyi and Petric[39] that Nb solubility in A-site compensated $SrTiO_3$ is successful up to at least Nb_x=0.30. Of note is the absence of the (100), (210) and (300) peaks for the Nb_x=0.10-0.30 samples in the XRD pattern. To examine this further a graph was made of the XRD pattern for $SrTiO_3$ and Nb_x=0.30 samples with the y-axis log-scaled to accentuate small peaks in order to determine if the peaks had just decreased or disappeared entirely (Figure 4.5). This pattern shows that the (210) and (300) peaks have disappeared completely from the Nb_x=0.30 sample and that the (100) peak remains but is much smaller therefore almost imperceptible on the linear y-axis pattern, in contrast to the log graph in Figure 4.2 for the non-stoichiometric $SrTiO_3$ samples.

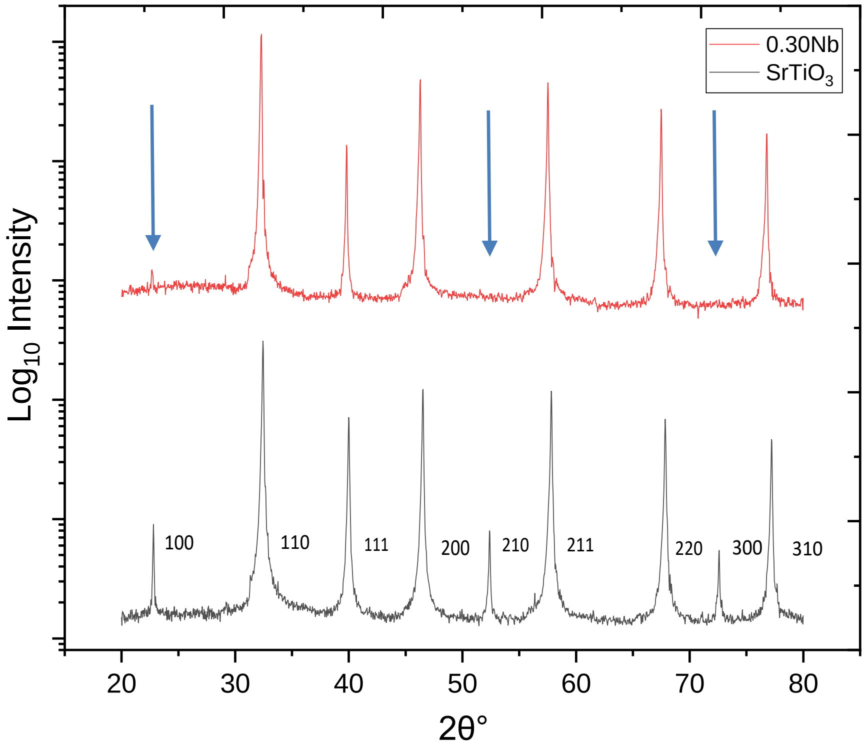

Figure 4.5: Log$_{10}$ XRD pattern of $Sr_{(1-x/2)}Ti_{(1-x)}Nb_xO_3$ samples where Nb_x= 0 and 0.30, illustrating reduced or missing (100), (210) and (300) peaks.

To further investigate the missing peaks, a model diagram was made of undoped $SrTiO_3$ using CrystalMaker software, which is able to construct the XRD crystal planes (shown in red). A diagram of undoped $SrTiO_3$ was used for initial illustrative purposes as it is hard to predict and accurately demonstrate the location of Nb-dopant ions and Sr vacancies. Illustrated below is the (100) plane which represents the (100) XRD peak that greatly decreases in the XRD pattern as the Nb content increases (Figure 4.6). However not only does the peak disappear as Nb content increases, more importantly it decreases as Sr-vacancy concentration also increases and it is this that is thought to cause the decrease in (100) peak; due to the interaction of x-rays with Sr-O planes in the extended perovskite structure which are systematically being removed. As the Sr content is intentionally decreased, there are less Sr atoms for diffraction to occur in the (100) plane, resulting in a reduced peak. Figure 4.7 is an illustration of the (210) plane in the $SrTiO_3$ crystal structure, representing the (210) peak in the XRD pattern which goes missing with increasing Sr vacancies and Nb dopant. As can be seen the (210) plane diffracts as a result of the presence of Sr-O bonds within the $SrTiO_3$ crystal structure, and as the Sr vacancies increase, this will reduce the amount of x-rays diffracting from the (210) plane containing Sr-O bonds therefore reducing the height of the peak.

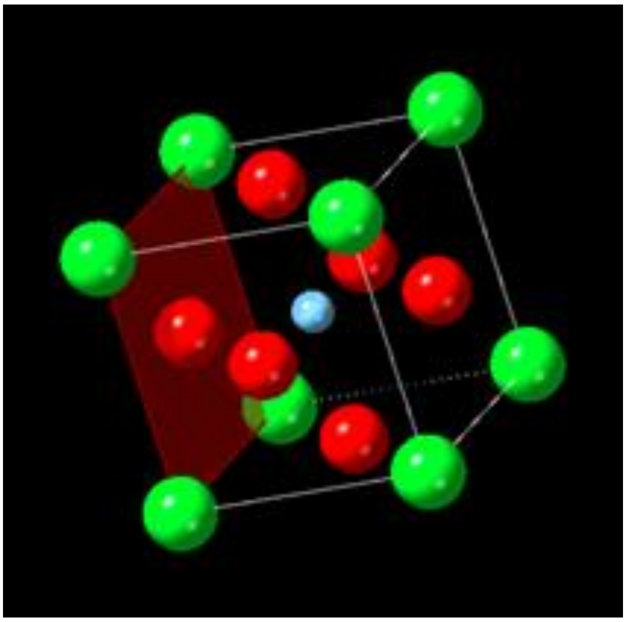

Figure 4.6: Illustration of the (100) plane in the $SrTiO_3$ unit cell, where the green ion is Sr, blue ion Ti and the red ion oxygen.

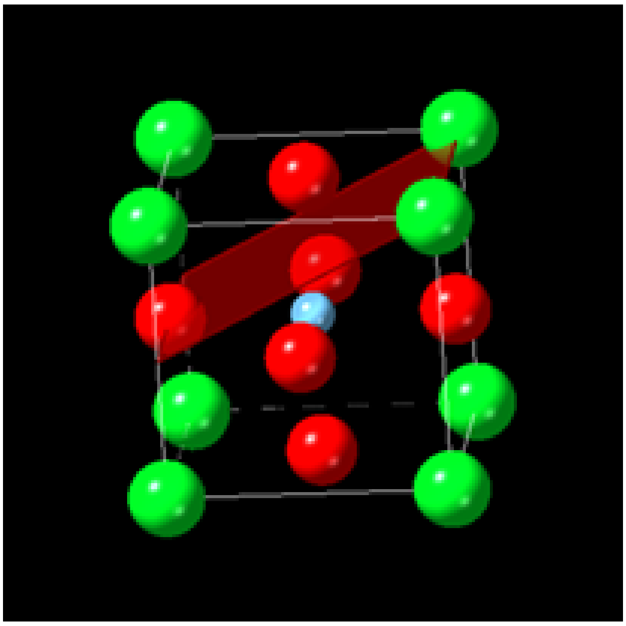

Figure 4.7: Illustration of the (210) plane in the $SrTiO_3$ unit cell, where the green ion is Sr, blue ion Ti and the red ion oxygen.

Figure 4.8 shown below of the (211) XRD peak of the $Sr_{(1-x/2)}Ti_{(1-x)}Nb_xO_3$ samples is of interest for two reasons. The first is the observed shifting of peaks to lower angles with increasing Nb and Sr-vacancy concentration suggesting an increase in lattice parameter. This was investigated further with Rietveld refinement below.

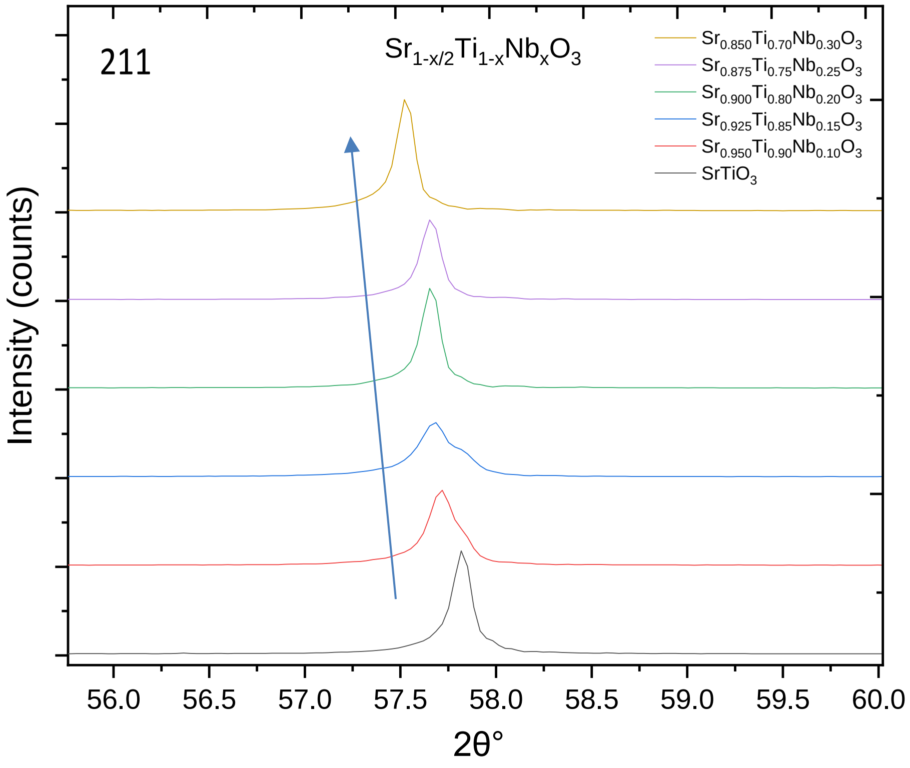

Figure 4.8: (211) peak of XRD analysis of $Sr_{(1-x/2)}Ti_{(1-x)}Nb_xO_3$ samples.

The second reason Figure 4.8 is of interest is that it is expected from the literature review for these samples to remain cubic with single peaks up $Nb_x=0.40$. However, as seen in the (211) peak the $Nb_x=0.10$, 0.15 and potentially 0.20 samples appear to have a slight splitting/asymmetry present. The initial fitting of the XRD data indicates that only cubic structures are present, despite the doublets seen. The doublets are seen from the (200) peak onwards throughout the rest of the pattern, unlike if the splitting were due to a rhombohedral or orthorhombic splitting yet were present despite $k_{\alpha 2}$ splitting peak removal via the program Highscore Plus. Initially it was thought that there could be two different cubic structures coexisting with slightly different d-spacings in order to accommodate the large Nb additions. However, this was investigated further on a second XRD diffractometer; a PANalytical Empyrean diffractometer. Samples of $SrTiO_3$ and $Nb_x=0.20$ were run at 40 mA, 40 kV with Cu radiation, and ran a 2 bounce monochromator with 1/32 degree fixed divergence slits with a 0.013° step size and 2000 seconds per step in an attempt to rule out any potential $k_{\alpha 2}$ peaks.

The results are shown below in Figure 4.9, including a focus on the (211) peak. This pattern illustrates that there are no secondary peaks, meaning any doublet peaks on the initial pattern are due to $k_{\alpha 2}$ splitting.

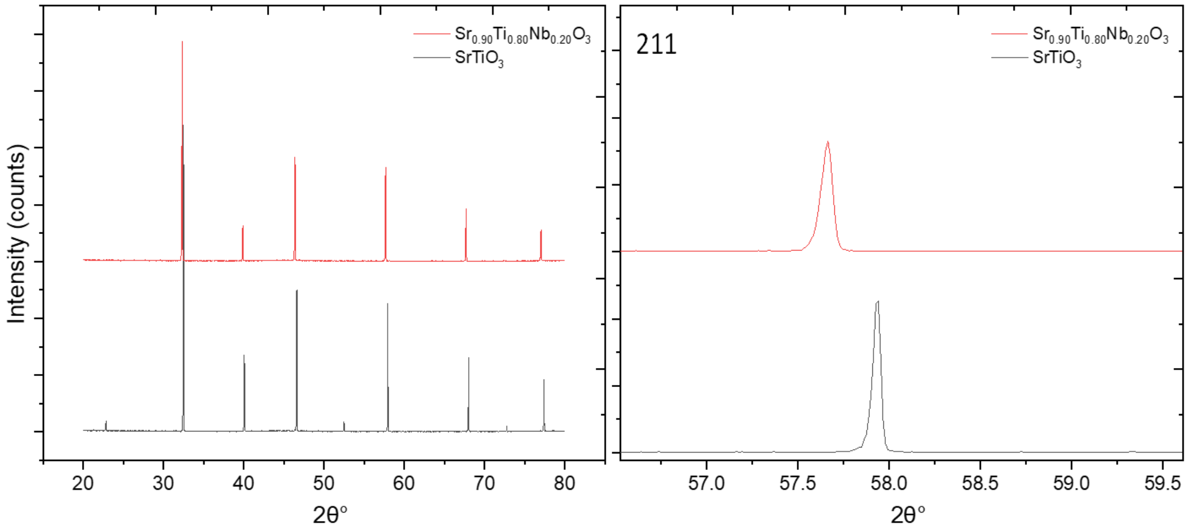

Figure 4.9: XRD pattern of cubic $SrTiO_3$ on PANalytical Empyrean diffractometer using 2 bounce monochromator with 1/32 degree fixed divergence slits.

Rietveld refinement of the $Sr_{(1-x/2)}Ti_{(1-x)}Nb_xO_3$ samples (Table 4-1) was carried out against a $SrTiO_3$ ICDD file (04-002-6528) for the $SrTiO_3$ sample and three Nb-doped $SrTiO_3$ ICDD files ($Sr_{0.99}Ti_{0.95}Nb_{0.05}O_3$ file for Nb_x=0.10 and 0.15 samples, a $Sr_{0.90}Ti_{0.80}Nb_{0.20}O_3$ file for Nb_x=0.20 and 0.25 and $Sr_{0.80}Ti_{0.60}Nb_{0.40}O_3$ for Nb_x=0.30). The correct stoichiometries of Sr, Ti and Nb were assigned accordingly for the initial refinement, before freeing up the occupancy. Figure 4.10 is a graphical representation from the Rietveld refinement data of the increase in lattice parameter of the cubic phase of each sample in the fitting. The black marker is the lattice parameter for undoped $SrTiO_3$. The elemental occupancies shown in Table 4-1 present slightly different values than those in the intended formula, however, it is known that there could be discrepancies from the fitting model due to the number of variables used in the fitting process. As such, the similarity to the intended formula is considered to be good.

As Figure 4.10 shows, the lattice parameter continually increases along with increasing Nb content. The unit cell parameter *a* calculated from the Rietveld refinement data was found to increase with increasing Nb content by an average of 6.7×10^{-4} Å per percentage of Nb from the Rietveld refinement lattice parameter data, vs. 4.6×10^{-4} Å per percentage of Nb for the raw XRD data. Notably it is not just an increase per % of Nb-dopant, but also the increase in Sr vacancies, as this is key to the flexibility of the structure being able to absorb large amounts of Nb on the B-site (64 pm Nb vs 60 pm Ti) due to the large Sr ionic radius (144 pm) and the space created by vacancies [16]. The raw XRD results are very similar to those found by Slater et al[38] discussed earlier that states that the addition of Nb to $SrTiO_3$ increases the size of the unit cell by 4.5 x 10^{-4} Å per percentage of Nb added for the $Sr_{1-x/2}Ti_{1-x}Nb_xO_3$ samples. N. Wang et al.[40] note that in the XRD pattern of Nb-doped $SrTiO_3$ peaks shifted to a lower angle illustrating the increase in Nb content and therefore the expansion of the unit cell, from incorporating the Nb^{5+} ion into the lattice to substitute for the Ti^{4+}. Wang et al. explain that the Ti^{4+} could be substituted instead of the Sr^{2+} due to a “lower dopant formation energy”.

Table 4-1: Rietveld refinement data for $Sr_{(1-x/2)}Ti_{(1-x)}Nb_xO_3$ samples.

Sample	**ICDD File**	**WRP**	**Rexp**	**Goodness of Fit**	**Lattice Parameter *a***	**Sr occ.**	**Ti occ.**	**Nb occ.**
$SrTiO_3$	04-002-6528	14.048	4.112	11.671	3.906 ± 0.00010	0.917	0.940	-
$Sr_{0.95}Ti_{0.90}Nb_{0.10}O_3$	04-016-4809	9.158	4.133	9.382	3.914 ± 0.00014	0.948	0.894	0.098
$Sr_{0.925}Ti_{0.85}Nb_{0.15}O_3$	04-016-4809	11.567	4.292	7.262	3.917 ± 0.00017	0.928	0.822	0.138
$Sr_{0.90}Ti_{0.80}Nb_{0.20}O_3$	04-018-5303	14.102	4.154	11.524	3.920 ± 0.00011	0.901	0.781	0.192
$Sr_{0.875}Ti_{0.75}Nb_{0.25}O_3$	04-018-5303	12.576	4.521	7.736	3.923 ± 0.00010	0.875	0.734	0.243
$Sr_{0.85}Ti_{0.70}Nb_{0.30}O_3$	04-017-9089	14.215	3.928	13.091	3.925 ± 0.00009	0.852	0.676	0.290

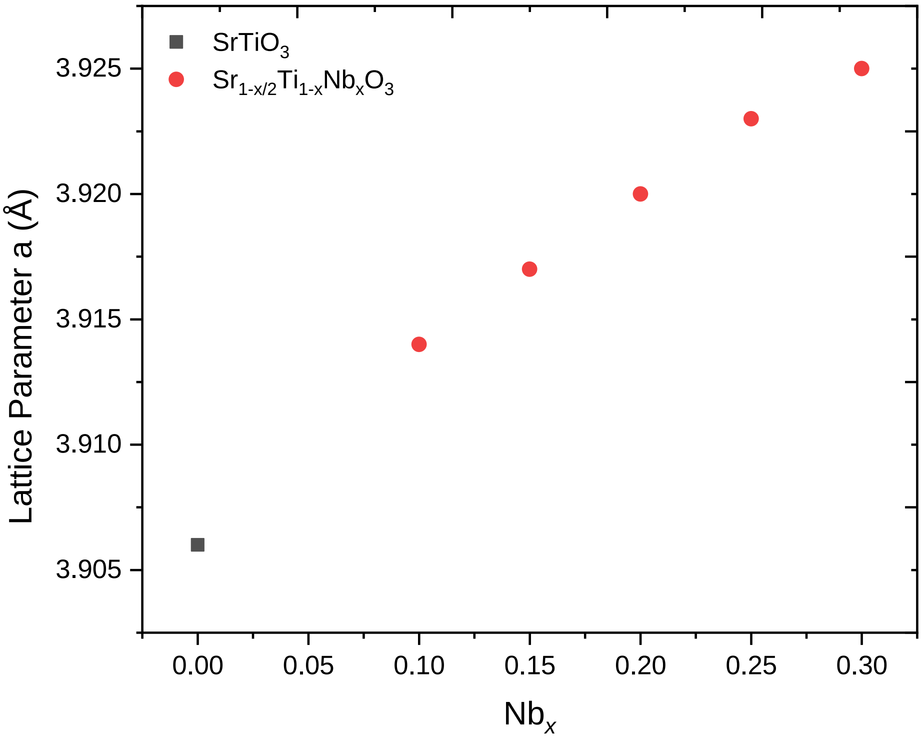

Figure 4.10: Changing lattice parameter with increasing Nb-content for $Sr_{(1-x/2)}Ti_{(1-x)}Nb_xO_3$ samples from Rietveld data (error bars smaller than data points).

$Sr_{0.9}Ti_{(1-x)}Nb_xO_3$ Samples:

The samples of the formula $Sr_{0.9}Ti_{(1-x)}Nb_xO_3$ where x=0.19, 0.15, 0.10, 0.05, 0.01, and 0.005 were subjected to X-ray diffraction analysis as sintered pellets. It is noted that $k\alpha_2$ stripping was carried out on the data before plotting (Figure 4.11). Peaks are labelled on the black pattern representing undoped $SrTiO_3$.

Figure 4.11 shows a single-phase cubic structure of the samples up to Nb_x=0.05. From there to Nb_x=0.005 there are small impurity peaks observed (highlighted by asterisks) which, when analysed using Highscore Plus software, were found to represent TiO_2. This suggests that between Nb_x=0.10 and Nb_x=0.05 when the Sr concentration is held at 0.90, the TiO_2 stops being fully absorbed into the $SrTiO_3$-based perovskite structure. Initially this was confusing as the Nb concentration is decreasing in these samples thus logically leaving more room for the Ti on the B-site, but actually it is thought that the TiO_2 is not being absorbed because there is not enough Nb present to electrostatically compensate for the large concentration of Sr vacancies in this sample set, whilst the relative Ti concentration is increasing. It is in the sample Nb_x=0.10 where the Ti and Sr concentration are in a 1:1 ratio, with the Nb compensating for the Sr vacancies, resulting in a charge balance. Below this Nb content there starts to become too much TiO_2 in relation to Sr to be absorbed into the perovskite system, and as such it appears as impurity peaks in the XRD pattern. From the Rietveld refinement data (Table 4-2) it can be seen that approximately 3 % of the Nb_x=0.05 to 0.005 phases fitted is TiO_2. For the samples Nb_x=0.15 and 0.10 approximately 0.5 % phase percentage is TiO_2. It is also possible that the secondary phase is Nb-doped TiO_2, but this is not visible in the XRD data.

As seen with the previous sample set, for the Nb_x=0.19 and 0.15 samples have the (100) and (210) peaks missing but less so the (300) peak. It is thought that this could be related to the A-site vacancies present in these sample sets, which can be confirmed by examining the upcoming B-site doped samples which do not possess A-site vacancies and are not missing the same peaks.

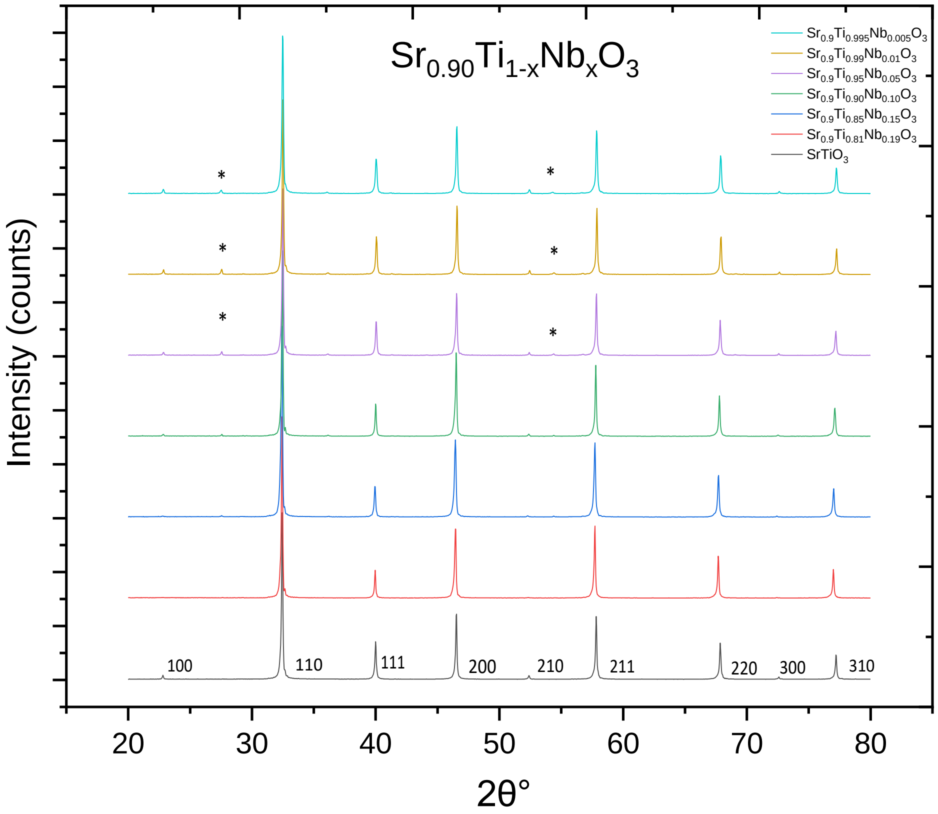

Figure 4.11: XRD pattern of $Sr_{0.9}Ti_{(1-x)}Nb_xO_3$ where x=0.19, 0.15, 0.10, 0.05, 0.01, 0.005, asterisks indicating TiO_2 phase.

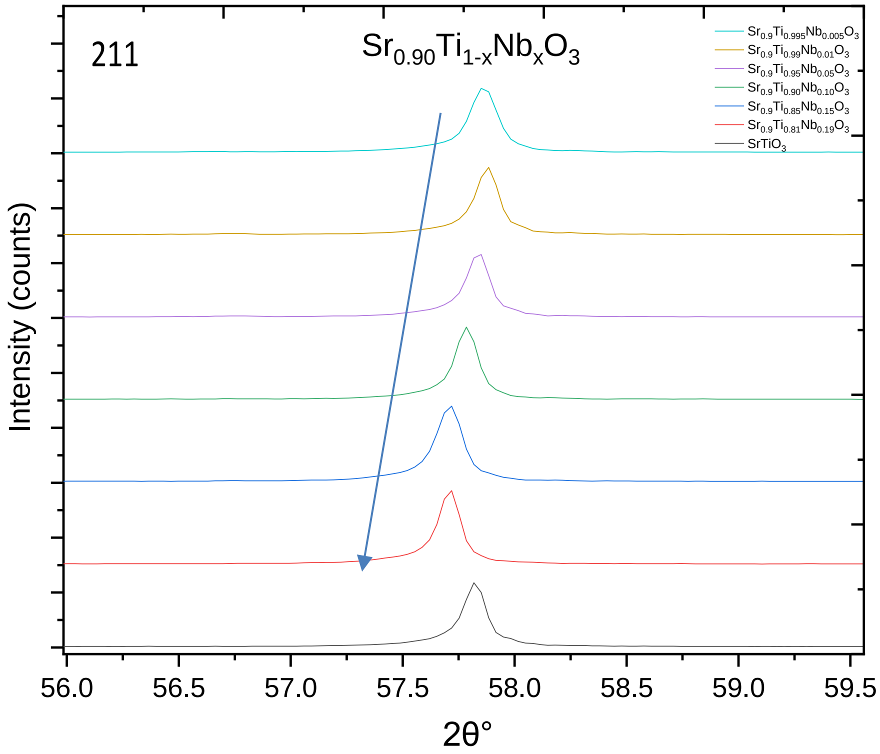

Figure 4.12: 211 peak of XRD analysis of $Sr_{0.9}Ti_{(1-x)}Nb_xO_3$ samples.

Figure 4.12 shows the 211 XRD peak and illustrates the same observation as the $Sr_{(1-x/2)}Ti_{(1-x)}Nb_xO_3$ samples; that the addition of Nb increases the size of the unit cell. This was found to be by an average of 10.3 x10^{-4} Å per percentage of Nb, with a fixed concentration of Sr vacancies (0.9). This is seen by the shift to lower angles of the samples compared to undoped $SrTiO_3$ as the Nb content increases. As seen in the Rietveld refinement data below (Table 4-2), the x=0.005 and x=0.01 samples have an almost identical unit cell size to that of undoped $SrTiO_3$.

Table 4-2: Rietveld refinement data for $Sr_{0.9}Ti_{(1-x)}Nb_xO_3$ samples.

Sample	**WRP**	**Rexp**	**Goodness of Fit**	**Phase % (STO)**	**Phase % (TiO_2)**	**Lattice Parameter *a***	**Sr occ.**	**Ti occ.**	**Nb occ.**
$SrTiO_3$	14.800	6.605	5.021	100	0	3.906 ± 0.00010	0.937	0.961	-
$Sr_{0.90}Ti_{0.995}Nb_{0.005}O_3$	13.263	6.031	4.835	97.2	2.8	3.907 ± 0.00009	0.927	0.947	0.005
$Sr_{0.90}Ti_{0.99}Nb_{0.01}O_3$	13.633	6.073	5.039	96.4	3.6	3.907 ± 0.00013	0.937	0.945	0.009
$Sr_{0.90}Ti_{0.95}Nb_{0.05}O_3$	14.185	6.216	5.207	97.2	2.8	3.911 ± 0.00009	0.922	0.917	0.037
$Sr_{0.90}Ti_{0.90}Nb_{0.10}O_3$	15.998	6.035	7.026	99.4	0.6	3.914 ± 0.000096	0.900	0.869	0.088
$Sr_{0.90}Ti_{0.85}Nb_{0.15}O_3$	13.055	5.691	5.261	99.5	0.5	3.916 ± 0.00010	0.903	0.823	0.139
$Sr_{0.90}Ti_{0.81}Nb_{0.19}O_3$	14.045	3.772	13.861	100%	0%	3.919 ± 0.00011	0.902	0.789	0.181

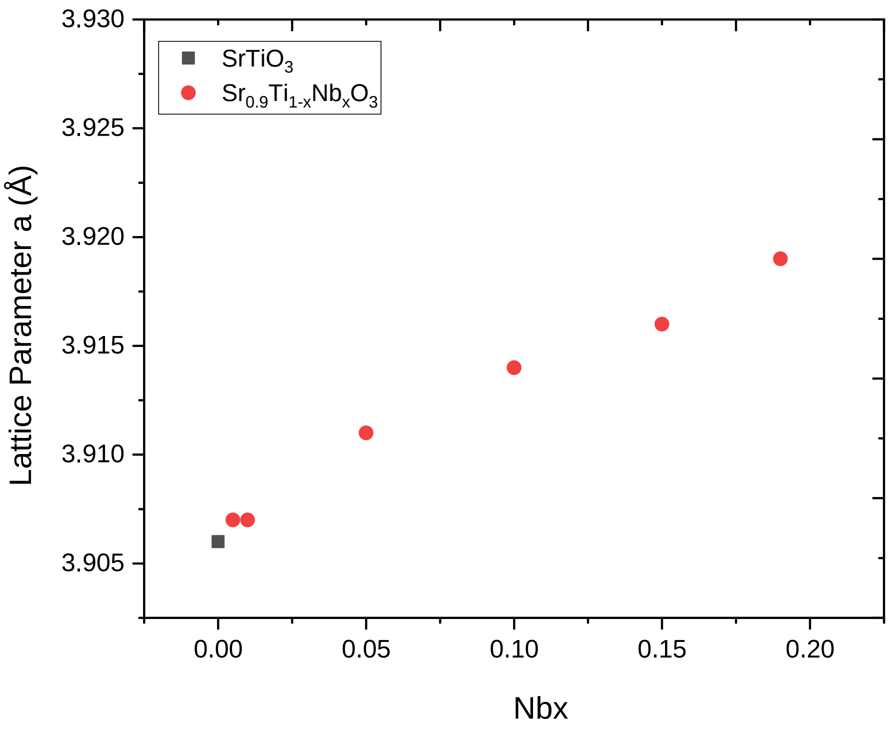

Figure 4.13: Changing lattice parameter with increasing Nb-content for $Sr_{0.9}Ti_{(1-x)}Nb_xO_3$ samples, according to Rietveld refinement data (error bars smaller than data points).

4.1.1.3 B-site Nb-Doped $SrTiO_3$

Samples of $SrTi_{(1-x)}Nb_xO_3$ were analysed by XRD and the patterns are shown below in Figure 4.14. Theoretical densities were calculated from the d-spacing of the (200) peak of the XRD data and compared to geometric values, and densities of 97-98 % for this sample set were achieved on sintering.

As can be seen from Figure 4.14 a single phase cubic perovskite structure was maintained for each sample. The approximate unit cell expansion for the $SrTi_{1-x}Nb_xO_3$ system was calculated from the raw XRD data to be 13 x 10^{-4} Å per percentage of Nb dopant; thought to be due to the larger ionic radius of Nb (64 pm) in comparison to Ti (60 pm)[16]. This is a greater increase in unit cell size per %Nb in comparison to the $Sr_{(1-x/2)}Ti_{(1-x)}Nb_xO_3$ samples. This illustrates the impact of Sr vacancies on the accommodation of Nb into the perovskite structure and suggests that significantly less Nb would be able to be added to this material system before secondary phases would appear. It is noted that this increase in unit cell parameter calculation is potentially much less accurate than the $Sr_{(1-x/2)}Ti_{(1-x)}Nb_xO_3$ equivalent because the concentration of Nb-addition in this sample set is much smaller and therefore the change in lattice parameter and peak position is small relative to the XRD step size (Figure 4.15).

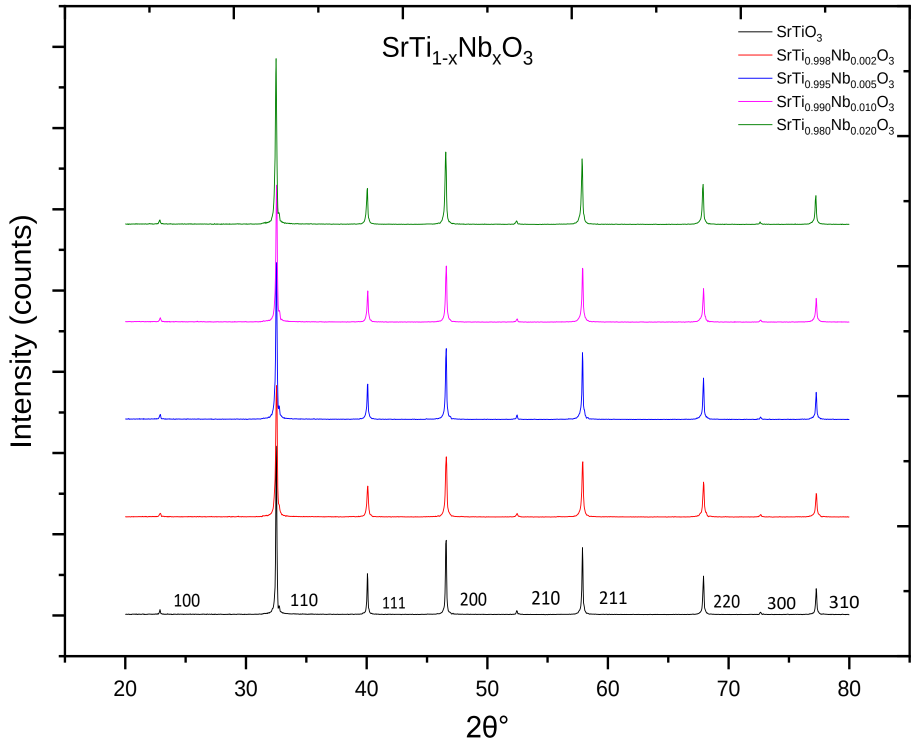

Figure 4.14: XRD pattern of $SrTi_{(1-x)}Nb_xO_3$ where x=0.002, 0.005, 0.010, 0.020.

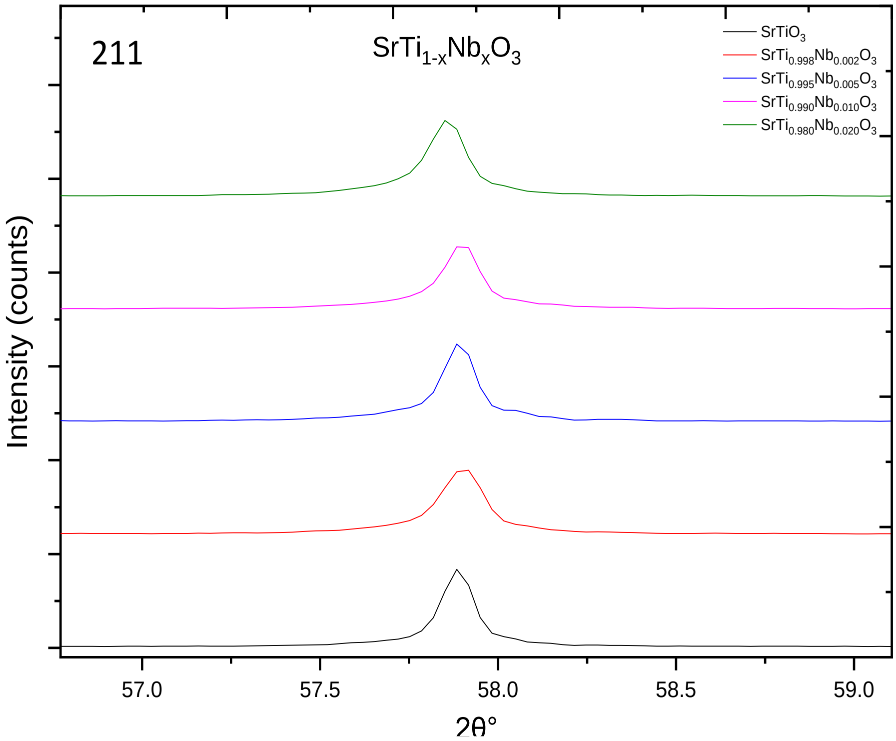

Figure 4.15: 211 peak of $SrTi_{(1-x)}Nb_xO_3$ samples.

4.1.1.4 Acceptor-Doped $SrTiO_3$

$SrTi_{(1-x)}Mn_xO_3$ Samples

Samples of $SrTi_{(1-x)}Mn_xO_3$ were analysed by XRD and the pattern are shown below in Figure 4.16. Theoretical densities were calculated from the d-spacing of the (200) peak of the XRD data and compared to geometric values, and densities of 80-95 % for this sample set were achieved on sintering.

As can be seen from Figure 4.16 a single phase cubic perovskite structure was maintained for each sample. Unit cell sizes were calculated from raw XRD data and it was found that there was an average decrease in unit cell size of 2.08×10^{-3} Å per % of Mn dopant substituted. It was intended for the Mn^{2+} to be substituted for Ti^{4+} on the B-site as described previously. The decrease in unit cell size, observed in Figure 4.17 as a shift in peaks to higher diffraction angles, is unexpected as the Mn^{2+} cation size (0.64 Å)[16] is larger than that of Ti^{4+} (0.60 Å) just as Nb is in the previous donor-doped sample set, and yet this sample set sees a decrease in lattice parameter. This is thought to be due to the lower charge on the ion, resulting in weaker covalent bonding and a larger unit cell. It could however be the case that the Mn actually substituted onto the Sr site, and as the Mn^{2+} ion is smaller than Sr^{2+}(1.44 Å)[16], this could explain the decrease in unit cell size. Another possibility for the decrease in unit cell size was proposed by Pan et al. 2019[81] who discovered a decrease in lattice parameter due to an increase in oxygen vacancies in the sample, which could be the case here due to the large concentration of acceptor dopants.

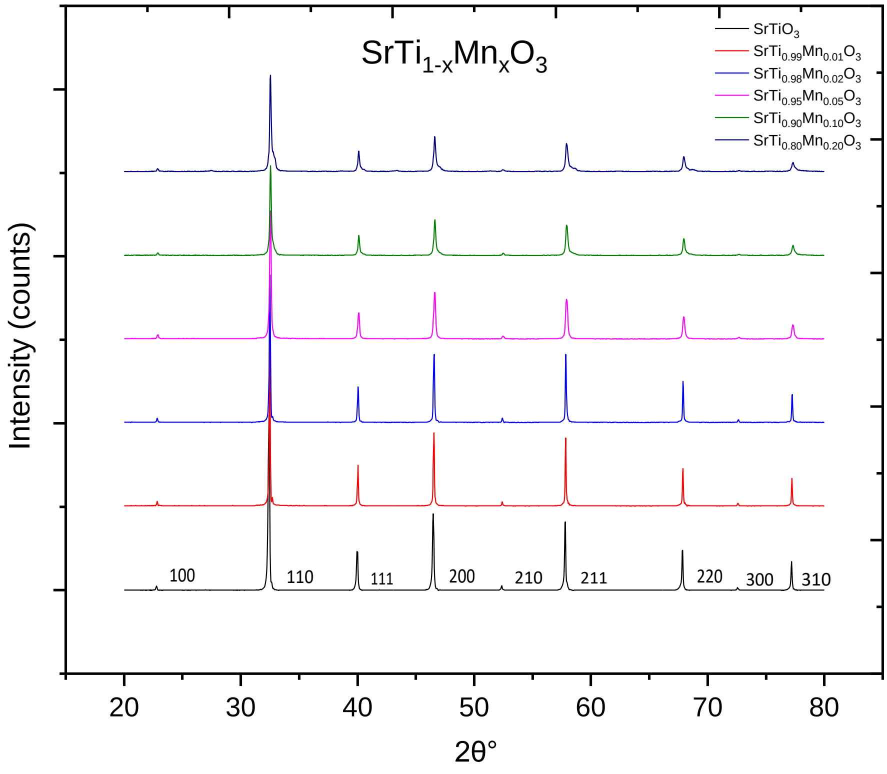

Figure 4.16: XRD pattern of $SrTi_{(1-x)}Mn_xO_3$ where x=0.002, 0.005, 0.010, 0.020.

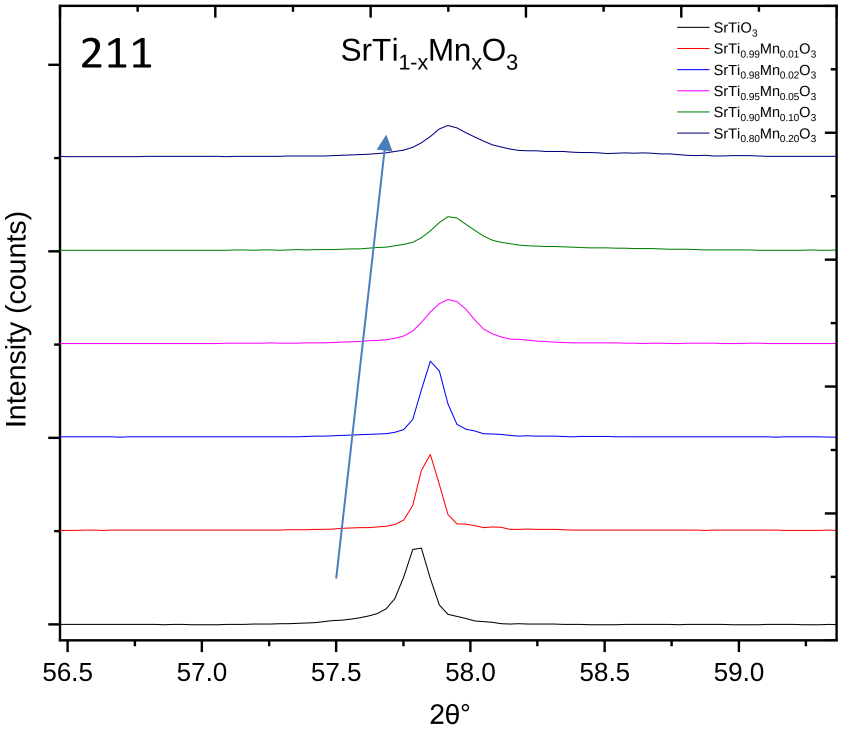

Figure 4.17: 211 peak of $SrTi_{(1-x)}Mn_xO_3$ samples.

$SrTi_{(1-x)}Co_xO_3$ Samples:

Samples of $SrTi_{(1-x)}Co_xO_3$ were analysed by XRD and the spectrum is shown below in Figure 4.18. Theoretical densities were calculated from the d-spacing of the (200) peak of the XRD data and compared to geometric values, and densities of 85-90 % for this sample set were achieved on sintering.

As can be seen from Figure 4.18 a single phase cubic perovskite structure was maintained for each sample. Unit cell sizes were calculated from raw XRD data and it was found that there was an average decrease in unit cell size of 2.49×10^{-3} Å per % of Co dopant substituted represented by a shift in peaks to lower d-spacings (higher diffraction angles) as seen in Figure 4.19. It was intended for the Co^{2+} to be substituted for Ti on the B-site as described previously. The decrease in unit cell size is strange as the Co^{2+} cation size (0.61 Å)[16] is marginally larger than that of Ti^{4+} (0.60 Å). Again, as with the Mn example, this is thought to be due to the lower charge on the ion, resulting in weaker covalent bonding and a larger unit cell. The exception with this sample set for unit cell size decrease is at the Co_x=0.20 sample. This could be due to the larger atomic radii finally overriding the lower charge at some point between x=0.10 and x=0.20, causing a shift to larger lattice parameters, notably the peak position is still only in line with undoped $SrTiO_3$. It is unknown if greater concentrations of Co would cause a shift to larger unit cell sizes or would just cause phase splitting as the saturation point of the cubic perovskite is reached. It could also be possible that this sample was mixed up, but it is unlikely.

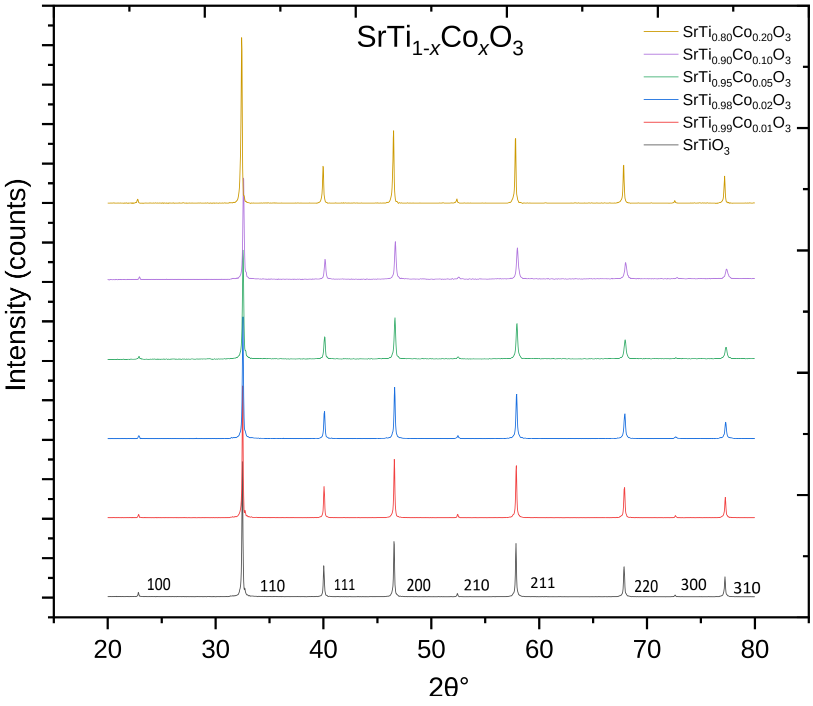

Figure 4.18: XRD pattern of $SrTi_{(1-x)}Co_xO_3$ where x=0.002, 0.005, 0.010, 0.020.

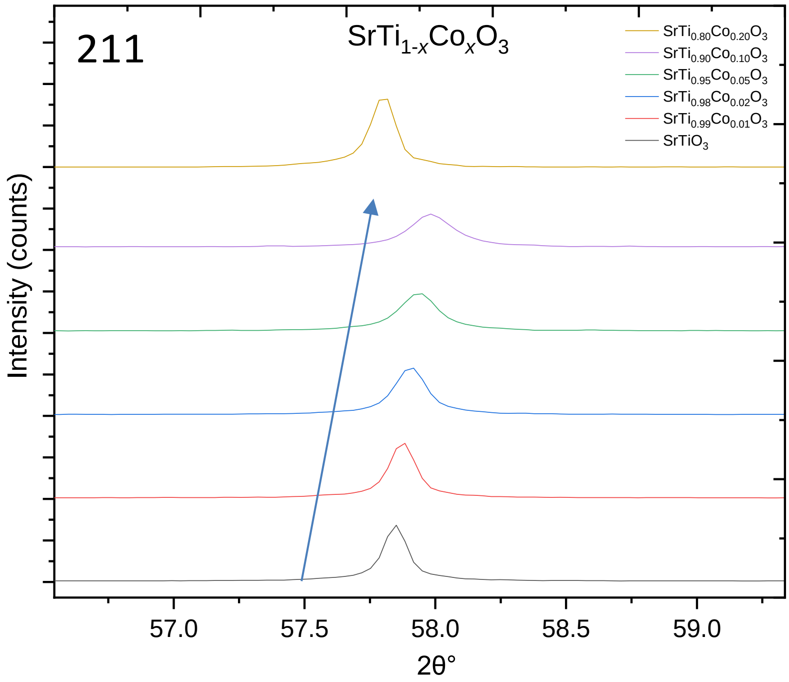

Figure 4.19: 211 peak of $SrTi_{(1-x)}Co_xO_3$ samples.

It is of note that all of the B-site doped material systems maintain the (100) and (210) XRD peak, confirming the loss of those peaks in earlier samples is related to A-site vacancies.

4.1.2 Scanning Electron Microscopy

4.1.2.1 A-Site Vacancy Compensation of Donors

The electrical properties of $SrTiO_3$-based materials are known to vary, as with many dielectrics, with the microstructure of the material and as such it is important to investigate these samples alongside any electrical measurements in order to draw meaningful conclusions from the data[104]. Samples of $SrTiO_3$, $Sr_{0.95}Ti_{0.90}Nb_{0.10}O_3$, $Sr_{0.90}Ti_{0.80}Nb_{0.20}O_3$ and $Sr_{0.85}Ti_{0.70}Nb_{0.30}O_3$ were mounted in resin and polished before being imaged by a scanning electron microscope, shown below Figure 4.21. The images produced are predominantly those using the backscattered electron technique which provide a good contrast between either grain orientation or composition. Undoped $SrTiO_3$ has normal grain growth with an average grain size of 2.63 μm (Table 4-3). The $Sr_{0.95}Ti_{0.90}Nb_{0.10}O_3$ sample appears to show bimodal or abnormal grain growth whereby some grains have grown much faster than the smaller grains surrounding it, in which case the average grain size displayed in is not particularly accurate. An average measurement of the larger grains results in a grain size of approximately 2 μm whereas the small grains have an average size of approximately 0.3 μm. Although only samples Nb_x=0.10, 0.20 and 0.30 were analysed under SEM, it is thought that the Nb_x=0.15 sample could have the same bimodal grain structure as the Nb_x=0.10 sample because the colour of the pellets was the same as one another. Samples higher in Nb content all turned a dark blue/grey colour whereas the Nb_x=0.10/0.15 samples were a light blue/beige colour (below).

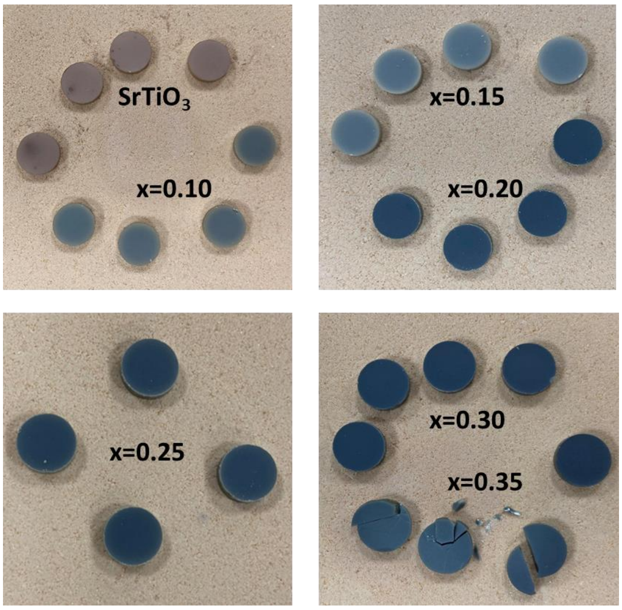

Figure 4.20: Picture showing sintered pellets of $SrTiO_3$ and $Sr_{1-x/2}Ti_{1-x}Nb_xO_3$ where x=0.10-0.35, increasing in dopant concentration from top left to bottom right.

Rheinheimer et al.[105] state that bimodal grain growth is common in $SrTiO_3$ ceramics between 1350 and 1400 °C, however both the Nb_x=0.10 and undoped $SrTiO_3$ samples were sintered at 1460 °C so this cannot be the direct cause. Most literature states that the difference in grain growth comes from either starting particle size or sintering time/regime and these samples, apart from varying in temperature by 10’s of degrees, were sintered under the same regime and processed at the same time and therefore the source of the differences in microstructure are likely to be compositional. Work by Wang et al. 2016[40] presents SEM results with a similar bimodal grain growth structure in a sample of $SrTi_{0.88}Nb_{0.12}O_3$, the Nb content of which is similar to that of $Sr_{0.95}Ti_{0.90}Nb_{0.10}O_3$ however without the non-stoichiometric Sr vacancies, but unfortunately no explanation for the effect is given. Nb is known to impede grain growth in $BaTiO_3$ ceramics[106] which could be the cause of the small grains seen in this sample, however this effect is caused by Nb segregation to the grain boundaries; the opposite appears to be the case in these samples.

Samples Nb_x=0.20 and 0.30 both appear to have a lighter coloured centre of the grain and a darker outer rim. The back scatter technique is capable of highlighting differences in elemental composition which suggests that this contrast in colour could be due to material segregation. Elemental analysis was carried out in the form of EDS (energy-dispersive X-ray spectroscopy) on the $Sr_{0.90}Ti_{0.80}Nb_{0.20}O_3$ sample and the image shown below (Figure 4.22). It is not immediately obvious as to a higher concentration of any element from the combined mapping, until a specific directed scan of individual spots was carried out (Figure 4.23). The results of the elemental mapping from spectrum 1 and 2 (Figure 4.24) show that the ratio of Ti and Nb is inverted between the lighter core and the darker shell. In the spectrum of the lighter core section of the grain the concentration of Nb is higher than Ti, and the reverse is true in the darker outer section of the grain. Although not shown here, the same is true across each grain analysed in Figure 4.23, i.e. pattern 1, 3, 5 and 7 all present higher Nb concentrations and pattern 2, 4, 6 and 8 all present higher Ti levels towards the outsides of the grains. The same effect is true in the $Sr_{0.85}Ti_{0.70}Nb_{0.30}O_3$ sample. This is in agreement with the paper by Chung et al. which suggests that there is Ti-segregation at grain boundaries in air sintered Nb-doped $SrTiO_3$ when examined by STEM [64] but is in disagreement with work by Baurer et al.[107] which reports that in furnace-cooled Nb-doped $SrTiO_3$ samples the Nb segregated toward the grain boundary; the opposite of which is clearly evidenced in this case. It is thought that this is due to the excess of Sr vacancies in the chemistry of this sample set as opposed to just B-site donor-doped $SrTiO_3$ which is known to encourage Ti-diffusion. It is possible that Nb is diffusing into the grain boundary as seen in $BaTiO_3$ ceramics from the shell, leaving the shell area around the core Ti-rich but the core itself still relatively Nb-rich.

The paper by Cho et al. 1994[36] as discussed in Section 2.2.3, researches a Nb-doped $SrTiO_3$ system. Samples air-sintered above the eutectic temperature had larger grains, samples sintered below the eutectic had a fine grained structure due to a compensation of Nb by Sr vacancies which increases the solubility of TiO_2. Larger grains occur when sintering above the eutectic because any excess TiO_2 forms a liquid phase which promotes grain growth. However, a lack of TiO_2 excess resulted in SrO RP phases and poor densities. In this work there is an excess of Sr relative to Ti due to the large amount of Nb dopant, however there are still a significant amount of Sr vacancies in the material which makes this sample set different to many seen in literature that use a simple B-site substitution doping regime. The large number of Sr vacancies could be increasing the solubility of TiO_2, yet there is less TiO_2 to form a liquid phase in each sample as Nb-substitution increases. It is also concluded from this research that Nb reduces the sintering temperature of $SrTiO_3$ as the Nb_x=0.2 to 0.3 samples all had to be sintered at temperatures lower than the eutectic temperature (1440 °C)[36] to avoid cracking or melting (1400-1430 °C), this effect was also seen by Pan et al. 2018[81].

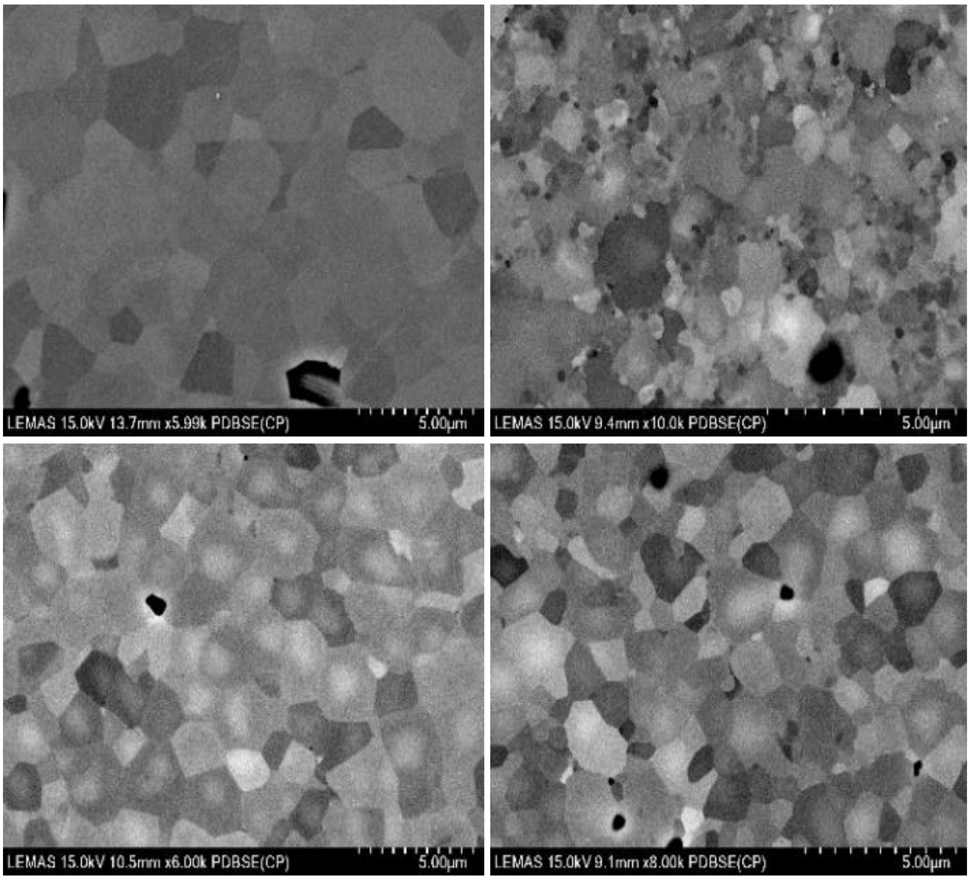

Figure 4.21: SEM images of samples – (a) $SrTiO_3$, (b) $Sr_{0.950}Ti_{0.90}Nb_{0.10}O_3$ (c) $Sr_{0.900}Ti_{0.80}Nb_{0.20}O_3$, (d) $Sr_{0.850}Ti_{0.70}Nb_{0.30}O_3$, 5 μm.

Table 4-3: Table showing the calculated average grain size of Nb-doped $SrTiO_3$ samples.

Sample	**Average Grain Size (μm)**
$SrTiO_3$	2.63
$Sr_{0.95}Ti_{0.90}Nb_{0.10}O_3$	0.83
$Sr_{0.90}Ti_{0.80}Nb_{0.20}O_3$	2.23
$Sr_{0.85}Ti_{0.70}Nb_{0.30}O_3$	1.41
$Sr_{0.90}Ti_{0.995}Nb_{0.005}O_3$	2.33
$Sr_{0.90}Ti_{0.95}Nb_{0.05}O_3$	9.36
$Sr_{0.90}Ti_{0.90}Nb_{0.10}O_3$	3.67
$Sr_{0.90}Ti_{0.95}Nb_{0.15}O_3$	3.34
$SrTi_{0.995}Nb_{0.005}O_3$	2.56
$SrTi_{0.990}Nb_{0.010}O_3$	4.65
$SrTi_{0.980}Nb_{0.020}O_3$	4.55

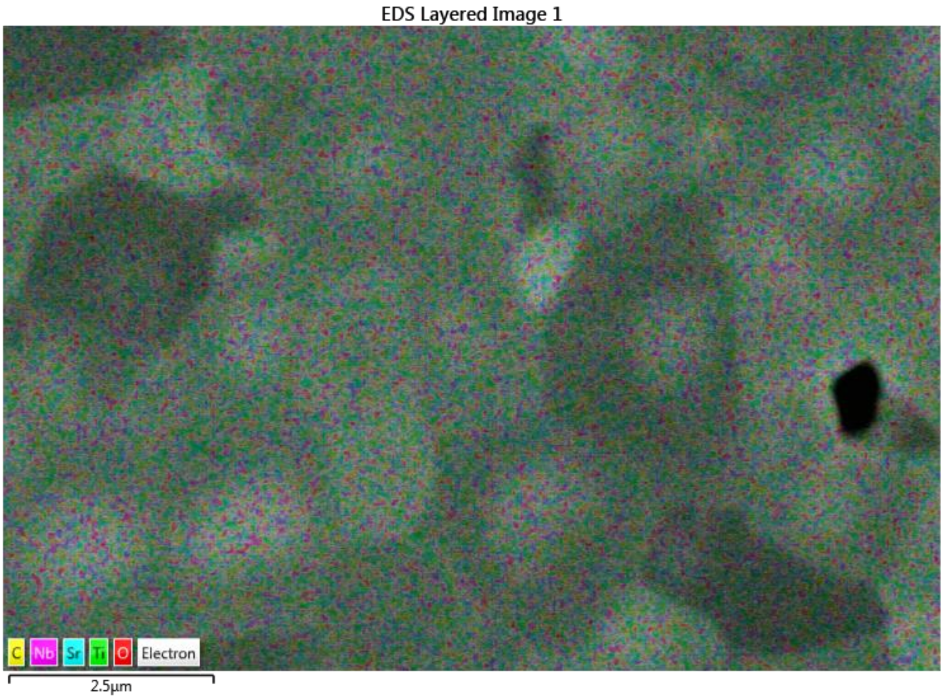

Figure 4.22: EDS image of $Sr_{0.90}Ti_{0.80}Nb_{0.20}O_3$ sample.

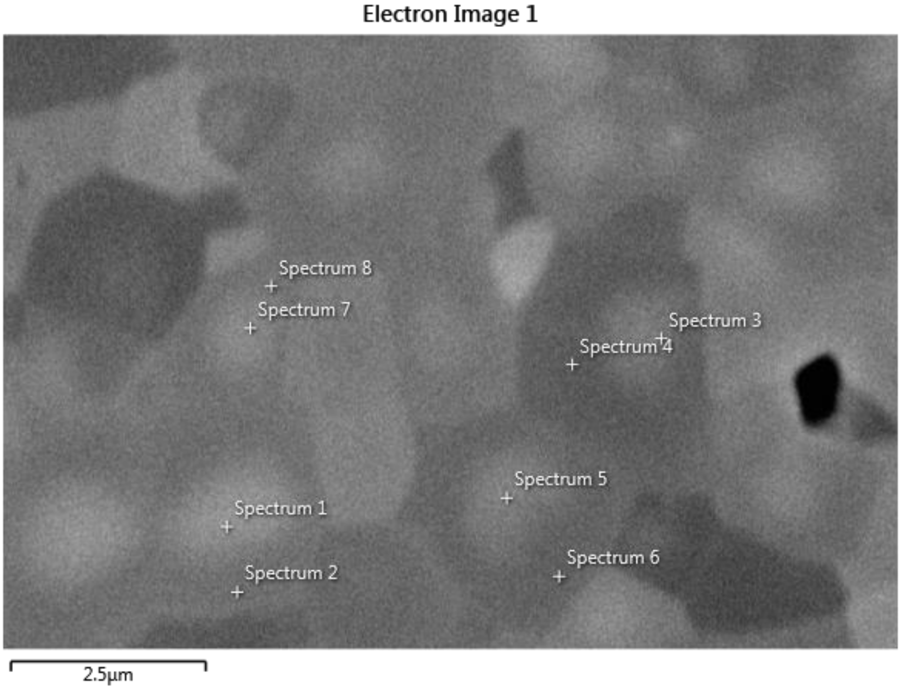

Figure 4.23: EDS image of $Sr_{0.90}Ti_{0.80}Nb_{0.20}O_3$ sample showing directed elemental analysis locations.

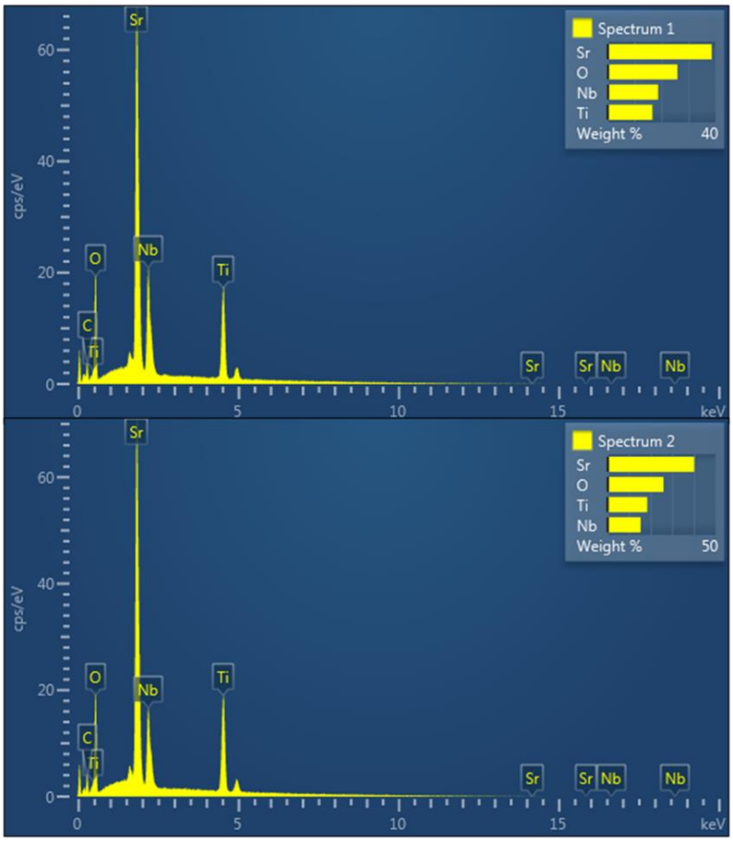

Figure 4.24: EDS elemental analysis results.

Figure 4.25 below shows the SEM images of the $Sr_{0.9}Ti_{1-x}Nb_xO_3$ samples where x= 0.005, 0.05, 0.10 and 0.20. The Nb_x=0.10 and 0.20 samples both show the same type of core-shell Ti/Nb structure as the previous A-site vacancy compensated samples. Interestingly the Nb_x=0.10 sample does not show the same bimodal grain growth as the $Sr_{0.95}Ti_{0.90}Nb_{0.10}O_3$ sample, the key difference between the samples being approximately 0.05 at% of Sr. There are also brighter areas located between grains in some areas of the micrographs of the x=0.05 and 0.10 samples (highlighted by red circles in Figure 4.25). Examination of elemental mapping data (Figure 4.26) shows this to be a concentration of Nb, which has presumably formed a liquid phase during sintering. The $Sr_{0.9}Ti_{0.95}Nb_{0.05}O_3$ sample shows much larger grains that the other samples confirmed by the average grain size (9.36 µm) shown in Table 4-3 probably due to an optimum amount of Nb-liquid phase to encourage grain growth without impeding it. Either side of this composition the grain size reverts to a smaller size closer to that of $SrTiO_3$. The same sample also shows what appears to be a dark pore (circled in yellow) in the bottom left of the image. Elemental mapping was consulted again (Figure 4.27) and this used in conjunction with secondary electron imaging confirmed that this area is in fact Ti-rich. The secondary electron image would have a brighter ring around the edge due to charging it if it was a pore which does not exist and is probably dark in shading due to the topography of the sample. This matches and supports the XRD pattern for this sample set which has secondary phase TiO_2 present. From this and also the XRD data it is clear that there is much less compensation balance within these samples resulting in separation of phases from the perovskite.

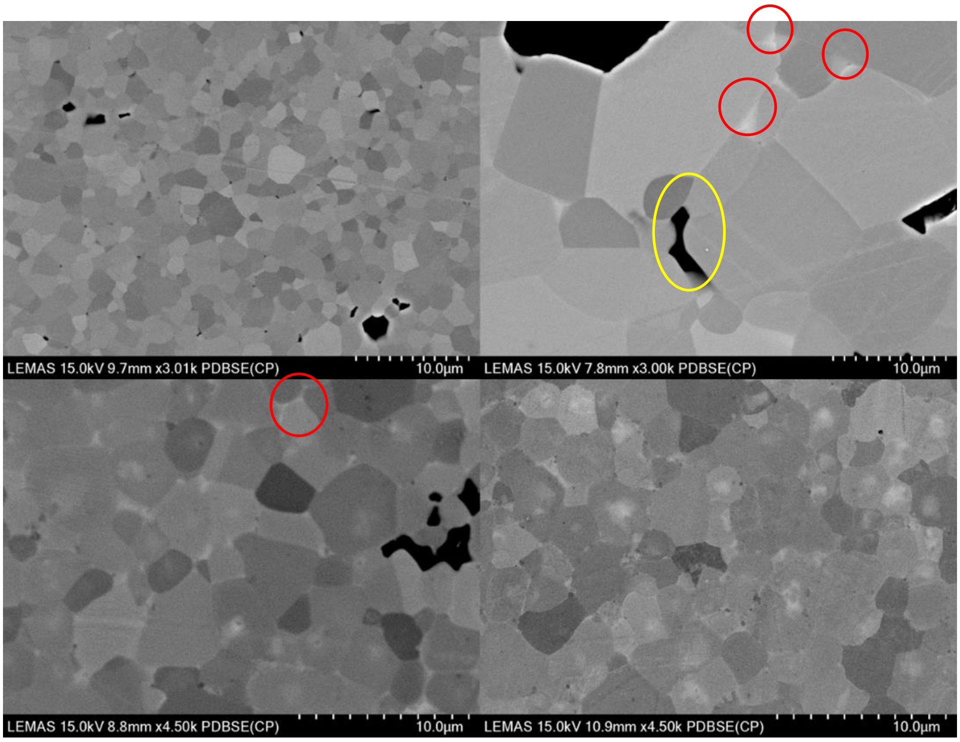

Figure 4.25: SEM images of samples – (a) $Sr_{0.90}Ti_{0.995}Nb_{0.005}O_3$ (b) $Sr_{0.90}Ti_{0.95}Nb_{0.05}O_3$ (c) $Sr_{0.90}Ti_{0.90}Nb_{0.10}O_3$, (d) $Sr_{0.90}Ti_{0.85}Nb_{0.15}O_3$, 10 µm.

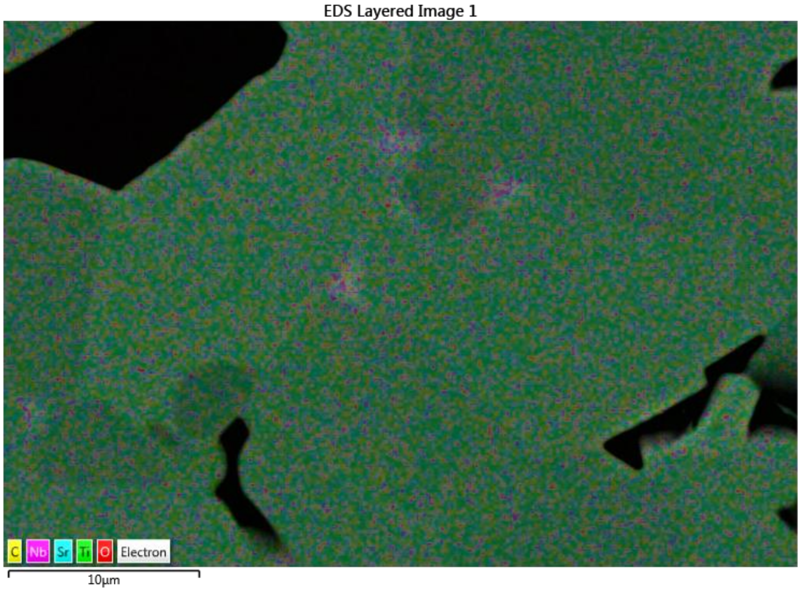

Figure 4.26: EDS image of $Sr_{0.90}Ti_{0.95}Nb_{0.05}O_3$ sample illustrating Nb concentration between grains.

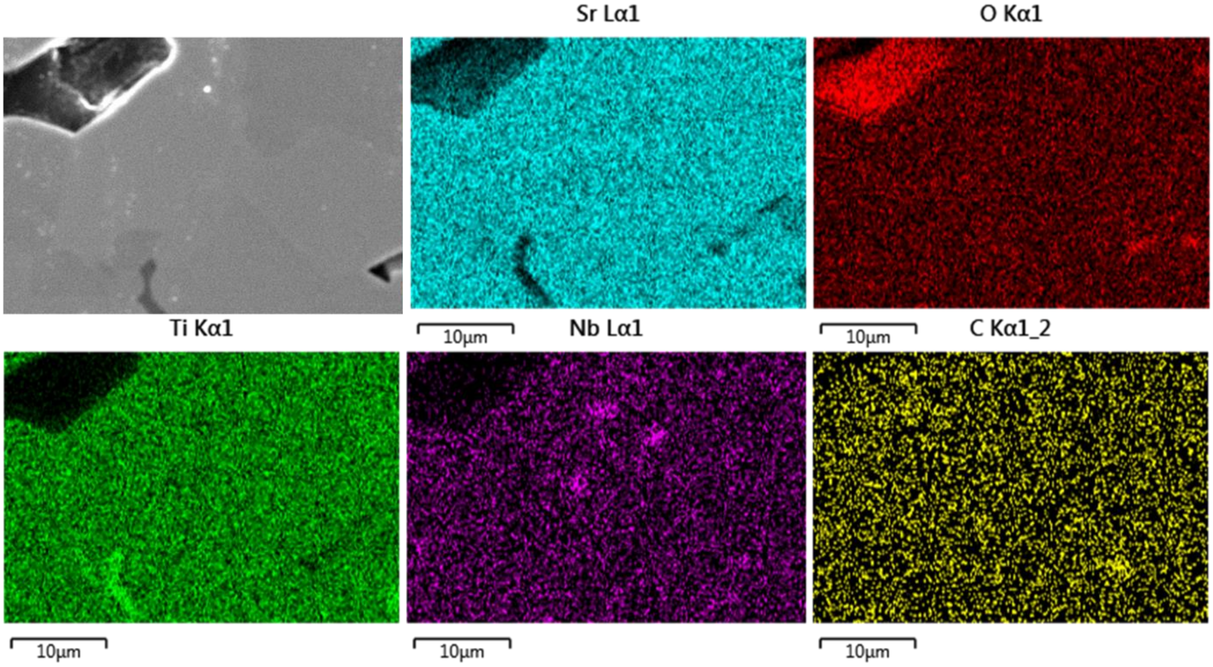

Figure 4.27: Secondary electron image and EDS elemental mapping of the $Sr_{0.90}Ti_{0.95}Nb_{0.05}O_3$ sample separating each element, highlighting Ti.

4.1.2.2 B-Site Nb-Doped $SrTiO_3$

Figure 4.28 below shows the SEM images of the of $SrTi_{1-x}Nb_xO_3$ samples where x= 0.005, 0.010, 0.020 top to bottom. It is clear from these images that there is not the same core and shell structure seen to the grains as with the previous Nb-doped samples, nor the same Nb concentration in between grain boundaries. From these images the average grain sizes were found to be 2.5, 4.6 and 4.6 μm, respectively (Table 4-3). This shows that between 0.5 % and 1 % Nb dopant the average grain size changes from approximately 2.5 to 4.5 μm where the average grain size of the 0.5 %Nb sample resembles the average grain size of the undoped $SrTiO_3$. The samples appear somewhat porous, but the density of this sample set was calculated to be 97-98 % theoretical density, indicating that the pores could have developed in polishing, where grains are removed from the sample as material is removed to create a polished surface which could happen with a softer material. There appears to be fairly normal grain growth across this sample set, but this is expected with such low levels of Nb addition to otherwise undoped $SrTiO_3$. This sample set was air-sintered at lower temperatures than the A-site vacancy sample sets (1350 °C 8hrs) and as such the small average grain size is expected from sintering below the eutectic temperature, again as explained by Cho et al. due to a compensation of Nb by Sr vacancies[36]. The porosity of the samples was also seen in the 1.0 at% Nb doped $SrTiO_3$ samples by Cho et al that were sintered at lower temperatures (1420 vs 1480 °C)[36].

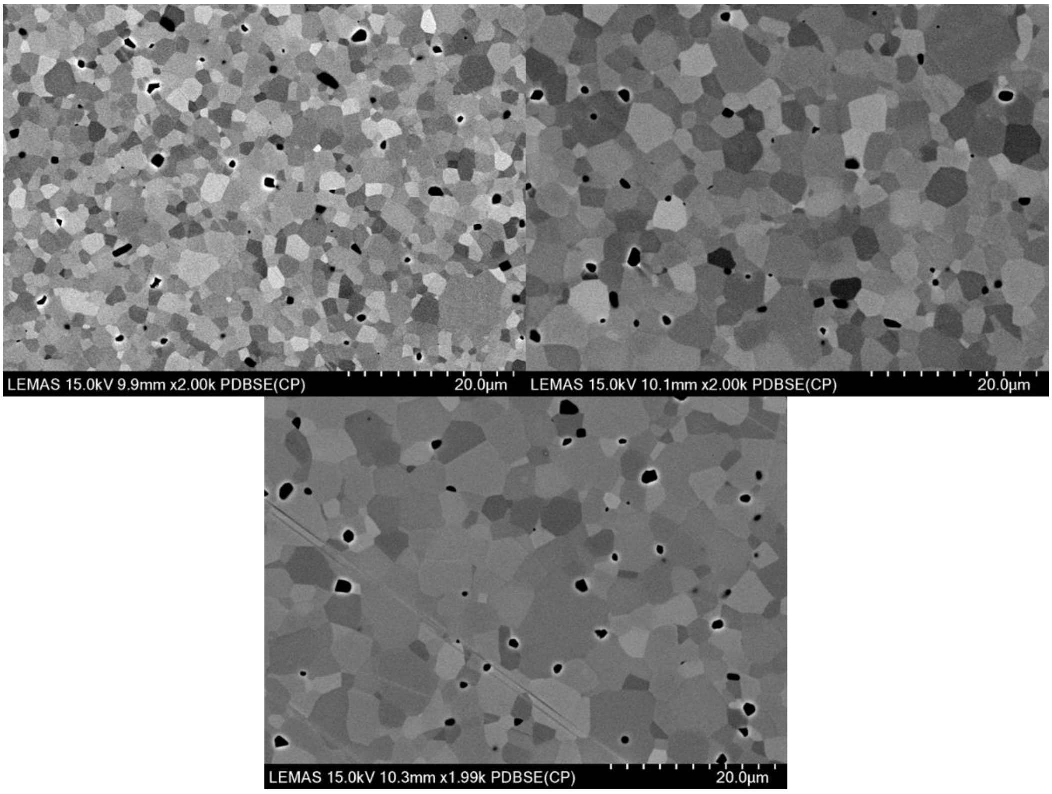

Figure 4.28: SEM images of $SrTi_{1-x}Nb_xO_3$ samples where x= 0.005, 0.010, 0.020 top to bottom, 20 μm.

4.1.3 Transmission Electron Microscopy

TEM was carried out on a sample of $Sr_{0.90}Ti_{0.80}Nb_{0.20}O_3$ when it was still considered a possibility that there could be two cubic unit cell sizes coexisting, as a way of confirming or ruling out this idea. Shown below is the FIB-prepared sample from a sintered pellet (Figure 4.29). It shows the granular structure of the sample, with a slightly amorphous region at the surface of the pellet below the coating which could exist due to volatility of material from the surface on sintering.

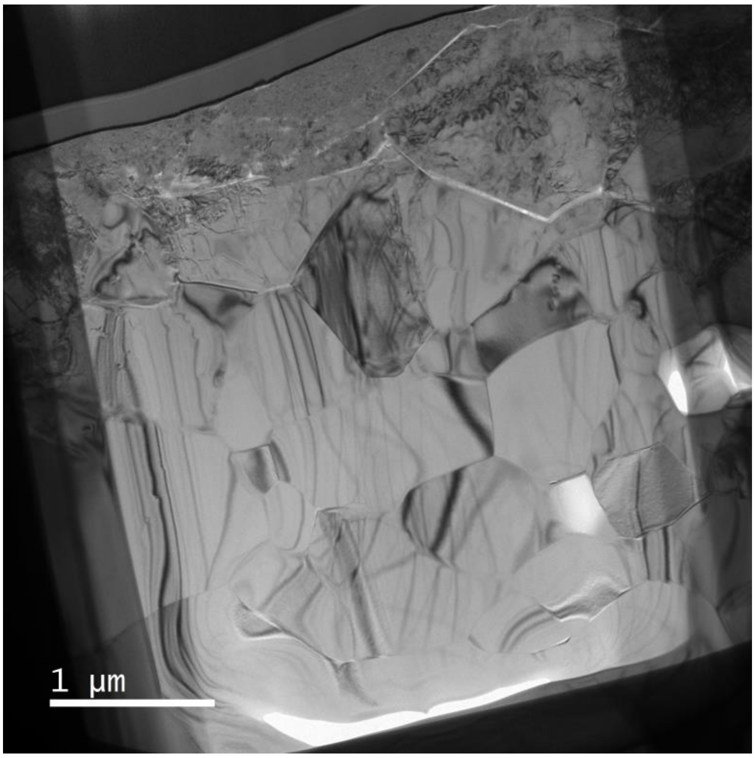

Figure 4.29: TEM image of FIB slice of $Sr_{0.90}Ti_{0.80}Nb_{0.20}O_3$ sample.

The image below (Figure 4.30) is a greater magnification of one of the grains in the above image. The red circles indicate the two areas from which the following diffraction patterns were produced (Figure 4.31). The darker area with the circle numbered 07 is on axis with the electron beam and clearly shows the cubic structure of the perovskite. The second circle labelled 08 is tilted off axis away from the beam and shows other directional planes within the crystal lattice. For clarity, the sample was not tilted in order to achieve the second diffraction pattern, this is just orientation variation within the sample itself. This is also evidenced from the changing brightness of the diffraction spots, the brightest spots being closer to the central axis of the beam. This is typical for a polycrystalline material.

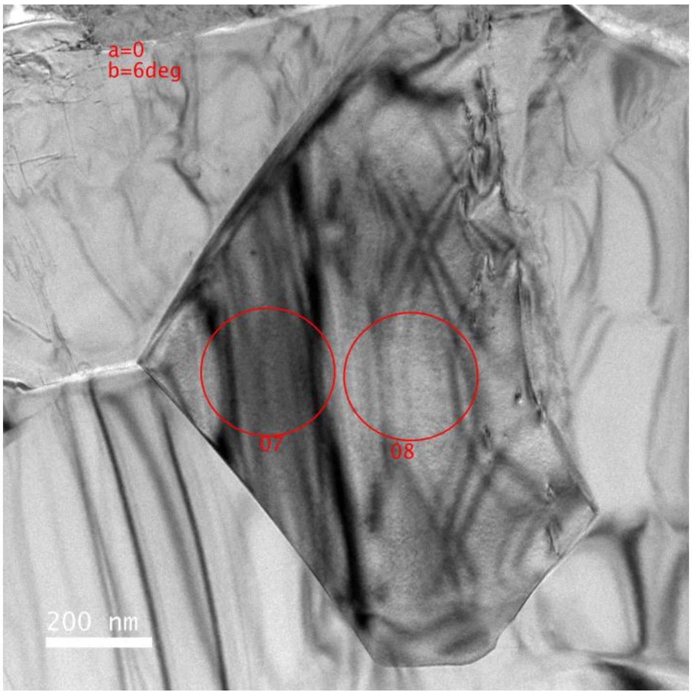

Figure 4.30: TEM image of $Sr_{0.90}Ti_{0.80}Nb_{0.20}O_3$ sample, 07 red circle refers to left diffraction pattern below and 08 circle refers to right diffraction patter in Figure 4.31.

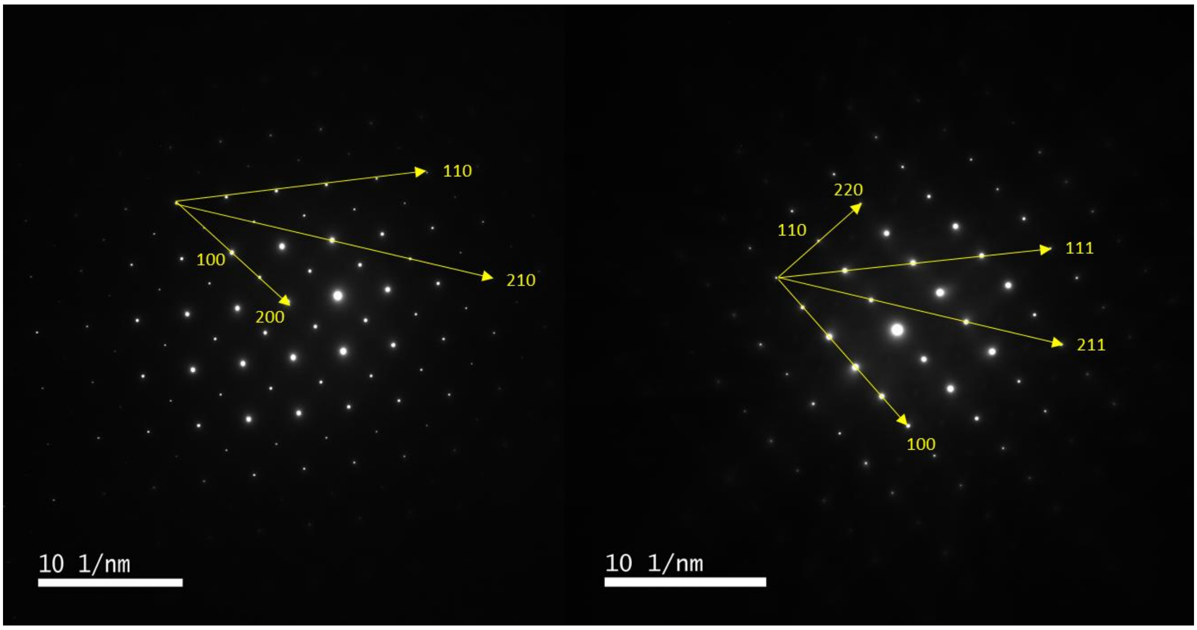

Figure 4.31: TEM diffraction patterns of $Sr_{0.90}Ti_{0.80}Nb_{0.20}O_3$ sample and measurements identifying crystal miller indices, left image is 07 area, right image is 08, from above.

In order to assign the diffraction patterns above to the relevant miller indices for the material, the scale bar was calibrated in the software ImageJ, and an average distance between diffraction spots taken by dividing the overall distance by the number of spots, and then inverted due to the pattern being created in inverse space. This number was then compared to a 5 % variance in the d-spacing of the XRD peaks for the same material due to a 5 % error in the accuracy of the TEM and allocated to the relevant peaks (Table 4-4). The only plane not to fit precisely within the 5 % error of the XRD d-spacings was the diffraction pattern for the (210) peak, which coincidentally was of very low intensity in the XRD data, as previously discussed, resulting in a potentially inaccurate XRD d-spacing value to begin with.

Table 4-4: Table of TEM diffraction pattern d-spacings and XRD peak assignment for $Sr_{0.90}Ti_{0.80}Nb_{0.20}O_3$ sample.

XRD peak	XRD d-spacing (Å)	5% variance in XRD (Å)	TEM d-spacing (Å)
(100)	3.891	3.696 – 4.085	4.015
(110)	2.760	2.622 – 2.898	2.848
(111)	2.256	2.143 – 2.369	2.337
(200)	1.955	1.858 – 2.053	2.011
(210)	1.749	1.661 – 1.836	1.651
(211)	1.598	1.517 – 1.677	1.629
(220)	1.384	1.315 – 1.453	1.429

The TEM diffraction patterns showed no evidence of two separate cubic unit cell sizes which encouraged a second look into the XRD data, revealing the cause to be recurrent kα2 peaks. It is of course noted that with this technique only a handful of grains/unit cells are examined in detail which is not necessarily a complete picture of the material as a whole.

4.2 Electrical Characterisation

Frequency dependent measurements highlight contributions from the bulk, grain boundaries and electrode effects[108]. Impedance measurements are often taken across a range of temperatures in order to highlight all of these effects because experimental frequencies are limited to a particular chosen range. One of the main pieces of information to determine from electrical measurements is whether the bulk electrical response is due to long range conductivity mechanisms or short range dipole relaxations[108]. Gerhardt identifies possible ambiguity in the fact that localised and delocalised conduction are both bulk processes which can result in the same capacitance[108]. So, in order to better interpret the data in this work plots of impedance, electric modulus (hereafter referred to as modulus) and permittivity (including tan δ) data will be examined in order to better understand the electrical mechanisms taking place. Gerhardt suggests that ionically conducting materials are generally best represented by impedance/modulus analysis because long range conductivity is the dominant mechanism in these materials, whereas dielectric materials are best assessed by permittivity and loss data analysis because localised relaxation mechanisms dominate. However, an issue arises if a material has both mechanisms occurring. A major question is how to identify when a localised relaxation mechanism ends, and long range conductivity takes over or vice versa. This can be difficult to answer because both of these phenomena are bulk effects which are proportional to the geometrical capacitance of the material and it is important to note that some mechanisms can be overshadowed by dominating factors for example resistance, therefore it is important to use all techniques combined to see the bigger picture.

Impedance measurements of all samples were taken on a Solartron analytical impedance analyser with a frequency sweep of 1MHz to 100 mHz at 1V between 100-600 °C. Complex impedance plots are representative of the most resistive contributions of the sample. In this case it is the higher temperatures that often result in complete or near complete semi-circles in impedance analysis. These semi-circles are representative of relaxation processes and the size and shape relates to the strength and type of the relaxation process at the experimental frequencies[108]. Temperatures above 150 °C are typically used to analyse ionic conductivity and analysis of dielectrics are carried out at temperatures below 25 °C. This is because above room temperature DC ionic conductivity effects take over and mask any AC relaxations[108]. AC measurements taken at intermediate temperatures make it possible to differentiate between localised defect relaxations from long range conductivity[108]. The presence of any electronic semiconductivity could also be hidden by resistive components that dominate the imaginary part of impedance[100].

Impedance data is dominated by the circuit element with the greatest resistance, and this can often overshadow other effects that are happening within a material, as discussed in the Research Methodology chapter, particularly for room temperature measurements. As such, plotting electric modulus alongside impedance plots can be informative. Electric modulus is said to be dominated by conductivity contributions and the smallest capacitances of a material[109] as the height of each peak is proportional to 1/C for each RC element[110]. Modulus data (M′/M″) can be effective at supressing grain boundary and electrode effects and provides more information about grain effects. This is because the capacitance of the grain boundary is orders of magnitude larger than that of the grains[111]. Peaks in a plot of M″ vs frequency are due to the grain response as the peaks representing the grain boundary are too weak to be resolved[109]. Modulus measurements can be a good way of estimating the migration and association enthalpies of defect complexes in a way that is not possible using impedance data alone[111], such as ion hopping rate and relaxation times[112].

When examining localised and delocalised conduction, both are bulk processes and result in the same capacitance, which can be difficult to interpret. Before being able to separate the difference between long range conductivity and localised relaxation mechanisms it is important to consider relaxation times (τ). Relaxation times can be calculated by the following Arrhenius equation[111]:

$$\tau = \tau_0 \exp\left(\frac{E_A}{kT}\right)$$

According to Gerhardt[108], “Each dielectric function has a relaxation of its own”, and these relaxation times are identified at different frequencies according to the function used to examine it[108]. For example, modulus (M*, M′ M″) appears at higher frequencies whereas complex permittivity (ε″) is seen at the lower frequencies. The general order in frequency of appearance provided by Gerhardt is (where ε is permittivity, γ is admittance, Z is impedance and M is electric modulus):

$$\tau_{\varepsilon} \geq \tau_{\gamma} > \tau_{\tan\delta} > \tau_{Z} > \tau_{M}$$

Whereby a peak in permittivity is normally found at the lowest frequencies and a peak in electric modulus appears at the highest frequencies. For example a peak in complex permittivity is normally not found in the experiment at the same time as a peak in complex Modulus (M″) at the same temperature because the range of frequencies to incorporate both is not large enough[108]. However, relaxation times examined by Z″ and M″ functions appear at similar frequencies so can be plotted together, hence the creation of Z″/M″ plots as a way to attempt to distinguish when localised relaxation mechanisms are taken over by long range conductivity mechanisms. Relaxation ratios ($r=\varepsilon_s/\varepsilon_\infty$) reflect the strength of a relaxation mechanism, and it can also be used as a way to estimate how close or far apart peaks that are plotted together will be. It is stated that a relaxation ratio of 200 is enough to lead to overlapping peaks and this is due to long range conductivity mechanisms[108]. However localised relaxation mechanisms result in a small relaxation ratio and separate Z″/M″ peaks.

In this analysis, rather than attempt to model impedance spectra with a complex equivalent circuit, representative information for each contribution will be extracted by analysing features of the spectra (e.g. local maxima in the imaginary components of impedance and modulus by referring to the behaviour of a single RC element. For a parallel combination of a capacitor (*C*) and resistor (*R*), the complex impedance (*Z**) is given by[99]:

$$Z^* = \frac{1}{\left(\frac{1}{R}+\frac{1}{-\frac{j}{\omega C}}\right)} = \frac{1}{\left(\frac{1}{R}+j\omega C\right)} = \frac{R}{1+j\omega CR} = \frac{R-j\omega CR^2}{1+\omega^2C^2R^2}$$

Where ω is the angular frequency and j is the square root of -1. Separating into real and imaginary parts gives:

$$Z' = \frac{R}{1+\omega^2C^2R^2} \quad \text{and} \quad Z'' = -\frac{\omega CR^2}{1+\omega^2C^2R^2}.$$

The complex electric modulus (*M**) is given by:

$$M^* = j\omega C_0 Z^*$$

where C_0 is the cell constant ($= \varepsilon_0 \frac{sample\ area}{sample\ thickness}$)

The real and imaginary parts are thus:

$$M' = \frac{\omega^2 C R^2}{1+\omega^2 C^2 R^2} C_0 \quad \text{and} \quad M'' = \frac{\omega R}{1+\omega^2 C^2 R^2} C_0$$

When plotting Z'' and M'' as a function of frequency, a peak in their behaviour often lies in the experimental range as discussed and this can be interpreted by finding the peak functions and their characteristic frequencies. Solving $\frac{dZ''}{d\omega} = 0$ and $\frac{dM''}{d\omega} = 0$ for ω, gives $\omega_0 = 1/(RC)$, which when substituted back into equations above for Z″ and M″ gives:

$$Z''_{max} = \frac{R}{2} \quad \text{and} \quad M''_{max} = \frac{C_0}{2C}.$$

4.2.1 Complex Impedance Analysis

Equivalent electrical circuit fitting was carried out on the impedance graphs that were produced using MTS Modulab software. The x-intercept resistance value (R) of each component part of the graph, be it grain or grain boundary when separate (Figure 4.32), was recorded alongside the temperature at which the measurement was taken as a separate Arrhenius plot (R1/R2 etc).

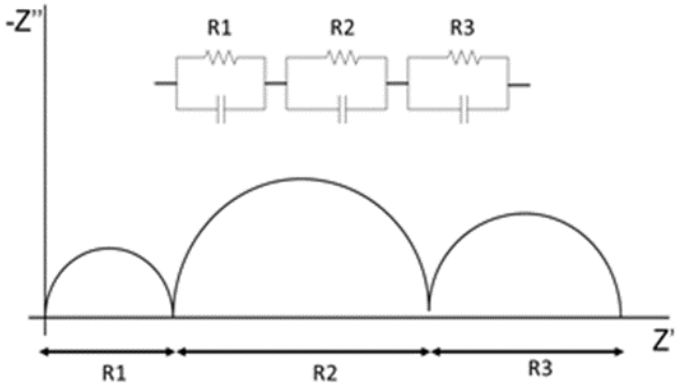

Figure 4.32: Illustration of resistance measurement from impedance data[99].

Using these values and the pellet dimensions, values for sample resistivity could be calculated. The inverse of this data was used to produce an Arrhenius plot of the natural log of conductivity vs 1/T. This was achieved by the below equations (where A is electrode area, L is pellet thickness and R is resistance):

$$Conductivity\ (\sigma) = Resistivity^{-1}$$

$$Resistivity = \frac{RA}{L}$$

From these graphs it was possible to extract a range of information including relative conductivities and activation energy of conduction mechanisms from the following equation[99]:

$$ln\sigma = ln\sigma_0 - \frac{E_A}{K_B T}$$

Conductivity graphs were made from the cooling data of experiments, so as not to be misled by any effects from the liberation of trapped charge carriers during the heating cycle. This information can help to paint an initial picture of the behaviour of the chemical defects within each sample under this specific electrical environment and temperature range and also provides a simple way of comparing the relative conductivities of each sample. It is noted that on most occasions the impedance plots at low to intermediate temperatures do not actually meet the x-axis in perfect semi-circles as shown above in Figure 4.32, but as circuit fitting software was used the information provided can be interpreted as largely correct, whilst handled with caution. This data is provided knowing that the later more in-depth analysis of the impedance and modulus data is a more accurate way to interpret the defect species behaviour.

4.2.1.1 Non-Stoichiometric $SrTiO_3$

Impedance measurements were taken, and the corresponding Arrhenius conductivity plots created in order to build a picture of the effects of excess and deficient Sr/Ti ratios on conductivity behaviour. Figure 4.33 below shows the natural log of conductivity vs 1/T graphs for the non-stoichiometric $SrTiO_3$ samples and undoped $SrTiO_3$. The first observation is that the plots for the two impedance contributions R1 (square markers) and R2 (circle markers) are the same shape as the two seen for undoped $SrTiO_3$ plot (black markers). This shows that the same mechanisms of the same species are likely taking place across all samples. The main difference between the Sr-deficient (left) and Sr-excess samples (right) is that the Sr-deficient samples are generally more conductive than undoped $SrTiO_3$, being higher up the y-axis, but that there is no significant difference in conductivity between each of the individual Sr-deficient samples themselves; the plots overlay each other. However, when examining the Sr-excess graph, there is a wider distribution in the conductivity between each of the Sr-excess samples. This indicates that the variation of Sr as an excess in $SrTiO_3$ has a greater impact on conductivity than an excess of Ti (/Sr deficiency).

Activation energies extracted from the gradient of the plots as described above, can be used to help to identify the conduction mechanism occurring. As shown below in Table 4-5, the activation energy of the R1 component for the Sr-deficient samples is approximately 0.8 eV, as is that for undoped $SrTiO_3$, whereas the activation energy for the R1 of the Sr-excess samples is approximately 1 eV. According to literature [113] both of these values relate to the diffusion of doubly-ionised oxygen vacancies and bulk contribution to conduction in $SrTiO_3$ by Abrantes (0.9 eV)[98]. The slight difference between the two values for Sr-excess and deficient samples suggests the barrier height for this mechanism to occur is slightly higher in the Sr-excess samples due to the higher activation energy. There are two different R2 values for all samples due to a change in gradient at approximately 300 °C, presumably caused by a change in conduction mechanism, and as such separate activation energies were calculated. R2 values for all samples between 600-300 °C are approximately 1.7-1.8 eV, which matches the activation energy data for the grain boundary contribution found by Abrantes 2000[98] for polycrystalline $SrTiO_3$ (1.7 eV). The exception is the 1.020 Sr-excess sample which has a slightly lower activation energy for R2 between 600-300°C (1.4 eV). Jose et al.[113] attribute this value to the movement of electrons ionised from Sr vacancies but this seems unlikely as this sample has the largest amount of excess Sr. In the paper by Abrantes there is no change in gradient for the R2 value with temperature as there is in this thesis, however their impedance measurements ceased at 300 °C and this observation is noted between 300-100 °C. The strange observation in this sample set is the slightly negative activation energy (positive gradient) for the lower temperature section of the R2 plots. This could be explained by proton conduction[100]. The numbers are so low, however, that the error in them could be such that they could be slightly positive numbers or even zero.

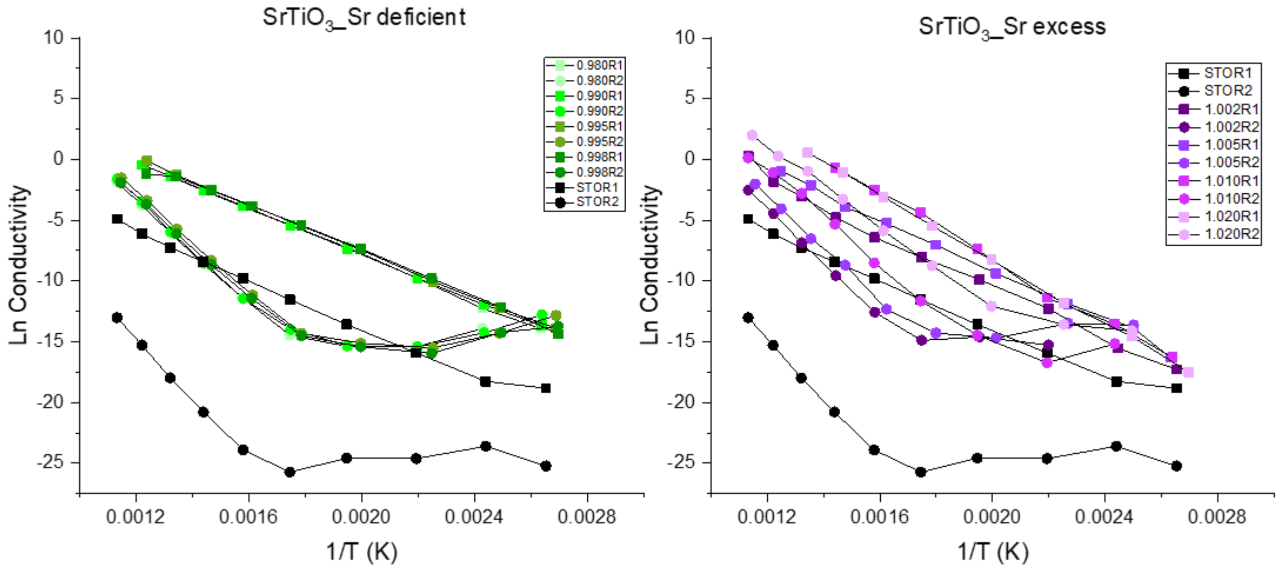

Figure 4.33: Graph of the natural log of conductivity vs 1/T for Sr excess and deficient samples.

Table 4-5: Activation energies of non-stoichiometric $SrTiO_3$ samples.

Sample	**R1 E_A (eV) 600-100°C**	**R2 E_A (eV) 600-300°C**	**R2 E_A (eV) 300-100°C**
$SrTiO_3$	0.82	1.84	0.07
0.980	0.83	1.79	-0.06
0.990	0.81	1.77	-0.13
0.995	0.82	1.74	-0.14
0.998	0.80	1.71	-0.10
1.002	0.95	1.78	0.23
1.005	0.92	1.69	-0.12
1.010	1.14	1.70	0.13
1.020	1.15	1.45	0.63

4.2.1.2 A-Site Vacancy Compensation of Donors

$Sr_{1-x/2}Ti_{1-x}Nb_xO_3$

Below in Figure 4.34 is the conductivity plot for the $Sr_{1-x/2}Ti_{1-x}Nb_xO_3$ sample set. As can be seen the shapes of the plot for each sample mostly again resemble those of $SrTiO_3$, with two R values and a change in gradient for the R2 values at approximately 300 °C. The resistivity of the R1 components of samples Nb_x=0.20-0.30 rises with increasing dopant content, whereas the R2 element decreases in resistivity as dopant increases but only slightly and the difference is barely discernible. Surprisingly the conductivity of samples, despite the large addition of the donor dopant Nb, is similar to that of undoped $SrTiO_3$.

The activation energies for the R1 component of these samples (approx. 0.2-0.3 eV) relates to electron or hole transport through the samples, as does the low temperature range for the R2 component for all doped samples. The high temperature range for the R2 components has values of approx. 1.6-1.7 eV which again could relate to data for the grain boundary contribution found by Abrantes 2000[98] for polycrystalline $SrTiO_3$ (1.7 eV).

The anomaly to the above description is the Nb_x=0.10 sample which only has one R plot, which changes gradient at 300 °C. As it is normally the R2 plots that observe a gradient change with temperature it could be that the R1 plot for Nb_x=0.10 is actually the same conduction mechanism as the R2 plots in the other samples, and that the R1 mechanism is missing or shielded. The activation energies for the R1 plot also match those of the other R2 values, which is further evidence that the same conduction mechanism as R2 is occurring. If the R1 and R2 components are the grain and grain boundary contributions of each sample, then the more conductive plot of R1 is likely to be the grain contribution, and the lower more resistive contribution (R2) that of the grain boundary contribution. When analysing this data alongside the SEM images shown in Section 4.1.2.1, it can be seen that the Nb_x=0.10 sample has very small abnormal grains (Figure 4.21), which could mean a dominating average grain boundary contribution as opposed to a grain contribution, which matches the observation above. The Nb_x=0.15 sample is also slightly anomalous with an R1 plot that only exists between 600-300 °C and has the same activation energy as that seen in the high temperature window of R2 for the other samples.

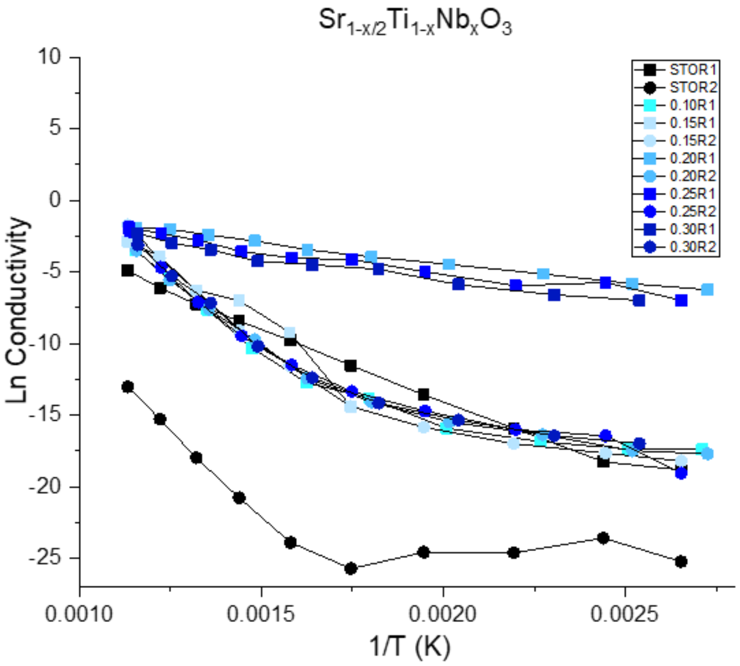

Figure 4.34: Graph of the natural log of conductivity vs 1/T for $Sr_{1-x/2}Ti_{1-x}Nb_xO_3$ samples.

Table 4-6: Activation energies for conduction mechanisms of $Sr_{1-(x/2)}Ti_{1-x}Nb_xO_3$ samples.

Sample	R1 E_A (eV) 600-300°C	R1 E_A (eV) 300-100°C	R2 E_A (eV) 600-300°C	R2 E_A (eV) 300-100°C
$SrTiO_3$	0.82		1.84	0.07
$Sr_{0.950}Ti_{0.90}Nb_{0.10}O_3$	1.72	0.32	-	
$Sr_{0.925}Ti_{0.85}Nb_{0.15}O_3$	1.53	-	1.77	0.28
$Sr_{0.900}Ti_{0.80}Nb_{0.20}O_3$	0.25		1.61	0.34
$Sr_{0.875}Ti_{0.75}Nb_{0.25}O_3$	0.27		1.56	0.48
$Sr_{0.850}Ti_{0.70}Nb_{0.30}O_3$	0.28		1.68	0.34

$Sr_{0.9}Ti_{1-x}Nb_xO_3$

Below is the conductivity graph for the $Sr_{0.9}Ti_{1-x}Nb_xO_3$ sample set. The $Sr_{0.90}Ti_{0.80}Nb_{0.20}O_3$ sample from the $Sr_{1-x/2}Ti_{1-x}Nb_xO_3$ sample set is included as a reference (blue markers) as it also has a Sr concentration of x=0.90. This sample is a good comparison to the $Sr_{0.90}Ti_{0.81}Nb_{0.19}O_3$ sample for the effect of decreasing the Nb content whilst maintaining the same Sr concentration to explore the charge compensation scheme at play in the A-site vacancy sample sets. It was found from XRD data (Figure 4.11) that there is not enough Nb present to electrostatically compensate for the large concentration of Sr vacancies in this sample set with the increasing Ti concentration, resulting in a secondary TiO_2 phase, also evidenced in the SEM images (Figure 4.25). As such this is presumably responsible for the increased number of R plots (or impedance semi-circles) for this sample set as the Nb content increases. Some will represent contributions from pure TiO_2 that are not in other sample sets, or even Nb-doped TiO_2. The samples with the excess TiO_2 phase in the XRD pattern (Nb_x=0.01 and Nb_x=0.005) (Figure 4.11) present more than the usual two R plots per sample (Table 4-7). It is noted that the R2 components of the samples do not have the same acute gradient change observed in undoped $SrTiO_3$ at approximately 300 °C but show a more gradual curved line. The resistivity seems to increase with decreasing Nb content for the samples Nb_x=0.10-0.01 for both the R1 and R2 plots. The Nb_x=0.19 and 0.15 samples have only R1 components, but that again resemble R2 components as seen in the above set for the $Sr_{0.95}Ti_{0.90}Nb_{0.10}O_3$ sample.

The activation energies show similar values to other samples with the exception of the R4 component of the $Sr_{0.9}Ti_{0.995}Nb_{0.005}O_3$ sample which had a value of approximately 2 eV.

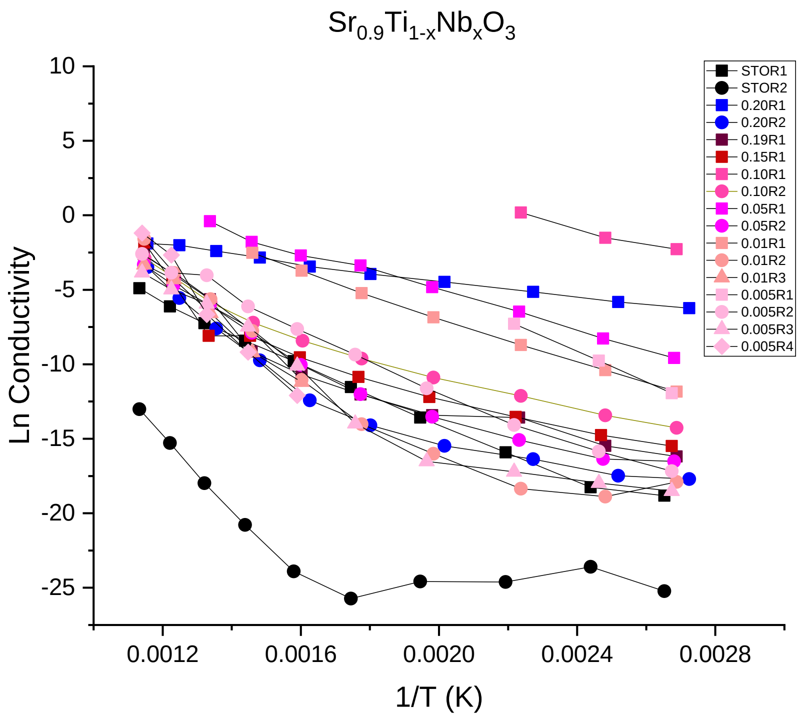

Figure 4.35: Graph of the natural log of conductivity vs 1/T for $Sr_{0.9}Ti_{1-x}Nb_xO_3$ samples.

Table 4-7: Activation energies for conduction mechanisms of $Sr_{0.9}Ti_{1-x}Nb_xO_3$ samples.

$Sr_{0.9}Ti_{1-x}Nb_xO_3$	R1 E_A (eV) 600-300°C	R1 E_A (eV) 300-100°C	R2 E_A (eV) 600-300°C	R2 E_A (eV) 300-100°C	R3 E_A (eV) 600-300°C	R3 E_A (eV) 300-100°C	R4 E_A (eV) 600-300°C	R4 E_A (eV) 300-100°C
$SrTiO_3$	0.82		1.84	0.07	-		-	
$Sr_{0.90}Ti_{0.80}Nb_{0.20}O_3$	0.25		1.61	0.34	-		-	
$Sr_{0.90}Ti_{0.81}Nb_{0.19}O_3$	1.37	0.38	-		-		-	
$Sr_{0.90}Ti_{0.85}Nb_{0.15}O_3$	1.15	0.44	-		-		-	
$Sr_{0.90}Ti_{0.90}Nb_{0.10}O_3$	0.47		0.92	0.44	-		-	
$Sr_{0.90}Ti_{0.95}Nb_{0.05}O_3$	0.57		1.21	0.44	-		-	
$Sr_{0.90}Ti_{0.99}Nb_{0.01}O_3$	0.65		1.69	0.40	1.6	-	-	
$Sr_{0.90}Ti_{0.995}Nb_{0.005}O_3$	-	0.57	0.95	0.67	1.38	0.24	2.16	-

4.2.1.3 B-site Nb-Doped $SrTiO_3$

Below is the conductivity graph for the $SrTi_{1-x}Nb_xO_3$ sample set. The $SrTi_{0.998}Nb_{0.002}O_3$ sample is the most resistive Nb-doped sample, falling between the two $SrTiO_3$ R plots. This was expected as it was thought that small levels of donor dopant Nb would annihilate any holes present without donating a large number of electrons, resulting in a higher resistivity. The conductivity begins to rise significantly with only small increases in Nb after this; the x=0.005, x=0.010 and x=0.020 samples being the most conductive by up to ten times in comparison to undoped $SrTiO_3$. This is in contrast to the work by Drozdz[62] (Figure 4.37) displaying results for similar samples which show $SrTiO_3$ to be the most conductive sample, with rising resistivity with increasing Nb dopant. The Sr-vacancy compensated materials as discussed earlier appear to have greater resistivity than the majority of these B-site Nb-doped $SrTiO_3$ samples, despite having up to ten times the amount of Nb-doping, or more in some cases, indicating that the Sr vacancies in that sample set are key to reducing conductivity in Nb-doped $SrTiO_3$.

The shape of the R1 and R2 plots for each of the B-site doped samples are similar to those of undoped $SrTiO_3$ with the exception that most of the R2 plots only exist between 600-300 °C. The R1 plot for the Nb_x=0.005 sample appears to be the most anomalous in that it is the most conductive despite being in the middle of the sample/dopant composition window. In the Nb$_x$=0.005-0.020 samples there were up to three impedance semi-circles present (R plots) indicating three RC circuit contributions. There is only one R plot for the most resistive Nb$_x$=0.002 sample. This difference indicates that the initial theory of very small levels of Nb "mopping up" charge carriers without contributing significantly more charge carriers could hold true. As the Nb concentration increases the number of contributions to impedance increases, which represent charge carriers and their relaxation mechanisms. This is expected from the donor dopant behaviour of Nb with no compensation scheme. The activation energies for conduction for the $Sr_{1-x/2}Ti_{1-x}Nb_xO_3$ samples are also generally lower than the $SrTi_{1-x}Nb_xO_3$ samples.

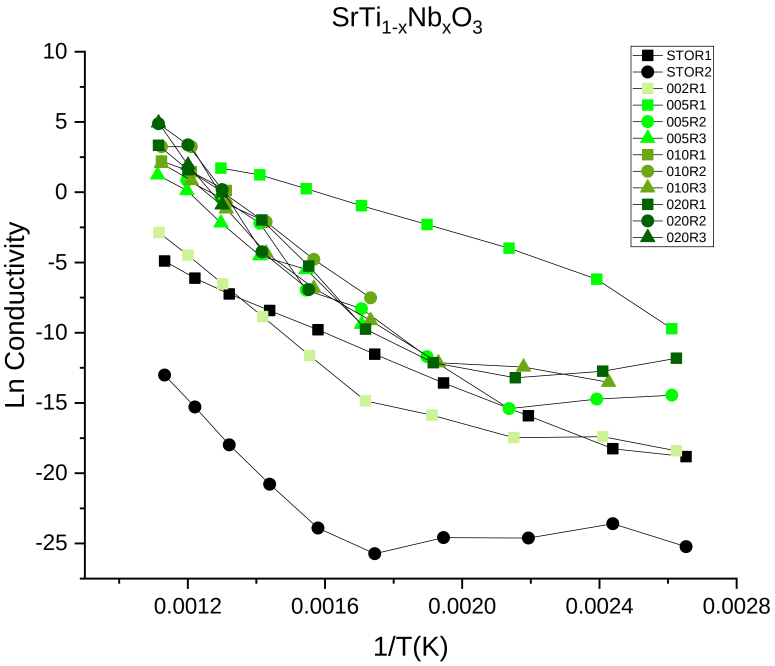

Figure 4.36: Graph of the natural log of conductivity vs 1/T for $SrTi_{1-x}Nb_xO_3$ samples.

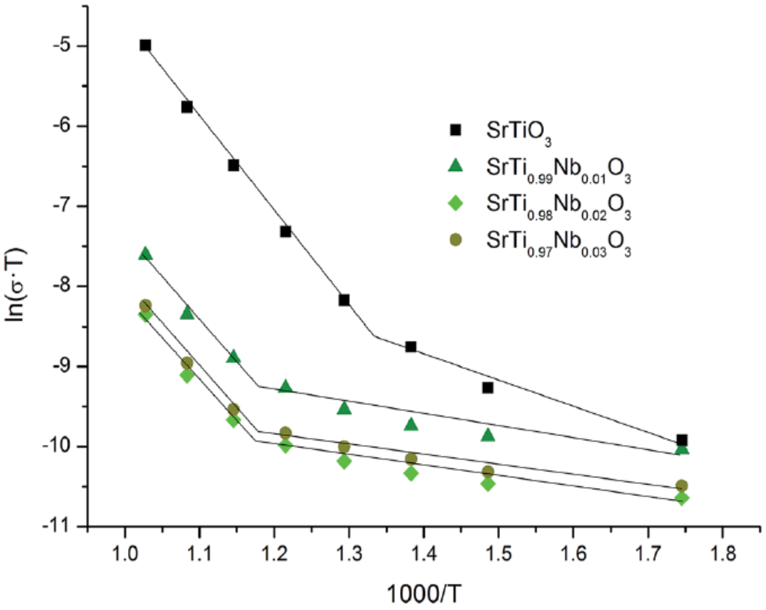

Figure 4.37: A conductivity graph taken from a 2017 paper by Drozdz for $SrTi_{1-x}Nb_xO_3$ samples [62].

Table 4-8: Activation energies for conduction mechanisms of $SrTi_{1-x}Nb_xO_3$ samples.

$SrTi_{1-x}Nb_xO_3$	R1Ea (eV) (600-300 °C)	R1Ea (eV) (300-100 °C)	R2Ea (eV) (600-300 °C)	R2Ea (eV) (300-100 °C)	R3Ea (eV) (600-300 °C)	R3Ea (eV) (300-100 °C)
$SrTiO_3$	0.82		1.84	0.07	-	-
0.002Nb	1.49	0.27	-	-	-	-
0.005Nb	0.71		1.61	0.27	1.51	-
0.010Nb	0.96	-	1.60		1.66	0.24
0.020Nb	1.74	0.05	2.46		2.70	

4.2.1.4 Acceptor-Doped $SrTiO_3$

Below are the conductivity graphs for the acceptor-doped $SrTi_{1-x}Mn_xO_3$ and $SrTi_{1-x}Co_xO_3$ sample sets (Figure 4.38). The colour of the markers for each sample darkens as the dopant amount increases. As can be seen, there are multiple R values in the low-Mn doped samples (Mn_x=0.01 and 0.02), and only one R value for the higher doped samples, indicating there is only one conduction mechanism occurring across all temperatures and frequencies measured, or that others are being shielded. It is thought that as the acceptor dopant increases and the conductivity of these samples rises significantly, one highly conductive mechanism will hide others, for example the movement of electrons or oxygen vacancies. Interestingly the R1 circuit element from the Mn_x=0.01 sample is actually more resistive than the R1 component of undoped $SrTiO_3$ at low temperatures (between 100-200 °C).

As can be seen again, there are two R values in the low-Co doped samples (Co_x=0.01 and 0.02), and only one R value for the higher doped samples (R1). In the case of the Co_x=0.01, 0.02 and 0.05 samples there is not much difference in the conductivity of some of the separate R plots per sample, (e.g. Co_x=0.02 R1/R2), yet two separate semi-circles were seen in the impedance data for these samples. This could mean that two separate mechanisms are happening but with similar activation energies. The activation energies for the conductivity data (Table 4-9 and Table 4-10) of the lower doped Mn/Co samples resembled those of oxygen vacancy activation energies (approx. 1 eV), and the activation energies of the higher-doped samples resembled that of electron/hole hopping (approx. 0.3-0.5 eV).

As can be seen from Figure 4.38 the Co-doped samples are more conductive than the Mn-doped samples. Both acceptor-doped sample sets are more conductive than the Nb-doped sample sets. It is of note that the acceptor-doped samples generally appear to have straight R1 plots, which in previous sample discussions correspond with conductive grain behaviour. This is in contrast to undoped $SrTiO_3$ and Nb-doped $SrTiO_3$ which all show either R1 *and* R2 components, *or* an R1 component very similar in behaviour to the R2 components with a gradient change at intermediate temperatures (basically an R2 component by another name). The activation energies for the highly-doped samples from both sets showed only R1 plots with activation energies of approximately 0.3-0.5 eV, showing the very conductive behaviour likely caused by an excess of electrons or holes in the samples[100]. The conductivity is so high in these samples that they will not be analysed in any greater detail in the next sections as the aim was to create samples that are as resistive as possible in order to be able to manipulate any defects that are present, and this is not likely to be possible with such conductive samples.

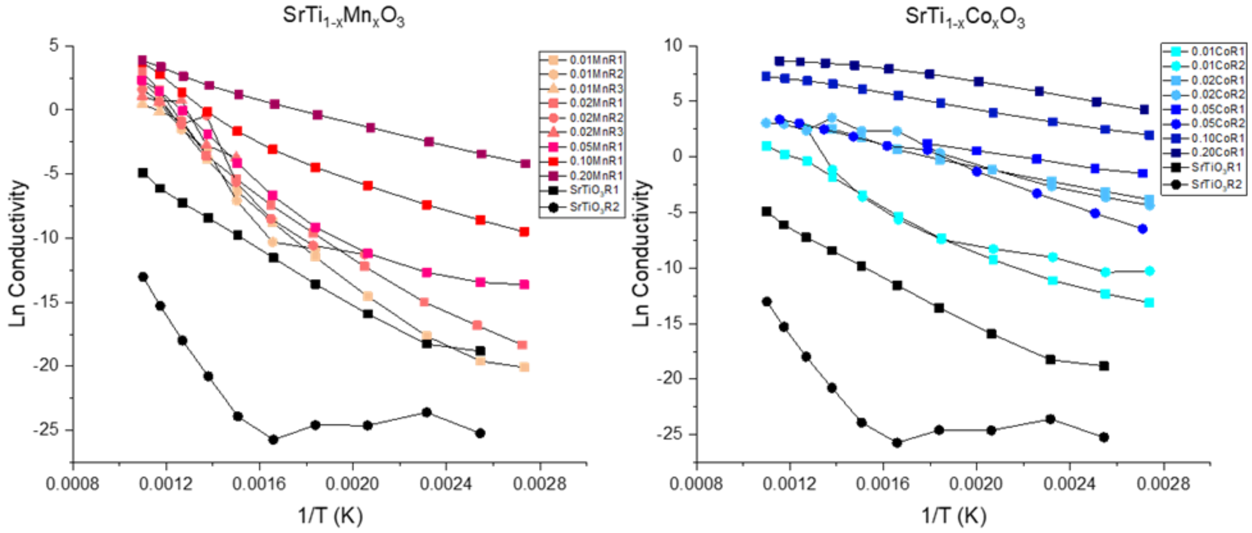

Figure 4.38: Graph of the natural log of conductivity vs 1/T for $SrTi_{1-x}Mn_xO_3$ and $SrTi_{1-x}Co_xO_3$ samples.

Table 4-9: Calculated activation energies from conductivity plots of $SrTi_{1-x}Mn_xO_3$ samples.

$SrTi_{1-x}Mn_xO_3$	**R1 E_A (eV) 600-300 °C**	**R1 E_A (eV) 300-100 °C**	**R2 E_A (eV) 600-300 °C**	**R2 E_A (eV) 300-100 °C**	**R3 E_A (eV) 600-100 °C**
$SrTiO_3$	0.82		1.84	0.07	-
0.01	1.22		1.61		1.22
0.02	1.11		1.31		1.14
0.05	1.37	0.43	-	-	-
0.10	0.69		-	-	-
0.20	0.41		-	-	-

Table 4-10: Calculated activation energies from conductivity plots of $SrTi_{1-x}Co_xO_3$ samples.

$SrTi_{1-x}Co_xO_3$	R1 E_A (eV) 600-300 °C	R1 E_A (eV) 300-100 °C	R2 E_A (eV) 600-300 °C	R2 E_A (eV) 300-100 °C
$SrTiO_3$	0.82		1.84	0.07
0.01	0.78		1.42	0.30
0.02	0.39		0.43	
0.05	0.26		0.55	
0.10	0.29		-	
0.20	0.25		-	

4.2.1.5 Oxygen Annealing

Sintered pellets of the $Sr_{1-x/2}Ti_{1-x}Nb_xO_3$ sample set (Nb_x=0, 0.10, 0.20 and 0.30) were placed in a tube furnace for approximately 9 hours purged with a supply of oxygen at a range of temperatures, ramp times and dwell times (Table 4-11): oxygen runs 1, 2 and 3 (blue, pink, green markers respectively). This was to determine if oxygen annealing would affect the concentration of oxygen vacancies in each sample and in turn affect the conductivity. Due to health and safety restrictions at the university, the oxygen supply to the furnace had to be switched off at the end of every day. As such the temperature at which the oxygen was switched off at varies in the table below according to the ramp rates and dwell times of the annealing run and the lowest temperature that was reached on cooling the furnace. This was done whilst still trying to ensure the oxygen was supplying the tube furnace for as long as possible while the samples were cooling. Impedance measurements were then taken of each of the pellets and conductivity plots were made in order to compare any changes to the conductivity following the oxygen annealing treatment (Figure 4.39). “Air” samples are the conductivity plots for the samples simply sintered as per the usual regime with no oxygen annealing treatment (red markers). It is noted that no colour change was observed to any of the pellets after any of the annealing runs.

From Figure 4.39, the conductivity plot for the $SrTiO_3$ samples show no significant difference between air sintering and those which were annealed in oxygen. There was no real pattern to the increase or decrease in conductivity across all sample compositions according to the oxygen annealing regime used. The difference to the conductivity plots for the Nb_x=0.10 samples was the introduction of the R1 mechanism peak (square markers) to the samples annealed in oxygen at low to medium temperatures, which was not present in the air sintered samples. It is noted from the SEM analysis (Figure 4.21) that the original air-sintered Nb_x=0.10 sample had bimodal grain growth with a large proportion of very small grains, it is possible that the annealing process afforded the smaller grains time to grow larger, affecting the impedance behaviour of the sample thus affecting the conductivity plots, but this was not confirmed. The Nb_x=0.20 and 0.30 samples displayed very similar shapes to the conductivity plots to the air-sintered samples. The only observable difference was to the low temperature end (350-100 °C) of the R2 impedance elements (circle markers), which show a dispersion between oxygen annealing regimes, but again there was no significant trend as to which annealing regime resulted in the least or most conductive samples. The R1 element for the Nb_x=0.20 and 0.30 samples appeared to show that samples from O_2 run 1 had the same conductivity as the air-sintered samples, both of which were less conductive than O_2 runs 2 and 3, and that the samples from O_2 run 3 were more conductive than O_2 run 2. This was surprising as it was hoped that the increased temperatures and lower cooling rates of O_2 runs 2 and 3 would decrease the oxygen vacancies in each sample, thus decreasing the conductivity. It could be possible that these observed differences are just due to minor sample differences and not as a result of the oxygen annealing process, in which case longer times and higher temperatures may be required. An effect of resistance to re-oxidisation was observed in Nb-doped $SrTiO_3$ samples by Slater et al. 1997[38] and was attributed to an oxygen transport issue in relation to high Nb-contents in dense ceramic samples. However in a paper by Maier and Randall the conductivity changes very little irrespective to annealing environment in Fe-doped $SrTiO_3$ due to the dominant charge carrier being “fixed by the dopant.”[114].

Table 4-11: Oxygen annealing regimes.

	Ramp (°C/hr)	Peak (°C)	Dwell (hrs)	Cool (°C/hr)	Temp. O_2 switched off
O_2 run 1	300	800	2	300	400
O_2 run 2	300	1000	2	300	300
O_2 run 3	600	1000	0.5	200	100

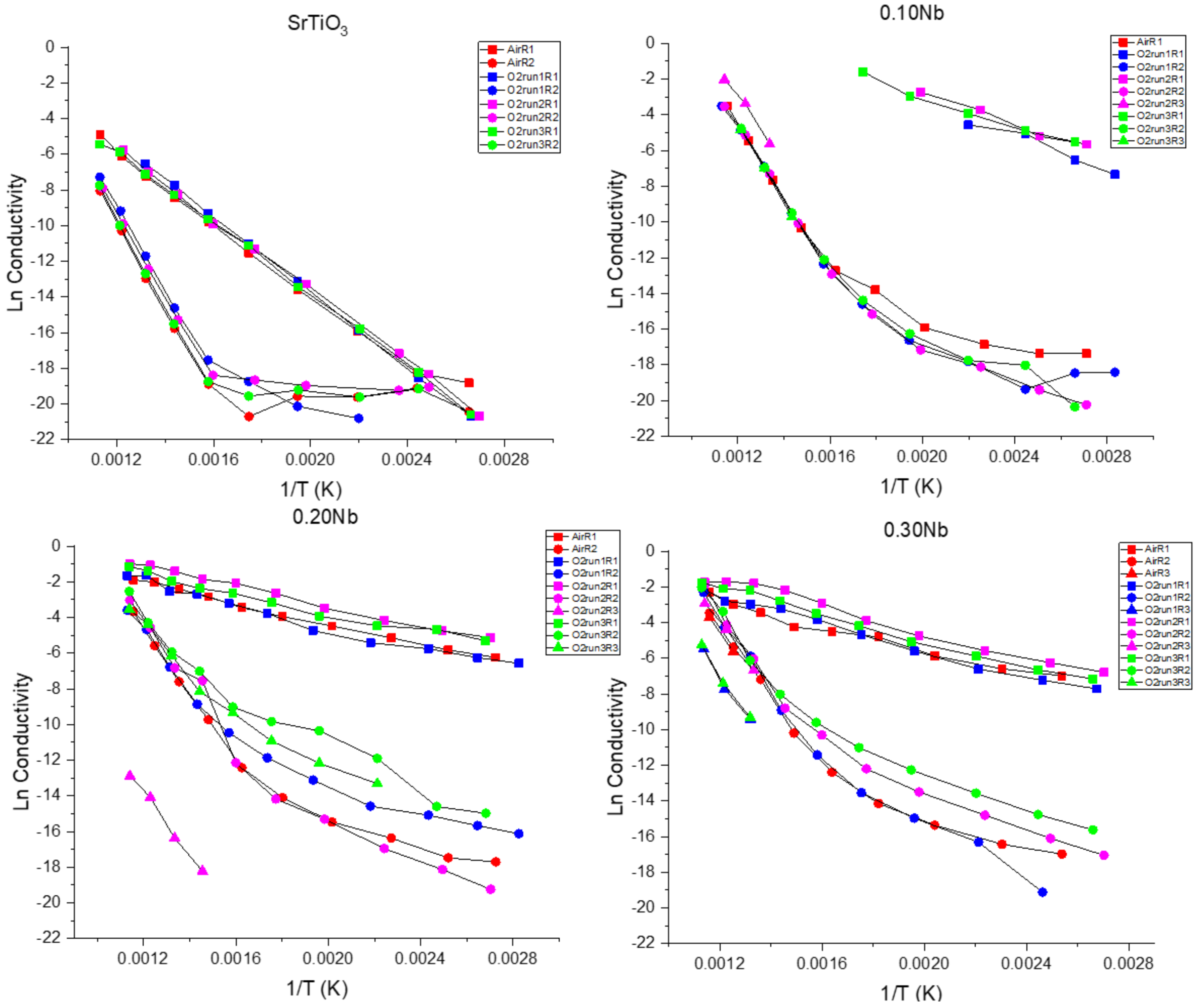

Figure 4.39: Ln Conductivity plots vs. 1/T for samples annealed in oxygen.

4.2.2 Bode Plot Analysis

4.2.2.1 $SrTiO_3$

Shown below is a series of Z″/M″ data plots for undoped $SrTiO_3$ (Figure 4.40). Each of the peaks are normalised to the maximum in the data set. The plots in the top row of graphs in the figure are the heating data, and the bottom row is the cooling data; equivalent temperatures are above and below one another. The green triangular markers represent the impedance data and the red square markers represent the modulus data. Combined plots of Z″/M″ were plotted with data as close to 100, 250, 400 and 550 °C where possible from the timed measurement loops within each experiment in order to compare mechanisms at similar temperatures across all samples. The normalised plots are on a log scale so as to best see any hidden minor Z″ peaks corresponding to the major M" peak. This will then indicate whether the M" and Z" peaks used later to calculate capacitance are from the same mechanism. The plots at 100 °C for $SrTiO_3$ (approx. 370 K) show no peaks and the plots appear close together. Gerhardt, when discussing TiO_2, attributes this to the current dissipation being minimal at this temperature[108]; the sample is very resistive. The plots at both 250 and 400 °C (520 and 670 K) show a single peak coinciding in both Z″ and M″, which move to higher frequencies with increasing temperatures. The plots for approximately 550 °C (820 K) show two peaks in both Z″ and M″ data; the major peak in Z″ overlapping the minor peak in M″, and vice versa, representing the bulk and grain boundary contributions to conductivity of $SrTiO_3$.

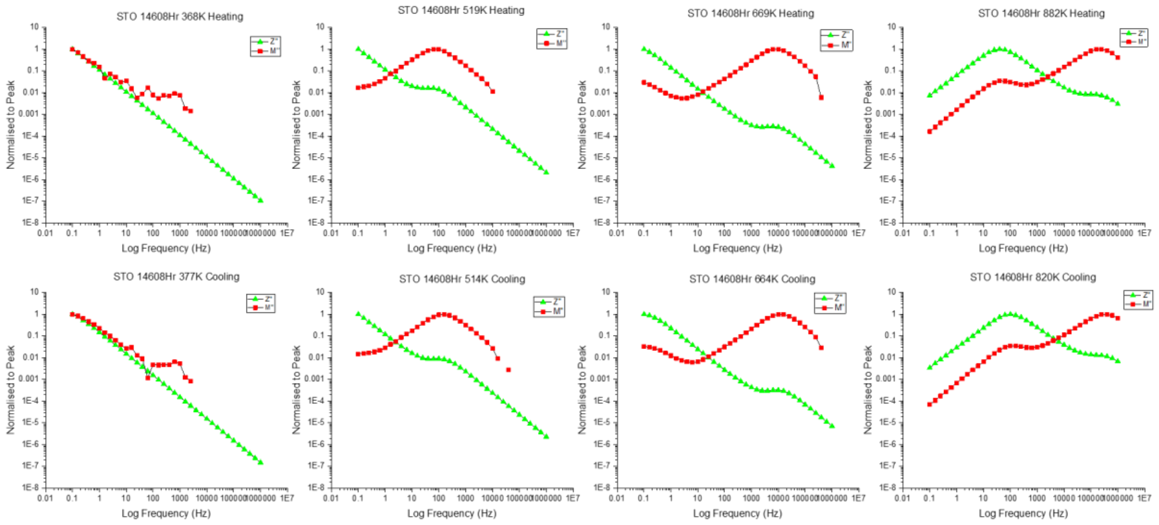

Figure 4.40: Normalised peaks of Z″ and M″ for $SrTiO_3$ on heating and cooling.

Figure 4.41 below shows the complex impedance plots for the cooling data of $SrTiO_3$. It shows large incomplete semicircles for the lower temperature measurements with the arcs decreasing in size and becoming complete with increasing temperature as conductivity increases. Common interpretation of complex impedance plots would suggest that the larger semi-circle represents the grain boundary element of the RC circuit for this sample, and the smaller semi-circle the grain contributions, which are better expanded upon with electric modulus analysis. There is a slight tail appearing on the end of some of the semi-circles which according to Gerhardt can be attributed to either grain boundary effects or the onset of DC conductivity[108].

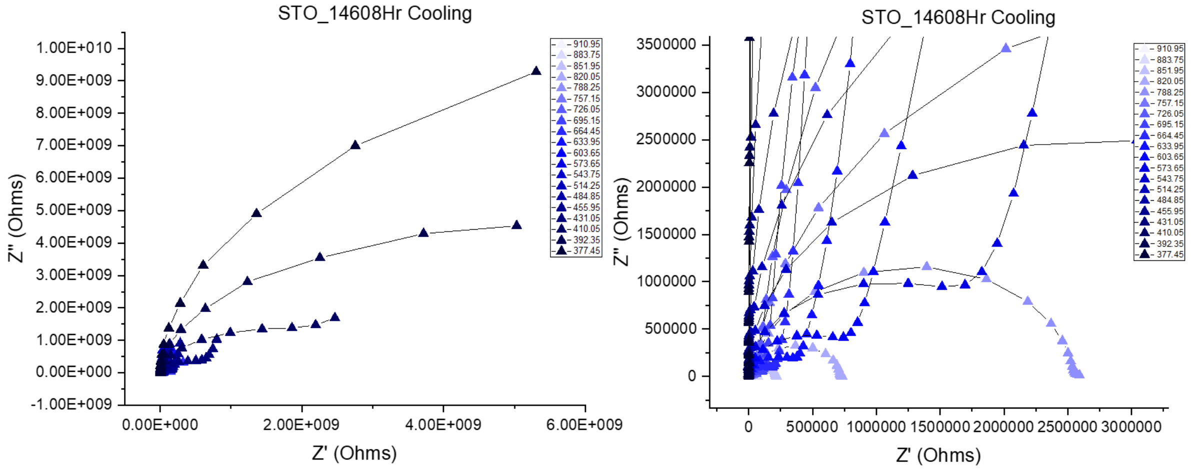

Figure 4.41: Complex impedance plots for cooling data of $SrTiO_3$ between 100-600 °C (380-900 K).

Figure 4.42 below represents the complex electric modulus plot for the cooling data of $SrTiO_3$ between 100-600 °C. The image on the right is a magnified image of the small semi-circle from the image on the left highlighted by a red circle. The two semi-circles indicate two relaxation processes. As noted in earlier descriptions of electric modulus, the largest contribution in this case is that of grain conductivity, and the smaller arc from the more resistive grain boundary contributions. The small semi-circle from the grain boundary contribution stops appearing on cooling in the lower temperature window between 360-100 °C.

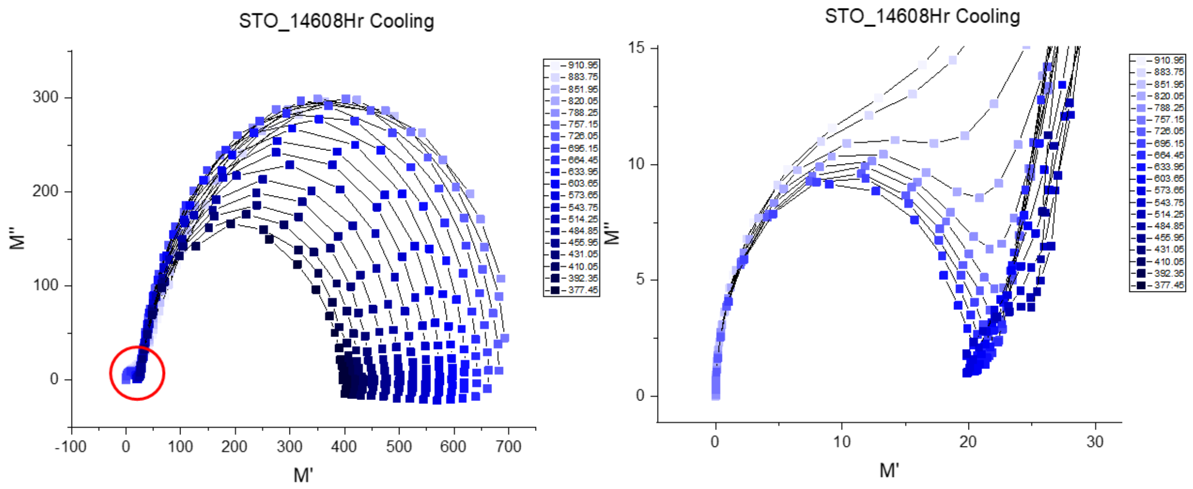

Figure 4.42: M′ vs. M″ for $SrTiO_3$ at temperatures of 100-600 °C (380-900 K).

Bode plots were produced of Log Z″ vs. Log frequency (Figure 4.43 below) for both heating and cooling data. The frequency at which the peak of Z″ occurred (ln f_{max} Z″) was taken for each temperature measurement for both heating and cooling data and an Arrhenius graph produced representing the activation energy of conduction relaxation mechanisms (Figure 4.44) from the following equation[47]:

$$f_{max} = f_o \exp\left(\frac{-E_a}{k_B T}\right)$$

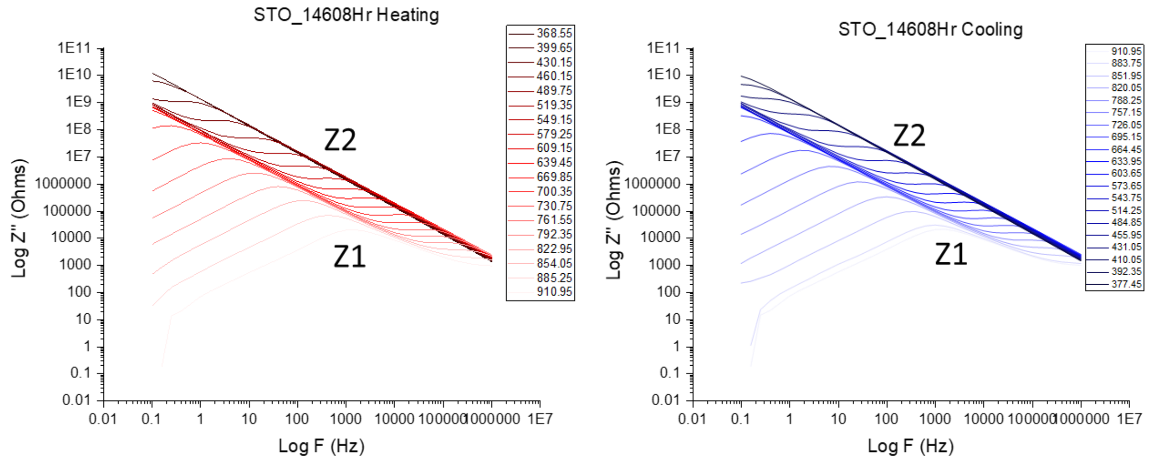

Figure 4.43: Frequency dependence of Log Z″ for $SrTiO_3$, heating and cooling between 100-600 °C.

The conductance Arrhenius graph produced from the $Z'' f_{max}$ data below shows two clear relaxation mechanisms (indicated by Z1/Z2 in Figure 4.43) occurring on both heating (H) and cooling (C) with very similar activation energies, indicating that the same relaxation mechanisms occurred through heating and cooling, at the same frequencies and temperatures. There was also no apparent change in the gradient of these relaxations, indicating the mechanisms did not change within these temperatures or frequencies.

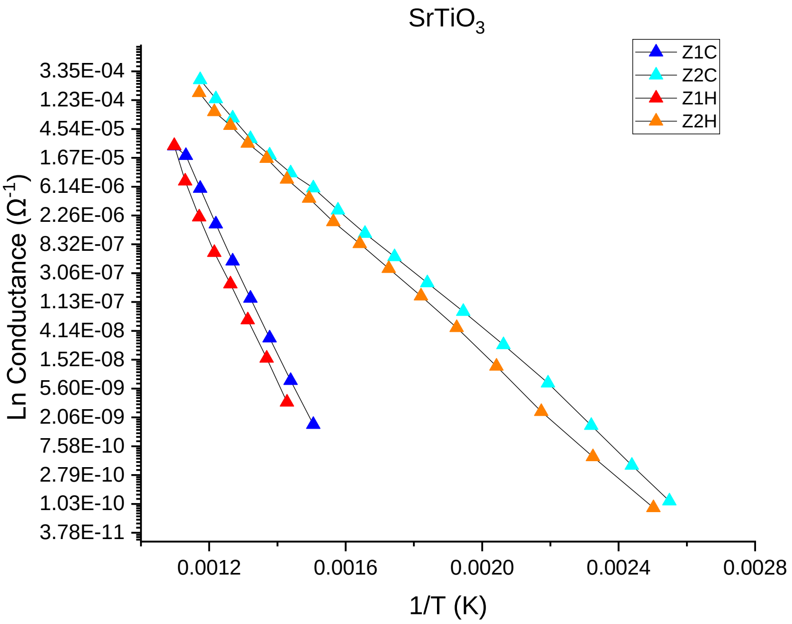

Figure 4.44: Conductance Arrhenius plot from $Z'' f_{max}$ data for $SrTiO_3$ heating (H) and cooling (C).

From the Z'' Bode plot above in Figure 4.43, it was then possible to plot capacitance vs. temperature for each sample by the following:

$$C = 1/(2\pi\, f_{max} R)$$

where $R = 2Z''_{max}$

The below capacitance data for undoped $SrTiO_3$ (Figure 4.45) is similar to that for $BaTiO_3$ in the paper by Irvine, Sinclair and West (1990)[30] which shows a temperature independent capacitance and a temperature dependent capacitance. The image on the right is a magnified version of the image on the left so as to best illustrate contributions with lower capacitances.

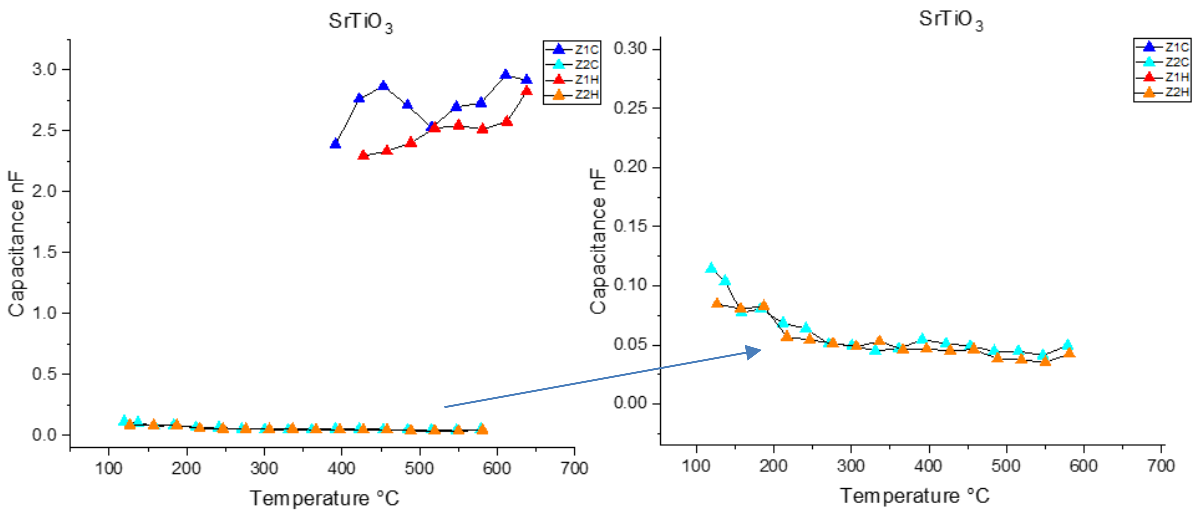

Figure 4.45: Capacitance vs temperature for $SrTiO_3$.

Table 4-12 below shows the activation energies and pre-exponential factor (σ_0) calculated for the relaxation mechanisms occurring from the Arrhenius conductance graph above (Figure 4.44). An approximate capacitance value for each mechanism is also displayed taken from Figure 4.45, and the temperature range over which each mechanism occurs.

Table 4-12: Calculated data for relaxation mechanisms from $Z''f_{max}$ data for undoped $SrTiO_3$.

Peak	**Peak Temp. Range (°C)**	**$Z''f_{max}$ Ea (eV)**	**Ln σ_0**	**Approx. Capacitance (nF)**
Z1C	600-400	2.11	16.60	3
Z2C	600-100	0.88	3.40	0.07

According to Jose et al. [113] who have assimilated activation energies from literature of $SrTiO_3$-based materials, the relaxation mechanisms shown in Figure 4.43 for the Z1C/H peaks (approx. 2.1 eV) relate to either the migration of Sr vacancies (approx. 2.8 eV) or the ionisation of electrons from Sr vacancies (approx. 1.5 eV):

$$V_{Sr}'' \leftrightarrow V_{Sr}' + e'$$

Unfortunately, the Z1 activation energy falls in the middle of these two values. The value for the Z1 peaks is a little different to that produced by Jose et al. but said paper relates to a Bi-doped $SrTiO_3$ Aurivillius phase so some variation may be expected. As identified in the complex modulus plot, the smaller semi-circle represents grain boundary contributions and stops appearing past approximately 400 °C. This is confirmed in Figure 4.45 and Table 4-12, identifying the smaller modulus semi-circle as relaxation mechanism Z1 extracted from imaginary impedance data. The relaxation mechanisms shown in this graph for the Z2 peaks for heating and cooling (approx. 0.9 eV) relate well to the diffusion of doubly ionised oxygen vacancies (approx. 0.7-1.2 eV). The energy barrier for the mobility of Ti vacancies is very high and unlikely to be seen in these experimental conditions[113]. Kolodiazhnyi, Blennow et al. and Waser [39], [115][45] all discuss the slow Sr-vacancy diffusion up to temperatures as high as 800 °C, and as such reaching an equilibrium could take considerably long times and high temperatures, so the act of moving the cation vacancies around the material structure may have its challenges. This supports the analysis that neither contribution is as a result of mobile cation species.

4.2.2.2 A-Site Vacancy Compensation of Donors

$Sr_{1-x/2}Ti_{1-x}Nb_xO_3$

Shown below is a series of normalised heating and cooling Z″/M″ plots for the $Sr_{0.95}Ti_{0.90}Nb_{0.10}O_3$ sample (Figure 4.46). Unlike the undoped $SrTiO_3$ sample, there is no Z″ peak in the graph measured at 250 °C. The Z″ peak is much broader when it appears in the 400 °C measurement suggesting an electrical heterogeneity, and moves to a higher frequency at 550 °C. The modulus data shows a small broad peak in the 400 °C plot which almost aligns with the Z″ peak but not quite, which indicates a localised relaxation mechanism of long-range interactions[101]. There is only one peak in both the M″ and Z″ data for this sample, in keeping with the previously presented modulus and impedance data for this sample. The behaviour of the Nb_x=0.10 sample could be attributed to the bimodal grain growth observed in the SEM analysis of the Nb_x=0.10 sample (Figure 4.21) and an overall electrical heterogeneity. A greater proportion of very small grains could lead to a much higher grain boundary contribution due to the greater ratio of grain boundaries to grain. The main difference in this sample compared to undoped $SrTiO_3$ is the M″ peak which has moved off the scale shown at high frequency, indicating the presence of a semi-conducting core. The blue colouration of the pellets also indicates the presence of Ti^{3+}, reduced from Ti^{4+} by an excess of electrons.

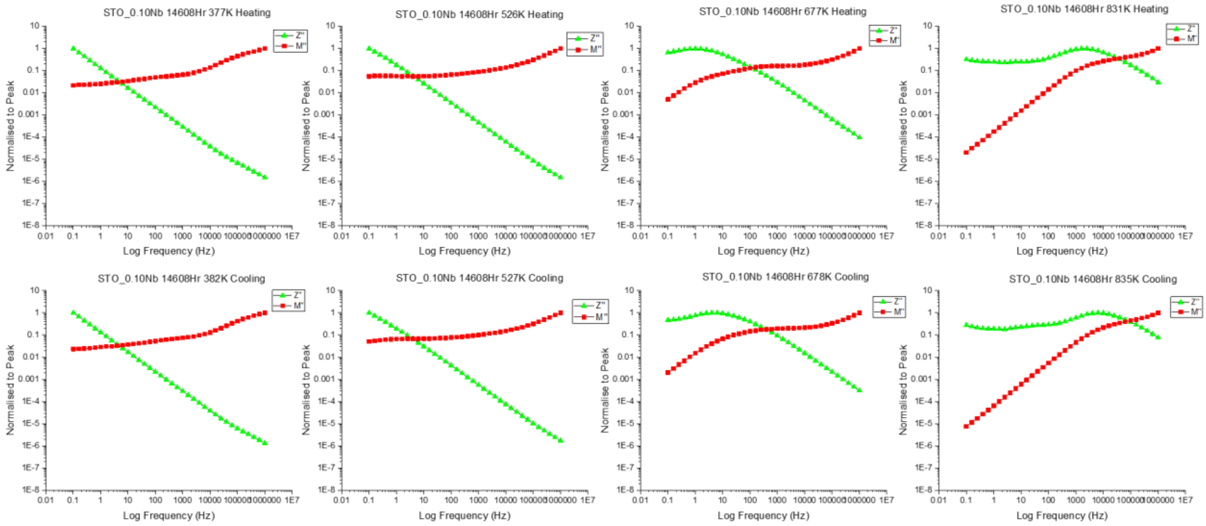

Figure 4.46: Normalised peaks of Z″ and M″ for $Sr_{0.95}Ti_{0.90}Nb_{0.10}O_3$ on heating and cooling.

Impedance data for the $Sr_{0.95}Ti_{0.90}Nb_{0.10}O_3$ sample is shown below (Figure 4.47). The initial observation is that most of the measurements up to approximately 700K (approx. 430 °C) are incomplete semi-circles. This suggests that the frequency range is not sufficient enough at these temperatures to result in a completed arc, indicating quite resistive behaviour, although the maximum of the Z′ measurements result in values of approximately $3x10^7$ Ω which is 2-3 orders of magnitude less resistive than undoped $SrTiO_3$.

Presentation of the modulus data for the $Sr_{0.95}Ti_{0.90}Nb_{0.10}O_3$ sample shown below (Figure 4.48) shows a completely different picture to that of undoped $SrTiO_3$. The arc of the largest contribution to modulus is an incomplete semi-circle and consists mainly of lower temperature measurements. The smaller modulus semi-circle is shown expanded on the right of Figure 4.48 and shows a much more temperature dispersed circle of the medium to higher temperature measurements compared to the smaller modulus semi-circle of $SrTiO_3$. It is clear that some of the higher temperature measurements do not have two contributions only one clear short arc. It is noted from the SEM images (Figure 4.21) that the $Sr_{0.95}Ti_{0.90}Nb_{0.10}O_3$ sample had bimodal grain growth with a large number of very fine grains and as such this could lead to a greater grain boundary contribution to the electrical properties on average, resulting in only one clear modulus semi-circle. In samples with a greater dopant content and a more normal grain growth with larger grains, two clear semi-circles are seen in the modulus data. It is expected that samples with lower dopant concentrations will behave more electrically heterogeneously compared to those with a higher dopant concentration.

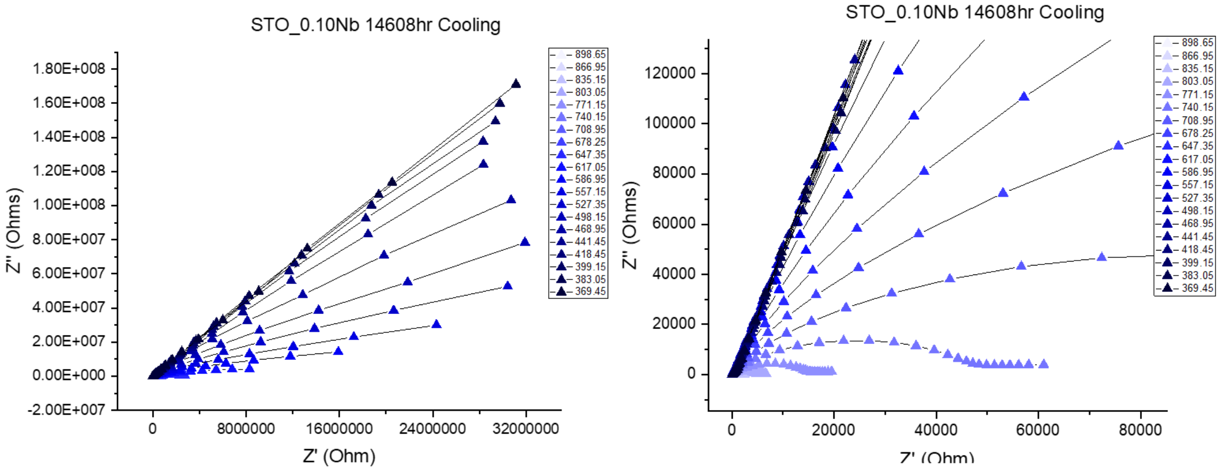

Figure 4.47: Complex impedance plots for cooling data of $Sr_{0.95}Ti_{0.90}Nb_{0.10}O_3$ between 100-600 °C (380-900 K).

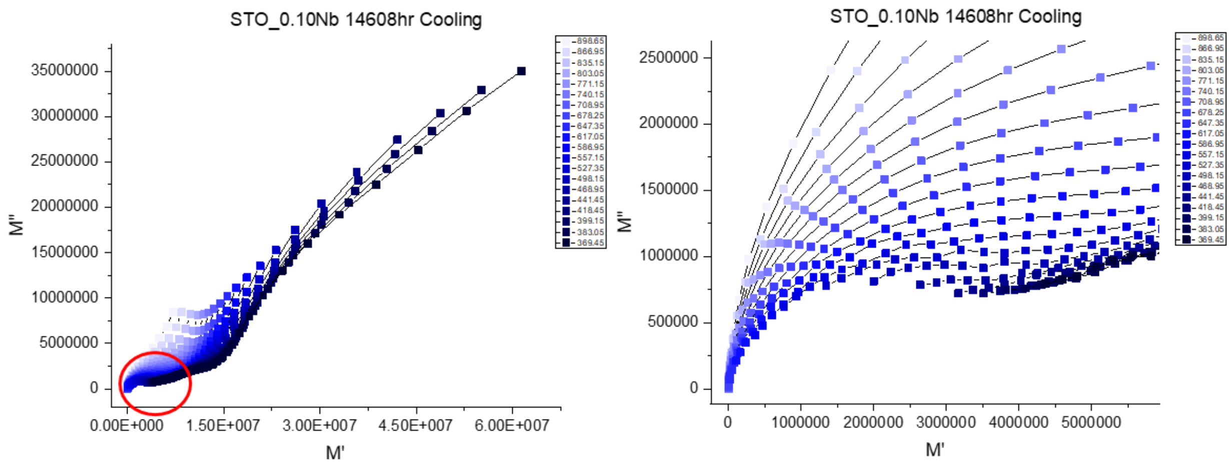

Figure 4.48: M′ vs. M″ for $Sr_{0.95}Ti_{0.90}Nb_{0.10}O_3$ at temperatures of 100-600 °C (380-900 K).

Below is the frequency dependent heating and cooling Log_{10} Z″ data (Figure 4.49) for $Sr_{0.95}Ti_{0.90}Nb_{0.10}O_3$. This shows the Z1 peak which is broader than that of the equivalent peak in $SrTiO_3$. There is also an extra peak appearing in the low frequency end at only high temperatures (hereafter labelled Z0.5), shown in the $Z''f_{max}$ conductance graph below (Figure 4.50) in yellow and green (heating and cooling, respectively). This peak persists in all samples up to $Sr_{0.85}Ti_{0.70}Nb_{0.30}O_3$ and remains unchanged in the high temperature range and at lower frequencies for all samples. There is also the change of the Z2 peak from undoped $SrTiO_3$ in the higher frequency end of the graph to a more temperature independent variation compared to Z1; the Z2 peak is much more compressed than in undoped $SrTiO_3$ (Figure 4.43). This high frequency peak becomes much more apparent in the Nb_x=0.20-0.30 samples shown later. When comparing the Arrhenius conductance graph below for the Nb_x=0.10 sample to undoped $SrTiO_3$ it seems that the gradients of the plots are much steeper, however this is due to the absence of the Z2 peak which has a much shallower gradient in the $SrTiO_3$ plot but could not be plotted in the Nb_x=0.10 sample as the Z2 contribution did not display peaks in the examined frequency range.

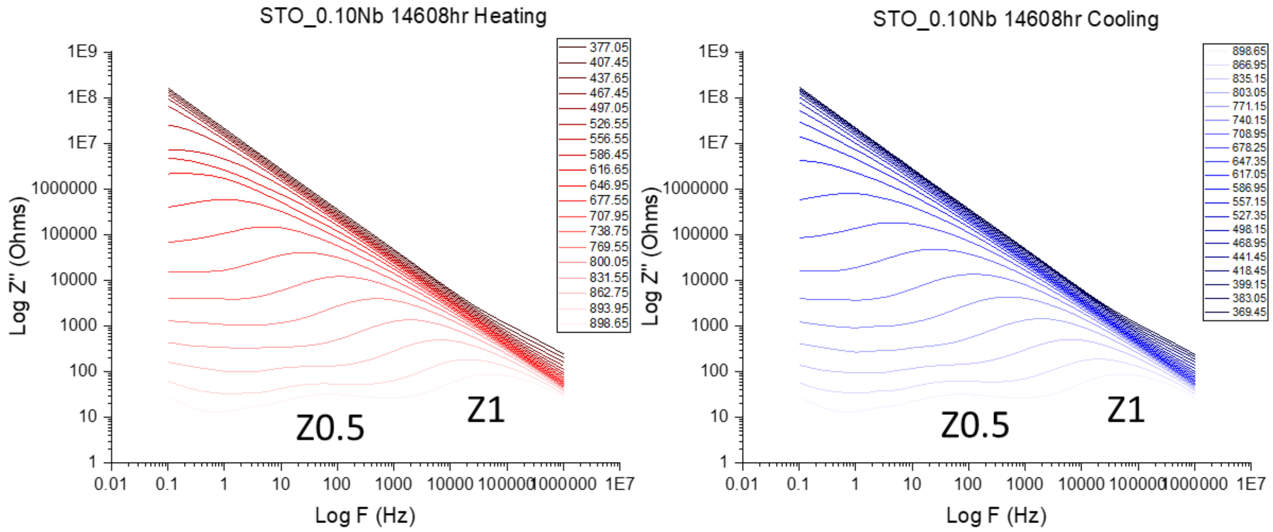

Figure 4.49: Frequency dependence of Log Z″ for $Sr_{0.95}Ti_{0.90}Nb_{0.10}O_3$, heating and cooling between 100-600 °C (380-900 K).

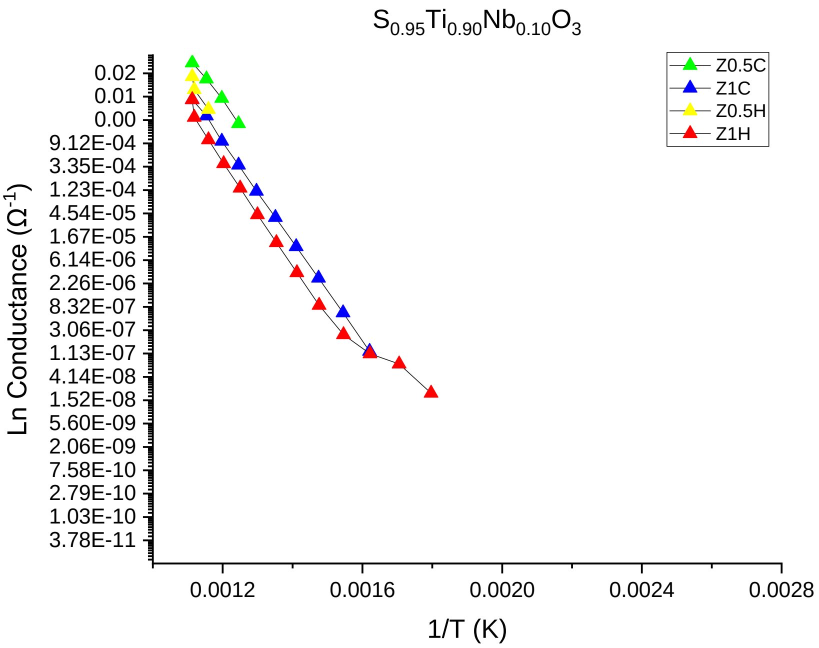

Figure 4.50: Conductance Arrhenius plot from $Z''f_{max}$ data for $Sr_{0.95}Ti_{0.90}Nb_{0.10}O_3$ heating and cooling.

It is noted that, as indicated in the structural characterisation chapter (Section 4.1.2.1), the $Sr_{0.925}Ti_{0.85}Nb_{0.15}O_3$ sample behaves electrically in a very similar way to the $Sr_{0.95}Ti_{0.90}Nb_{0.10}O_3$ sample. The graphs below of capacitance vs. temperature are for the Nb_x=0.10 and 0.15 samples (Figure 4.52 and Figure 4.53). They both show a strong temperature dependent capacitance for the Z0.5 peaks, and a somewhat temperature independent capacitance for the Z1 peak. The only significant difference in the two samples is what appears to be a hysteresis effect in the capacitance data on heating and cooling (Figure 4.53) which is also visible in the conductance Arrhenius plot of the $Z''f_{max}$ (Figure 4.51) where the Z1 peak under heating deviates significantly from the cooling Z1 peak at low temperatures. A possible reason for this is the evaporation of water from a sample on heating vs. cooling.

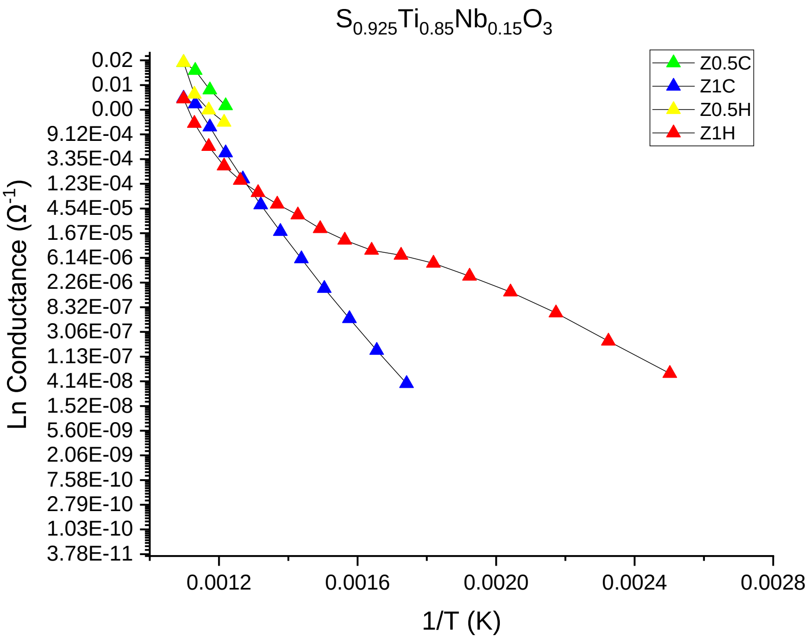

Figure 4.51: Conductance Arrhenius plot from $Z''f_{max}$ data for $Sr_{0.925}Ti_{0.85}Nb_{0.15}O_3$ on heating and cooling.

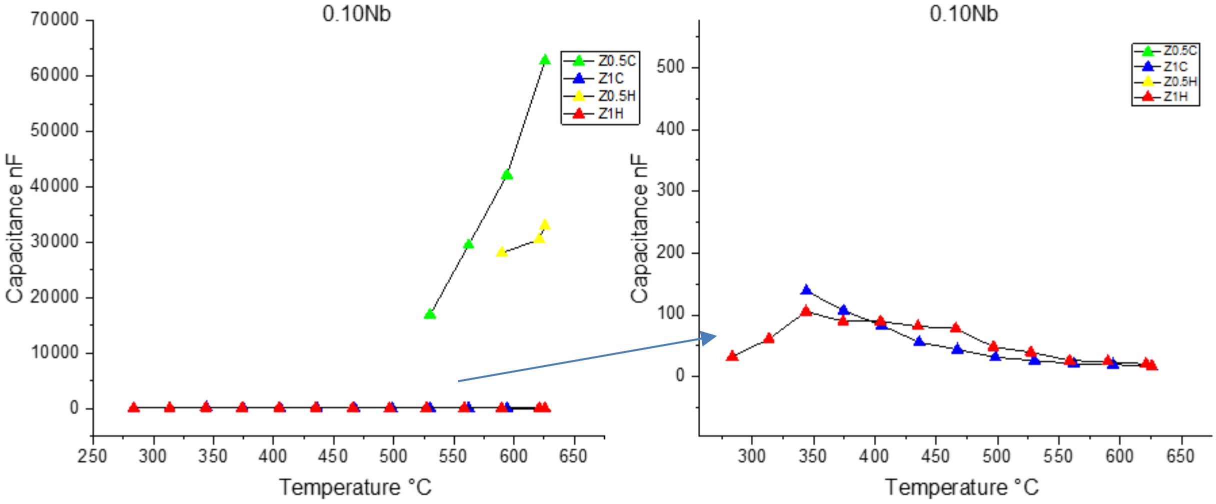

Figure 4.52: Capacitance vs temperature for $Sr_{0.95}Ti_{0.90}Nb_{0.10}O_3$.

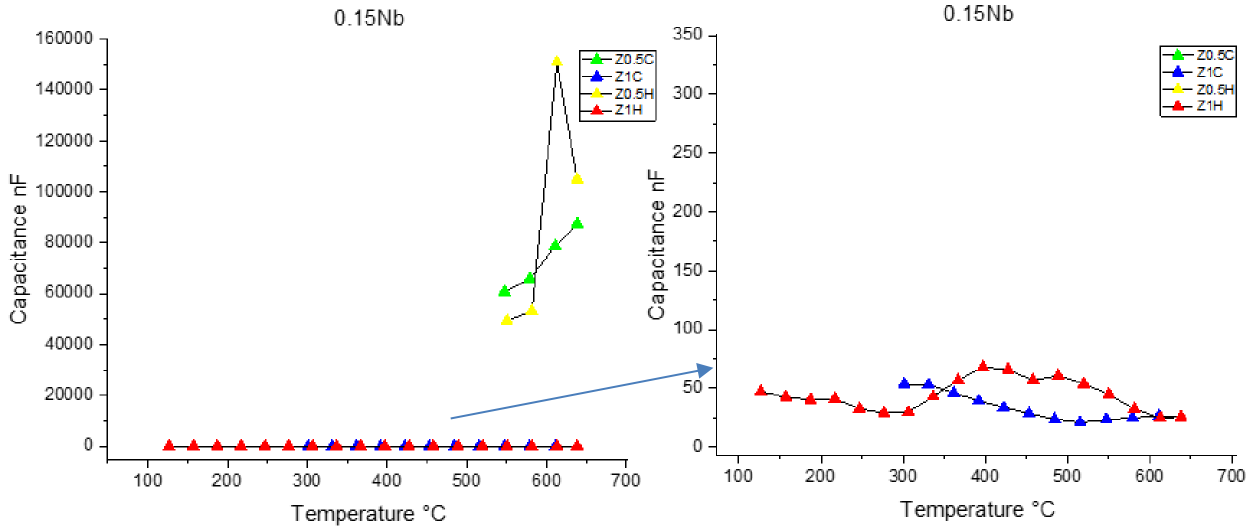

Figure 4.53: Capacitance vs temperature for $Sr_{0.925}Ti_{0.95}Nb_{0.15}O_3$.

Table 4-13 lists the calculated activation energies for the conductance graph produced from the $Z''f_{max}$ data for the $Sr_{0.95}Ti_{0.90}Nb_{0.10}O_3$ sample. The Z0.5 peaks that appear at high temperatures and low frequencies on heating and cooling have activation energies of approximately 2.3 eV (heating) and 1.7 eV (cooling). The heating plot could be inaccurate due to the gradient being calculated from only 3 data points. As such, if the cooling data (1.7 eV) is taken to be more accurate, according to Jose et al. 2018, this peak can be attributed to the electrons that are ionised from Sr vacancies[113][51] with an approximate activation energy of 1.5 eV which in literature are found to transfer across grain boundaries[116] but this cannot be guaranteed from this experiment alone. It could also relate to a Schottky barrier at the electrode/sample interface. This peak appears for the first time in the $Sr_{0.95}Ti_{0.90}Nb_{0.10}O_3$ sample where Sr vacancies are introduced and becomes more prominent with each sample as the Sr vacancies increase to compensate for the Nb-dopant. Further sample sets will have to be analysed before conclusions can be drawn.

Table 4-14 shows the calculated activation energies, σ_0 values and capacitances for the $Sr_{0.925}Ti_{0.85}Nb_{0.15}O_3$ sample. It shows nearly the same temperature ranges for each peak as the Nb_x=0.10 sample, but lower activation energies and σ_0 values for each peak. This could indicate that there are more of the charge carrier species available due to the increase in donor dopant and a lower activation barrier for each relaxation process. The capacitances for the Nb_x=0.15 sample are higher.

Table 4-13: Calculated data for relaxation mechanisms from $Z''f_{max}$ data for $Sr_{0.95}Ti_{0.90}Nb_{0.10}O_3$.

Peak	Peak Temp. Range (°C)	$Z''f_{max}$ Ea (eV)	Ln σ_0	Approx. Capacitance (nF)
Z0.5C	600-575	1.69	18.40	60,000
Z1C	600-300	1.83	18.60	150

Table 4-14: Calculated data for relaxation mechanisms from $Z''f_{max}$ data for $Sr_{0.925}Ti_{0.95}Nb_{0.15}O_3$.

Peak	Peak Temp. Range (°C)	$Z''f_{max}$ Ea (eV)	Ln σ_0	Approx. Capacitance (nF)
Z0.5C	600-550	1.28	12.27	90,000
Z1C	600-300	1.60	17.00	50

Shown below are the normalised Z″/M″ plots for both the $Sr_{0.90}Ti_{0.80}Nb_{0.20}O_3$ and $Sr_{0.85}Ti_{0.70}Nb_{0.30}O_3$ samples (Figure 4.54, Figure 4.55). Both samples show one peak in Z″ and M″ which overlap at 100 and 250 °C and develop a second smaller peak in the 400 and 550 °C plots for modulus, and a second larger peak in impedance. The peaks move to higher frequencies with increasing temperature, and both sets of peaks for both samples overlap, indicating long range conduction mechanisms.

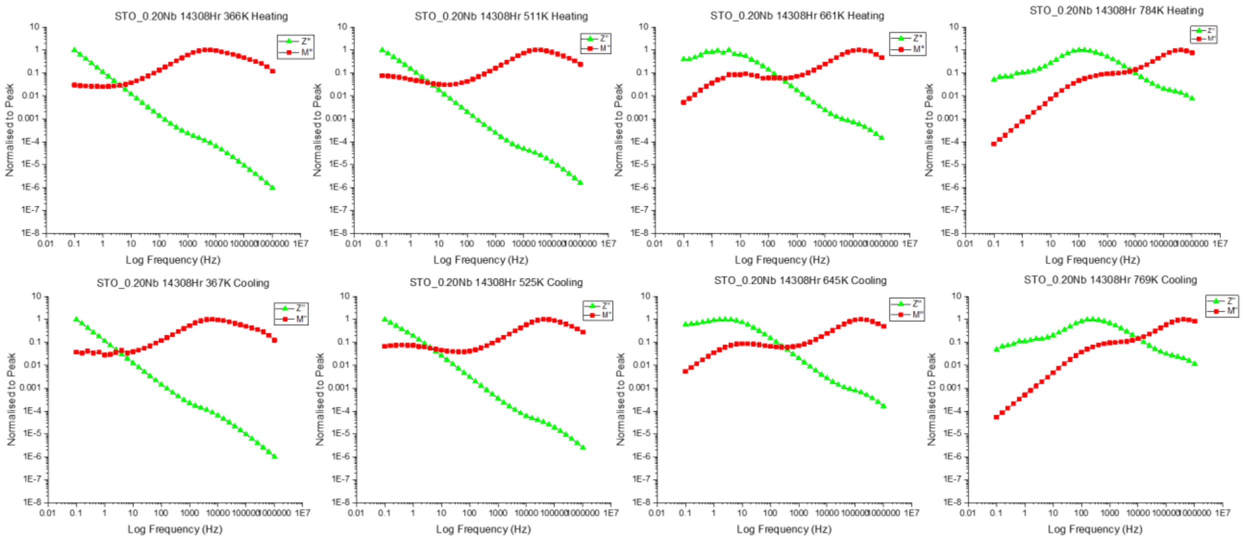

Figure 4.54: Normalised peaks of Z″ and M″ plots for $Sr_{0.90}Ti_{0.80}Nb_{0.20}O_3$ on heating and cooling.

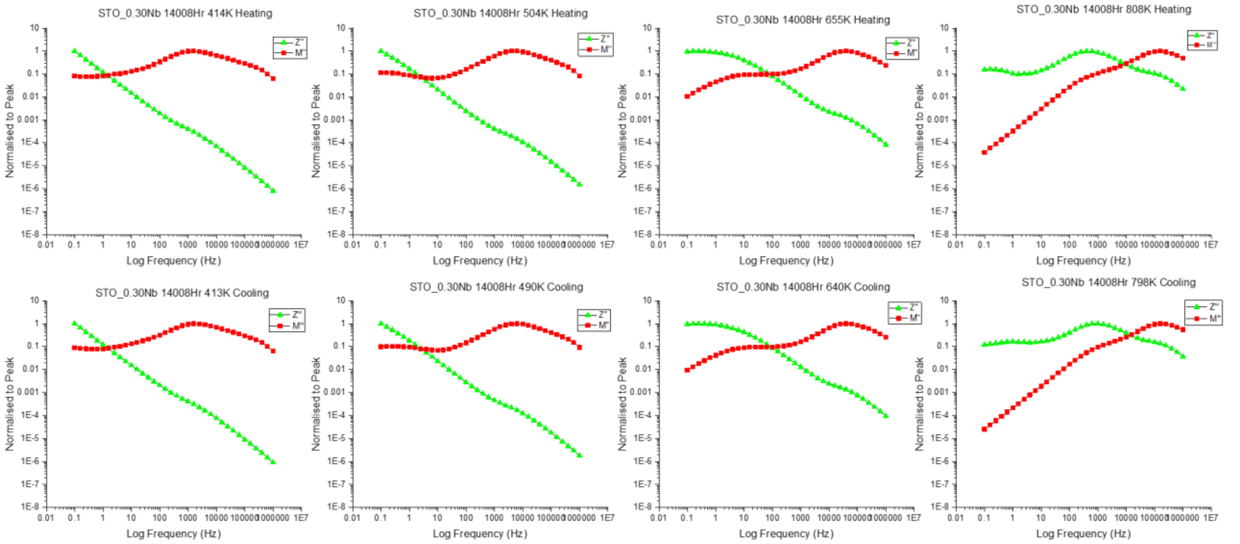

Figure 4.55: Normalised peaks of Z″ and M″ plots for $Sr_{0.85}Ti_{0.70}Nb_{0.30}O_3$ on heating and cooling.

Impedance analysis of $Sr_{0.90}Ti_{0.80}Nb_{0.20}O_3$ (Figure 4.56) shows incomplete semi-circles for the low to intermediate temperature measurements, with high temperature measurements showing semi-circles with tails coming off (right hand image) which again indicates the onset of DC conductivity[108] from the semi-conducting core evidenced in the SEM data (Figure 4.21). The modulus plot for $Sr_{0.90}Ti_{0.80}Nb_{0.20}O_3$ is shown in Figure 4.57. There are two semi-circles present again similar to that of undoped $SrTiO_3$, but the modulus values for both semi-circles are significantly smaller in comparison to $SrTiO_3$. The arc for both the grain and grain boundary contributions are slightly asymmetrical, indicating more complex relaxation behaviour occurring. Two complete modulus semi-circles are also seen for the remaining Nb_x=0.25 and 0.30 samples.

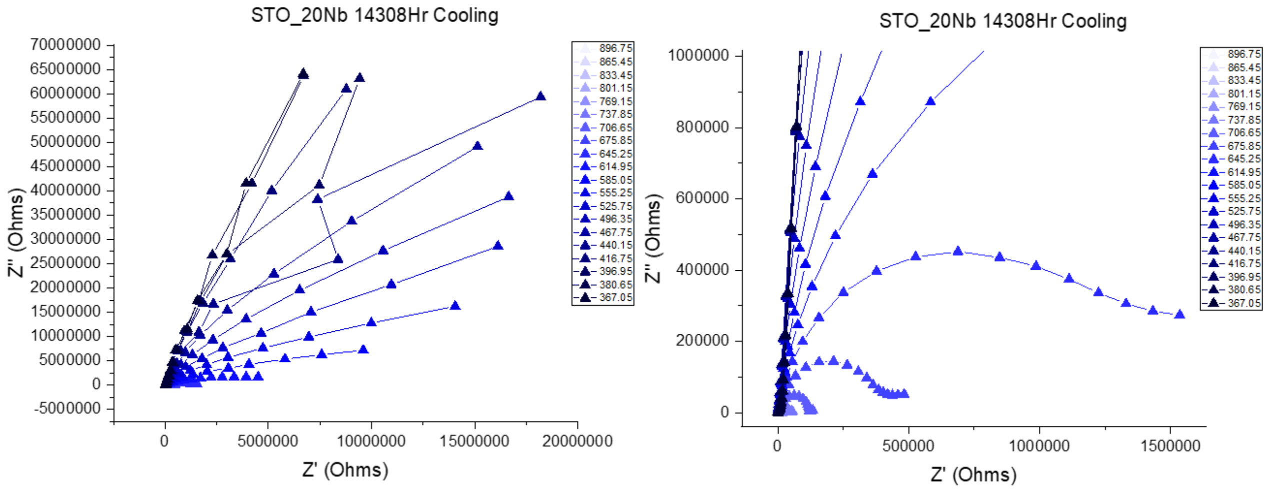

Figure 4.56: Complex impedance plots for cooling data of $Sr_{0.90}Ti_{0.80}Nb_{0.20}O_3$ between 100-600 °C (380-900 K).

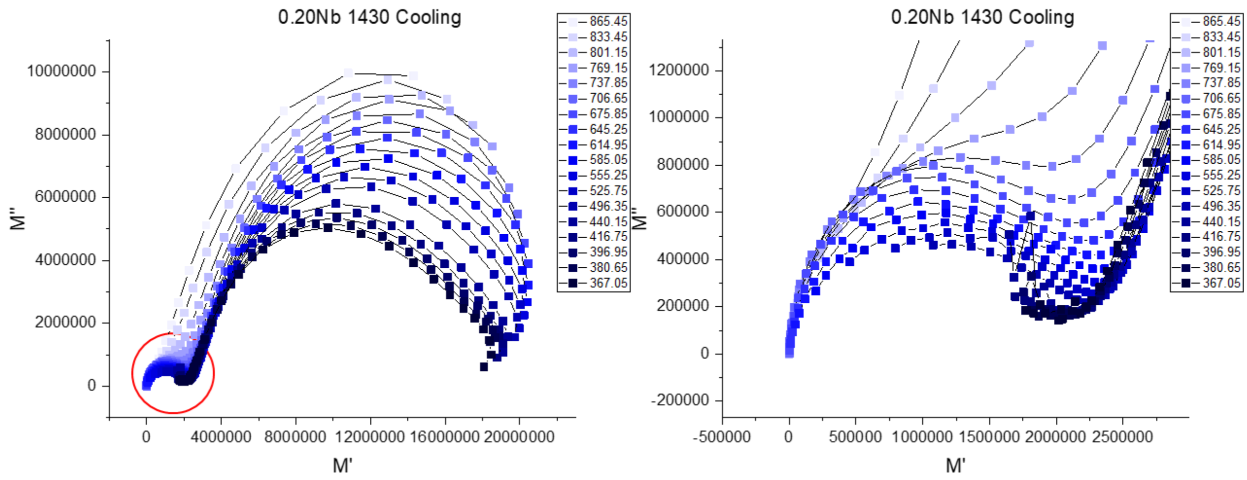

Figure 4.57: M′ vs. M″ for $Sr_{0.90}Ti_{0.80}Nb_{0.20}O_3$ at temperatures of 100-600 °C (380-900 K).

The complex impedance data and the Z″ Bode plots for the Nb_x=0.20, 0.25 and 0.30 samples are almost identical to each other so only the Nb_x=0.20 sample data is shown below (Figure 4.58). The graphs for conductance Arrhenius plots of the $Z''f_{max}$ data for each sample are illustrated in (Figure 4.59). The only difference between the samples seems to be a change in mechanism to the Z1 peak heating data for the $Sr_{0.875}Ti_{0.75}Nb_{0.25}O_3$ sample, shown by two significantly different activation energies for the Z1H plot and a deviation away from the cooling data.

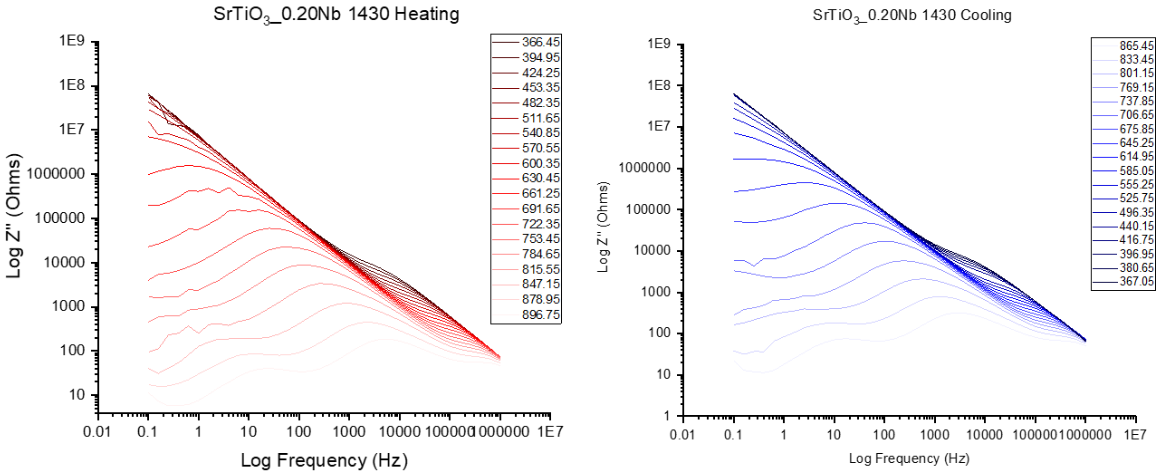

Figure 4.58: Frequency dependence of Log Z″ for $Sr_{0.90}Ti_{0.80}Nb_{0.20}O_3$, heating and cooling between 100-600 °C (380-900 K).

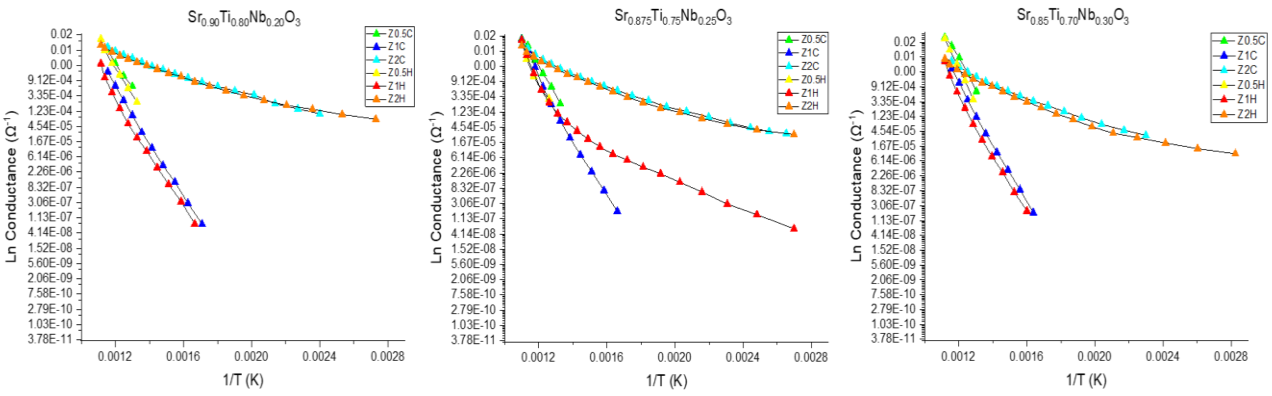

Figure 4.59: Conductance Arrhenius plot from $Z''f_{max}$ data for $Nb_x=0.20$ (left) 0.25 (middle) and 0.30 (right) heating and cooling.

Capacitance plots for the $Nb_x=0.20$ and 0.30 are shown below (Figure 4.60, Figure 4.61). They show a temperature independent capacitance (Z2H/C) and two temperature dependent capacitances (Z0.5H/C and Z1H/C) for both samples. The behaviour of the Z1H/C plots for the $Nb_x=0.2/0.3$ samples have a U-shape with a drop in capacitance at approximately 450-500 °C before increasing again up to the maximum measurement temperature. It is clear in both cases that there appears to be an element of hysteresis in the Z0.5 peaks in both samples.

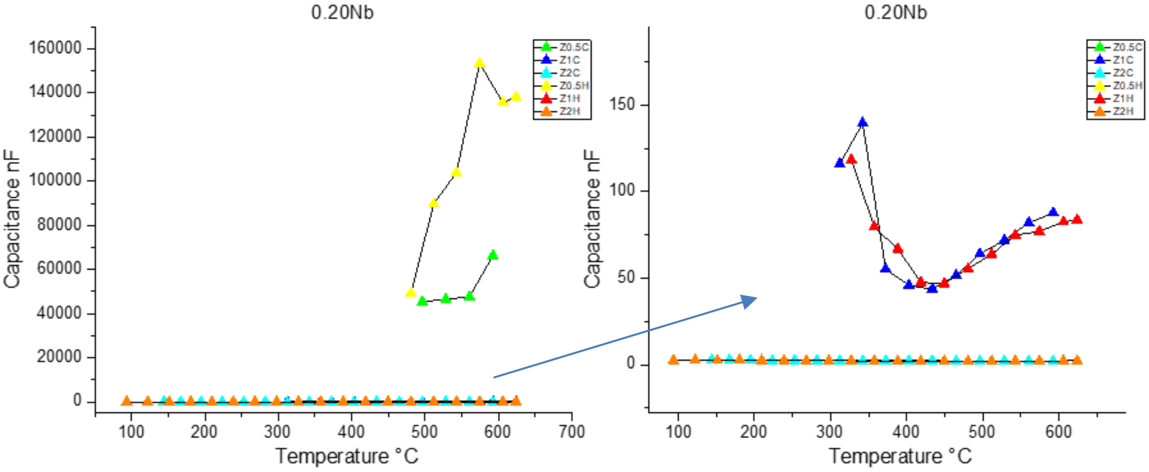

Figure 4.60: Capacitance vs. temperature for $Sr_{0.90}Ti_{0.80}Nb_{0.20}O_3$.

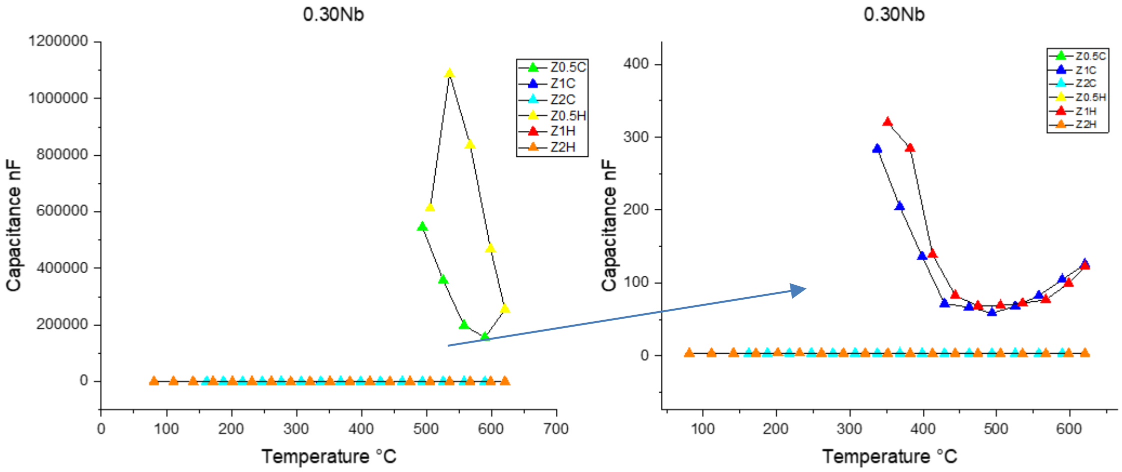

Figure 4.61: Capacitance vs. temperature for $Sr_{0.85}Ti_{0.70}Nb_{0.30}O_3$.

Table 4-15 and Table 4-16 below show the calculated activations energies, σ_0 values and capacitances for the Nb_x=0.20 and 0.30 samples. The activation energies for the Nb_x=0.30 sample are higher than those for the Nb_x=0.20 sample, as are the σ_0 and capacitance values. The Z1H/C capacitance plots for these samples are much more temperature dependent than the equivalent plots for the Nb_x=0.10 and 0.15 samples. As shown in both of these samples, the Z0.5 and Z1 peaks have approximately the same activation energies but very different capacitances. Again, this suggests that the same relaxation mechanism is occurring but across a different part of the microstructure e.g. grain vs. grain boundary. The activation energies for the Z1 peaks shown for both samples varies between 1.5-1.7 eV approximately, and is thought to represent electron transport across a grain boundary[116] from ionised Sr vacancies. The Z2 peak again repeatedly returns a value of approximately 0.3-0.4 eV which according to Zhong et al. and Pan et al. can be attributed to the first ionisation of oxygen vacancies that result in electrons which couple with an off-centre Ti ion[84][81]. However, according to Higuchi et al. it could be the result of hole hopping[60] so there is more information needed to determine which mechanism is the most likely explanation.

It is noted from the SEM imaging of this sample set (Section 4.1.2.1) that the Nb_x=0.2 and 0.3 samples show a core-shell type of structure, and it is considered that there are actually 3 areas within the microstructure of those samples: the core, the shell and the grain boundary. It is possible that the three main peaks seen in the impedance data could be allocated to those three areas of the microstructure, although it is not the intention of this work to be so stringent with the allocation of RC elements to microstructure, but to understand that a more complex defect mechanistic-type of approach could be more appropriate.

Table 4-15: Calculated data for relaxation mechanisms from $Z''f_{max}$ data for $Sr_{0.90}Ti_{0.80}Nb_{0.20}O_3$.

Peak	**Peak Temp. Range (°C)**	**$Z''f_{max}$ Ea (eV)**	**Ln σ_0**	**Approx. Capacitance (nF)**
Z0.5C	600-500	1.42	14.06	70,000
Z1C	600-300	1.55	14.15	125
Z2C	600-100	0.30	-1.03	3

Table 4-16: Calculated data for relaxation mechanisms from $Z''f_{max}$ data for $Sr_{0.85}Ti_{0.70}Nb_{0.30}O_3$.

Peak	**Peak Temp. Range (°C)**	**$Z''f_{max}$ Ea (eV)**	**Ln σ_0**	**Approx. Capacitance (nF)**
Z0.5C	600-500	1.70	18.61	600,000
Z1C	600-300	1.72	17.21	300
Z2C	600-150	0.38	-0.50	3

Permittivity vs. temperature readings were taken for all samples on heating and cooling up to 650 °C (Figure 4.62). All readings showed an element of hysteresis at the peaks, where there is a difference between the peak on heating vs. cooling. Small peaks were seen in the permittivity of the Nb_x=0.10 and 0.15 samples at approximately 400-450 °C accompanied by a barely discernible peak in tan δ (Figure 4.63, right). The permittivity of these samples then accelerates upwards to very high permittivities of approximately 220,000, accompanied by very high loss values. The Nb_x=0.20-0.30 samples have slight peaks in the permittivity at approximately 250-300 °C, but the corresponding peaks in tan δ are at lower temperatures (100-200 °C). These samples also then increase to very high permittivities (approximately 100,000 for Nb_x=0.20 and 0.30 samples, and 200,000 for the Nb_x=0.25 sample) as temperature continues to increase but a second peak is seen at approximately 550 °C as the tan δ again rises steeply. All samples have a smaller tan δ peak than undoped $SrTiO_3$.

Work by C. Wang et al. was carried out on the dielectric properties of $SrTiO_3$ ceramic and single crystal samples[117] across a sweep of frequencies and at temperatures up to 800 °C. They showed two clear peaks in the permittivity similar to those seen in the Nb_x=0.20-0.30 samples but at approximately 280 °C and 690 °C. These were attributed to "thermally activated Debye-type relaxations"[117] in the samples, which were said to be related to oxygen vacancy movement within the samples.

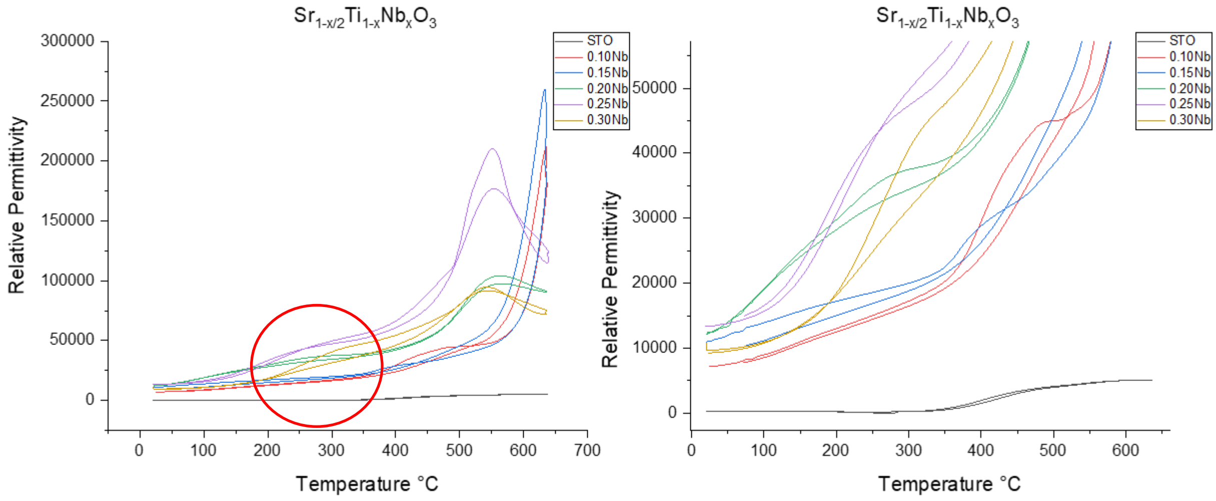

Figure 4.62: Relative permittivity vs. temperature for $Sr_{1-x/2}Ti_{1-x}Nb_xO_3$ samples.

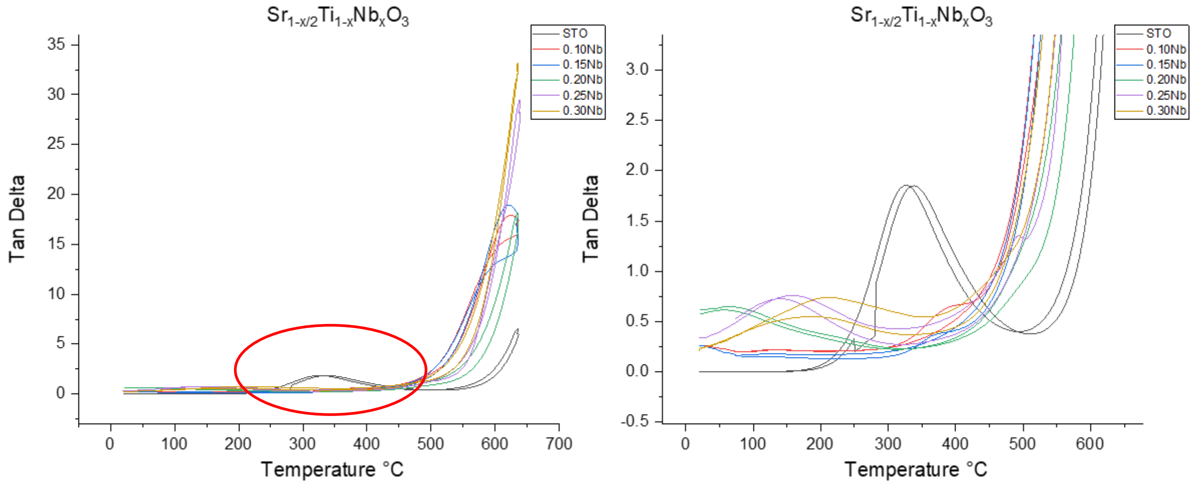

Figure 4.63: Tan δ values vs. temperature for $Sr_{1-x/2}Ti_{1-x}Nb_xO_3$ samples at $1x10^3$ Hz.

Room temperature relative permittivity and tan δ measurements were taken and plotted against composition (Figure 4.64). As can be seen the relative permittivity increases with Nb content and there is a peak at the Nb_x=0.20 and 0.25 samples, accompanied by a drop in tan δ for the Nb_x=0.25 and 0.30 samples.

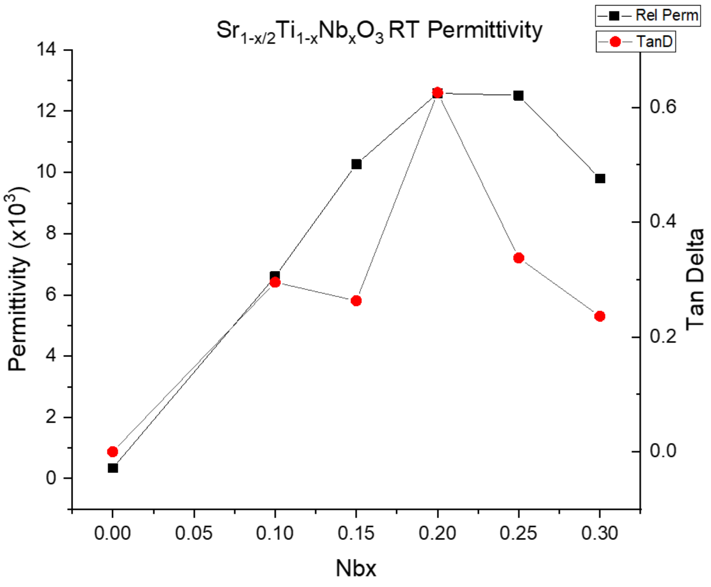

Figure 4.64: Room temperature permittivity measurements of $Sr_{1-x/2}Ti_{1-x}Nb_xO_3$ samples.

$Sr_{0.9}Ti_{1-x}Nb_xO_3$

Below are the normalised Z″/M″ plots for the $Sr_{0.90}Ti_{0.81}Nb_{0.19}O_3$ sample (Figure 4.65). This figure is again significantly different to the nearly equivalent $Sr_{0.90}Ti_{0.80}Nb_{0.20}O_3$ sample. There is only one normalised modulus peak and one impedance peak (except at 550 °C) which increases with temperature and moves to higher frequencies with increasing temperature, as does the impedance peak. There is not complete overlapping of peaks, but some, indicating longer range conduction mechanisms. The main difference is that it is the major modulus peak and the major impedance peak that are overlapping in contrast the $Sr_{0.90}Ti_{0.80}Nb_{0.20}O_3$ sample which had the major impedance peak overlapping the minor modulus peak. There is also an M″ peak moving out of the assessed frequency range suggesting a bulk response semi-conducting core as with the previous A-site vacancy sample set.

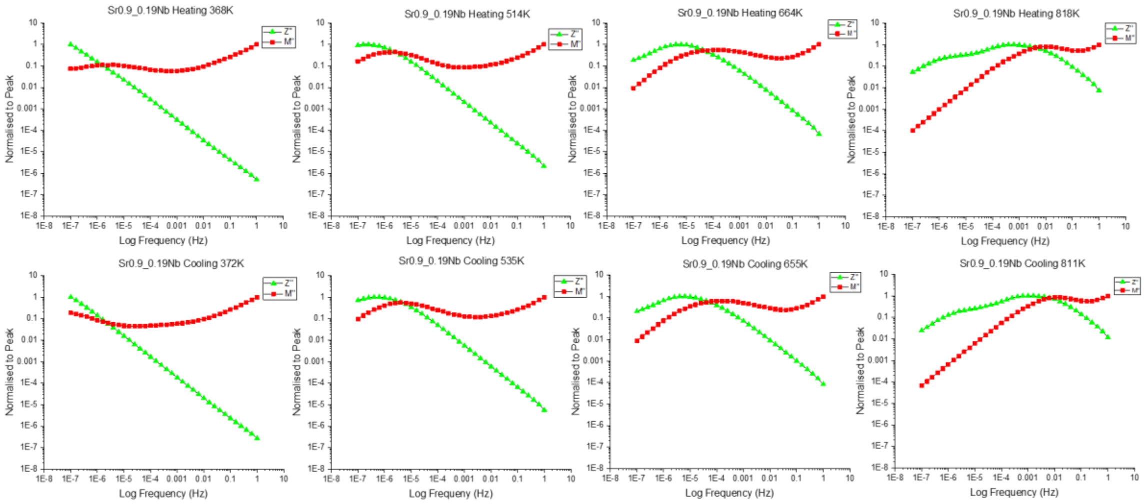

Figure 4.65: Normalised peaks of Z″ and M″ for $Sr_{0.90}Ti_{0.81}Nb_{0.19}O_3$ on heating and cooling.

The complex impedance data is shown below in Figure 4.66 for the $Sr_{0.90}Ti_{0.81}Nb_{0.19}O_3$ sample and shows a similar pattern to that of the $Sr_{0.90}Ti_{0.80}Nb_{0.20}O_3$ sample but with more curved arcs. In addition, they do not appear to have the same tails present at the end of the semi-circles when complete. Below is also the plot of complex electric modulus for the $Sr_{0.90}Ti_{0.81}Nb_{0.19}O_3$ sample (Figure 4.67). Unlike the $Sr_{0.90}Ti_{0.80}Nb_{0.20}O_3$ sample, there is only one observed completed semi-circle followed by a tail similar to that seen in the $Sr_{0.95}Ti_{0.90}Nb_{0.10}O_3$ sample. A temperature dispersion occurs at the top of the semi-circle at high temperatures (600-450 °C) which is not present at low and intermediate temperatures - as it can be seen the data plots are very close together for the darker lower temperature measurements.

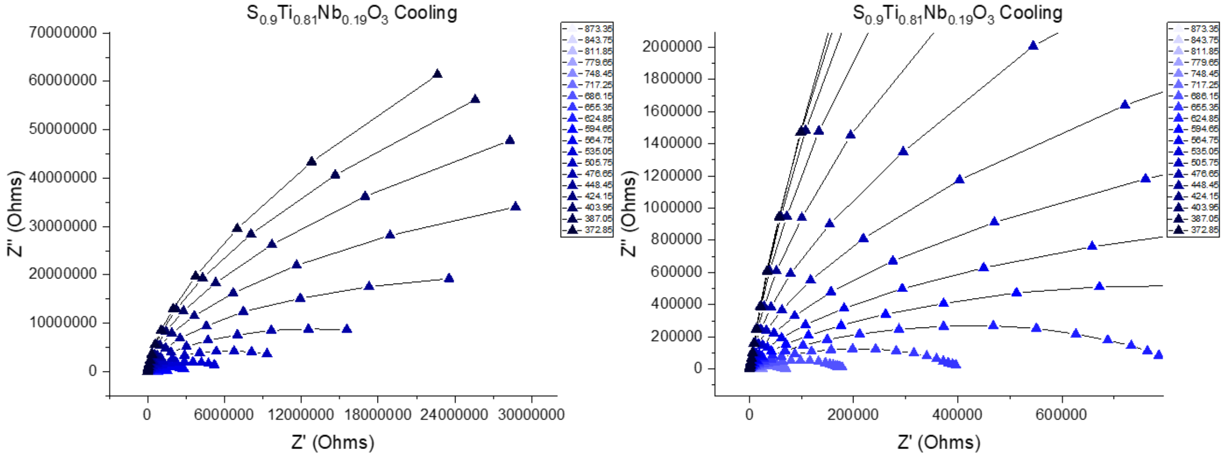

Figure 4.66: Complex impedance plots for cooling data of $Sr_{0.90}Ti_{0.81}Nb_{0.19}O_3$ between 100-600 °C (380-900 K).

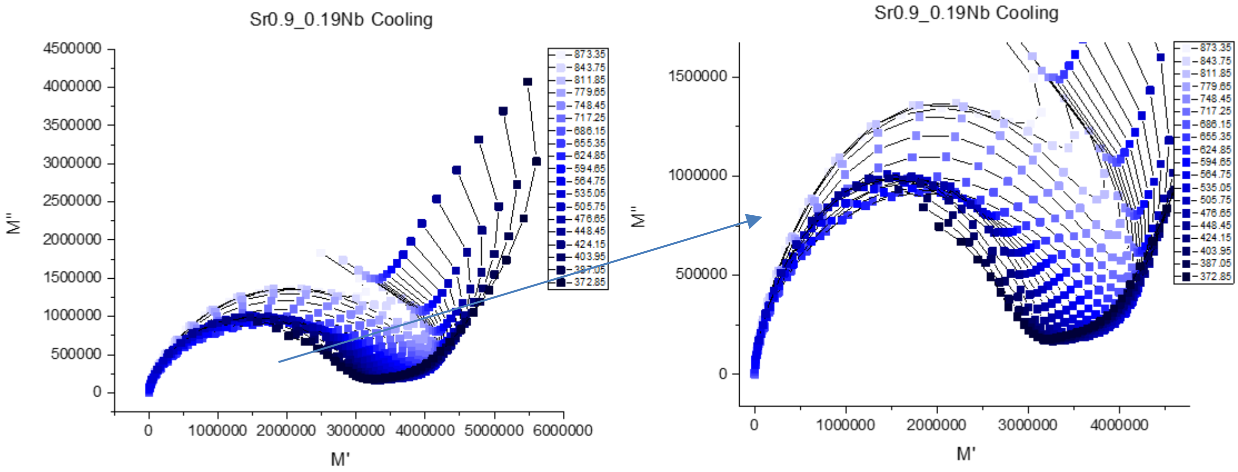

Figure 4.67: M′ vs. M″ for $Sr_{0.90}Ti_{0.81}Nb_{0.19}O_3$ at temperatures of 100-600 °C (380-900 K).

Shown below is the Bode plot of Log Z″ on heating and cooling for the $Sr_{0.90}Ti_{0.81}Nb_{0.19}O_3$ sample. These graphs are markedly different from the above $Sr_{0.90}Ti_{0.80}Nb_{0.20}O_3$ sample (Figure 4.58) that was previously examined despite the only difference between the compositions being 1 at% more Nb and less Ti content. The main difference is that the Z2H/C peak at the high frequency end of the plot is missing completely but the M″ peak is still present. There is good similarity between the heating and cooling data for this sample however, just as there was for the $Sr_{0.90}Ti_{0.80}Nb_{0.20}O_3$ sample. When comparing the $Z''f_{max}$ Arrhenius graphs for the two samples (Figure 4.59 above and Figure 4.69 below) there is a gradient change to the Z1H/C peak for the $Sr_{0.90}Ti_{0.81}Nb_{0.19}O_3$ sample at approximately 400 °C, whereas the $Sr_{0.90}Ti_{0.80}Nb_{0.20}O_3$ sample had no gradient change for this peak. There was a similar mechanism change in the Z1H plot for the $Sr_{0.875}Ti_{0.70}Nb_{0.25}O_3$ sample heating data at the same approximate temperature. This could relate to the temperature dispersion that occurs in the above complex modulus plot above (Figure 4.67) as it occurs at a similar temperature.

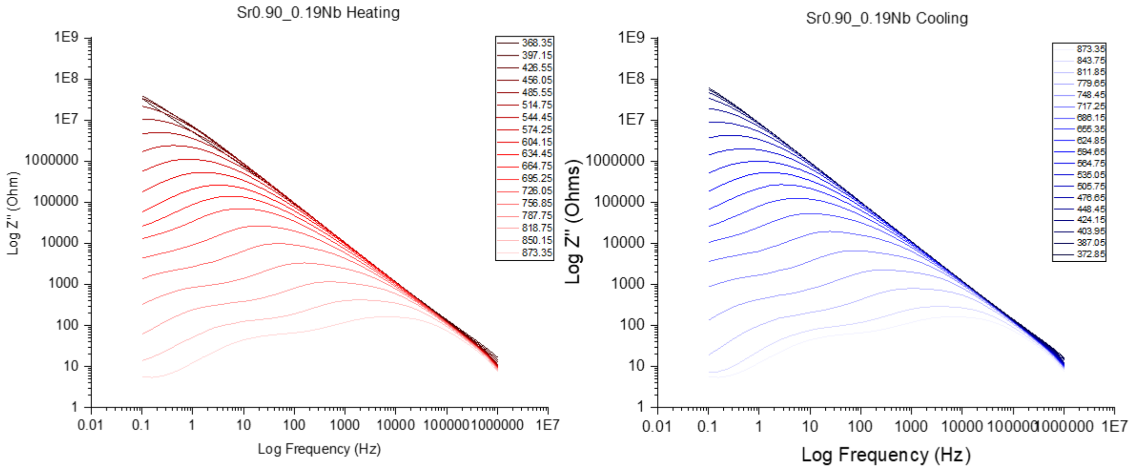

Figure 4.68: Frequency dependence of Log Z″ for $Sr_{0.90}Ti_{0.81}Nb_{0.19}O_3$, heating and cooling between 100-600 °C (380-900 K).

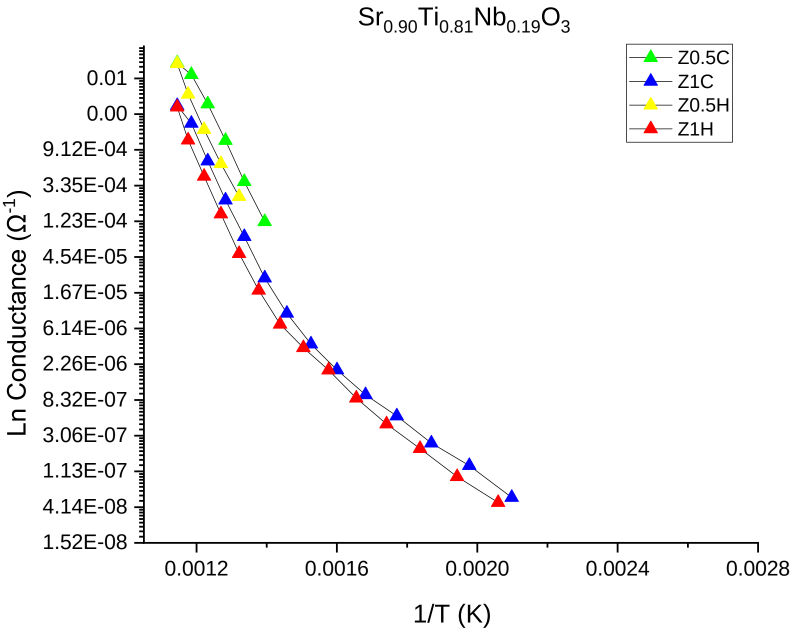

Figure 4.69: Conductance Arrhenius plot from Z″f_{max} data for $Sr_{0.90}Ti_{0.81}Nb_{0.19}O_3$ heating and cooling.

The capacitance graph below (Figure 4.70) was produced from the impedance data and shows a high capacitance temperature dependent plot (Z0.5) which has a hysteresis effect between heating and cooling, and a slightly more temperature independent plot for the Z1 peak.

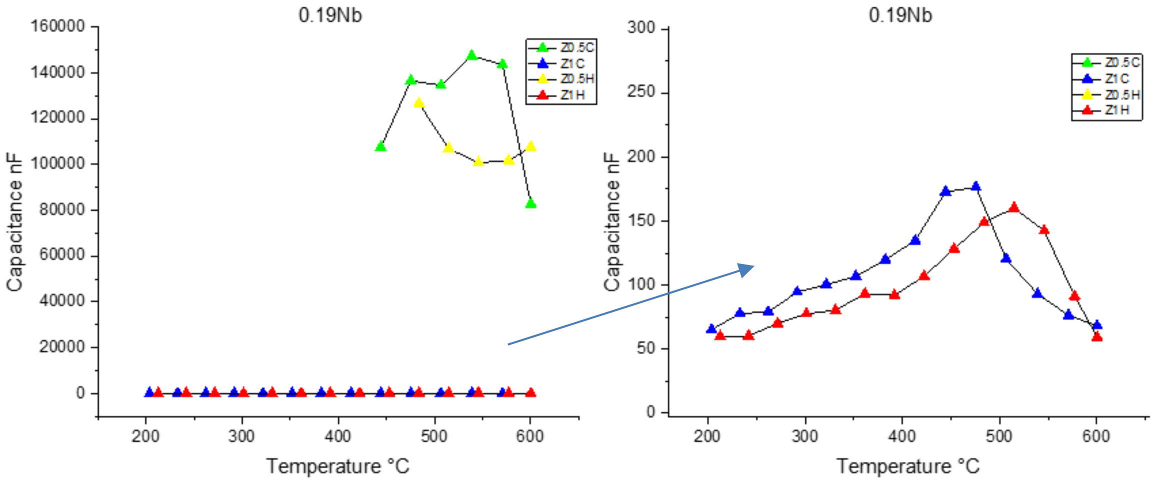

Figure 4.70: Capacitance vs temperature for $Sr_{0.90}Ti_{0.81}Nb_{0.19}O_3$.

Comparing the values below in Table 4-17 to the activation energies for the Arrhenius conductance plot for the $Sr_{0.90}Ti_{0.80}Nb_{0.20}O_3$ sample above in Table 4-15, it can be seen that the activation energies for both the Z0.5 and Z1 peaks for the Nb_x=0.19 sample are slightly higher than those for the Nb_x=0.20 sample. When attempting to assign the activation energies, it can be seen that the initial slope for the Z1 peak between 180-440 °C relates to the diffusion of doubly ionised oxygen vacancies (0.7 eV). From there it changes to a value of 1.8 eV which as discussed previously relates to electron conduction across a grain boundary from ionised Sr vacancies[116]. As can be seen from the table, the Z0.5 peak, which only exists between 600-450 °C, has very similar activation energies and σ_0 values to the section of the Z1 peak between 600-450 °C, yet they have vastly different capacitance values. This again suggests that it is the same mechanism occurring but in different parts of the microstructure of the sample.

Table 4-17: Calculated data for relaxation mechanisms from $Z''f_{max}$ data for $Sr_{0.90}Ti_{0.81}Nb_{0.19}O_3$.

Peak	Peak Temp. Range (°C)	$Z''f_{max}$ Ea (eV)	Ln σ_0	Approx. Capacitance (nF)
Z0.5C	600-450	1.60	16.91	150,000
Z1C (600-440 °C)	600-200	1.71	16.44	175
Z1C (440-180 °C)		0.67	-1.40	

Analysis of the $Sr_{0.90}Ti_{0.85}Nb_{0.15}O_3$ sample again shows vast differences in the electrical properties in comparison to the previous sample set with a sample of similar composition ($Sr_{0.925}Ti_{0.85}Nb_{0.15}O_3$). The compositional difference in this case is just 2.5 at% Sr content. The complex impedance plot for this sample (Figure 4.71) is similar to that of $Sr_{0.90}Ti_{0.81}Nb_{0.19}O_3$, but a wider temperature range of measurements successfully forming complete semi-circles.

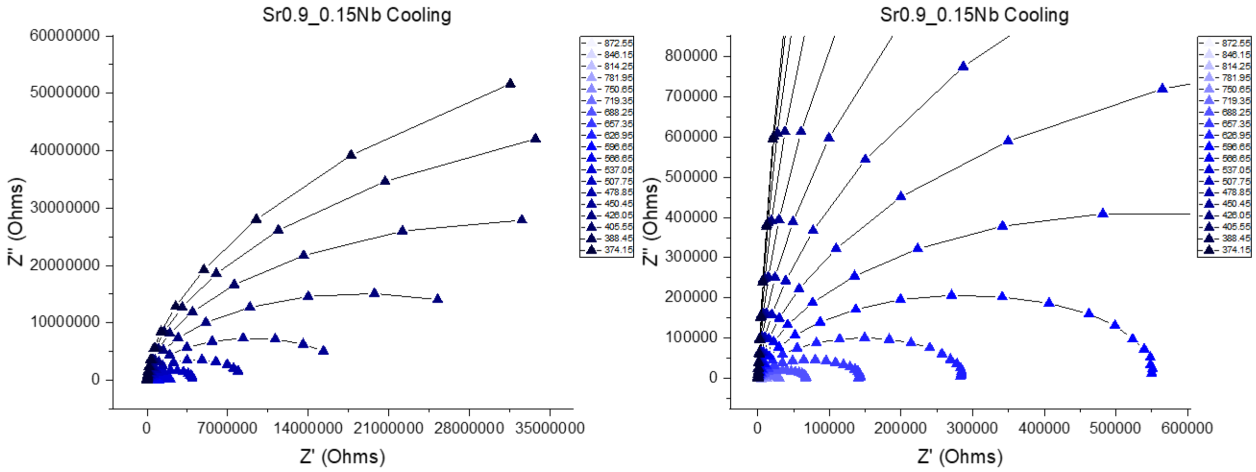

Figure 4.71: Complex impedance plots for cooling data of $Sr_{0.90}Ti_{0.85}Nb_{0.15}O_3$ between 600-100 °C (380-900 K).

The electric modulus data is very similar to the previous sample ($Sr_{0.90}Ti_{0.81}Nb_{0.19}O_3$) with both the shape of the complex modulus plot, and the temperature independent capacitance, so neither graphs were shown here. This was surprising due to the significant differences in both the real and imaginary parts of impedance data.

The Log Z″ Bode plots for the heating and cooling data (Figure 4.72) show differences, with the heating graph showing one narrow peak in Z″ and the cooling data showing a much broader peak with the beginning of the previously-observed Z0.5 peak appearing at low frequencies and high temperatures. The differences are further illustrated with the respective Arrhenius conductance graph (Figure 4.73) showing the deviation between the heating and cooling plot for Z1 along with a change in gradient indicating a change in mechanism. When examining the calculated activation energies from this plot (Table 4-18) it shows an apparent transition at approximately 350 °C from either electron/hole hopping or singly ionised to doubly-ionised oxygen vacancies.

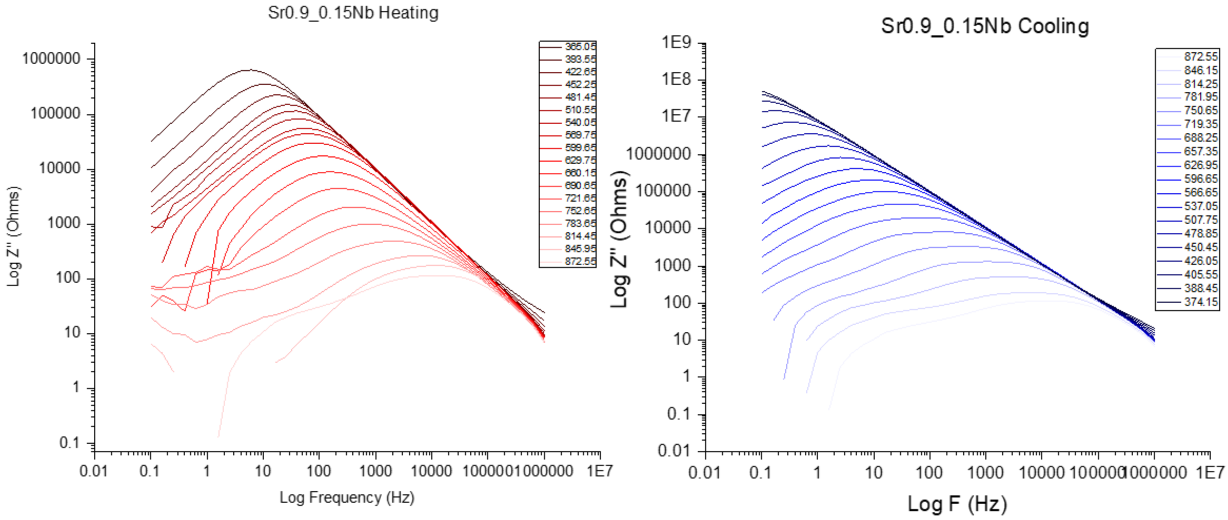

Figure 4.72: Frequency dependence of Log Z″ for $Sr_{0.90}Ti_{0.85}Nb_{0.15}O_3$, heating and cooling between 100-600 °C (380-900 K).

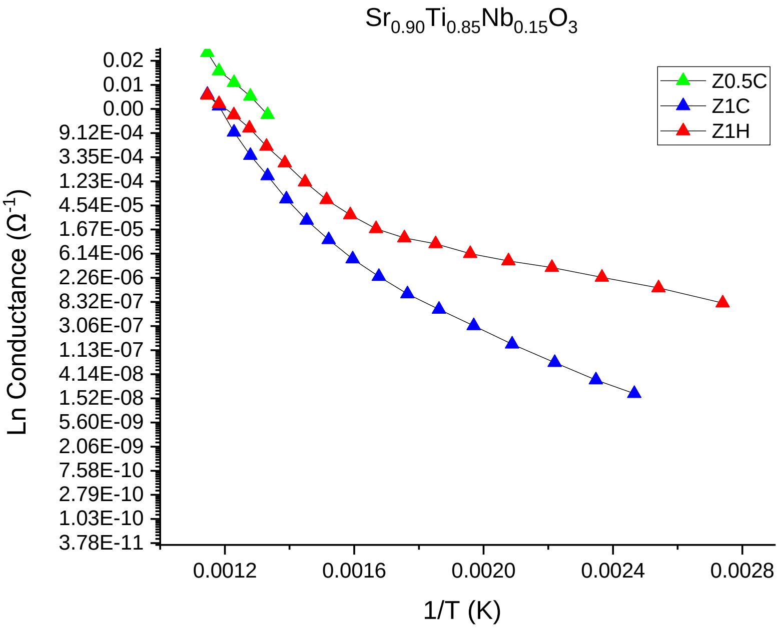

Figure 4.73: Conductance Arrhenius plot from Z″f_{max} data for $Sr_{0.90}Ti_{0.85}Nb_{0.15}O_3$ heating and cooling.

The capacitance graph is shown below for the $Sr_{0.90}Ti_{0.85}Nb_{0.15}O_3$ sample (Figure 4.74) and illustrates the separation between the heating and cooling in the Z1 plots at about 400-500 °C. It also illustrates the lack of Z0.5 peak, which was present in the similar $Sr_{0.925}Ti_{0.85}Nb_{0.15}O_3$ sample in the previous section.

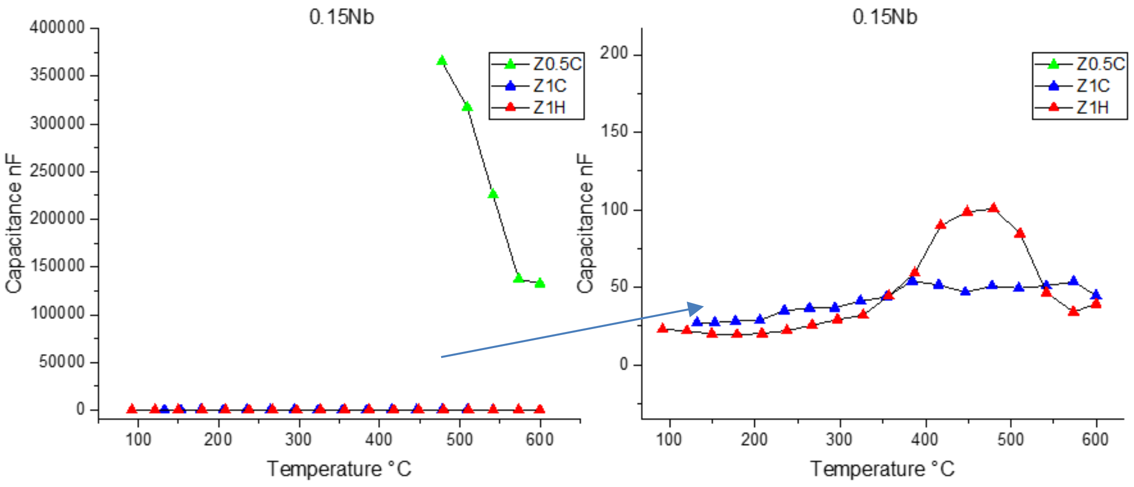

Figure 4.74: Capacitance vs temperature for $Sr_{0.90}Ti_{0.85}Nb_{0.15}O_3$.

Table 4-18: Calculated data for relaxation mechanisms from $Z''f_{max}$ data for $Sr_{0.90}Ti_{0.85}Nb_{0.15}O_3$.

Peak	Peak Temp. Range (°C)	$Z''f_{max}$ Ea (eV)	Ln σ_0	Approx. Capacitance (nF)
Z0.5C	600-450	1.13	11.23	350,000
Z1C (600-400 °C)	600-100	1.42	13.36	100
Z1C (400-100 °C)		0.55	-2.37	

The above trend continues into the $Sr_{0.90}Ti_{0.90}Nb_{0.10}O_3$ sample (Appendix). The complex impedance plots become more semi-circular at cooler temperatures. The disparity between the heating and cooling real and imaginary impedance data still exists, with the heating data showing more complete peaks across a range of frequencies and temperatures whereas the cooling data shows a more frequency and temperature independent behaviour. The activation energies of the $Z''f_{max}$ Arrhenius data show evidence of a transition between singly- and doubly-ionised oxygen vacancies at approximately 350 °C or electron/hole hopping. Interestingly, this sample is the only A-site vacancy sample to display a singular Z″ peak. (Figure 4.75). The electric modulus data of this sample varies from the $Sr_{0.95}Ti_{0.90}Nb_{0.10}O_3$ sample by the first modulus semi-circle being much less temperature-disperse.

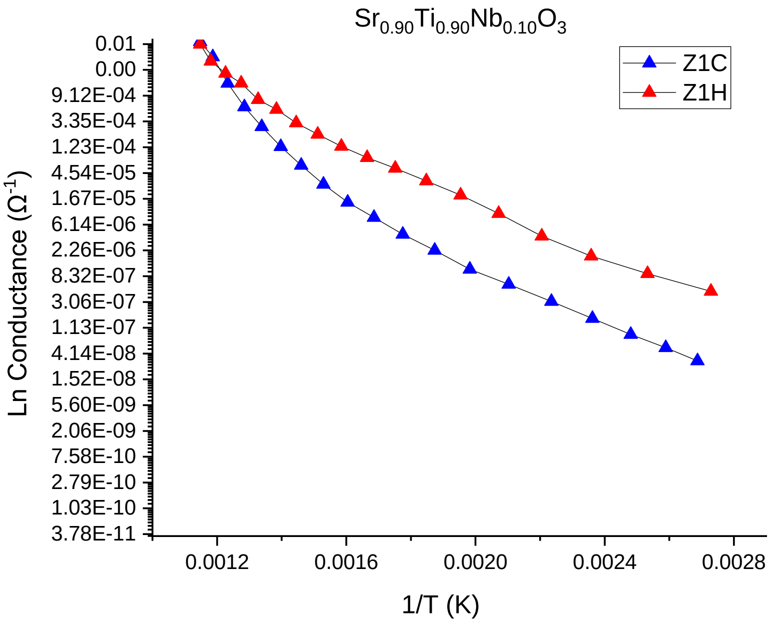

Figure 4.75: Conductance Arrhenius plot from $Z''f_{max}$ data for $Sr_{0.90}Ti_{0.90}Nb_{0.10}O_3$ heating and cooling.

The next three samples in this sample set (Nb_x=0.05, 0.01 and 0.005) were identified by XRD analysis to have a secondary TiO_2 phase present, due to the insufficient Nb-levels to compensate for the high level of Sr vacancies. These three samples tip the ratio of Sr/Ti and are the first samples in the A-site vacancy sample set to have more Ti than Sr, but it is not all completely incorporated into the solid solution due to the previously mentioned secondary phase.

The Z″ Bode plot (Figure 4.76) shows the reappearance of the Z2 peak on heating and cooling in the high frequency side of the graph which has been missing so far in the $Sr_{0.9}$ sample set, and the presence of the Z0.5 peak at low frequency on cooling extends to a much greater temperature range than for those seen previously but is still not seen in the heating data. The respective conductance Arrhenius graph shows the Z1 and Z2 peaks and a gradient change for the Z1H/C peaks at approximately 350 °C, and the calculated activation energies (Table 4-19) display values representing the diffusion of oxygen vacancies (0.8 eV) from 100-350 °C, followed by a change to electrons ionised from Sr vacancies transferring across grain boundaries (1.5 eV)[118], [113], [116]. The Z2 peak displays a value representative of singly-ionised oxygen vacancies (0.5 eV)[116] or electron/hole hopping.

The capacitance data in Figure 4.78 shows a much lower capacitance for the Z0.5C plot compared to all previous samples. It also shows some of the separation between the Z1 heating and cooling data which is not as obvious on the Arrhenius plot from Z″f_{max} data. The capacitance for the Z0.5 peak is surprisingly small compared to other samples that display the same peak.

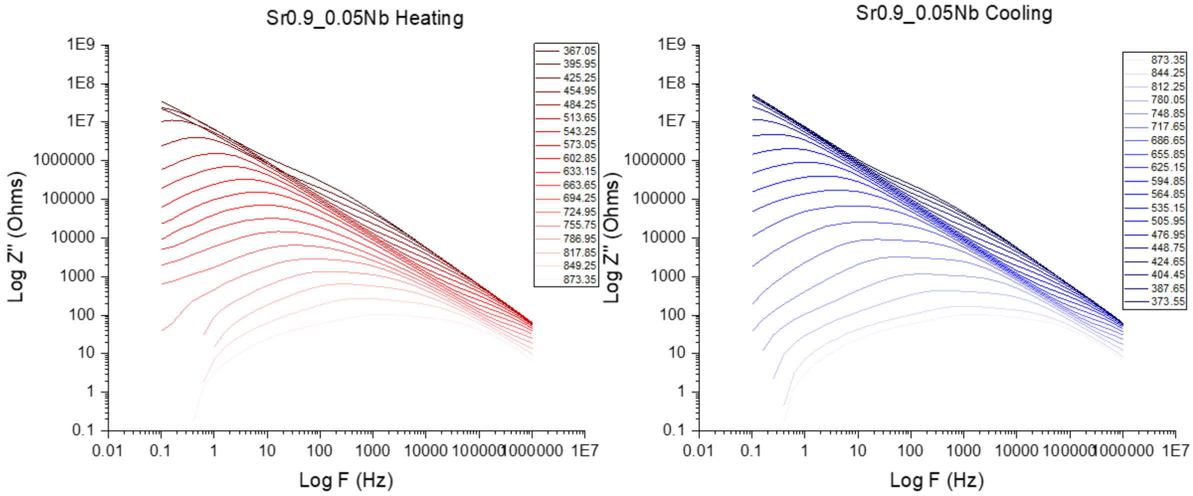

Figure 4.76: Frequency dependence of Log Z″ for $Sr_{0.90}Ti_{0.95}Nb_{0.05}O_3$, heating and cooling between 100-600 °C (380-900 K).

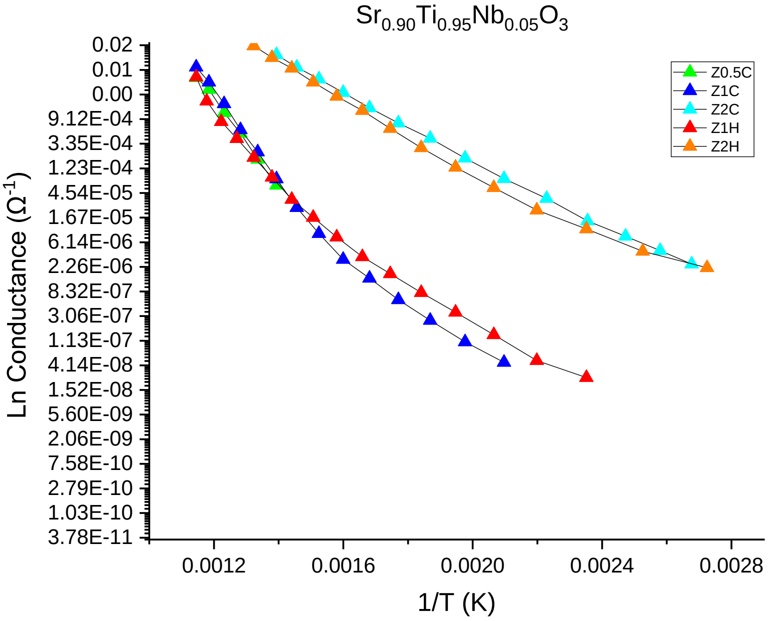

Figure 4.77: Conductance Arrhenius plot from Z″f_{max} data for $Sr_{0.90}Ti_{0.95}Nb_{0.05}O_3$ heating and cooling.

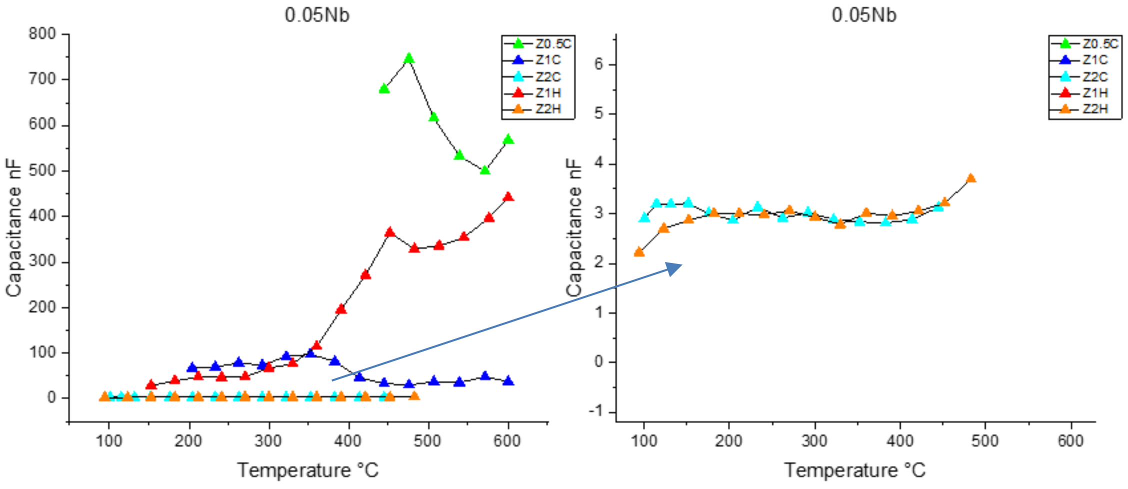

Figure 4.78: Capacitance vs temperature for $Sr_{0.90}Ti_{0.95}Nb_{0.05}O_3$.

Table 4-19: Calculated data for relaxation mechanisms from $Z''f_{max}$ data for $Sr_{0.90}Ti_{0.95}Nb_{0.05}O_3$.

Peak	**Peak Temp. Range (°C)**	**$Z''f_{max}$ Ea (eV)**	**Ln σ_0**	**Approx. Capacitance (nF)**
Z0.5C	600-450	1.54	15.31	750
Z1C (600-400 °C)	600-200	1.59	16.36	100
Z1C (400-100 °C)		0.83	1.78	
Z2C	500-100	0.57	4.73	4

The plot of complex electric modulus (Figure 4.79) shows a very similar picture to that of the $Sr_{0.90}Ti_{0.80}Nb_{0.20}O_3$ sample, with a small and large semi-circle, but a distribution of temperatures at the transition between the two circles (right). The plot of combined normalised Z″/M″ peaks return to no overlap between the Z″ and M″ peaks unlike the previous three samples in this set, suggesting a return to more short range relaxation mechanisms. There is also minimal difference between the heating and cooling data in this sample.

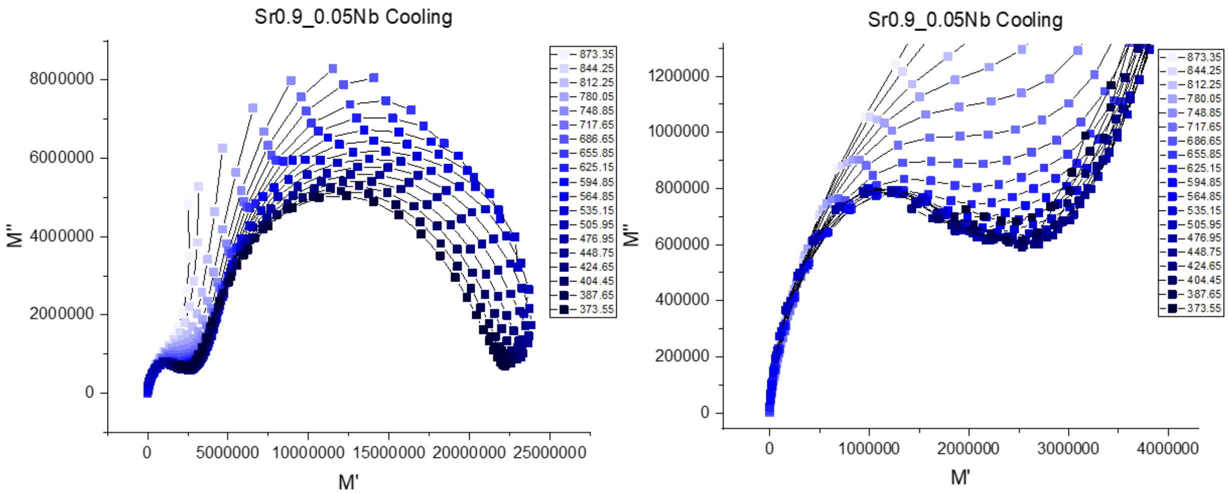

Figure 4.79: M′ vs. M″ for $Sr_{0.90}Ti_{0.95}Nb_{0.05}O_3$ at temperatures of 600-100 °C (380-900 K).

The Bode plots of Log Z″ are shown below (Figure 4.80) of the $Sr_{0.90}Ti_{0.99}Nb_{0.01}O_3$ and $Sr_{0.90}Ti_{0.995}Nb_{0.005}O_3$ samples. It was initially examined and found that the heating and cooling data for each sample are almost identical so only the cooling data for both samples are presented. The respective Arrhenius graphs of conductance are shown underneath and illustrate the main differences are the gradient and conductance of the Z2H/C plots. All collected data from Arrhenius conductance graphs and capacitance graphs are tabulated together for comparison purposes in (Table 5-3). Again, the capacitances of the Z0.5 peaks are considerably lower than for previous A-site vacancy samples.

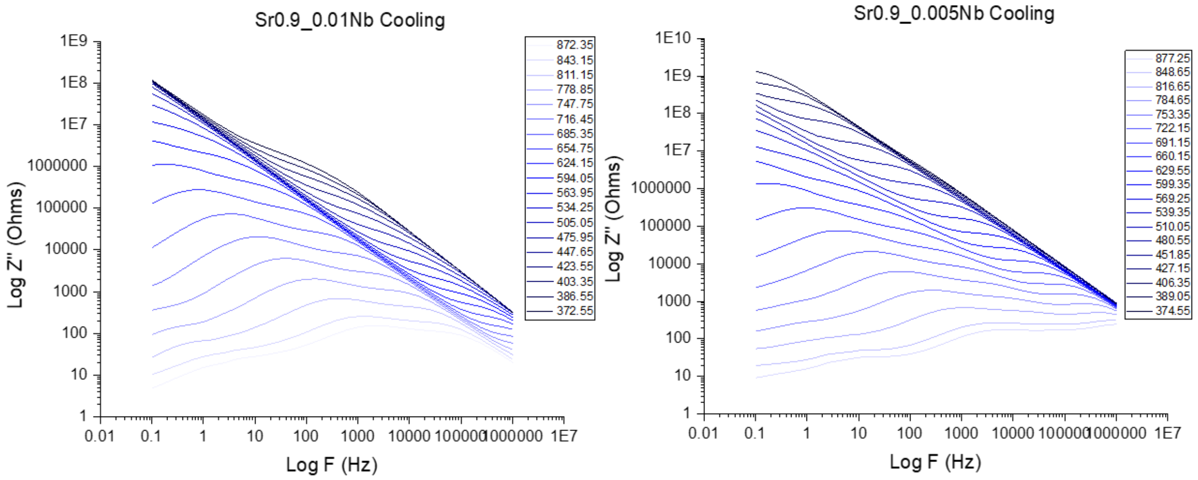

Figure 4.80: Frequency dependence of Log Z″ for $Sr_{0.90}Ti_{0.99}Nb_{0.01}O_3$ and $Sr_{0.90}Ti_{0.995}Nb_{0.005}O_3$ samples, cooling between 600-100 °C (380-900 K).

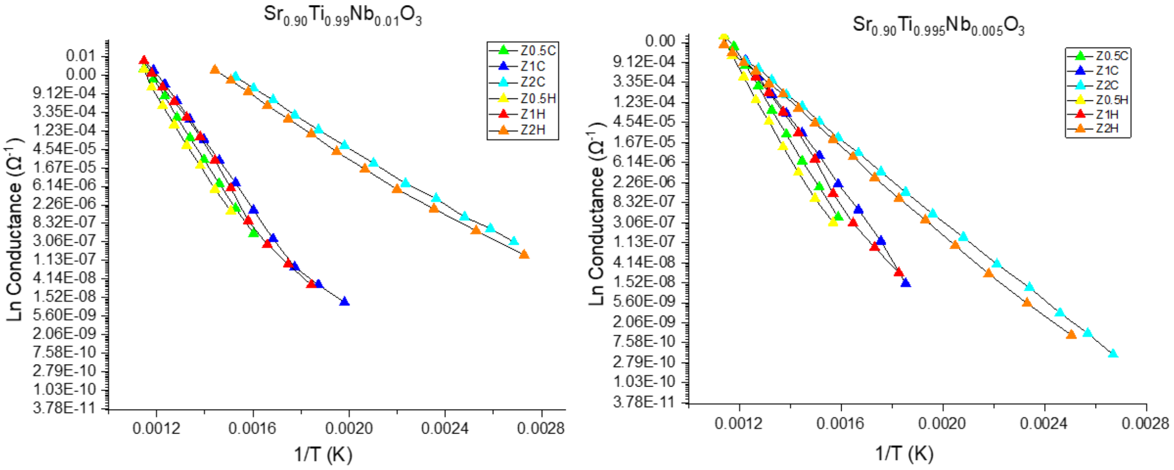

Figure 4.81: Conductance Arrhenius plot from $Z''f_{max}$ data for $Sr_{0.90}Ti_{0.99}Nb_{0.01}O_3$ and $Sr_{0.90}Ti_{0.995}Nb_{0.005}O_3$ samples heating and cooling.

Below are the electric modulus plots for the $Sr_{0.90}Ti_{0.99}Nb_{0.01}O_3$ and $Sr_{0.90}Ti_{0.995}Nb_{0.005}O_3$ samples. Both samples have a third semi-circle present, but the difference in the shape and size distribution between the arcs is most significant in the $Sr_{0.90}Ti_{0.995}Nb_{0.005}O_3$ sample. Both samples from the XRD analysis have approximately 3% TiO_2 secondary phase, and the third small semi-circle is the same in both samples, so it is presumed that the TiO_2 phase is responsible for this third arc in the modulus data. TiO_2 is insulative, and modulus is influenced by the most conductive elements of a material, so it would make sense that TiO_2 is represented by the smallest arc in modulus.

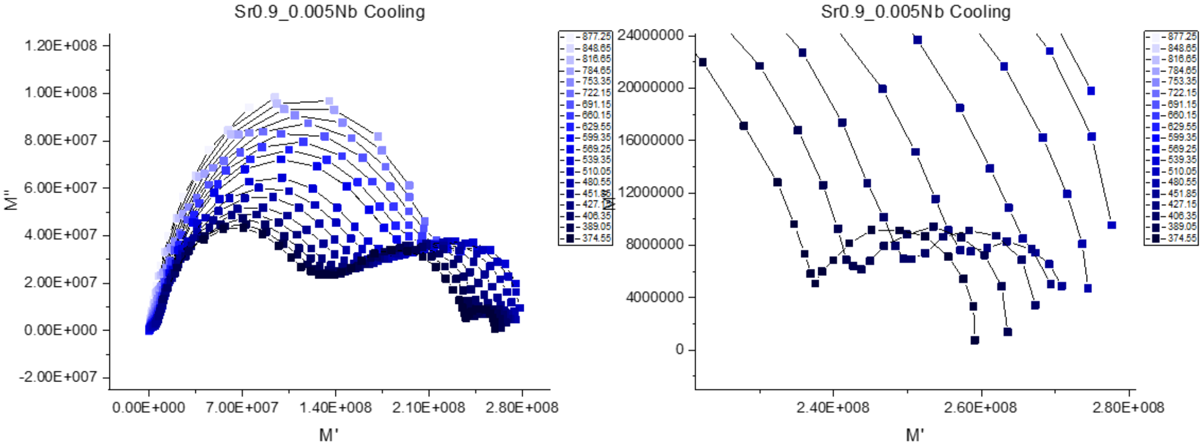

Figure 4.82: M′ vs. M″ for $Sr_{0.90}Ti_{0.99}Nb_{0.01}O_3$ and $Sr_{0.90}Ti_{0.995}Nb_{0.005}O_3$ samples at temperatures of 600-100 °C (380-900 K).

4.2.2.3 B-Site Nb-Doped $SrTiO_3$

Below are the normalised Z″/M″ plots for both the $SrTi_{0.998}Nb_{0.002}O_3$ and $SrTi_{0.98}Nb_{0.02}O_3$ samples to compare the two extremes of this sample set (Figure 4.83 and Figure 4.84). Both samples show no peak in Z″ until approximately 400 °C. The peak in Z″ that then appears in the low frequency region overlaps with the minor peak in the M″ data. Both samples have a second smaller peak in Z″ which overlaps with the major peak in M″ at 400 and 550 °C for modulus, and a second larger peak in impedance. The peaks move to higher frequencies with increasing temperature, and both sets of peaks for both samples overlap, indicating long range conduction mechanisms at the two higher temperature readings. The main difference, however, is that the peak representing the bulk modulus in the Nbx=0.02 sample moves off the scale at high temperatures and frequencies, indicating a semiconducting core from electron conduction as a result of Nb-doping. These samples had a blue coloration which is due to the electrons donated from the Nb reducing Ti^{4+} to Ti^{3+}.

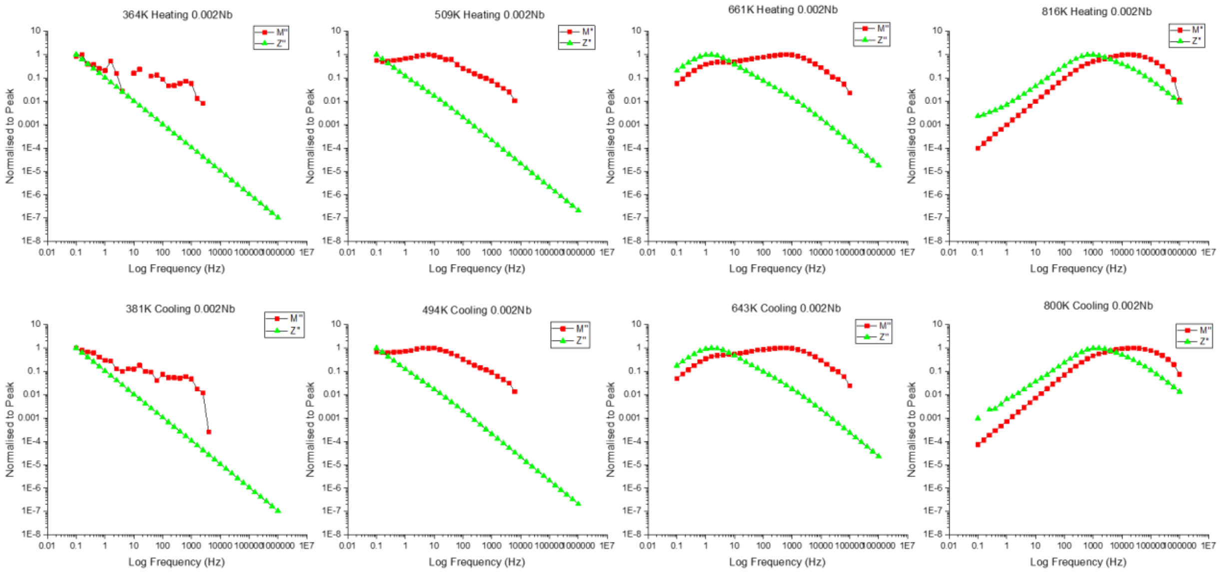

Figure 4.83: Normalised peaks of Z″ and M″ for $SrTi_{0.998}Nb_{0.002}O_3$ on heating and cooling.

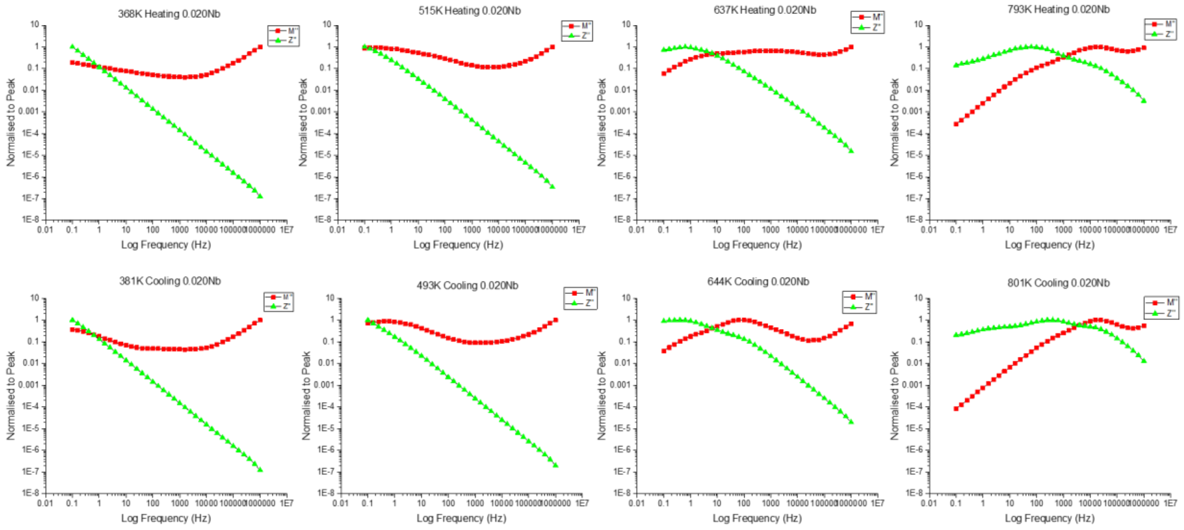

Figure 4.84: Normalised peaks of Z″ and M″ for $SrTi_{0.98}Nb_{0.02}O_3$ on heating and cooling.

The Bode plots of Log Z″ are shown below for the B-site Nb-doped samples (Figure 4.85). An extra peak is observed in the frequency dependent Z″ plot for the Nb_x=0.005 sample (named Z1.5 as it appears to be in the middle of the traditional Z1 and Z2 peaks at intermediate to high frequencies) compared to all previous samples so the main peaks that are present (Z0.5/Z1/Z2) will be compared.

The respective Arrhenius graphs of conductance from the Z″ data are shown below in Figure 4.86. A significant observation for the Nb_x=0.002 sample is the large difference in positioning of the Z1 peak for heating compared to cooling. This is not observed in other samples to this degree. There is also only a Z1 peak for this sample; the Z0.5 and Z2 are missing. This could be due to the very small concentration of Nb dopant which could be supplying enough donor electrons to annihilate any holes present in the material but not enough to behave as charge carriers, indicating the Z2 peak is related to electron or hole hopping. This could also be the reason for this sample being the most resistive in the complex impedance analysis (Section 4.2.1.3). The extracted information of activation energy, σ_0 and capacitance from the Z″ data are listed below in Table 5-4. It can be seen that the conductivity for the samples increases greatly with only the small increase in Nb, which is in contrast to the samples analysed previously with large concentrations of A-site vacancies. In the Nb_x=0.010 and 0.020 samples there is minimal difference between the Z0.5/Z1/Z2 peaks in their position, activation energy or σ_0 value. This suggests that the same relaxation mechanisms are occurring in both samples.

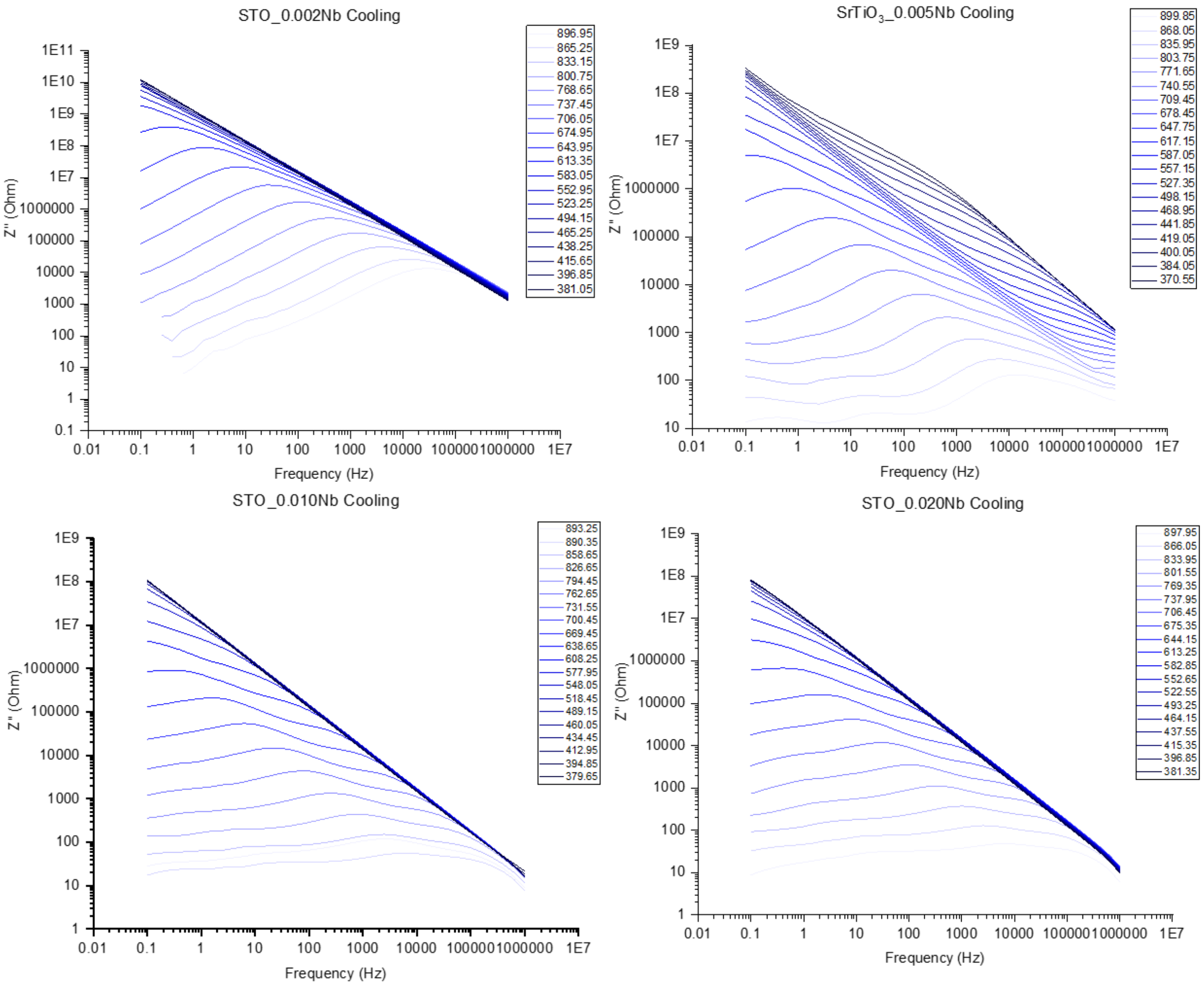

Figure 4.85: Frequency dependence of Log Z″ for $SrTi_{1-x}Nb_xO_3$ samples, cooling between 600-100 °C (380-900 K).

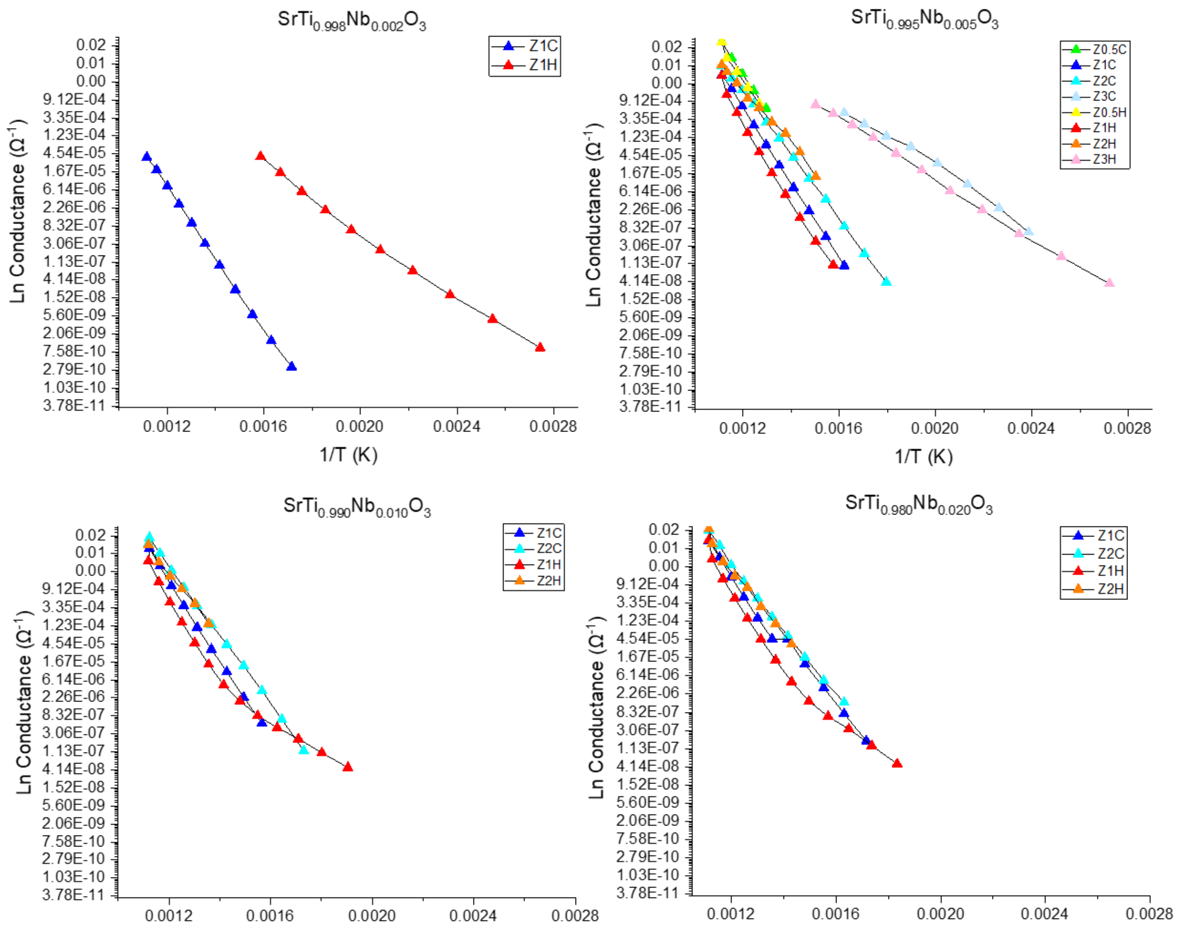

Figure 4.86: Conductance Arrhenius plot from Z″f_{max} data for $SrTi_{1-x}Nb_xO_3$ samples heating and cooling.

5 Discussion

Table 5-1 below lists potential mechanisms for defect formation in undoped and doped $SrTiO_3$. The conventional way of writing the equations doesn't always fit the experiments. i.e. in case Equation 1, the experiment to introduce a Sr vacancy doesn't result in excess SrO. Hence it is necessary to introduce "nul" which represents a completely empty unit cell. So in the instance of Equation 1 the Sr vacancy is caused by deliberately batching with too little strontium. Where there is nul on the LHS, there will always need to be an A-site, B-site and 3 O sites on the RHS [99]. If this is a departure from traditional Kroger Vink notation, then it is done for the sake of clarity.

In undoped $SrTiO_3$, we assume that the Equations 1 to 4 are negligible except in the case of deliberate or accidental non-stoichiometric $SrTiO_3$ (i.e. [Sr]/[Ti] ≠ 1)[99]. However, we can assume that oxygen vacancies are created via Equation 5, or due to small levels of acceptor impurities, Equation 11 (not necessarily Co, potentially Al/Fe etc.). Note that at high P_{O2} levels, the impurities may also be compensated by hole creation. Hence, in nominally undoped $SrTiO_3$ it is likely that at least two conduction species are present: oxygen vacancies and holes. This is supported by the Z1 and Z2 peaks in the Bode plots of Z'' for undoped $SrTiO_3$. It is unlikely to see both electron and hole conduction simultaneously in the same sample as the minority species should be annihilated by the majority carrier. The analysis in this thesis attempts a novel explanation for these phenomena as opposed to the conventional conclusion that this is the presentation of spatially separated bulk and grain boundary behaviour of the same species; but instead different species. A comparison of the pre-exponential factor (σ_0) determined from Arrhenius plots should indicate whether the concentration of charge carriers associated with a particular mechanism (identified from the activation energy) increases or decreases with doping concentration.

In the A-site vacancy samples it was intentional to invoke Equation 8 to compensate for Sr-deficiency by Nb-doping (or vice-versa). The only possible charge carriers resulting from this mechanism would be Sr vacancies, but it is not known how mobile these species are over the temperature range of the impedance measurements in this study. However, it seems likely that the Nb doping is not completely compensating for the Sr vacancies and electronic conduction still dominates in these samples, especially in the samples that have a strong blue colouration (Nb_x=0.20-0.30), with a M'' peak that moves to high frequencies and can't be seen in the scale shown. It would seem therefore that Equation 8 is not completely dominant and that there is some electron compensation (Equation 7) and titanium reduction from Ti^{4+} to Ti^{3+} resulting in the blue colouration of the samples (Equation 6). These electrons could also be annihilating oxygen vacancies.

Generally, we would consider cation vacancies to be immobile over most of the temperature range in these experiments. This does not mean that they are completely static; under the appropriate combinations of temperature and electric field they may be able to jump sites (e.g. during high temperature poling), but generally their movement can be discounted from the low field conductivity measurements. So, when authors refer to activation energies due to ionisation of Sr vacancies they are usually referring to hole conduction[50], [113] (Equation 1). However, the assumption is that in the Sr-deficient Nb-doped sample sets, the Sr vacancies are already doubly ionised and that compensation by holes is limited by the presence of the Nb. Looked at another way - electrons donated from the Nb annihilate the holes from the Sr-vacancy formation, like combining Equations 1 and 7 in our list of defect chemistry equations.

For the B-site Nb-doping Equations 7 through 10 are all "possible", but it is necessary to determine which is the most dominant or most likely compensation mechanism. Before carrying out any experiments, it was hypothesised that Equations 7 and 10 would be the most likely to occur. There is also the likelihood that undoped $SrTiO_3$ is acceptor doped by impurities (Equation 12) and that at very low Nb concentrations, the electrons from Equation 7 cancel the holes from the acceptor impurities. Experimental data must be considered to determine which mechanisms are taking in place in these material sets, and to what effect introducing large amounts of Sr vacancies has on the presence of defect species.

Table 5-1: Mechanisms for defect formation[99]**.**

Sr-Vacancy	**Equation**	**Effect**
1	$Sr_{Sr}^{\times} + \frac{1}{2}O_2 \rightarrow V_{Sr}'' + SrO + 2h^{\cdot}$ $nul + TiO_2 + \frac{1}{2}O_2 \rightarrow V_{Sr}'' + Ti_{Ti}^{\times} + 3O_O^{\times} + 2h^{\cdot}$	hole compensation
2	$Sr_{Sr}^{\times} + O_O^{\times} \rightarrow V_{Sr}'' + V_O^{\cdot\cdot} + SrO$ $nul + TiO_2 \rightarrow V_{Sr}'' + V_O^{\cdot\cdot} + Ti_{Ti}^{\times} + 2O_O^{\times}$	partial Schottky
Ti-Vacancy		
3	$T_i^{\times} + O_2 \rightarrow V_{Ti}'''' + TiO_2 + 4h^{\cdot}$ $nul + SrO + O_2 \rightarrow V_{Ti}'''' + Sr_{Sr}^{\times} + 3O_O^{\times} + 4h^{\cdot}$	hole compensation
4	$T_i^{\times} + 2O_O^{\times} \rightarrow V_{Ti}'''' + 2V_O^{\cdot\cdot} + TiO_2$ $nul + SrO \rightarrow V_{Ti}'''' + 2V_O^{\cdot\cdot} + Sr_{Sr}^{\times} + O_O^{\times}$	partial Schottky
O-Vacancy		
5	$O_O^{\times} \rightarrow V_O^{\cdot\cdot} + \frac{1}{2}O_2 \uparrow +2e'$	electron compensation
6	$Ti_{Ti}^{\times} + e' \rightarrow Ti_{Ti}'$	Ti reduction
Nb-doping		
7	$Nb_2O_5 + 2Ti_{Ti}^{\times} \rightarrow 2Nb_{Ti}^{\cdot} + 2TiO_2 + \frac{1}{2}O_2 \uparrow + 2e'$ $nul + 2SrO+Nb_2O_5 \rightarrow 2Sr_{Sr}^{\times} + 2Nb_{Ti}^{\cdot} + 6O_O^{x} + \frac{1}{2}O_2$ $\uparrow + 2e'$	electron compensation
8	$Nb_2O_5 + Sr_{Sr}^{\times} + 2Ti_{Ti}^{\times} \rightarrow 2Nb_{Ti}^{\cdot} + V_{Sr}'' + SrO + 2TiO_2$ $nul + SrO + Nb_2O_5 \rightarrow 2Nb_{Ti}^{\cdot} + Sr_{Sr}^{\times} + V_{Sr}'' + 6O_O^{\times}$	Sr vacancy compensation
9	$2Nb_2O_5 + 5Ti_{Ti}^{\times} \rightarrow 4Nb_{Ti}^{\cdot} + V_{Ti}'''' + 5TiO_2$ $nul + 5SrO + 2Nb_2O_5 \rightarrow 5Sr_{Sr}^{\times} + 4Nb_{Ti}^{\cdot} + V_{Ti}'''' + 15O_O^{\times}$	Ti vacancy compensation
10	$2Ti_{Ti}^{\times} + 3O_O^{\times} + V_O^{\cdot\cdot} + Nb_2O_5 \rightarrow 2Nb_{Ti}^{\cdot} + 4O_O^{\times} + \frac{1}{2}O_2$	oxygen vacancy annihilation

Co-doping		
11	$Ti_{Ti}^{\times} + O_O^{\times} + CoO \rightarrow Co_{Ti}'' + V_O^{\cdot\cdot} + TiO_2$ $nul + SrO + CoO \rightarrow Sr_{Sr}^{\times} + Co_{Ti}'' + 2O_O^{\times} + V_O^{\cdot\cdot}$	oxygen vacancy compensation
12	$Ti_{Ti}^{\times} + CoO \rightarrow Co_{Ti}'' + \frac{1}{2}O_2 \uparrow + 2h^{\cdot}$	hole compensation

Below is the compiled data for all Nb doped samples, including the peak temperature range, the capacitance, the σ_0, and the activation energy of each mechanism (Table 5-3 and Table 5-4). The table immediately below (Table 5-2) shows the room temperature capacitances taken on a Berlincourt d_{33} meter measured at 1 kHz. The values displayed match up with the “Z2” capacitance range in the accumulated data below, with the exception of the Nb_x=0.10 and 0.15 samples which do not display a Z2 peak in the impedance data in order to be able to extract capacitance data. This supports the method of extraction of capacitance data from the imaginary impedance data as valid as it matches the capacitance data from a separate analysis method. This also indicates that the overriding contributor to the average capacitance or general electrical properties could be the Z2 peak, as these are the values that are displayed for each sample when room temperature measurements were taken. When two capacitors are in series, the following equation applies[99]:

$$C_T = \left(\frac{1}{\frac{1}{C_1} + \frac{1}{C_2}}\right) = \frac{C_1 C_2}{C_1 + C_2}$$

If C_2 is a very large capacitance value such as those for the Z0.5 peak, then you can rule out the bottom C_1 as the following, resulting in cancellation of the C_2:

$$= \frac{C_1 \cancel{C_2}}{\cancel{C_2}}$$

This is why the smallest (bulk) capacitance is the one that is measured as the average total capacitance, as shown by the table below (Table 5-2).

Table 5-2: Room temperature capacitance values for $Sr_{1-x/2}Ti_{1-x}Nb_xO_3$ samples.

Sample	RT C (nF)
$SrTiO_3$	0.13
Nb0.10	2.44
Nb0.15	4.20
Nb0.20	5.71
Nb0.25	5.20
Nb0.30	4.41

The Z0.5 peak in the Arrhenius conductance graphs from the Z″ data shows activation energies between 1.3-1.7 eV and only occurs in the higher temperature range (between 400-600 °C) and the low frequency range. It also consistently has very high capacitance values for all samples, indicating that the relaxation mechanism could be occurring in a resistive section of the material such as the grain boundary. The high capacitance indicates it could also be an electrode effect with mixed conduction[100]. The Z0.5 peak occurring only in the high temperature region is thought to be due to the extra energy needed to cross the more resistive grain barrier.

The Z0.5 peak is missing in samples $SrTiO_3$, $Sr_{0.9}Ti_{0.9}Nb_{0.10}O_3$ and $SrTi_{0.998}Nb_{0.002}O_3$ and present in all other samples. Initially it was thought that this meant the Z0.5 peak was related to Sr vacancies, because there are Sr vacancies in both of the A-site vacancy sample sets, and there are likely to be Sr vacancies created in the B-site Nb-doped sample set to charge compensate for the Nb (Equation 8). It is thought that in the Nb_x=0.002 B-site doped sample the Nb concentration is so low that the electrons donated by the Nb annihilate any holes present resulting in no compensating Sr vacancies or donated electrons, which is also why this sample is the most resistive out of all Nb-doped samples. To investigate if the Z0.5 is a result of a Sr-deficiency, however, when consulting the Bode plots for Sr-deficient non-stoichiometric $SrTiO_3$ samples the Z0.5 peak was not present. It *was* however present in the Sr-excess samples, see below (Figure 5.1) but not in the $Sr_{1.002}TiO_2$ sample. This indicates that the Z0.5 peak could in some way be related to a non-stoichiometry between Sr/Ti, and that the non-stoichiometry in $Sr_{1.002}TiO_3$ was not sufficient enough to cause the Z0.5 peak. This is supported by the fact that the Z0.5 peak is also not present in undoped $SrTiO_3$ or $Sr_{0.9}Ti_{0.9}Nb_{0.10}O_3$ where the Sr and Ti levels are balanced. One consideration was that it was related to an excess of Sr relative to Ti; perhaps related to the production of SrO[45]:

$$\frac{1}{2}O_2(g) + 2e' + Sr_{Sr}^{x} \rightleftarrows V_{Sr}'' + SrO_{SP}$$

There is discussion in literature that the formation of compensating Sr vacancies (Equation 8) lead to the Sr and O migrating to the grain boundaries to form SrO layers[65], [66] which could be the case for the B-site Nb-doped samples. A migration of Sr to the grain boundaries and the formation of RP phases could also be true for the Sr-excess samples. However, in the A-site vacancy sample sets we would not expect there to be SrO in the grain boundaries as they were made to be compositionally significantly Sr-deficient. There are also three samples in Sr0.9 set (Nb_x=0.05-0.005) which tip the ratio and have a higher relative Ti content compared to Sr and the Z0.5 peak is still present. It could be possible that the Z0.5 peak represents the transition of electrons across a grain boundary composed of either an excess of Sr *or* Ti, or electrons across an electrode. It is noted that the samples with the Ti secondary phase in the Sr0.9 sample set had much smaller capacitance values for the Z0.5 peak. These samples could have an excess of Ti in the grain boundaries, leading to a thicker grain boundary as well as the secondary phase TiO_2, resulting in the lower capacitance values for the Z0.5 peak. The presence of a Schottky barrier[116] or space charge region at the grain boundary is not ruled out as a possible explanation for the Z0.5 peak as it would occur at low frequencies and high temperatures and require extra energy to cross; a Schottky barrier at the grain boundary is another similar explanation caused by an excess of Sr or Ti, or at the electrode interface.

The activation energies for the Z0.5 and Z1 peaks in the Arrhenius conductance graphs are often very similar if not the same. They were clearly separate peaks however, occurring in different frequency ranges. This indicates it could be the same defect species moving through different microstructural areas of the material for example the resistive grain boundary or more conductive bulk.

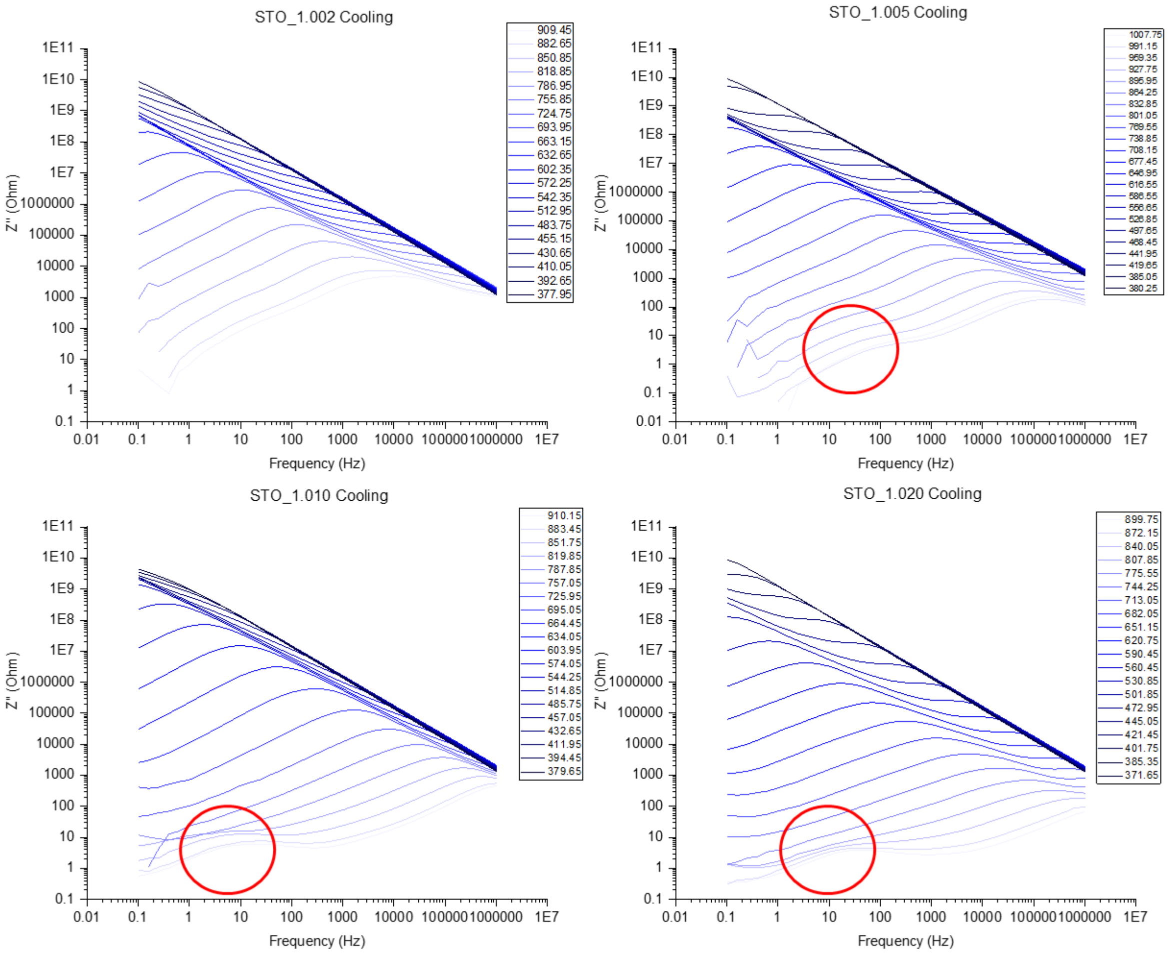

Figure 5.1: Frequency dependence of Log Z″ for Sr-excess non-stoichiometric $SrTiO_3$ samples between 600-100°C.

In the conductance Arrhenius graphs for all Nb-doped samples the Z1 peaks frequently present an activation energy of approximately 1.4-1.8 eV. For the $Sr_{0.9}$ sample set this activation energy only exists between temperatures of 600-300 °C; after that the Z1 has an activation energy between 0.5-0.9 eV. This was separated in the table below (Table 5-3) to Z1a and Z1b for clarity. The Z1b (low temperature section) peak in Table 5-3 for the $Sr_{0.9}Ti_{1-x}Nb_xO_3$ samples where Nb_x=0.005, 0.01 and 0.05, has an activation energy between 0.7 and 1 eV which is indicative of oxygen vacancies. These samples are the only Nb-doped samples to have a composition with an excess of Ti relative to Sr. As discussed by Chan et al. and referenced in Section 2.2.1, an excess of Ti can result in the formation of oxygen vacancies via the following equation[46]:

$$TiO_2 \rightleftarrows Ti_{Ti}^{x} + 2O_O + V_{Sr}'' + V_O^{\bullet\bullet}$$

For the Z1b peak that occurs in the remaining $Sr_{0.9}$ samples the activation energy is approximately 0.5 to 0.7 eV. This could still represent oxygen vacancies. When consulting the σ_0 value for this sample set it is found to decrease with increasing Nb concentration. Equation 10 shows a mechanism whereby the addition of Nb annihilates oxygen vacancies so as the dopant composition increases from Nb_x=0.005 to Nb_x=0.19, the σ_0 value decreases representing a decrease in the number of oxygen vacancies[119] as the Nb content increases, annihilating more oxygen vacancies:

$$Nb_2O_5 + V_O^{\cdot\cdot} \rightarrow 2Nb_{Ti}^{\cdot} + 4O_O^{\times} + \frac{1}{2}O_2$$

The Z1 peak for the $Sr_{1-x/2}$ samples and the remaining Z1a (high temperature) peak for the $Sr_{0.9}$ samples has an activation energy of approximately 1.6-1.9 eV. The values for σ_0 do not particularly change with increasing donor dopant or Sr vacancy content in the samples with intentional A-site vacancies. The σ_0 value does, however, increase for the Z1 peak across the B-site Nb-doped samples, which also has an activation energy of approximately 1.7-1.9 eV. The activation energy similarity indicates that it is the same charge carrier species for the Z1 peak across all samples, but that the species is increasing only in the B-site Nb-doped sample set as Nb concentration increases. As previously discussed, as Nb is added to the B-site of $SrTiO_3$, electrons are donated by the Nb, and Sr vacancies are produced in order to charge compensate[62]. As the Nb increases, the number of electrons in the system increases, as do the number of Sr vacancies, raising the σ_0 value and the conductivity of the samples (Equations 7 and 8). It is thought that the Z1 peak could represent the conduction of electrons from the ionisation of Sr vacancies from the below equation:

$$V_{Sr}'' \leftrightarrow V_{Sr}' + e'$$

If this is the case it would be expected that the σ_0 value would increase with increasing Sr vacancy concentration. However, the σ_0 does not increase in the $Sr_{1-x/2}$ samples because of the charge compensation scheme at play; the Sr vacancies were intentionally added by the leaving out of Sr in the sample preparation process; they were not created as a result of Nb doping. The Sr vacancies present can still be ionised resulting in the Z1 peak, but the number of charge carriers is not increasing because as the Nb dopant increases in each sample, as do the number of Sr vacancies to match it. The observation of the σ_0 values not increasing with increasing dopant concentration in the $Sr_{1-x/2}$ sample set shows why these samples did not increase vastly in conductivity in Section 4.2.1.2 despite the large increase in Nb content compared to the B-site Nb-doped sample set. The intentional introduction of large levels of Sr vacancies from the outset, without them being produced as a response to the donor dopant addition meant an equilibrium was reached whereby the Sr vacancies increased as the Nb content rose, or vice versa, in order to stem the increase in production of charge carriers able to contribute to conduction. The lack of increase in σ_0 observed in the Z1a peak for the $Sr_{0.9}$ samples is due to a self-compensation scheme that must be happening in the system that remains after it begins to eject the excess Ti as a secondary phase. The large number of pre-existing Sr vacancies compensates for the Nb addition. The rise in conductivity of the $Sr_{0.9}$ samples in Section 4.2.1.2 was observed due to the increase in oxygen vacancy concentration from the excess of Ti and lack of charge compensation provided by the small levels of Nb-dopant. The Z1 peak in general across all samples has capacitance values between 20-300 nF. This is larger than that seen for the Z2 peak but magnitudes smaller than that of the Z0.5 peak, suggesting that the charge carrier species is moving through a more conductive area of the material, such as the bulk/grain.

The Z2 peak consistently displays values of approximately 0.3-0.4 eV which according to literature could be attributed to two possible mechanisms. The first is the single ionisation of oxygen vacancies [84][81][116]. The second is the result of electron or hole hopping[60]. A key sample to help distinguish that the second possibility was most likely is the Nb_x=0.002 B-site doped sample. The Nb_x=0.002 sample only has the Z1 peak and one R1 impedance contribution in the complex impedance analysis. If the donated electrons from the Nb_x=0.002 B-site doped sample are annihilating any holes present from acceptor impurities, and the Nb_x=0.002 sample has no Z2 peak, it could be inferred that the Z2 peak represents hole conduction. Equivalently the Z2 peak could represent electron conduction from the electrons donated from the Nb, but in the case of the Nb_x=0.002 they are not observed as a peak because they are annihilating holes and not contributing to conduction. There are other mechanism equations that suggest the donor electrons from Nb could locate at and reduce Ti^{4+} ions to Ti^{3+} ions (Equation 6), however the association of a free electron at a Ti ion does not necessarily remove that electron from conduction as these electrons are thought to contribute to conduction by hopping between Ti ions. The presence of Ti^{3+} in titanates is normally associated with a blue colouration of the sample, as seen in some of the higher Nb-doped samples in this thesis. Hence any blue coloration is a sign that there is at least electron conduction. This would indicate Equations 6 and 7 above are taking place (electron production). In the $Sr_{1-x/2}$ sample set the blue colouration is only in the Nb_x=0.20-0.30 samples, and these are the only samples in that set with a Z2 peak. Other samples that have no Z2 peak are $Sr_{0.9}Nb_x$=0.10, 0.15 and 0.19 This could be a microstructural phenomenon, i.e. if the Z2 peak is a bulk observation and these samples all have largely grain boundary based contributions then it may not appear.

In conclusion, it is thought that the Z0.5 high temperature low frequency peak observed in the Z″ Bode plots represents the effects of charge carriers across grain boundaries due to excess Sr or Ti. Z1 represents the ionisation of Sr vacancies and oxygen vacancies in the bulk, including perhaps Schottky barrier/space charge phenomena. Finally, the Z2 peak represents electron hopping in the bulk, and perhaps locating around Ti^{4+} ions reducing them to Ti^{3+} and the highly conductive core of the sample grains seen in SEM data, and resulting in the blue colouration of the pellets.

Table 5-3: Table of compiled data for A-site vacancy samples.

			$Sr_{1-x/2}Ti_{1-x}Nb_xO_3$					$Sr_{0.9}Ti_{1-x}Nb_xO_3$					
Cooling Data	**Peak**	**0**	**0.10**	**0.15**	**0.20**	**0.25**	**0.30**	**0.005**	**0.01**	**0.05**	**0.10**	**0.15**	**0.19**
Ea (eV)	**Z0.5**	-	1.69	1.28	1.42	1.64	1.70	0.77	1.72	1.54	-	1.13	1.60
	Z1 (Z1a/Z1b)	2.11	1.83	1.60	1.55	1.73	1.72	0.65	1.54 0.97	1.59 0.83	1.34 0.49	1.42 0.55	1.71 0.67
	Z2	0.88	-	-	0.299	0.317	0.38	0.381	0.667	0.575	-	-	-
σ_0	**Z0.5**	-	9.77E+07	2.14E+05	1.28E+06	2.22E+07	1.21E+08	2.52E+03	3.55E+07	4.44E+06	-	7.56E+04	2.21E+07
	Z1 (Z1a/Z1b)	1.62E+07	1.20E+08	2.42E+07	1.40E+06	4.03E+07	2.99E+07	5.58E+02	5.23E+06 5.05E+01	1.27E+07 5.92E+00	1.17E+05 8.56E-02	6.33E+05 9.33E-02	1.38E+07 2.46E-01
	Z2	2.94E+01	-	-	3.56E-01	3.08E-01	6.08E-01	1.09E+01	2.74E+02	1.13E+02	-	-	-
Capacitance (nF)	**Z0.5**	-	60,000	90,000	70,000	355,000	600,000	350	400	750	-	350,000	140,000
	Z1 (Z1a/Z1b)	3	150	50	125	300	300	20	20	100	35	50	175
	Z2	0.07	-	-	3	4	3	1	1	3	-	-	-
Temp Range (°C)	**Z0.5**	-	600-575	600-550	600-500	600-450	600-500	600-350	600-350	600-450	-	600-475	600-450
	Z1 (Z1a/Z1b)	600-400	600-300	600-300	600-300	600-350	600-300	550-275	600-280 280-230	600-400 400-100	600-400 400-100	600-400 400-100	600-440 440-190
	Z2	600-100	-	-	600-100	600-100	600-150	600-100	400-100	450-100	-	-	-

Table 5-4: Table of compiled data for B-site Nb-doped samples.

		$SrTi_{1-x}Nb_xO_3$				
Cooling Data	**Peak**	**0**	**0.002**	**0.005**	**0.01**	**0.02**
Ea (eV)	**Z0.5**	-	-	1.72	1.60	1.87
	Z1	2.11	1.95	1.80	1.84	1.94 1.60
	Z2	0.88	-	0.73	1.64	1.57
σ_0	**Z0.5**	-	-	1.03E+08	1.52E+07	5.37E+08
	Z1	1.62E+07	1.43E+05	4.67E+07	1.81E+08	7.85E+08 1.05E+07
	Z2	2.94E+01	-	6.02E+02	2.72E+07	9.45E+06
Capacitance (nF)	**Z0.5**	-	-	130,000	150,000	120,000
	Z1	3	0.6	120	250	250
	Z2	0.07	-	1	15	20
Temp Range (°C)	**Z0.5**	-	-	600-500	600-525	600-450
	Z1	600-400	600-300	600-350	600-350	600-300
	Z2	600-100	-	400-100	600-300	600-350

6 Conclusions

Samples of non-stoichiometric, acceptor-doped, and Nb-doped $SrTiO_3$ were produced using the mixed oxide solid state reaction technique. All samples were analysed using XRD and impedance spectroscopy and some samples were further analysed using permittivity vs. temperature measurements and SEM/TEM analysis. XRD analysis revealed the increase in unit cell size by the addition of Nb on the Ti B-site, but that the inclusion of Sr vacancies allowed more Nb incorporation. B-site doping of both acceptors (Co and Mn) and donor dopant Nb proved that the absent 100/210 peaks was as a result of large amounts of A-site vacancies. Finally, XRD analysis provided the first indication of TiO_2 phase segregation due to insufficient charge compensation by Nb in the $Sr_{0.9}$ sample set. This was confirmed in the SEM images of this sample set with TiO_2 separation confirmed by elemental analysis.

Initial impedance spectroscopy analysis revealed high conductivities in acceptor-doped $SrTiO_3$, ruling samples with high levels of acceptor doping out from further studies into defect dipoles due to the inability to align possible defects with a field. Small amounts of Nb doping on the B-site resulted in increasing conductivity. This was not found to be the case with the A-site vacancy compensation scheme samples, however the $Sr_{0.9}$ sample set did see increases in conductivity.

Deeper analysis of the impedance and modulus data revealed that the electrical behaviour of all Nb-doped $SrTiO_3$ samples appears to be dominated by electron conduction produced from a variety of defect mechanisms. In the B-site Nb-doped samples these electrons are much more influential in the conductivity than in the A-site vacancy samples, as evidenced by the blue colouration of pellets at much smaller Nb concentrations, indicating the reduction of Ti^{4+} to Ti^{3+} and the observed higher conductivity reported in Section 4.2.1.3. The influence of Sr vacancies is apparent from the lack of increase in conductivity in the $Sr_{1-x/2}$ samples (Section 4.2.1.2) despite ten times the increase in Nb content. The addition of large concentrations of Sr vacancies to the perovskite system enabled it structurally to accommodate large amounts of Nb, but it also significantly reduced the effect of increasing conductivity seen by Nb doping. Equivalently, the large amount of Nb doping enabled the $SrTiO_3$ system to tolerate large amounts of Sr deficiencies (up to 15%) by charge compensation. The vacancy/donor compensation scheme is key to maintaining the $SrTiO_3$ perovskite structure as proved by the $Sr_{0.9}$ sample set which began to eject TiO_2 as a secondary phase. The level of Nb in the lower doped samples was insufficient to charge compensate for the level of Sr vacancies present.

Despite the influence of Sr vacancies, the majority of the normalised Z″/M″ comparison plots showed long range interactions indicating charge carriers such as electrons and oxygen vacancies are mostly at play, suggesting that none of the relaxation mechanisms observed were due to local defect pairings such as defect dipoles. This does not mean that defect dipoles are not present, but that they are not contributing to the conduction and relaxation peaks observed in the impedance analysis of the materials. There was also a Nb-rich semiconducting core observed in the $Sr_{1-x/2}$ samples resulting in a high conductivity and a missing bulk modulus peak The challenge will be to reduce the conductivity of these materials sufficiently to be able to orient any defect dipoles.

Understanding which defect mechanisms are taking place in a material in order to produce charge carriers is important as it can then inform decisions in the future as to how best to modify the samples and processing conditions to affect change in the material properties. The conclusions of this thesis are "tentative", as they are currently unproven by physical characterisation techniques (see Future Work). This thesis has, however, successfully shown the importance of manipulating the defect chemistry of a system in order to create a balanced vacancy compensation scheme. This fundamental research shows the interplay of A-site vacancies and high levels of donor doping and their effect on maintaining a single phase perovskite-structured $SrTiO_3$, whilst also affecting the electrical properties of the material in a way that is not achieved by B-site doping alone.

6.1 Future Work

This thesis is the stepping stone of research into engineering and manipulating chemical defects in perovskite oxides in order to tune electrical properties. From these initial investigations there are a number of subsequent experiments that could be carried out in the future to develop on the results obtained in this work.

One important way to investigate the defect chemistry of a system is to carry out sintering and annealing studies in a variety of atmospheres to observe how the electrical properties of the samples change. A major improvement to the experimental technique used in this thesis would be to carry out impedance analysis tests inside a furnace whilst the test samples are subjected to different atmospheres, for example oxygen or H_2/argon combinations. Impedance and conductivity graphs could then be made to determine the theoretical dependence on oxygen partial pressure and temperature simultaneously, which could confirm which defect mechanisms are at play in each sample, particularly those with oxygen vacancies.

A new co-doping study should be carried out with the addition of Mn alongside the donor dopant Nb to the A-site vacancy compensation sample set. This may help to trap free electrons [15] and may play a role in controlling oxygen vacancy concentration [14]. This was observed by Ryu and Dickey in work on Mn/Y co-doped $BaTiO_3$ which saw an increase in resistivity in comparison to purely Mn-doped $BaTiO_3$[58]. Once conductivity has been minimised as much as possible an in depth poling study should be carried out, with variations in poling time, voltages, and temperatures. Initial work of this type has been carried out but is not reported in this thesis as it was incomplete.

Due to the impact of the Covid-19 pandemic there were significant laboratory closures and restrictions on travel, making it difficult to carry out work at external research facilities and employ techniques such as EPR and neutron diffraction to provide quantifiable characterisation of the defects present in these materials. It is clear from this research that oxygen vacancies play some part in the defect chemistry and electrical transport properties of the materials in this thesis, as with many perovskite oxides. Neutron diffraction is a useful technique to analyse the oxygen vacancy concentration and how it varies with dopant concentration in conjunction with A-site vacancies. This could in turn help to identify any oxygen vacancy-based defect dipoles. EPR is used extensively in literature to characterise defects and their associations and environments which would be useful moving forward to then attempt to manipulate said defects in these materials.

Undoped $SrTiO_3$ has a low temperature incipient ferroelectric phase. Low temperature characterisation experiments should be carried out on the A-site vacancy sample sets in order to observe any changes in phase transition. This could be done using low-temperature XRD experiments and also by repeating experiments such as permittivity vs. temperature at low temperatures and impedance analysis using the new cryostat situated at the University of Leeds. These low temperature techniques could also be used to investigate the bulk response of these materials as it has not been possible in the current temperature range due to the high levels of electronic conduction.

The new understanding of the defect chemistry of these systems should now lead to a strategy for characterising and manipulating defect dipoles in the future.

References

[1] F. Yuan, *Structural Health Monitoring in Aerospace Structures*. Elsevier, 2016.

[2] K. Uchino, *Advanced Piezoelectric Materials*. Woodhead Publishing Series, 2010.

[3] B. Jaffe, W. R. Cook., and H. Jaffe, *Piezoeletric ceramics*. Academic Press Inc. London, 1971.

[4] A. J. Moulson and J. M. Herbert, *Electroceramics*, 2nd ed. Chichester: John Wiley and Sons, 2003.

[5] J. C. Slater, 'The lorentz correction in barium titanate', *Phys. Rev.*, vol. 78, no. 6, pp. 748–761, 1950, doi: 10.1103/PhysRev.78.748.

[6] W. Heywang, K. Lubitz, and W. Wersing, *Piezoelectricity: Evolution and Future of a Technology*. Springer Science, 2008.

[7] T. D. Huan, V. Sharma, G. A. Rossetti, and R. Ramprasad, 'Pathways towards ferroelectricity in hafnia', *Phys. Rev. B - Condens. Matter Mater. Phys.*, vol. 90, no. 6, p. 064111, 2014.

[8] Y. Xu, *Ferroelectric Materials and Their Applications*. Amsterdam: Elsevier B.V, 1991.

[9] L. Stoica, 'Relaxor-PbTiO3 single crystals and polycrystals: processing, growth and characterisation', University of Leeds, 2016.

[10] C. Hammond, *The Basics of Crystallography and Diffraction*. Oxford University Press, 1997.

[11] U. of Cambridge, 'Lattice Planes and Miller Indices', *DoITPoMS*. https://www.doitpoms.ac.uk/tlplib/miller_indices/index.php (accessed Oct. 25, 2021).

[12] S. Shahrokhi *et al.*, 'Emergence of Ferroelectricity in Halide Perovskites', *Small Methods*, vol. 4, p. 2000149, 2020, doi: 10.1002/smtd.202000149.

[13] J. Rödel, W. Jo, K. T. P. Seifert, E. M. Anton, T. Granzow, and D. Damjanovic, 'Perspective on the development of lead-free piezoceramics', *J. Am. Ceram. Soc.*, vol. 92, no. 6, pp. 1153–1177, 2009, doi: 10.1111/j.1551-2916.2009.03061.x.

[14] D. M. Smyth, *The Defect Chemistry of Metal Oxides*. Oxford University Press, 2000.

[15] H. T. Stokes, E. H. Kisi, D. M. Hatch, and C. J. Howard, 'Group-theoretical analysis of octahedral tilting in ferroelectric perovskites', *Acta Crystallogr. Sect. B Struct. Sci.*, vol.

58, no. 6, pp. 934–938, 2002, doi: 10.1107/S0108768102015756.

[16] R. D. Shannon, ‘Revised effective ionic radii and systematic studies of interatomic distances in halides and chalcogenides’, *Acta Crystallogr. Sect. A*, vol. 32, no. 6, pp. 751-, 1976, doi: 10.1107/S0567739476001551.

[17] M. H. Park *et al.*, ‘Ferroelectricity and Antiferroelectricity of Doped Thin HfO2-Based Films’, *Adv. Mater.*, vol. 27, no. 11, pp. 1811–1831, 2015, doi: 10.1002/adma.201404531.

[18] X. Sang, E. D. Grimley, T. Schenk, U. Schroeder, and J. M. Lebeau, ‘On the structural origins of ferroelectricity in HfO2 thin films’, *Appl. Phys. Lett.*, vol. 106, p. 162905, 2015, doi: 10.1063/1.4919135.

[19] S. Starschich and U. Boettger, ‘An extensive study of the influence of dopants on the ferroelectric properties of HfO2’, *J. Mater. Chem. C*, vol. 5, pp. 333–338, 2017, doi: 10.1039/c6tc04807b.

[20] A. Kholkin, N. A. Pertsev, and A. V. Goltsev, ‘Piezoelectricity and Crystal Symmetry’, in *Piezoelectric and Acoustic Materials for Transducer Applications*, A. Safari and E. K. Akdogan, Eds. Springer, 2008.

[21] A. J. Moulson and J. M. Herbert, *Electroceramics: Materials, Properties, Applications*. Springer Science, 1990.

[22] S. Zhang, R. Xia, and T. R. Shrout, ‘Lead-free piezoelectric ceramics vs. PZT?’, *J. Electroceramics*, vol. 19, pp. 251–257, 2007, doi: 10.1007/s10832-007-9056-z.

[23] I. Coondoo, N. Panwar, and A. Kholkin, ‘Lead-free piezoelectrics: Current status and perspectives’, *J. Adv. Dielectr.*, vol. 3, no. 2, p. 1330002, 2013, doi: 10.1142/s2010135x13300028.

[24] M. Barsoum, *Fundamentals of Ceramics*. CRC Press, 2019.

[25] M. Trainer, ‘Ferroelectrics and the Curie Weiss Law’, *Eur. J. Phys.*, vol. 21, pp. 459–464, 2000.

[26] P. V. Lambeck and G. H. Jonker, ‘Ferroelectric domain stabilization in BaTiO3 by bulk ordering of defects’, *Ferroelectrics*, vol. 22, no. 1, pp. 729–731, 1978, doi: 10.1080/00150197808237382.

[27] Y. A. Genenko, J. Glaum, M. J. Hoffmann, and K. Albe, ‘Mechanisms of aging and

fatigue in ferroelectrics', *Mater. Sci. Eng. B Solid-State Mater. Adv. Technol.*, vol. 192, no. C, pp. 52–82, 2015, doi: 10.1016/j.mseb.2014.10.003.

[28] C. Housecroft and A. Sharpe, *Inorganic Chemistry*, 3rd ed. Essex: Pearson Education Ltd., 2008.

[29] P. Chand and A. Bain, *Ferroelectrics: Principles and Applications*. Wiley and Sons, 2017.

[30] J. T. S. Irvine, D. C. Sinclair, and A. R. West, 'Electroceramics: Characterization by Impedance Spectroscopy', *Adv. Mater.*, vol. 2, no. 3, pp. 132–138, 1990, doi: 10.1002/adma.19900020304.

[31] Y. Saito *et al.*, 'Lead-free piezoceramics', *Nature*, vol. 432, pp. 84–87, 2004, doi: 10.1038/nature03028.

[32] J. Rodel, K. Webber, R. Dittmer, W. Jo, M. Kimura, and D. Damjanovic, 'Transferring lead-free piezoelectric ceramics into application', *J. Eur. Ceram. Soc.*, vol. 35, no. 6, pp. 1659–1681, 2015.

[33] J. Rödel and J. F. Li, 'Lead-free piezoceramics: Status and perspectives', *MRS Bull.*, vol. 43, no. 8, pp. 576–580, 2018, doi: 10.1557/mrs.2018.181.

[34] P. K. Panda and B. Sahoo, 'PZT to lead free piezo ceramics: A review', *Ferroelectrics*, vol. 474, no. 1, pp. 128–143, 2015, doi: 10.1080/00150193.2015.997146.

[35] F. W. Lytle, 'X-ray diffractometry of low-temperature phase transformations in strontium titanate', *J. Appl. Phys.*, vol. 35, no. 7, pp. 2212–2215, 1964, doi: 10.1063/1.1702820.

[36] S. G. Cho and P. F. Johnson, 'Evolution of the microstructure of undoped and Nb-doped SrTiO3', *J. Mater. Sci.*, vol. 29, no. 18, pp. 4866–4874, Sep. 1994, doi: 10.1007/BF00356536.

[37] H. S. Tewari, V. K. Shelke, N. K. Gaur, and R. K. Singh, 'Synthesis and Electrical Characterisation of the System Sr1-xYxTi1-xCoxO3', *Mater. Sci. Forum*, vol. 223–224, pp. 257–260, 1996, doi: 10.4028/www.scientific.net/msf.223-224.257.

[38] P. R. Slater, D. P. Fagg, and J. T. S. Irvine, 'Synthesis and electrical characterisation of doped perovskite titanates as potential anode materials for solid oxide fuel cells', *J. Mater. Chem.*, vol. 7, pp. 2495–2498, 1997, doi: 10.1039/a702865b.

[39] T. Kolodiazhnyi and A. Petric, ‘The applicability of Sr-deficient n-type SrTiO3 for SOFC anodes’, *J. Electroceramics*, vol. 15, no. 1, pp. 5–11, 2005, doi: 10.1007/s10832-005-0375-7.

[40] N. Wang *et al.*, ‘Structural and dielectric behavior of giant permittivity SrNbxTi1−xO3 ceramics sintered in nitrogen atmosphere’, *Ceram. Int.*, vol. 42, no. 12, pp. 13593–13600, 2016, doi: 10.1016/j.ceramint.2016.05.153.

[41] M. S. J. Marshall, A. E. Becerra-toledo, L. D. Marks, and M. R. Castell, ‘Defects on Strontium Titanate’, in *Defects at Oxide Surfaces*, Springer, 2015, pp. 327–345.

[42] P. Blennow, K. K. Hansen, L. R. Wallenberg, and M. Mogensen, ‘Electrochemical characterization and redox behavior of Nb-doped SrTiO3’, *Solid State Ionics*, vol. 180, no. 1, pp. 63–70, 2009, doi: 10.1016/j.ssi.2008.10.011.

[43] V. V. Lemanov, ‘Phase transitions in SrTiO3-based solid solutions’, *Phys. Solid State*, vol. 39, no. 9, pp. 1468–1473, 1997, doi: 10.1134/1.1130100.

[44] M. Bäurer, H. Kungl, and M. J. Hoffmann, ‘Influence of sr/ti stoichiometry on the densification behavior of strontium titanate’, *J. Am. Ceram. Soc.*, vol. 92, no. 3, pp. 601–606, 2009, doi: 10.1111/j.1551-2916.2008.02920.x.

[45] R. Meyer and R. Waser, ‘Resistive donor-doped SrTiO3 sensors: I, basic model for a fast sensor response’, *Sensors Actuators, B Chem.*, vol. 101, no. 3, pp. 335–345, 2004, doi: 10.1016/j.snb.2004.04.004.

[46] N. H. Chan, R. K. Sharma, and D. M. Smyth, ‘Nonstoichiometry in SrTiO3’, *J. Electrochem. Soc.*, vol. 128, no. 8, pp. 1762–1768, 1981.

[47] H. Trabelsi *et al.*, ‘Effect of oxygen vacancies on SrTiO3 electrical properties’, *J. Alloys Compd.*, vol. 723, pp. 894–903, 2017, doi: 10.1016/j.jallcom.2017.06.313.

[48] X. Wang, Q. Hu, G. Zang, C. Zhang, and L. Li, ‘Dielectric relaxation properties of SrTiO3 ceramics modulated by stoichiometry’, *Ceram. Int.*, vol. 44, no. 5, pp. 4740–4743, 2018, doi: 10.1016/j.ceramint.2017.12.057.

[49] X. Wang *et al.*, ‘Oxygen-vacancy-related high-temperature dielectric relaxation in SrTiO3 ceramics’, *J. Appl. Phys.*, vol. 107, no. 11, p. 114101, 2010, doi: 10.1063/1.3430987.

[50] R. A. De Souza, ‘Oxygen Diffusion in SrTiO3 and Related Perovskite Oxides’, *Adv.*

Funct. Mater., vol. 25, no. 40, pp. 6326–6342, 2015, doi: 10.1002/adfm.201500827.

[51] S. H. Kim, J. H. Moon, J. H. Park, J. G. Park, and Y. Kim, ‘Analysis of defect formation in Nb-doped SrTiO3 by impedance spectroscopy’, *J. Mater. Res.*, vol. 16, no. 1, pp. 192–196, 2001, doi: 10.1557/JMR.2001.0031.

[52] R. Waser, ‘Bulk Conductivity and Defect Chemistry of Acceptor-Doped Strontium Titanate in the Quenched State’, *J. Am. Ceram. Soc.*, vol. 74, no. 8, pp. 1934–1940, 1991, doi: 10.1111/j.1151-2916.1991.tb07812.x.

[53] M. Schie, R. Waser, and R. A. De Souza, ‘A simulation study of oxygen-vacancy behavior in strontium titanate: Beyond nearest-neighbor interactions’, *J. Phys. Chem. C*, vol. 118, no. 28, pp. 15185–15192, 2014, doi: 10.1021/jp504436t.

[54] E. Echeverri and O. Arnache, ‘Structural and impedance analysis of Co-doped SrTiO3 perovskite’, *J. Phys. Conf. Ser.*, vol. 687, p. 012040, 2016, doi: 10.1088/1742-6596/687/1/012040.

[55] C. Mitra, C. Lin, A. B. Posadas, and A. A. Demkov, ‘Role of oxygen vacancies in room-temperature ferromagnetism in cobalt-substituted SrTiO3’, *Phys. Rev. B - Condens. Matter Mater. Phys.*, vol. 90, p. 125130, 2014, doi: 10.1103/PhysRevB.90.125130.

[56] D. D. Cuong, B. Lee, K. M. Choi, H. S. Ahn, S. Han, and J. Lee, ‘Oxygen vacancy clustering and electron localization in oxygen-deficient SrTiO3: LDA+U study’, *Phys. Rev. Lett.*, vol. 98, no. 11, pp. 1–4, 2007, doi: 10.1103/PhysRevLett.98.115503.

[57] M. Valant, T. Kolodiazhnyi, I. Arčon, F. Aguesse, A. K. Axelsson, and N. M. Alford, ‘The origin of magnetism in Mn-doped SrTiO3’, *Adv. Funct. Mater.*, vol. 22, no. 10, pp. 2114–2122, 2012, doi: 10.1002/adfm.201102482.

[58] G. Ryn and E. Dickey, ‘Co-doping strategies for controlling electrical conductivity of BaTiO3 ceramics.’, in *ISAF2020*, 2020.

[59] R. Meyer, A. F. Zurhelle, R. A. De Souza, R. Waser, and F. Gunkel, ‘Dynamics of the metal-insulator transition of donor-doped SrTiO3’, *Phys. Rev. B*, vol. 94, no. 11, p. 115408, 2016, doi: 10.1103/PhysRevB.94.115408.

[60] T. Higuchi, T. Tsukamoto, N. Sata, and M. Ishigame, ‘Electronic structure of-type by photoemission spectroscopy’, *Phys. Rev. B - Condens. Matter Mater. Phys.*, vol. 57, no. 12, pp. 6978–6983, 1998, doi: 10.1103/PhysRevB.57.6978.

[61] J. Nishiyama, K. Kanehara, H. Takeda, T. Tsurumi, and T. Hoshina, ‘Doping effect of Nb on ionic polarization of SrTiO3’, *J. Ceram. Soc. Japan*, vol. 127, no. 6, pp. 357–361, 2019, doi: 10.2109/jcersj2.19031.

[62] E. Drozdz and A. Kolezyński, ‘The structure, electrical properties and chemical stability of porous Nb-doped SrTiO3-experimental and theoretical studies’, *RSC Adv.*, vol. 7, no. 46, pp. 28898–28908, 2017, doi: 10.1039/c7ra04205a.

[63] R. Moos and K. H. Hardtl, ‘Defect Chemistry of Donor-Doped and Undoped Strontium Titanate Ceramics between 1000° and 1400°C’, *J. Am. Ceram. Soc.*, vol. 80, no. 10, pp. 2549–2562, 2005, doi: 10.1111/j.1151-2916.1997.tb03157.x.

[64] S.-Y. Chung, S.-J. L. Kang, and V. P. Dravid, ‘Effect of Sintering Atmosphere on Grain Boundary Segregation and Grain Growth in Niobium-Doped SrTiO3’, *J. Am. Ceram. Soc.*, vol. 85, no. 11, pp. 2805–2810, 2004, doi: 10.1111/j.1151-2916.2002.tb00532.x.

[65] J. Karczewski, B. Riegel, M. Gazda, P. Jasinski, and B. Kusz, ‘Electrical and structural properties of Nb-doped SrTiO3 ceramics’, *J. Electroceramics*, vol. 24, no. 4, pp. 326–330, 2010, doi: 10.1007/s10832-009-9578-7.

[66] G. Xiao, X. Dong, K. Huang, and F. Chen, ‘Synthesis and characterizations of A-site deficient perovskite Sr 0.9Ti0.8-xGaxNb0.2O3’, *Mater. Res. Bull.*, vol. 46, no. 1, pp. 57–61, 2011, doi: 10.1016/j.materresbull.2010.09.044.

[67] J. T. S. Irvine, P. R. Slater, and P. A. Wright, ‘Synthesis and electrical characterisation of the perovskite niobate-titanates, Sr1-x/2Ti1-xNbxO3’, *Ionics (Kiel).*, vol. 2, no. 3–4, pp. 213–216, 1996, doi: 10.1007/BF02376024.

[68] T. Fujii, Y. Hishinuma, T. Mita, and T. Arakawa, ‘Preparation of Nb doped PZT film by RF sputtering’, *Solid State Commun.*, pp. 1799–1802, 2009, doi: 10.1016/j.ssc.2009.07.021.

[69] W. R. Brant, S. Schmid, Q. Gu, R. L. Withers, J. Hester, and M. Avdeev, ‘Temperature and composition dependent structural investigation of the defect perovskite series Sr1-xTi1-2xNb2xO 3, 0≤x≤0.2’, *J. Solid State Chem.*, vol. 183, no. 9, pp. 1998–2003, 2010, doi: 10.1016/j.jssc.2010.06.002.

[70] T. A. Whittle, W. R. Brant, J. R. Hester, Q. Gu, and S. Schmid, ‘Tailoring phase transition temperatures in perovskites: Via A -site vacancy generation’, *Dalt. Trans.*, vol. 46, no. 22, pp. 7253–7260, 2017, doi: 10.1039/c7dt00352h.

[71] J. N. Baker, P. C. Bowes, J. S. Harris, and D. L. Irving, ‘Mechanisms governing metal vacancy formation in BaTiO3 and SrTiO3’, *J. Appl. Phys.*, vol. 124, no. 11, p. 114101, 2018, doi: 10.1063/1.5044746.

[72] Z. H. Zhao, Y. Dai, and F. Huang, ‘The formation and effect of defect dipoles in lead-free piezoelectric ceramics: A review’, *Sustain. Mater. Technol.*, vol. 20, p. e00092, 2019, doi: 10.1016/j.susmat.2019.e00092.

[73] G. Arlt and H. Neumann, ‘Internal bias in ferroelectric ceramics: Origin and time dependence’, *Ferroelectrics*, vol. 87, no. 1, pp. 109–120, 1988, doi: 10.1080/00150198808201374.

[74] J. Shi, W. Tian, X. Liu, and H. Fan, ‘Electric-field induced phase transition and fatigue behaviors of (Bi0.5+x/2Na0.5-x/2)0.94Ba0.06Ti1-xFexO3 ferroelectrics’, *J. Am. Ceram. Soc.*, vol. 100, no. 3, pp. 1080–1090, 2017, doi: 10.1111/jace.14683.

[75] W. L. Warren, D. Dimos, G. E. Pike, K. Vanheusden, and R. Ramesh, ‘Alignment of defect dipoles in polycrystalline ferroelectrics’, *Appl. Phys. Lett.*, vol. 67, no. June, p. 1689, 1995, doi: 10.1063/1.115058.

[76] W. L. Warren, G. E. Pike, K. Vanheusden, D. Dimos, B. A. Tuttle, and J. Robertson, ‘Defect-dipole alignment and tetragonal strain in ferroelectrics’, *J. Appl. Phys.*, vol. 79, no. 12, pp. 9250–9257, 1996, doi: 10.1063/1.362600.

[77] S. Liu and R. E. Cohen, ‘Multiscale simulations of defect dipole-enhanced electromechanical coupling at dilute defect concentrations’, *Appl. Phys. Lett.*, vol. 111, no. 8, pp. 1–6, 2017, doi: 10.1063/1.4989670.

[78] T. Wang *et al.*, ‘Origin of superior hardening properties in KCuTa3O9-doped K0.5Na0.5NbO3 lead-free piezoelectric ceramics’, *Ceram. Int.*, vol. 43, no. 17, pp. 15666–15677, 2017, doi: 10.1016/j.ceramint.2017.08.126.

[79] J. Yin, C. Li, B. Wu, Z. Li, and J. Wu, ‘Defect-induced superior piezoelectric response in perovskite KNbO3’, *J. Eur. Ceram. Soc.*, vol. 41, no. 4, pp. 2506–2513, 2021, doi: 10.1016/j.jeurceramsoc.2020.11.055.

[80] R. A. Maier, E. Cockayne, M. P. Donohue, G. Cibin, and I. Levin, ‘Substitutional Mechanisms and Structural Relaxations for Manganese in SrTiO3: Bridging the Concentration Gap for Point-Defect Metrology’, *Chem. Mater.*, vol. 32, no. 11, pp. 4651–4662, 2020, doi: 10.1021/acs.chemmater.0c01082.

[81] W. Pan *et al.*, 'Defect structure and dielectric behavior in SrTi1-x(Zn1/3Nb2/3)xO3 ceramics', *J. Alloys Compd.*, vol. 784, pp. 1303–1310, 2019, doi: 10.1016/j.jallcom.2019.01.156.

[82] W. Pan, M. Cao, H. Hao, Z. Yao, Z. Yu, and H. Liu, 'Defect engineering toward the structures and dielectric behaviors of (Nb, Zn) co-doped SrTiO3 ceramics', *J. Eur. Ceram. Soc.*, vol. 40, no. 1, pp. 49–55, 2020, doi: 10.1016/j.jeurceramsoc.2019.09.027.

[83] Z. He *et al.*, 'Origin of low dielectric loss and giant dielectric response in (Nb+Al) co-doped strontium titanate', *J. Am. Ceram. Soc.*, vol. 101, no. 11, pp. 5089–5097, 2018, doi: 10.1111/jace.15762.

[84] B. Zhong, Z. Long, C. Yang, Y. Li, and X. Wei, 'Colossal dielectric permittivity in co-doping SrTiO3 ceramics by Nb and Mg', *Ceram. Int.*, vol. 46, no. 12, pp. 20565–20569, 2020, doi: 10.1016/j.ceramint.2020.05.174.

[85] T. Li *et al.*, 'Giant strain with low hysteresis in A-site-deficient (Bi0.5Na0.5)TiO3-based lead-free piezoceramics', *Acta Mater.*, vol. 128, pp. 337–344, 2017, doi: 10.1016/j.actamat.2017.02.037.

[86] Z. Zhao, Y. Dai, X. Li, Z. Zhao, and X. Zhang, 'The evolution mechanism of defect dipoles and high strain in MnO2-doped KNN lead-free ceramics', *Appl. Phys. Lett.*, vol. 108, no. 17, p. 172906, 2016, doi: 10.1063/1.4948305.

[87] Y. Zhen, Z. Cen, L. Chen, P. Zhao, X. Wang, and L. Li, 'The effect of microstructure on piezoelectric properties and temperature stability for MnO doped KNN-based ceramics sintered in different atmospheres', *J. Alloys Compd.*, vol. 752, pp. 206–212, 2018, doi: 10.1016/j.jallcom.2018.04.138.

[88] F. Zeng *et al.*, 'Large electric field-induced strain in BiFeO3-based ceramics by tuning defect dipoles and phase structure', *Ceram. Int.*, vol. 47, no. 10, pp. 14097–14106, 2021, doi: 10.1016/j.ceramint.2021.01.280.

[89] A. E. McHale, *Phase Diagrams and Ceramics Processes*. New York: Springer Science, 2013.

[90] M. N. Rahaman, *Sintering of Ceramics*. CRC Press, 2007.

[91] U. of Cambridge, 'X-Ray Diffraction', *DoITPoMS*. https://www.doitpoms.ac.uk/tlplib/xray-diffraction/index.php (accessed Oct. 25, 2021).

[92] H. M. Rietveld, ‘A profile refinement method for nuclear and magnetic structures’, *J. Appl. Crystallogr.*, vol. 2, no. 2, pp. 65–71, 1969, doi: 10.1107/s0021889869006558.

[93] R. Hammond, C. Brydson, ‘Generic Methodologies for Nanotechnology’, in *Nanoscale Science and Technology*, M. Kelsall, R. Hamley, I. Geoghegan, Ed. Wiley, 2005, pp. 68–84.

[94] M. I. Mendelson, ‘Average Grain Size in Polycrystalline Ceramics’, *J. Am. Ceram. Soc.*, vol. 52, no. 8, pp. 443–446, 1969, doi: 10.1111/j.1151-2916.1969.tb11975.x.

[95] J. Macdonald, ‘Impedance Spectroscopy and its use in analysing the steady-state AC response of solid and liquid electrolytes.’, *J. Electroanal. Chem*, vol. 223, pp. 25–50, 1987.

[96] E. J. Abram, D. C. Sinclair, and A. R. West, ‘A Strategy for Analysis and Modelling of Impedance Spectroscopy Data of Electroceramics: Doped Lanthanum Gallate’, *J. Electroceramics*, vol. 10, pp. 165–177, 2003, doi: 10.1023/B:JECR.0000011215.56084.87.

[97] R. Schmidt, *Impedance spectroscopy of electroceramics*. Nova Science Publishers, Inc, 2007.

[98] J. C. C. Abrantes, J. A. Labrincha, and J. R. Frade, ‘Representations of impedance spectra of ceramics. Part II. Spectra of polycrystalline SrTiO3’, *Mater. Res. Bull.*, vol. 35, no. 6, pp. 965–976, 2000, doi: 10.1016/S0025-5408(00)00281-6.

[99] A. Bell, ‘In Communication with Andrew Bell’. .

[100] D. C. Sinclair, ‘In Communication with Derek Sinclair’. 2022.

[101] M. Coşkun, A. O. Polat, F. M. Coşkun, Z. Durmuş, C. M. Caglar, and A. Türüt, ‘The electrical modulus and other dielectric properties by the impedance spectroscopy of LaCrO3 and LaCr0.90Ir0.10O3 perovskites’, *RSC Adv.*, vol. 8, no. 9, pp. 4634–4648, 2018, doi: 10.1039/c7ra13261a.

[102] A. Barranco, F. Calderon-Pinar, O. Garcia-Zaldivar, and Y. Gonzalez-Abreu, ‘Relaxor Behaviour in Ferroelectric Ceramics’, in *Advances in Ferroelectrics*, A. Peláiz-Barranco, Ed. IntechOpen, 2012.

[103] V. V. Lemanov, A. V. Sotnikov, E. P. Smirnova, M. Weihnacht, and R. Kunze, ‘Perovskite CaTiO3 as an incipient ferroelectric’, *Solid State Commun.*, vol. 110, no. 11,

pp. 611–614, 1999, doi: 10.1016/S0038-1098(99)00153-2.

[104] C. Bae, J. G. Park, and Y. H. Kim, ‘Effect of sintering condition on the morphology of abnormally grown grains in Nb-doped SrTiO3 ceramics’, *J. Korean Phys. Soc.*, vol. 32, no. SUPPL. 1, pp. 361–363, 1998.

[105] W. Rheinheimer, E. Schoof, M. Selzer, B. Nestler, and M. J. Hoffmann, ‘Non-Arrhenius grain growth in strontium titanate: Quantification of bimodal grain growth’, *Acta Mater.*, vol. 174, pp. 105–115, 2019, doi: 10.1016/j.actamat.2019.05.040.

[106] O. Eibl, P. Pongratz, P. Skalicky, and H. Schmelz, ‘Formation of (111) Twins in BaTiO3 Ceramics’, *J. Am. Ceram. Soc.*, vol. 70, no. 8, p. C-195-C-197, 1987, doi: 10.1111/j.1151-2916.1987.tb05724.x.

[107] M. Bäurer, L. F. Zagonel, N. Barrett, and M. J. Hoffmann, ‘Changes in macroscopic behaviour through segregation in niobium doped strontium titanate’, *J. Phys. Conf. Ser.*, vol. 94, no. 1, p. 012015, 2008, doi: 10.1088/1742-6596/94/1/012015.

[108] R. Gerhardt, ‘Impedance and Dielectric Spectroscopy Revisited: Distinguishing Localised Relaxation from Long-Range Conductivity’, *J. Phys. Chem. Solids*, vol. 55, no. 12, pp. 1491–1506, 1994.

[109] J. Liu, Q. Liu, Z. Nie, S. Nie, D. Lu, and P. Zhu, ‘Dielectric relaxations in fine-grained SrTiO3 ceramics with Cu and Nb co-doping’, *Ceram. Int.*, vol. 45, no. 8, pp. 10334–10341, 2019, doi: 10.1016/j.ceramint.2019.02.089.

[110] I. M. Hodge, M. D. Ingram, and A. R. West, ‘Impedance and modulus spectroscopy of polycrystalline solid electrolytes’, *J. Electroanal. Chem.*, vol. 74, no. 2, pp. 125–143, 1976, doi: 10.1016/S0022-0728(76)80229-X.

[111] P. Sarkar and P. S. Nicholson, ‘Electric Relaxation Studies of Defects and Defect Associates in Dilute Ceria-Lanthanum Oxide Solid Solutions’, *J. Am. Ceram. Soc.*, vol. 72, pp. 1447–1449.

[112] S. Thakur, R. Rai, I. Bdikin, and M. A. Valente, ‘Impedance and modulus spectroscopy characterization of Tb modified Bi0.8A0.1Pb0.1Fe0.9Ti0.1O3 ceramics’, *Mater. Res.*, vol. 19, no. 1, pp. 1–8, 2016, doi: 10.1590/1980-5373-MR-2015-0504.

[113] R. Jose, P. Vineetha, M. A. Rafiq, and K. Venkata Saravanan, ‘Investigation into defect chemistry and relaxation processes in niobium doped and undoped SrBi4Ti4O15 using

impedance spectroscopy', *RSC Adv.*, vol. 8, no. 60, pp. 34437–34448, 2018, doi: 10.1039/c8ra06621c.

[114] R. A. Maier, C. A. Randall, and J. Stevenson, 'Low-Temperature Ionic Conductivity of an Acceptor-Doped Perovskite: I. Impedance of Single-Crystal SrTiO3', *J. Am. Ceram. Soc.*, vol. 99, no. 10, pp. 3350–3359, 2016, doi: 10.1111/jace.14348.

[115] P. Blennow, A. Hagen, K. K. Hansen, L. R. Wallenberg, and M. Mogensen, 'Defect and electrical transport properties of Nb-doped SrTiO3', *Solid State Ionics*, vol. 179, no. 35–36, pp. 2047–2058, 2008, doi: 10.1016/j.ssi.2008.06.023.

[116] F. Horikiri *et al.*, 'The influence of grain boundary on the conductivity of donor doped SrTiO3', *Solid State Ionics*, vol. 177, no. 26-32 SPEC. ISS., pp. 2555–2559, 2006, doi: 10.1016/j.ssi.2006.03.023.

[117] C. C. Wang *et al.*, 'Oxygen-vacancy-related dielectric relaxations in SrTiO3 at high temperatures', *J. Appl. Phys.*, vol. 113, no. 9, p. 094103, 2013, doi: 10.1063/1.4794349.

[118] J. C. C. Abrantes, A. Feighery, A. A. L. Ferreira, J. A. Labrincha, and J. R. Frade, 'Impedance spectroscopy study of niobium-doped strontium titanate ceramics', *J. Am. Ceram. Soc.*, vol. 85, no. 11, pp. 2745–2752, 2002, doi: 10.1111/j.1151-2916.2002.tb00523.x.

[119] Y. Li, M. Borbely, and A. Bell, 'The influence of oxygen vacancies on piezoelectricity in samarium-doped Pb(Mg1/3Nb2/3)O3-PbTiO3 ceramics', *J. Am. Ceram. Soc.*, vol. 104, no. 6, pp. 2678–2688, 2021, doi: 10.1111/jace.17619.

Appendix

A-Site Vacancy Compensation of Donors

$Sr_{1-x/2}Ti_{1-x}Nb_xO_3$

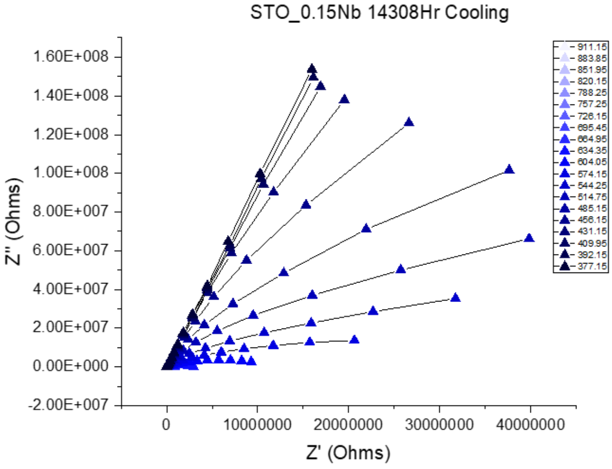
STO_0.15Nb 14308Hr Cooling

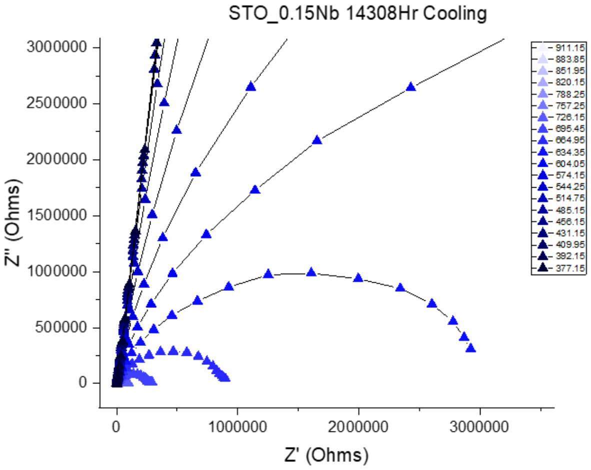
STO_0.15Nb 14308Hr Cooling

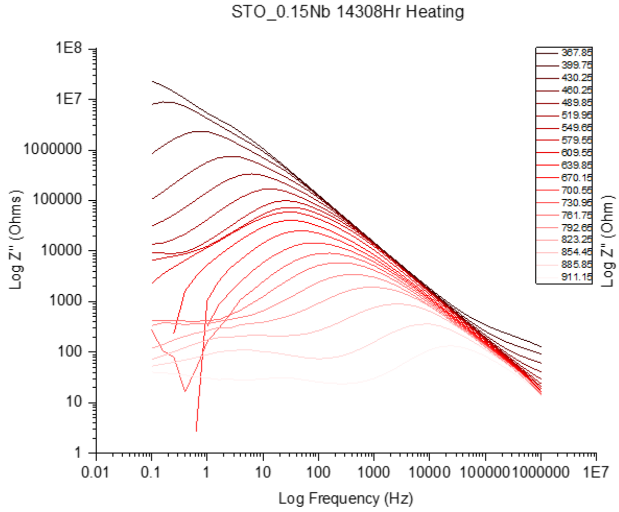
STO_0.15Nb 14308Hr Heating

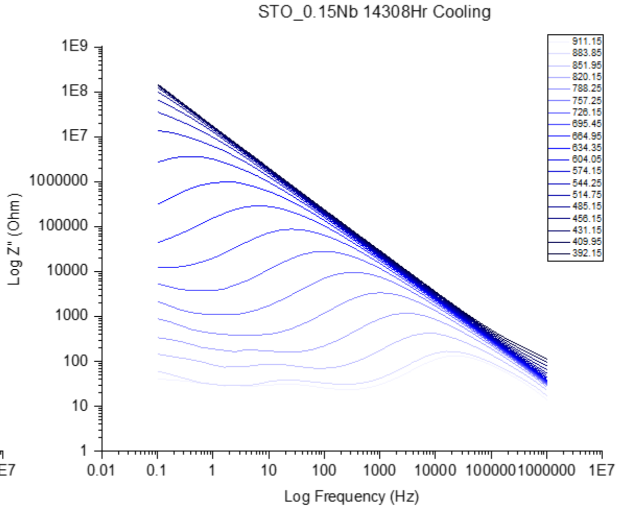
STO_0.15Nb 14308Hr Cooling

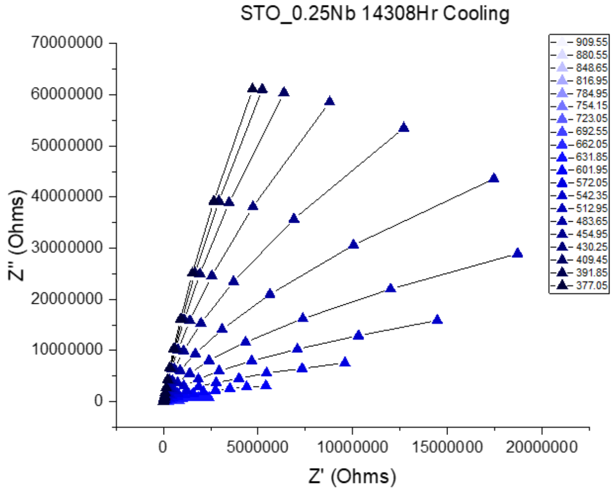
STO_0.25Nb 14308Hr Cooling
Z'' (Ohms)
Z' (Ohms)
70000000
60000000
50000000
40000000
30000000
20000000
10000000
0
0
5000000
10000000
15000000
20000000
909.55
880.55
848.65
816.95
784.95
754.15
723.05
692.55
662.05
631.85
601.95
572.05
542.35
512.95
483.65
454.95
430.25
409.45
391.85
377.05

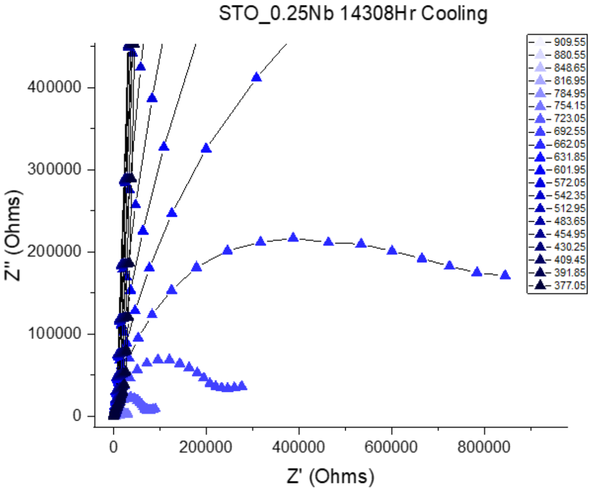
STO_0.25Nb 14308Hr Cooling
Z'' (Ohms)
Z' (Ohms)
400000
300000
200000
100000
0
0
200000
400000
600000
800000
909.55
880.55
848.65
816.95
784.95
754.15
723.05
692.55
662.05
631.85
601.95
572.05
542.35
512.95
483.65
454.95
430.25
409.45
391.85
377.05

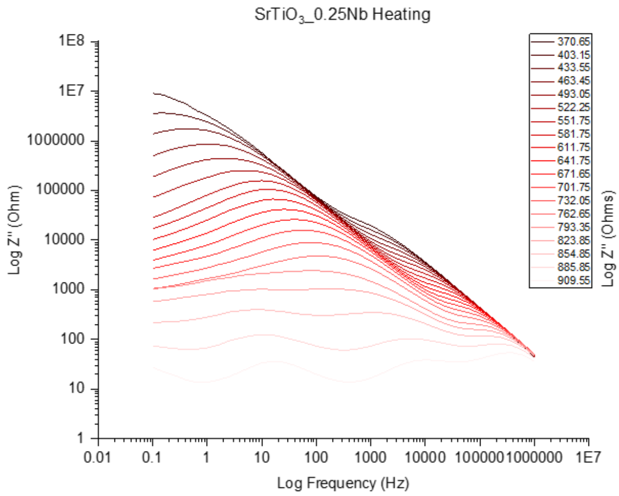
SrTiO$_3$_0.25Nb Heating
Log Z'' (Ohm)
Log Frequency (Hz)
1E8
1E7
1000000
100000
10000
1000
100
10
1
0.01
0.1
1
10
100
1000
10000
100000
1000000
1E7
370.65
403.15
433.55
463.45
493.05
522.25
551.75
581.75
611.75
641.75
671.65
701.75
732.05
762.65
793.35
823.85
854.85
885.85
909.55

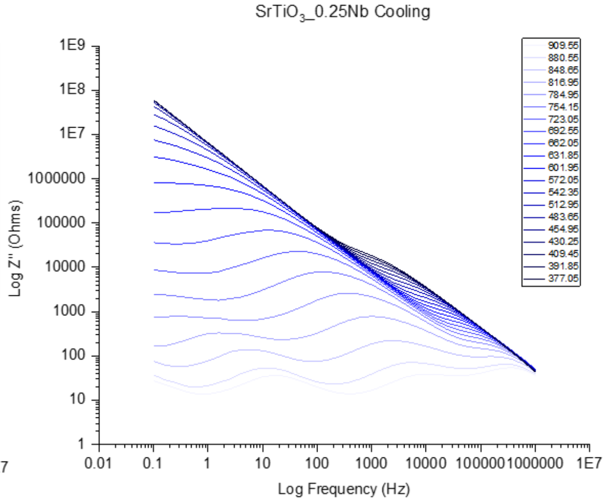
SrTiO$_3$_0.25Nb Cooling
Log Z'' (Ohms)
Log Frequency (Hz)
1E9
1E8
1E7
1000000
100000
10000
1000
100
10
1
0.01
0.1
1
10
100
1000
10000
100000
1000000
1E7
909.55
880.55
848.65
816.95
784.95
754.15
723.05
692.55
662.05
631.85
601.95
572.05
542.35
512.95
483.65
454.95
430.25
409.45
391.85
377.05

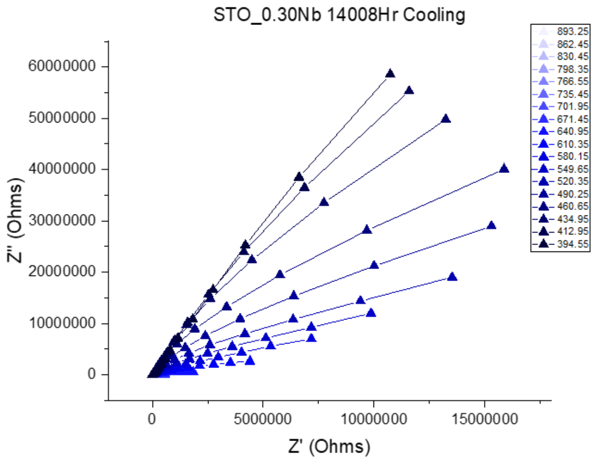
STO_0.30Nb 14008Hr Cooling
Z'' (Ohms)
Z' (Ohms)
60000000
50000000
40000000
30000000
20000000
10000000
0
0
5000000
10000000
15000000
893.25
862.45
830.45
798.35
766.55
735.45
701.95
671.45
640.95
610.35
580.15
549.65
520.35
490.25
460.65
434.95
412.95
394.55

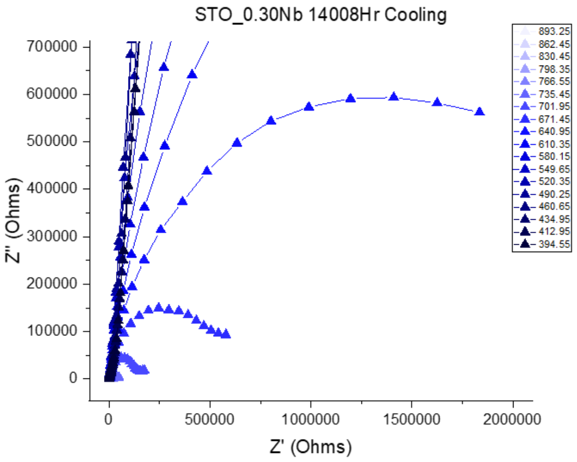
STO_0.30Nb 14008Hr Cooling
Z'' (Ohms)
Z' (Ohms)
700000
600000
500000
400000
300000
200000
100000
0
0
500000
1000000
1500000
2000000
893.25
862.45
830.45
798.35
766.55
735.45
701.95
671.45
640.95
610.35
580.15
549.65
520.35
490.25
460.65
434.95
412.95
394.55

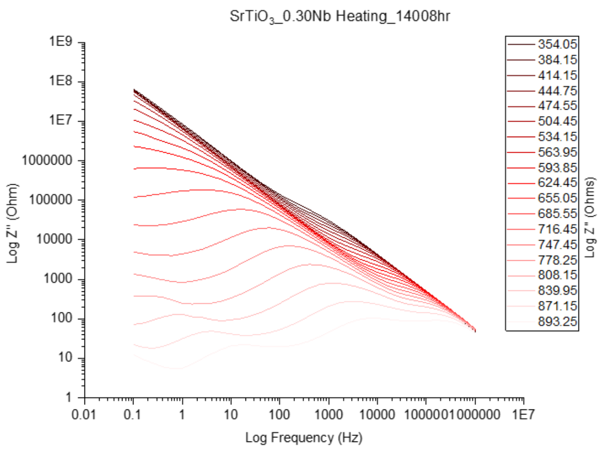

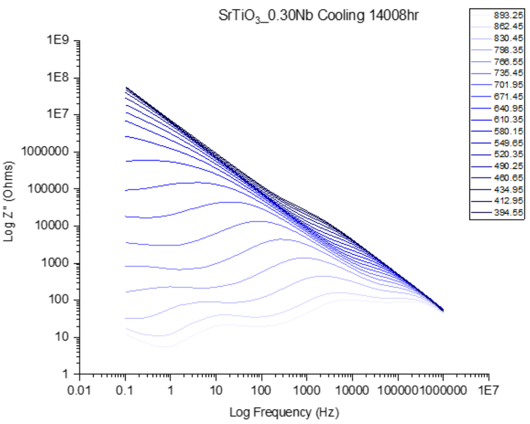

$Sr_{0.9}Ti_{1-x}Nb_xO_3$

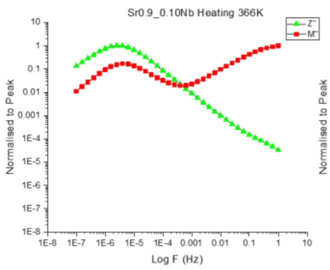

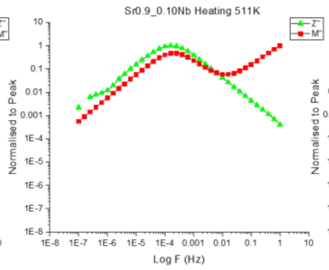

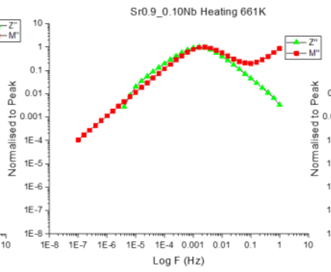

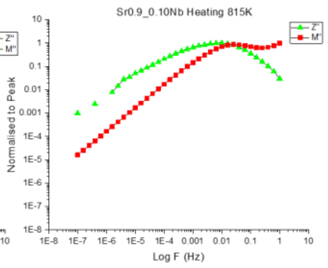

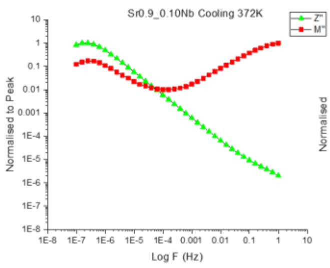

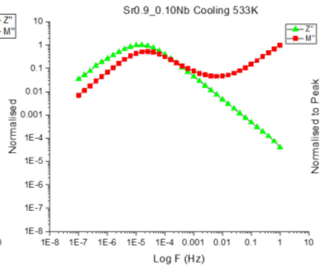

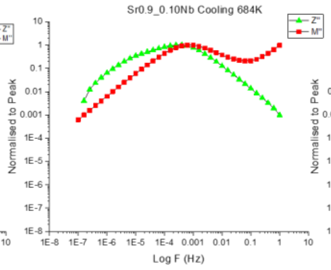

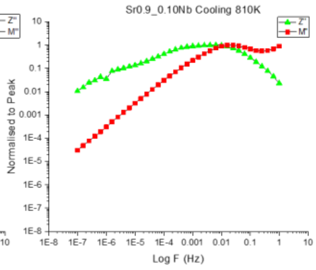

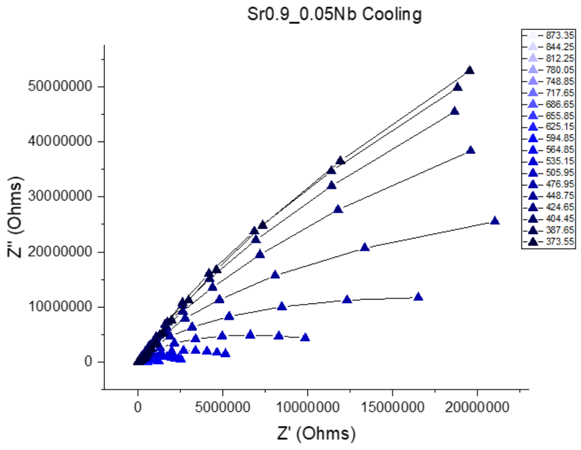

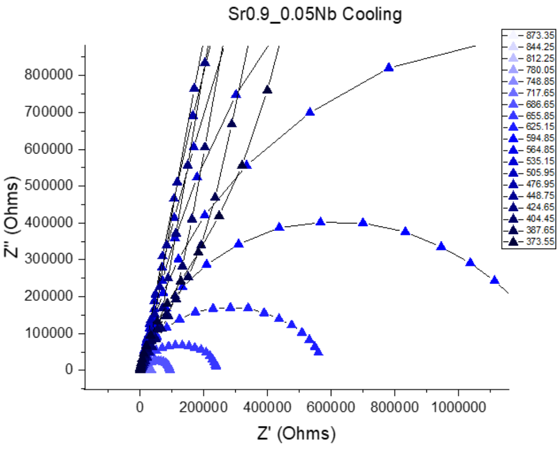

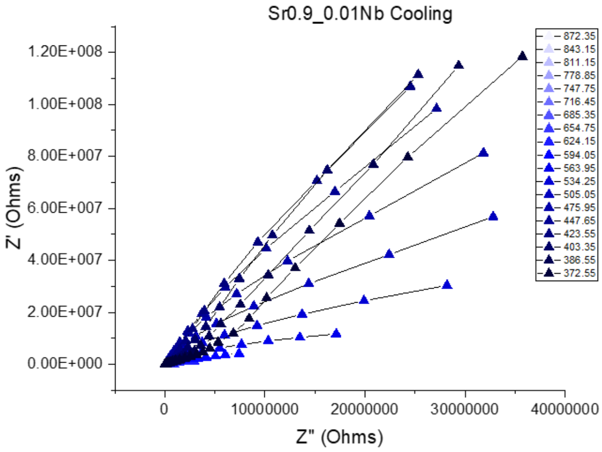
Sr0.9_0.01Nb Cooling
Z' (Ohms)
Z'' (Ohms)
1.20E+008
1.00E+008
8.00E+007
6.00E+007
4.00E+007
2.00E+007
0.00E+000
0
10000000
20000000
30000000
40000000
872.35
843.15
811.15
778.85
747.75
716.45
685.35
654.75
624.15
594.05
563.95
534.25
505.05
475.95
447.65
423.55
403.35
386.55
372.55

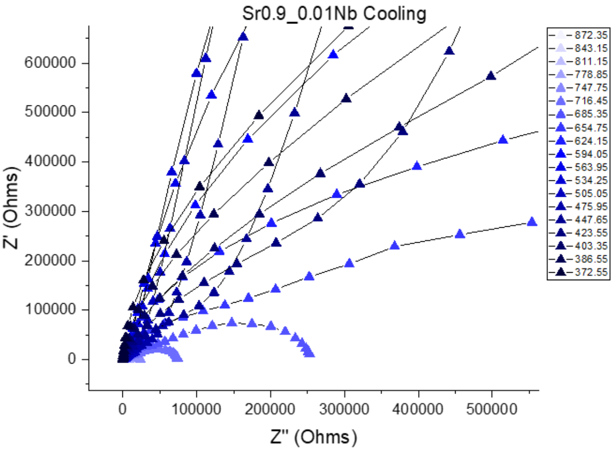
Sr0.9_0.01Nb Cooling
Z' (Ohms)
Z'' (Ohms)
600000
500000
400000
300000
200000
100000
0
0
100000
200000
300000
400000
500000
872.35
843.15
811.15
778.85
747.75
716.45
685.35
654.75
624.15
594.05
563.95
534.25
505.05
475.95
447.65
423.55
403.35
386.55
372.55

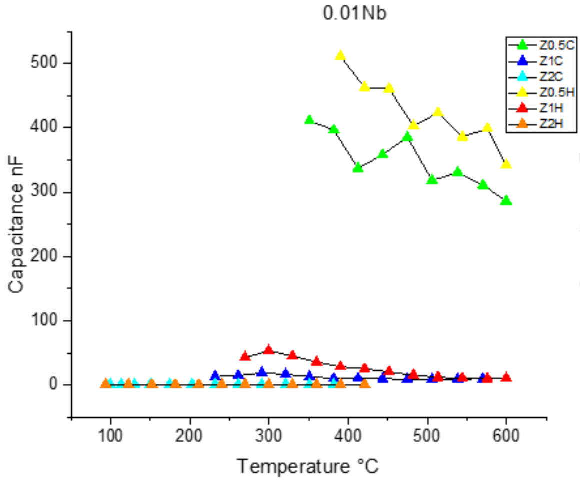
0.01Nb
Capacitance nF
Temperature °C
500
400
300
200
100
0
100
200
300
400
500
600
Z0.5C
Z1C
Z2C
Z0.5H
Z1H
Z2H

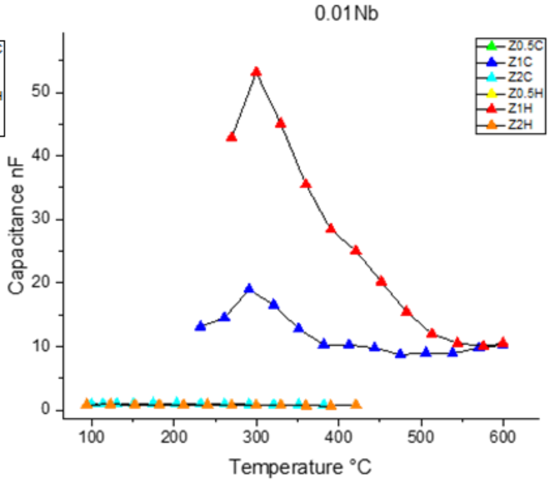
0.01Nb
Capacitance nF
Temperature °C
50
40
30
20
10
0
100
200
300
400
500
600
Z0.5C
Z1C
Z2C
Z0.5H
Z1H
Z2H

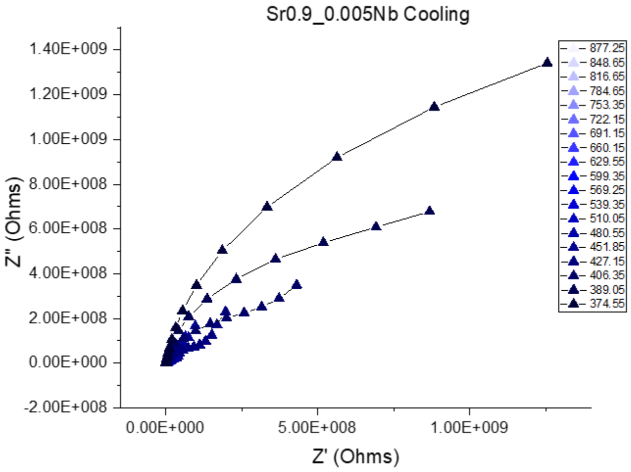
Sr0.9_0.005Nb Cooling
Z'' (Ohms)
Z' (Ohms)
1.40E+009
1.20E+009
1.00E+009
8.00E+008
6.00E+008
4.00E+008
2.00E+008
0.00E+000
-2.00E+008
0.00E+000
5.00E+008
1.00E+009
877.25
848.65
816.65
784.65
753.35
722.15
691.15
660.15
629.55
599.35
569.25
539.35
510.05
480.55
451.85
427.15
406.35
389.05
374.55

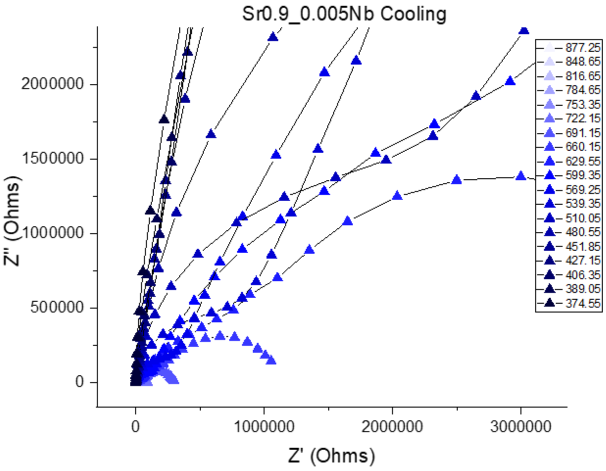
Sr0.9_0.005Nb Cooling
Z'' (Ohms)
Z' (Ohms)
2000000
1500000
1000000
500000
0
0
1000000
2000000
3000000
877.25
848.65
816.65
784.65
753.35
722.15
691.15
660.15
629.55
599.35
569.25
539.35
510.05
480.55
451.85
427.15
406.35
389.05
374.55

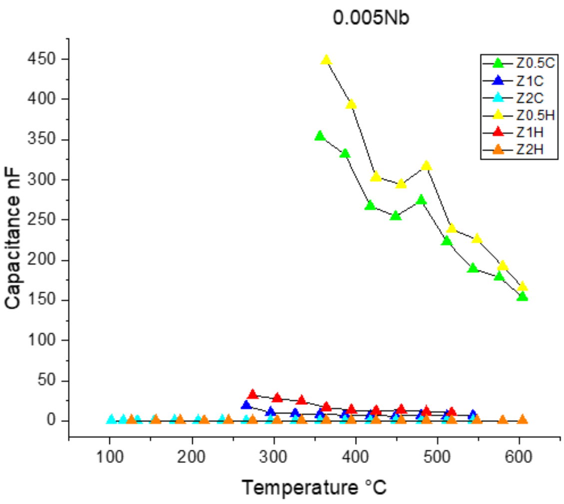

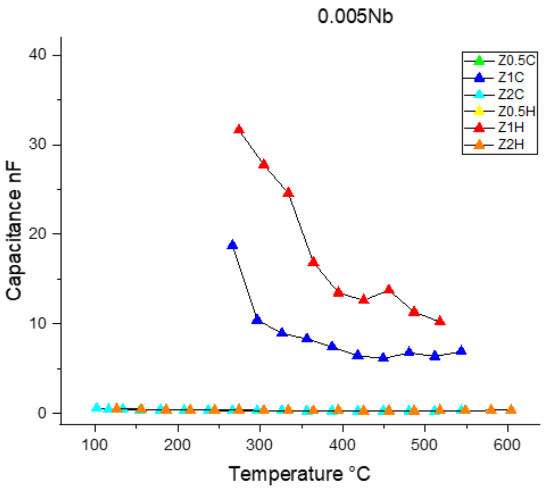

B-Site Nb-Doped $SrTiO_3$

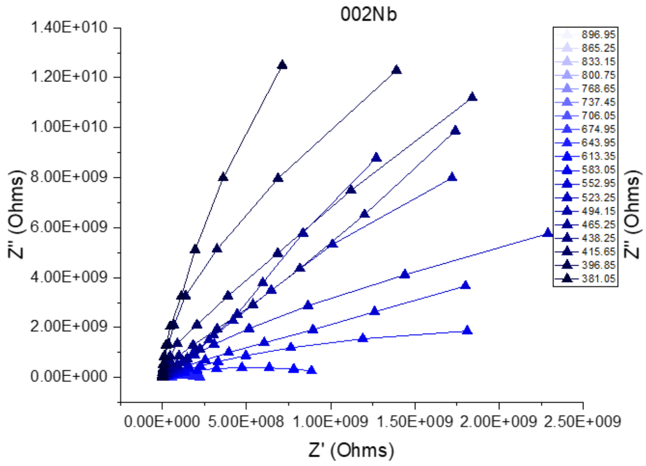

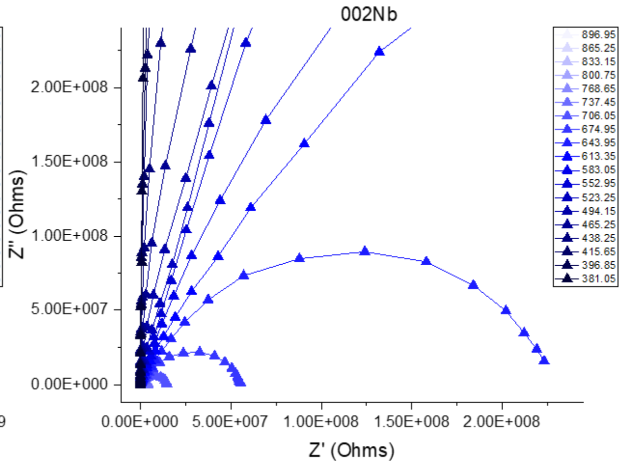

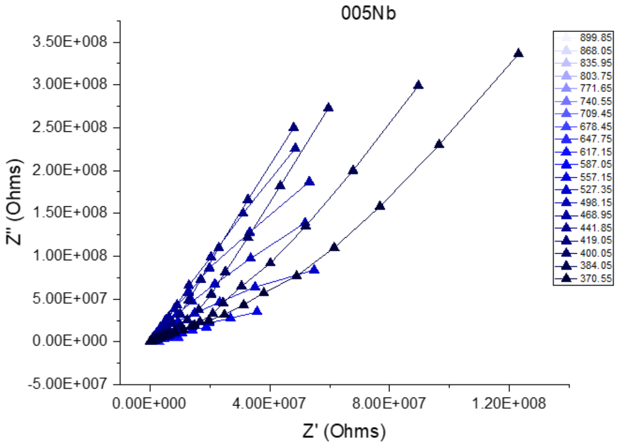

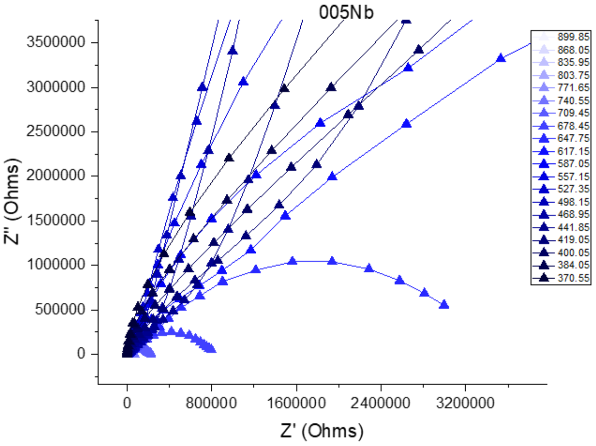

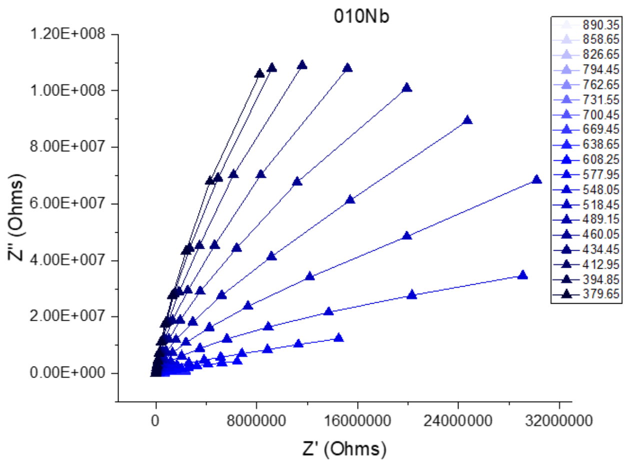
010Nb
Z'' (Ohms)
Z' (Ohms)
1.20E+008
1.00E+008
8.00E+007
6.00E+007
4.00E+007
2.00E+007
0.00E+000
0
8000000
16000000
24000000
32000000
890.35
858.65
826.65
794.45
762.65
731.55
700.45
669.45
638.65
608.25
577.95
548.05
518.45
489.15
460.05
434.45
412.95
394.85
379.65

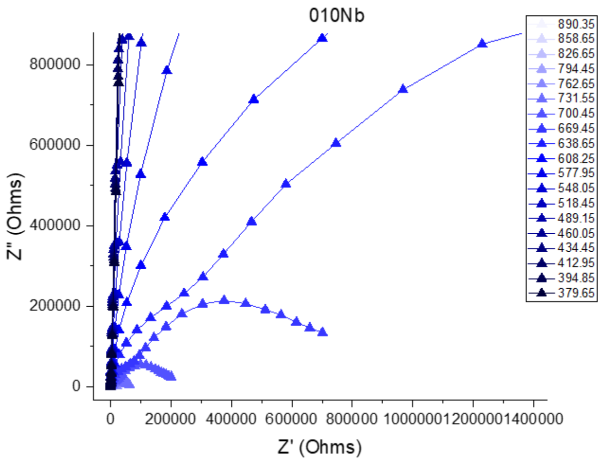
010Nb
Z'' (Ohms)
Z' (Ohms)
800000
600000
400000
200000
0
0
200000
400000
600000
800000
1000000
1200000
1400000
890.35
858.65
826.65
794.45
762.65
731.55
700.45
669.45
638.65
608.25
577.95
548.05
518.45
489.15
460.05
434.45
412.95
394.85
379.65

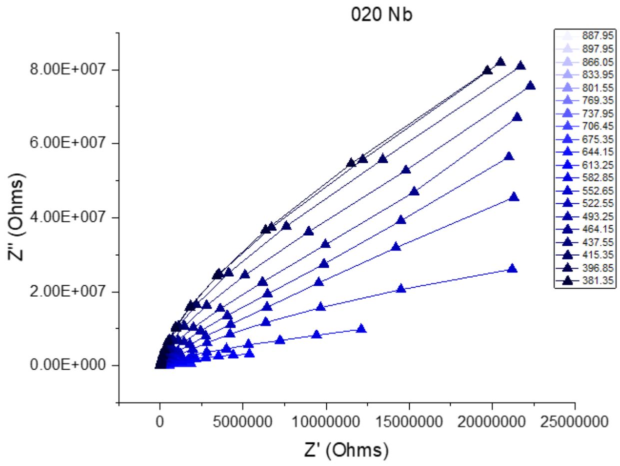
020 Nb
Z'' (Ohms)
Z' (Ohms)
8.00E+007
6.00E+007
4.00E+007
2.00E+007
0.00E+000
0
5000000
10000000
15000000
20000000
25000000
887.95
897.95
866.05
833.95
801.55
769.35
737.95
706.45
675.35
644.15
613.25
582.85
552.65
522.55
493.25
464.15
437.55
415.35
396.85
381.35

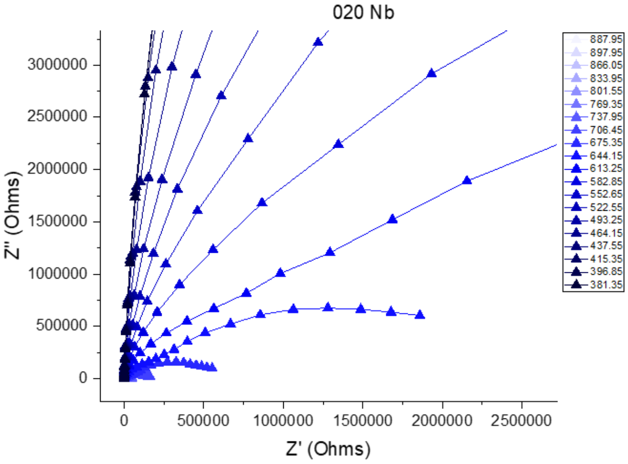
020 Nb
Z'' (Ohms)
Z' (Ohms)
3000000
2500000
2000000
1500000
1000000
500000
0
0
500000
1000000
1500000
2000000
2500000
887.95
897.95
866.05
833.95
801.55
769.35
737.95
706.45
675.35
644.15
613.25
582.85
552.65
522.55
493.25
464.15
437.55
415.35
396.85
381.35

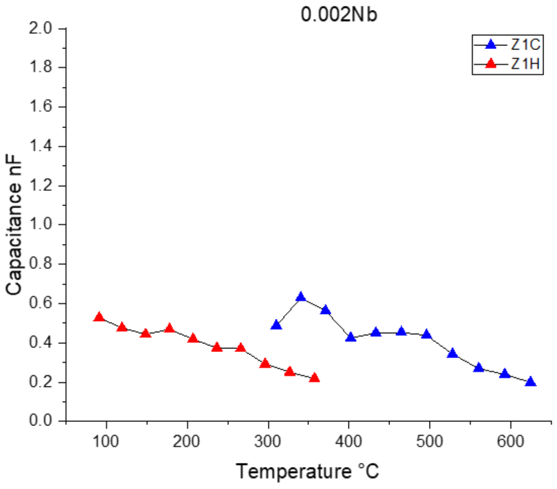
0.002Nb
Capacitance nF
Temperature °C
2.0
1.8
1.6
1.4
1.2
1.0
0.8
0.6
0.4
0.2
0.0
100
200
300
400
500
600
Z1C
Z1H

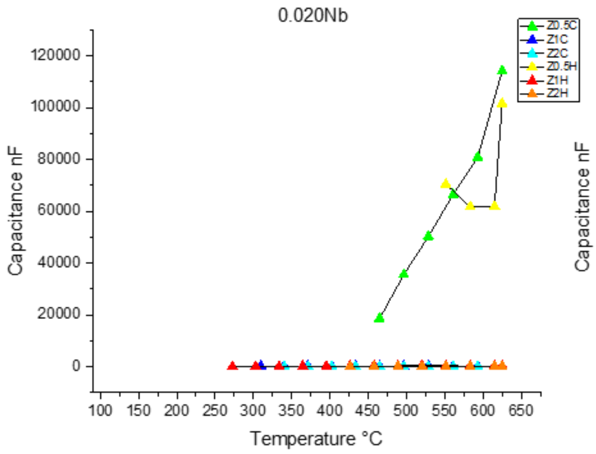

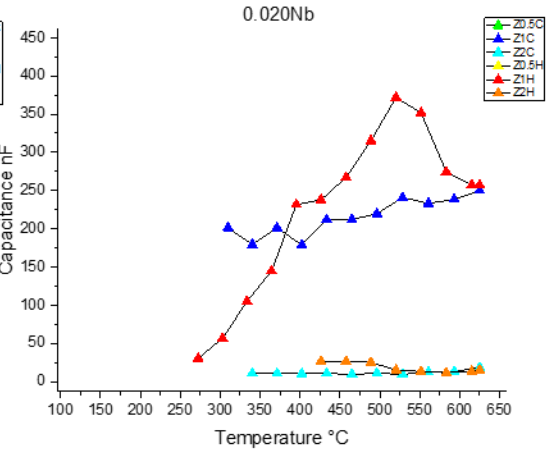

Non-stoichiometric $SrTiO_3$